

This item was submitted to Loughborough's Institutional Repository (<https://dspace.lboro.ac.uk/>) by the author and is made available under the following Creative Commons Licence conditions.



For the full text of this licence, please go to:  
<http://creativecommons.org/licenses/by-nc-nd/2.5/>



# Thesis Access Form

Copy No.....Location.....

Author S. J. Howell-Smith

Title Tribological optimisation of the internal combustion engine piston to bore conjunction through surface modification

Status of access ~~OPEN~~ / ~~RESTRICTED~~ / CONFIDENTIAL

Moratorium Period:.....years, ending...../.....20.....

Conditions of access approved by (CAPITALS):.....

Supervisor (Signature).....

Department of Wolfson School of Mechanical and Manufacturing Engineering

Author's Declaration: *I agree the following conditions:*

Open access work shall be made available (in the University and externally) and reproduced as necessary at the discretion of the University Librarian or Head of Department. It may also be digitised by the British Library and made freely available on the Internet to registered users of the EThOS service subject to the EThOS supply agreements.

*The statement itself shall apply to ALL copies including electronic copies:*

**This copy has been supplied on the understanding that it is copyright material and that no quotation from the thesis may be published without proper acknowledgement.**

**Restricted/confidential work:** All access and any photocopying shall be strictly subject to written permission from the University Head of Department and any external sponsor, if any.

Author's signature.....Date.....

users declaration: for signature during any Moratorium period (Not Open work): <i>I undertake to uphold the above conditions:</i>			
Date	Name (CAPITALS)	Signature	Address

# **Tribological optimisation of the internal combustion engine piston to bore conjunction through surface modification**

**S. J. Howell-Smith**

BEng, MSc

A Thesis submitted in partial fulfilment of the requirements for the  
Degree of Doctor of Philosophy of Loughborough University

Wolfson School of Mechanical & Manufacturing Engineering  
Loughborough University  
Loughborough, UK

© S. J. Howell-Smith

November 2010



CERTIFICATE OF ORIGINALITY

This is to certify that I am responsible for the work submitted in this thesis, that the original work is my own except as specified in acknowledgments or in footnotes, and that neither the thesis nor the original work contained therein has been submitted to this or any other institution for a degree.

..... ( Signed )

..... ( Date )



*Dedicated to Stanislaus Howell-Smith*

## Acknowledgments

---

I wish to whole-heartedly thank my supervisors, and in particular Prof. Homer Rahnejat who first introduced me to the term ‘tribology’ and the ensuing journey of discovery.

I also thank my employers, for the significant time and resources required to undertake this. Specific thanks go to Robertino Wild, Martin Keswick, Nick Farnsworth, Jim Johnson and Martin Case.

Many other individuals have also assisted and deserve my thanks: Bob Temple, Paul King, Sashi Balakrishnan, Andrew Luther, Bryn Littlefair, Mircea Teodorescu, Mike Gore, Ramin Rahmani and James Baker. I look forward to continuing to work with you all.

I thank my wife Yoko and son James for their unremitting love, support, and understanding.

## Abstract

---

Internal combustion (IC) engines used in road transport applications employ pistons to convert gas pressure into mechanical work. Frictional losses abound within IC engines, where only 38-51% of available fuel energy results in useful mechanical work. Piston-bore and ring-bore conjunctions are fairly equally responsible for circa 30% of all engine friction - equivalent to 1.6% of the input fuel each. Therefore, reduction in piston assembly friction would have a direct impact on specific performance and / or fuel consumption.

In motorsport, power outputs and duty cycles greatly exceed road applications. Consequently, these engines have a shorter useful life and a high premium is placed on measures which would increase the output power without further reducing engine life. Reduction of friction offers such an opportunity, which may be achieved by improved tribological design in terms of reduced contact area or enhanced lubrication or both. However, the developments in the motorsport sector are typically reactive due to a lack of relative performance or an *ad-hoc* reliance, based upon a limited number of actual engine tests in order to determine if any improvement can be achieved as the result of some predetermined action. A representative scientific model generally does not exist and as such, investigated parameters are often driven by the supply chain with the promise of improvement. In cylinder investigations are usually limited to bore surface finish, bore and piston geometrical form, piston skirt coatings and the lubricant employed. Of these investigated areas newly emerging surface coatings are arguably seen as predominate.

This thesis highlights a scientific approach which has been developed to optimise piston-bore performance. Pre-existing methods of screening and benchmarking alterations have been retained such as engine testing. However, this has been placed in the context of validation of scientifically driven development. A multi-physics numerical model is developed, which combines piston inertial dynamics, as well as thermo-structural strains within a thermo-elastohydrodynamic tribological framework. Experimental tests were performed to validate the findings of numerical models. These tests include film thickness measurement and in-cylinder friction measurement, as well as the numerically-indicated beneficial surface modifications. Experimental testing was performed on an in-house motored engine at Capricorn Automotive, a dynamometer mounted single-cylinder 'fired' engine at Loughborough University, as well as on other engines belonging to third party clients of Capricorn. The diversity of tests was to ascertain the generic nature of any findings.

The multi-physics multi-scale combined numerical-experimental investigation is the main contribution of this thesis to knowledge. One major finding of the thesis is the significant role that bulk thermo-structural deformation makes on the contact conformity of piston skirt to cylinder liner contact, thus advising piston skirt design. Another key finding is the beneficial role of textured surfaces in the retention of reservoirs of lubricant, thus reducing friction.

**Keywords:** Piston skirt lubrication, Thermo-elastohydrodynamics, Thermo-elastic global deformation, Laser surface texturing, Plateau honing

## Table of contents

---

Thesis Access Form .....	i
Acknowledgments.....	i
Abstract .....	ii
Table of contents.....	iii
List of tables and figures .....	vii
Nomenclature .....	xiii
Nomenclature .....	xiii
Glossary of terms .....	xvi
Chapter 1 Introduction .....	1
1.1 Problem definition.....	1
1.2 Piston assembly preamble .....	4
1.2.1 Piston assembly components.....	4
1.2.2 Piston assembly sources of friction .....	7
1.2.3 Factors influencing piston assembly drag .....	8
1.2.4 Research focus.....	13
1.3 Aims and objectives .....	13
1.3.1 Objectives .....	13
1.3.2 Limitation in research scope.....	14
1.4 Methodology .....	14
1.4.1 Numerical methodology .....	14
1.4.2 Experimental methodology .....	15
1.5 Structure of this thesis and third party contributory acknowledgments.....	16
Chapter 2 Literature review .....	18
2.1 Introduction .....	18
2.2 Surface contact and lubrication: A historical perspective .....	18
2.2.1 Body contact and deflection .....	19
2.2.2 The importance of lubrication in engineering .....	20
2.2.3 Principles of lubrication .....	21
2.2.4 Measurements in lubricated contacts .....	24
2.3 Internal combustion engine tribology .....	25
2.3.1 Historical development of the internal combustion engine.....	25
2.3.2 Numerical predictions of piston-lubricated conjunctions .....	27

2.3.3 Experimental measurements of piston-skirt oil film thickness .....	31
2.3.4 Piston slap and dynamics .....	36
2.3.5 Use of finite element analysis .....	38
2.3.6 Cylinder finish and wear .....	41
2.3.7 Piston and cylinder friction .....	42
2.3.8 Coatings, surface treatments and lubricant additives .....	46
Chapter 3 Piston assembly dynamics.....	52
3.1 Overview .....	52
3.2 Piston kinematics .....	53
3.2.1 Calculation of piston vertical position.....	55
3.2.2 Calculation of piston velocity.....	57
3.2.3 Calculation of piston acceleration .....	58
3.3 Theoretical analysis.....	59
3.3.1 Dynamics of piston axial, lateral, and titling motions.....	59
Chapter 4 Tribology of the piston skirt conjunction.....	63
4.1 The skirt-to-bore contact .....	63
4.2 Contact geometry .....	64
4.3 Contact conjunction .....	65
4.4 Elastic film shape .....	66
4.5 Contact deformation.....	67
4.6 Lubricant rheological state.....	71
4.7 Contact loads and moments .....	73
4.8 Method of solution .....	74
4.9 Calculation of thermo-elastic deformation.....	82
4.9.1 A brief history of the finite element method .....	82
4.9.2 An overview of the finite element method .....	83
4.9.3 General applied methodology .....	85
4.9.4 Contact analysis.....	86
Chapter 5 Development of test rigs and components .....	89
5.1 Introduction .....	89
5.2 Test engine choice.....	89
5.3 Component development CRF450R .....	91
5.3.1 Cylinder bore / bore surface .....	91
5.3.2 Piston sub-assembly .....	100

5.4 Development of etching processes and component modification.....	110
5.4.1 Piston skirt etching .....	110
5.4.2 Bore surface etching using a laser method .....	113
5.4.3 Impression modification of the cylinder bore surface.....	115
5.5 Development / instrumentation for film thickness measurement.....	117
5.6 Development of a floating liner .....	120
5.7 CRF Engine installation, instrumentation, and test procedure.....	121
5.7.1 Test cell installation: .....	121
5.7.2 Test cell instrumentation: .....	122
5.7.3 CRF test procedure .....	127
5.8 Development of motored engine tester .....	128
5.8.1 Discussion .....	128
5.8.2 Motored engine concept .....	128
5.8.3 Choice of base motored engine .....	130
5.8.4 Development of representative in-cylinder pressure and side force .....	131
5.8.5 Calculation of crank-shaft torque due to gas pressure.....	133
5.8.6 Development of an air-spring motored engine.....	134
Chapter 6 Experimental results .....	141
6.1 Oil film thickness results.....	141
6.2 Cylinder bore experimental results .....	141
6.3 Experimental results for differing piston configurations .....	152
Chapter 7 Numerical results.....	160
7.1 Preamble.....	160
7.2 EHL of ‘cold’ skirt profile .....	161
7.3 EHL of ‘hot’ thermally deformed piston skirt conjunction .....	169
7.4 Thermo-elastic distortion .....	172
7.4.1 Procedure for evaluation of thermo-structural deformation.....	172
7.4.2 Calculation of thermal distortion.....	173
7.4.3 Calculation of thermo-structural distortion .....	176
7.5 Thermo-elastic EHL.....	180
7.6 Surface modification .....	184
Chapter 8 Overall conclusion & suggestions for future work .....	190
8.1 Overall conclusions.....	190
8.2 Achievement of aims.....	191

8.3 Contributions to knowledge .....	192
8.4 Critical assessment and suggestions for future work. ....	192
References.....	194
Appendix 1 Side force validation .....	211
A1.1 Methodology .....	211
A1.2 Connecting rod dynamics.....	211
A1.2.1 Component forces.....	214
A1.3 Validation of side force .....	217
A1.2 Single-cylinder model .....	218
A1.4 Operating conditions and results .....	220
Appendix 2 Gudgeon-pin contributory torque.....	225
A2.1 Introduction .....	225
A2.2 Calculation of gudgeon pin torque .....	225
Appendix 3 FE contact ‘footprints’ .....	229
Appendix 4 Development of CRF floating liner.....	234
A4.1 Design and development .....	234
Appendix 5 Input parameters and boundary conditions .....	241
A5.1 QSTS Thermal boundary conditions.....	241
A5.2 QSTS Structural analysis loads .....	243
A5.3 Lubricant properties QSTS thermo-elastic analysis.....	244
A5.4 Calculation of part operating temperatures .....	244
Appendix 6 Peer-reviewed publications .....	247

## List of tables and figures

Table 1.1 Potential engine and transmission savings.....	1
Figure 1.1 Proportion of energy and losses in an IC engine .....	2
Figure 1.2 Frictional losses in an IC engine simulating urban driving .....	3
Figure 1.3 Frictional loss contribution from various IC engine sub-systems .....	4
Figure 1.4 The piston assembly. ....	5
Figure 1.5 The piston assembly .....	6
Figure 1.6 Simplified forces on the piston assembly .....	6
Figure 1.7 Piston cooling / squirt jets (PCJ) .....	9
Figure 1.8a Torque plate honing .....	10
Figure 1.8b Torque plate honing and cylindricity comparison .....	10
Figure 1.9 Integrated numerical-experimental approach .....	14
Figure 1.10 Flowchart for planned investigation .....	16
Figure 2.1 A structure discretised into elements.....	19
Table 2.1 Characteristic properties of some synthetic lubricants .....	21
Figure 2.2 Lubricant entrainment in a converging gap .....	22
Figure 2.3 Structure of amorphous paraffin.....	23
Figure 2.4 Increasing skirt-to-bore contact area for differing skirt types .....	33
Figure 2.5 AE 'X-Piston' and resulting reduction in fuel consumption .....	35
Figure 2.6 Piston skirt-bore contact pressure.....	40
Figure 2.7 'Floating liner' .....	46
Figure 3.1 Piston assembly mechanism (zero offset) .....	53
Figure 3.2 Piston assembly mechanism (offset) .....	54
Figure 3.3 Free-body diagram of forces on the piston.....	60
Figure 4.1 Friction force at 2000rpm for differing skirt combinations.....	63
Figure 4.2 Coordinates used for piston to bore analysis .....	65
Figure 4.3 Piston profiles (exaggerated diagrammatically) .....	68
Figure 4.3a Sign conventions for stresses within a solid volume .....	71
Figure 4.4 Flowchart of numerical procedure.....	81
Figure 4.5 Types of tetrahedral element .....	84
Figure 4.6 General element recommendations .....	85
Figure 4.7 Contact elements .....	87
Figure 4.8 Contact skewing due to relative displacement of bodies.....	87



Figure 4.9 FE Flowchart determining thermo-structural global deformation.....	88
Table 5.1 Criteria for engine selection.....	89
Table 5.2 Engine characteristics CRF.....	90
Figure 5.1 Cutaway of CRF450R engine.....	90
Figures 5.2 CRF450R cylinder barrel .....	90
Figure 5.3 Replaceable liner .....	91
Figure 5.4 Replaceable liner carrier.....	91
Table 5.3 % by weight composition replacement water jacket .....	92
Table 5.4 % by weight composition for manufactured CRF liners .....	92
Figure 5.5 Detail design for replacement ‘wet’ cylinder liners .....	93
Figure 5.6 Bore surface coatings .....	94
Table 5.5 Developed bore surface finishes .....	96
Figure 5.7a Roughness parameters .....	97
Figure 5.7b Definition of cross-hatch angle (CHA) .....	97
Figure 5.8 ‘Plateau’ finish.....	99
Figure 5.9 ‘Standard’ finish .....	99
Figure 5.10 Fatigue data, AA2618.....	100
Table 5.6 Developed gudgeon-pin material.....	101
Figures 5.11 Replacement piston showing part variation table .....	102
Figure 5.12 High endurance gudgeon pin.....	103
Figure 5.13 Structural analysis of piston assembly .....	103
Figure 5.14 Piston to bore clearance for a given application.....	104
Figure 5.15 Radial and elliptical construction of piston outside form.....	105
Table 5.7 Equation based elliptic piston OD forms.....	106
Figure 5.16 Major and minor axis radial drops (P1084).....	106
Figure 5.17 P1084 Selection of manufactured derivative parts .....	107
Figure 5.18 Industry standard and developed skirt finishes .....	107
Figure 5.19 Piston ring terminology .....	109
Table 5.8 SEM analysis of OEM compression ring working face.....	109
Table 5.9 SEM analysis of OEM oil rail working face.....	110
Figure 5.20 Laser used for piston skirt etching.....	111
Figure 5.21 Section through skirt etching pre and post polishing .....	111
Table 5.10 Skirt laser processing parameters.....	111
Figure 5.22 Skirt etching after polishing and non-contact surface plot.....	112

Figure 5.23 Type 30 etching trace in direction of entrainment.....	112
Table 5.11 Calculated roughness parameters (TalyMap Gold) .....	113
Table 5.12 Laser specification for bore surface etching .....	113
Figure 5.24 Etch pattern and region of application, CRF .....	114
Figure 5.25 Processed etching, CRF .....	114
Figure 5.26 Type ‘A’ indentation .....	116
Figure 5.27 Resulting bore surface indentations.....	116
Figure 5.28 Etched and run component .....	117
Figure 5.29 Piezoelectric sensor bonded to liner outer surface .....	117
Figure 5.30 Example pulse from steel-oil-air interfaces.....	119
Figure 5.31 Example pulse from steel-oil-air interfaces (FFT) .....	119
Figure 5.32 Schematic of the ultrasonic pulsing and receiving apparatus.....	120
Figure 5.33 Test cell with CRF engine mounted and guarding removed .....	121
Figure 5.34 S3000 dynamometer performance curve.....	122
Figure 5.35 Instrumentation used for CRF testing.....	123
Table 5.13 Recorded data streams (PXI) .....	124
Figure 5.36 Lambda sensor installation .....	124
Table 5.14 Typical spread-sheet output to calculate correction factor .....	125
Figure 5.37 10 cycle average recorded CRF in-cylinder pressure.....	126
Table 5.15 CRF test procedure .....	127
Figure 5.38 Illustration of fired engine frictional reduction resolution .....	128
Figure 5.39 Air spring principal for pressure generation.....	129
Table 5.16 Free forces and moments .....	129
Table 5.17 Motored engine details.....	130
Figure 5.40 In-cylinder pressure CRF vs. ASME.....	132
Figure 5.41 Side force due to gas pressure CRF vs. ASME.....	132
Figure 5.42 Contribution to crank torque due to gas pressure .....	134
Figure 5.43 ASME base frame and modal analysis results .....	134
Figure 5.45 ASME test rig lubrication system schematic diagram .....	135
Figure 5.46 Specification of sump cooling system.....	136
Figure 5.47 ASME pneumatic supply and in-cylinder control schematic .....	137
Figure 5.48 Rotary valve operation .....	138
Figure 5.49 Over-pressurisation valve and cylinder head cut-away.....	138
Table 5.18 Material properties, ASME cylinder heads.....	139

Figure 5.50 ASME 964 base engine dynamometer results (WOT) .....	139
Figure 6.1 in-cylinder film thickness measurement (1,800rpm).....	141
Figure 6.2 AA2618 and cast iron liner types vs. baseline wet liner .....	143
Figure 6.3 A DLC coated liner vs. baseline wet liner.....	145
Figure 6.4 Effects of improved surface roughness and laser texturing.....	147
Figure 6.5 Flow around high pressure regions.....	148
Figure 6.6(a) Model of laser ablated textures at the TDC position.....	149
Figure 6.6(b) Flow pattern with laser textured bore surface.....	149
Figure 6.7 Comparison between bore construction and localised indentation .....	151
Figure 6.8 The effect of various piston coatings / surface treatments .....	155
Figure 6.9: Benchmarking of pistons with different honing angle .....	157
Figure 6.10 ASME: Baseline part (STD) vs. oil temperature.....	159
Figure 7.1 Localised piston skirt contact .....	161
Figure 7.2 Localised bore thrust wear.....	161
Figure 7.3 The undeformed CRF ‘cold’ piston skirt axial profile .....	164
Figure 7.4 Hydrodynamic pressure distribution at Pmax (11°) .....	165
Figure 7.5 Cold skirt isobaric pressures (Pmax, 11°).....	166
Figure 7.6 Oil film thickness contour for case in fig. 7.5 .....	167
Figure 7.7 Centre line (90°) lubricant film thickness from fig. 7.6 .....	168
Figure 7.8 Skirt profile after ‘hot’ thermal analysis (Pmax).....	170
Figure 7.9 Lubricant generated pressure (iso-viscous ‘hot’) .....	171
Figure 7.10 Isobaric pressure for ‘hot’ skirt profile (Pmax).....	171
Figure 7.11 Diagrammatic representation of skirt deformation.....	173
Figure 7.12 Temperature gradient within a spark ignition piston.....	174
Figure 7.13 Piston thrust axis thermal deformation.....	174
Table 7.1 Mean heat transfer coefficients used in diesel piston analysis .....	174
Figure 7.14 P1084 Predicted temperature.....	175
Figure 7.15 P1084 Thermal displacement .....	175
Figure 7.16 ‘Wet’ liner surface temperature differential .....	176
Figure 7.17 ‘Wet’ liner surface temperature profile .....	176
Figure 7.18 Thermal distribution in liner.....	176
Figure 7.19 Resulting thermal displacement (x,y,z) .....	176
Figure 7.20 QSTS constraints .....	177
Figure 7.21 QSTS loads .....	177

Figure 7.22 CRF skirt and bore distortion .....	178
Figure 7.24a ATDC 11° footprint .....	180
Figure 7.24b ATDC 18° footprint .....	180
Figure 7.24c ATDC 26° footprint .....	180
Figure 7.24d ATDC 79° footprint .....	180
Figure 7.24e Relative footprint position of piston within liner .....	180
Figure 7.25 Lubricant pressure distribution (hot constrained skirt) .....	181
Figure 7.26a Film thickness ( $\mu\text{m}$ ) contour (hot constraint skirt) .....	181
Figure 7.26b Lubricant mass flow vector plot (hot constraint skirt) .....	182
Figure 7.27a Film thickness prediction overlay and actual run part .....	183
Figure 7.27b Parameter variation through skirt centre .....	183
Figure 7.28 Modified skirt surface featuring an introduced sinusoidal waveform .....	186
Figure 7.29 Lubricant reaction pressure vs. position on piston skirt .....	187
Figure 7.30 Lubricant reaction pressure vs. position on piston skirt .....	188
Figure 7.31 Unwrapped film thickness on piston skirt .....	188
Figure 7.32 Comparison of predicted film thicknesses .....	189
Figure A1.1 Kinematics of crank-slider mechanism .....	212
Figure A1.2 Resolved force diagram on piston .....	214
Figure A1.3 Resolved force diagram on the connecting rod .....	215
Figure A1.4 ADAMS single-cylinder engine assembly .....	219
Table A1.1 Parts in the multi-body single-cylinder engine model .....	219
Table A1.2 Constraints imposed in the multi-body single-cylinder engine model .....	219
Figure A1.5 Combustion force on piston crown .....	220
Figure A1.6 Vertical force due to inertia .....	221
Figure A1.7 Resulting vertical force on piston .....	221
Figure A1.8 Piston velocity .....	222
Figure A1.9 Resulting piston acceleration .....	222
Figure A1.10 Horizontal piston-bore force not including rod inertia .....	223
Figure A1.11 Horizontal force due to rod inertia .....	223
Figure A1.12 Total resulting piston horizontal force .....	224
Table A2.1 Friction coefficients as per Fox (2005) .....	227
Figure A2.1 Pin bore friction measurements .....	227
Figure A2.2 Connecting-rod small end friction coefficients .....	228
Figure A2.3 Connecting-rod small end resulting torque .....	228

Figure A3.1 Piston to bore contact results .....	229
Figure A3.2 FE contact analyses ‘footprints’ .....	232
Table A3.1 Computational requirements for one crank angle .....	233
Figure A3.3 Typical solution time per crank angle investigated .....	233
Figure A4.1 Kistler 9131B Force transducer specification.....	234
Figure A4.2 Kistler 9131B transducer ‘pairing’ within assembly .....	235
Table A4.1 Physical and mechanical properties of construction .....	236
Figure A4.3 Modal analysis of ‘floating liner’ .....	236
Table A4.2 Modal analysis tabulated results .....	237
Figure A4.4 Upper detail of floating liner assembly .....	237
Figure A4.5 Flowchart and physical components used in data acquisition.....	239
Figure A4.6 Calibration of floating liner and charge amplifier set-up .....	239
Figure A4.7 LabView block programming interface.....	240
Figure A4.8 LabView operator interface / results screen .....	240
Table A5.1 Thermal boundary constraints for QSTS analysis .....	242
Table A5.2 QSTS analysis applied loads.....	243
Table A5.3 QSTS analysis applied loads.....	243
Table A5.4 Lubricant properties .....	244
Figure A5.1 Retained hardness at temperature (softening curves), AA4032-T6.....	245
Figure A5.2 Hardness measurements on piston after running.....	245
Figure A5.3 Retained hardness vs. temperature, AA4032-T6.....	246

## Nomenclature

---

$a$	Height measured from centre of gudgeon pin to piston crown ( $m$ )
$a_r$	Ring radial wall thickness ( $m$ )
$a_p$	Piston acceleration ( $ms^{-2}$ )
$b$	Distance to piston centre of mass below crown ( $m$ )
$c$	Radial clearance between piston and liner ( $m$ )
$C_p$	Offset of gudgeon pin from centre line ( $m$ )
$C_g$	Centre of mass offset along the z axis from piston centre axis ( $m$ )
$d_b$	Bore diameter ( $m$ )
$d_{ij}$	Etch depth ( $m$ )
$e_b$	Lateral displacement of lower end of the piston skirt ( $m$ )
$e_l$	Lateral displacement of gudgeon pin ( $m$ )
$e_t$	Lateral displacement of upper end of the piston skirt ( $m$ )
$\ddot{e}_b$	Lateral acceleration of lower end of the piston skirt ( $ms^{-2}$ )
$\ddot{e}_t$	Lateral acceleration of upper end of the piston skirt ( $ms^{-2}$ )
$E'$	Effective modulus of elasticity ( $Pa$ )
$f_{con}$	Connecting rod force ( $N$ )
$f_g$	Gas (combustion) force ( $N$ )
$f_{gg}$	Inertial force of gudgeon pin due to primary motion ( $N$ )
$f_{gp}$	Inertial force of piston due to primary motion ( $N$ )
$f_{ig}$	Inertial force of gudgeon pin due to secondary motion ( $N$ )
$f_{ip}$	Inertial force of piston due to secondary motion ( $N$ )
$f_{r1}$	Reaction due to lubricant at thrust side ( $N$ )
$f_{r2}$	Reaction due to lubricant at anti-thrust side ( $N$ )
$F_R$	Radial force at con-rod big end articulation point ( $N$ )
$F_T$	Tangential force ( $N$ )
$h$	Film shape ( $m$ )
$h_r$	Ring axial width ( $m$ )
$H$	Substrate hardness ( $N/m^2$ )

$I_p$	Piston inertia about its centre of mass ( $Kg.m^2$ )
$l$	Rod length ( $m$ )
$m_g$	Mass of gudgeon pin ( $Kg$ )
$m_p$	Mass of piston ( $Kg$ )
$m_{fr1}, m_{fr2}$	Hydrodynamic reaction moments ( $Nm$ )
$M$	Ring bending moment ( $Nm$ )
$p_l$	Piston length ( $m$ )
$p$	Generated lubricant pressure ( $Pa$ )
$P$	Atmospheric pressure ( $mbar$ )
$P_d$	Dry air pressure ( $mbar$ )
$P_{sat}$	Saturation vapour pressure of water ( $mbar$ )
$P_v$	Vapour pressure of water vapour ( $mbar$ )
$r$	Radius ( $m$ )
$s$	Surface profile ( $m$ )
$t$	Time ( $s$ )
$T$	Crank-shaft torque ( $Nm$ )
$T_C$	Ambient temperature ( $^{\circ}C$ )
$T_K$	Ambient temperature ( $K$ )
$u$	Speed of entraining motion ( $ms^{-1}$ )
$v_p$	Piston velocity ( $ms^{-1}$ )
$W$	Applied load ( $N$ )
$x, y$	Cartesian coordinates
$\dot{x}$	Piston velocity ( $ms^{-1}$ )
$y_p$	Piston displacement from TDC ( $m$ )
$\alpha$	Pressure-viscosity of lubricant ( $m^2/N$ )
$\beta$	Piston tilt due to secondary motion ( $rad$ )
$\chi$	Relative humidity (%)
$\delta$	Elastic deformation ( $m$ )
$\Delta$	Global deformation (macro) ( $m$ )
$\phi$	Connecting rod angle from translation axis, small end ( $rad$ )
$\varphi$	Angle from ring centre (opposite gap) ( $rad$ )

$\psi$	Piston pin offset divided by crank radius
$\Psi$	Plasticity index / Piston skirt end mid-position
$\eta$	Dynamic viscosity at any pressure ( $Pa.s$ )
$\eta_o$	Dynamic viscosity at atmospheric pressure ( $Pa.s$ )
$\lambda$	Combustion excess air factor (lambda)
$\Lambda$	Crank radius divided by rod length
$\theta$	Crank angle from piston translation axis ( $rad$ )
$\rho$	Density ( $Kg/m^3$ )
$\rho_o$	Lubricant density at atmospheric condition ( $Kg/m^3$ )
$\omega$	Crankshaft angular velocity ( $rad/s$ )
$\Omega$	Connecting rod centre of rotation



## Glossary of terms

---

AFR	Air fuel ratio
ASME	Air spring motored engine
ATDC	After top dead centre
BDC	Bottom dead centre
c/w	Continuous wave
CHA	Cross hatch angle (inclusive) from plane perpendicular to motion
CI	Compression ignition / cast iron
cold profile	Geometric form assuming macro rigid room temperature bodies
CRF	Honda CRF450R
CVD	Chemical vapour deposition
DLC	Diamond like carbon
DOF	Degrees of freedom
EGT	Exhaust gas temperature
EHL	Elastohydrodynamics
EP	Extreme pressure
FMEP	Friction mean effective pressure
footprint	Contact area between bodies
GRF	Global reference frame
HD	Hydrodynamics
HTC	Heat transfer coefficient
hot profile	Geometric form assuming macro rigid bodies but with thermal effects
IC	Internal combustion
ID	Internal diameter
IMEP	Indicated mean effective pressure
LIF	Laser induced fluorescence
LST	Laser surface texturing
NASCAR	National Association for Stock Car Auto Racing (USA)
Ni-SiC	Electrolytic nickel coating with co-deposited silicon carbide particulate
NVH	Noise, vibration and harshness
OD	Outside diameter
OE/OEM	Original equipment / original equipment manufacture
PCJ	Piston cooling jet

plateau	Removal of asperity peaks by means of secondary processing
PACVD	Plasma assisted chemical vapour deposition
PRV	Pressure reducing valve
PVD	Physical vapour deposition
QSTS	Quasi static thermo-structural
rpm	Revolutions per minute
RSF	Reduced surface finish
SI	Spark ignition
TDC	Top dead centre
UPR	Ultrasonic pulsar receiver
VAR	Vacuum arc re-melted
WOT	Wide open throttle

# Chapter 1

## Introduction

### 1.1 Problem definition

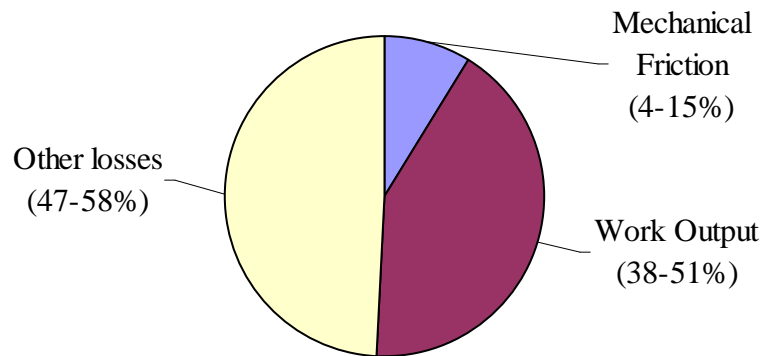
In 2005 the UK Chancellor of the Exchequer announced a review of forward implications on the UK regarding the economics of climate change. A review presented by **Stern (2006)** contained the following statements:

“The scientific evidence that climate change is a serious and urgent issue is now compelling. It warrants strong action to reduce greenhouse gas emissions around the world to reduce the risk of very damaging and potentially irreversible impacts on ecosystems, societies and economies..... Reversing the trend to higher global temperatures requires an urgent, world-wide shift towards a low-carbon economy. Delay makes the problem much more difficult and action to deal with it much more costly”. According to the Stern review, road transport accounts for 10.5% of global greenhouse-gas emissions and this is expected to double by 2050. Carbon-based emissions from road transport throughout the world are, therefore, under increasing scrutiny due to their contribution to the overall emissions. Increasingly stringent Governmental regulations throughout the world are forcing automotive manufacturers to improve economy whilst reducing emissions. The King Review (**King, 2007**) stated 22% of UK total emissions (in 2005) are from the road transportation sectors and an 80% reduction in  $\text{CO}_2 \text{ km}^{-1}$  should be targeted by 2050. Amidst an estimated doubling of UK transportation throughout this timeframe, the effective reduction is 90%. **King (2007)** also details potential engine and transmission efficiency savings (table 1.1).

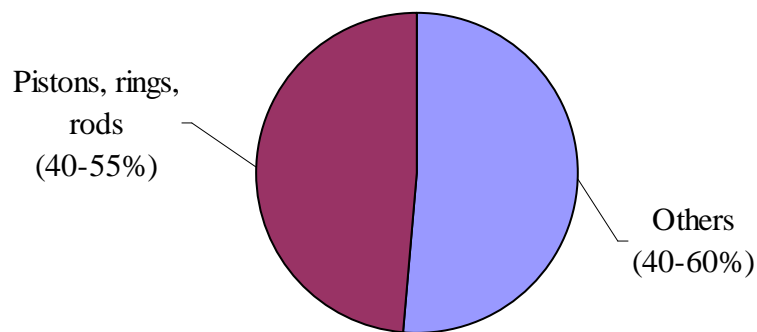
Technology	Efficiency saving	Cost per vehicle (£)
Direct injection and lean burn	10 – 13 %	200 – 400
Variable valve actuation	5 – 7%	175 – 250
Downsizing engine capacity with turbocharging or supercharging	10 – 15%	150 – 300
Dual clutch transmission	4 – 5%	400 – 600
Stop–start	3 – 4% *	100 – 200
Stop–start with regenerative braking	7%*	350 – 450
Electric motor assist	7%*	1,000
Reduced mechanical friction components	3 – 5%	Negligible

Table 1.1 Potential engine and transmission savings (**King, 2007**)

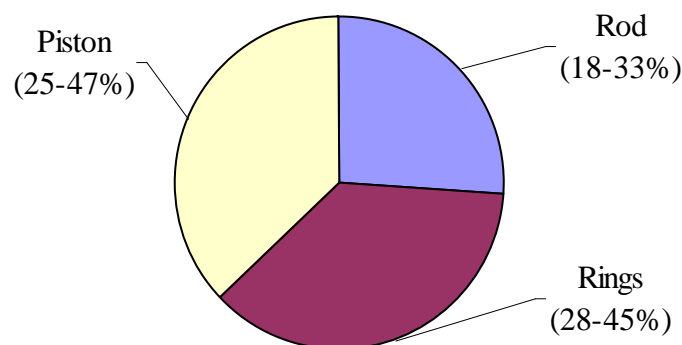
Table 1.1 states the case for ‘Reduced mechanical friction components’. Power-train efficiency is also cited by the **World Energy Council (2007)** as a technology to be considered towards 2050 CO<sub>2</sub> reduction. A reduction in power-train efficiency (losses) therefore results in reduced CO<sub>2</sub>. **Richardson (2000)** also presented power-train losses based on the total IC engine fuel energy input (Figure 1.1) showing relative contributions.



(a) Distribution of total energy in fired engine



(b) Distribution of total engine mechanical friction



(c) Distribution of piston, rings and rod friction

Figure 1.1 Proportion of energy and losses in an IC engine (after **Richardson (2000)**)

According to **Richardson (2000)** of the engine mechanical friction sources, the piston and rings account for the major frictional losses. Indeed each of these losses (piston rings and piston) accounts for 1.6% of input fuel. In terms of work output (assuming nil contribution towards ‘other losses’), each of these sources has the potential to contribute 3% (6% additional mechanical work).

**Andersson (1991)** and **Taylor (1992)** have accounted for approximately 55% of all losses in an engine as thermal losses (see figure 1.2). From the remaining 45%, approximately 25% of the energy loss is due to mechanical losses by all the reciprocating / rotating inertial members within the internal combustion engine: piston assembly, journal and big end bearings, valve train and other ancillaries. A further 15% is lost due to pumping, resulting in approximately 10% output power remaining. The piston assembly therefore accounts for a sizeable proportion of the mechanical losses (approximately 8%), making a viable case for overall engine performance improvement. As this mechanical loss is a total loss from the system, any improvements made should directly improve not only fuel consumption for a specific case, but also the total emissions for a given duty.

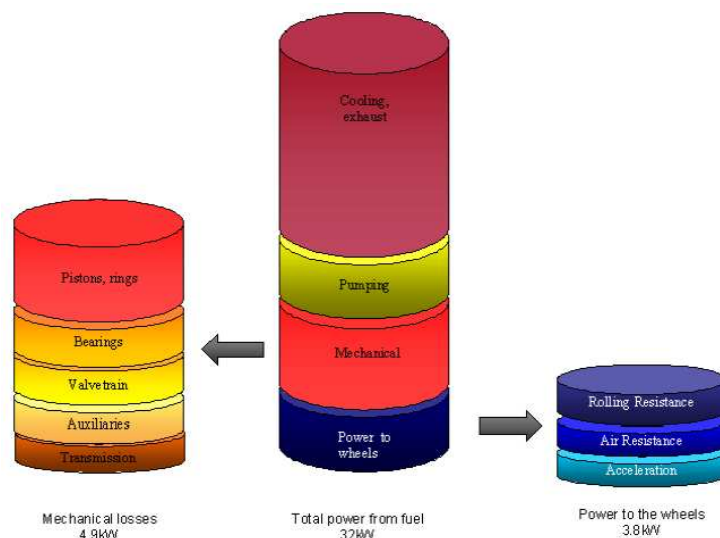


Figure 1.2 Frictional losses in an IC engine simulating urban driving as measured by Andersson (1991)

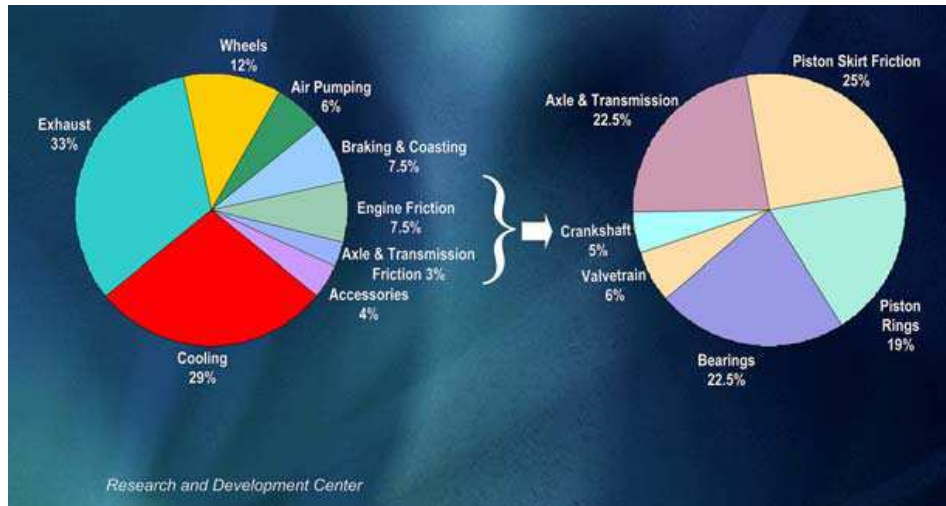


Figure 1.3 Frictional loss contribution from various IC engine sub-systems  
(after **Tung and McMillan, (2004)**)

**Tung and McMillan (2004)** (see figure 1.3) and **Carden (2008)** both further expand on this assessment of various losses stating the piston skirt to be the greatest contributor to a piston assembly's friction.

## 1.2 Piston assembly preamble

With the exception of Mazda on limited models, the piston assembly of nearly all road vehicles whether spark ignited (SI) or with compression ignition (CI) contains similar components. Furthermore, nearly all the road vehicles with the exception of relatively small units operate as four-stroke engines. The components of the piston assembly often vary greatly in material, design and layout. However, it is generally possible to identify the major components discussed herein. A typical piston assembly is shown below in figure 1.4.

### 1.2.1 Piston assembly components

The piston assembly consists of the piston (E), rings (A) and the working bore surface (F). It also contains the gudgeon pin (C) and the pin retaining clips (B), as well as the connecting rod (D). For the purposes of this work, the connecting rod is considered to be extraneous to the definition of the piston assembly with the exception of its inertial contribution.

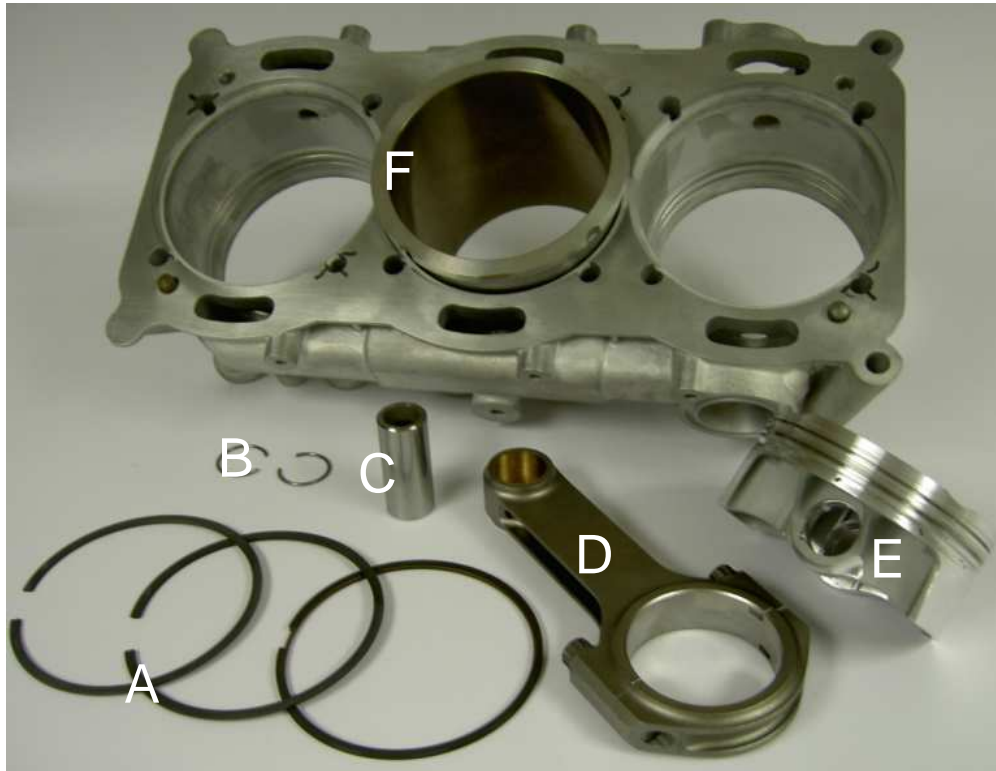


Figure 1.4 The piston assembly.

The primary function of the piston assembly is to transform the combustion gas pressure into crank torque (work). The piston translates along the cylinder axis in a reciprocating manner, transferring thrust to the connecting-rod and ultimately the crankshaft. Combustion parameters, component geometry, parasitic losses and relative position in the rotational cycle dictate the resulting instantaneous induced inertial torque.

The assembly of these parts is shown diagrammatically in Figure 1.5 and brief descriptions for these and other related components are given below:

**(a) Piston:** The piston may be regarded as a pressure-tight cylindrical plunger, which is subjected to the expanding gas pressure, resulting from the combustion process. Its function is to convert the gas pressure loading into a driving thrust along the connecting rod axis. Therefore, it has also to act as a guide for the upper portion of the connecting-rod.

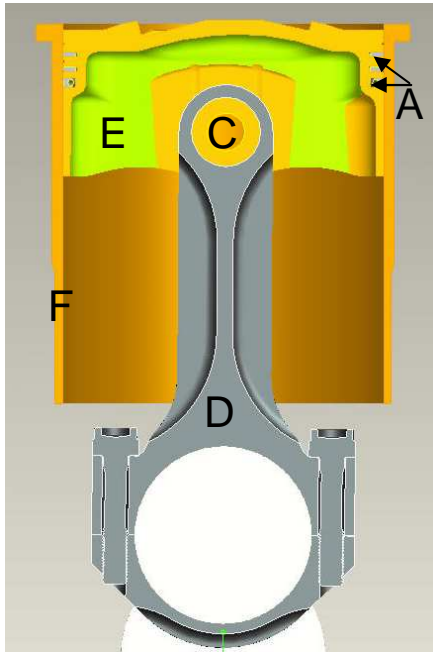


Figure 1.5 The piston assembly

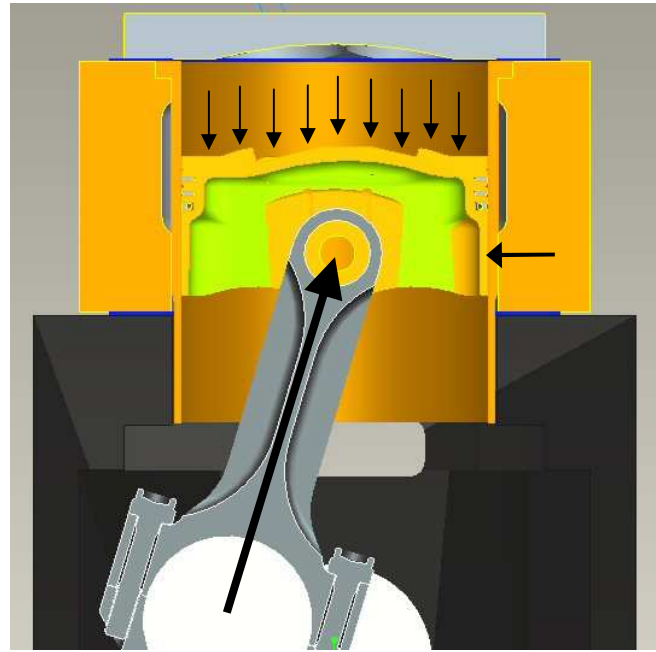


Figure 1.6 Simplified forces on the piston assembly

**(b) Piston rings:** The piston rings are assumed to be circular whilst *in-situ* (note this is not the case whilst they are in ‘free-state’, when they are considered as incomplete rings). The rings seal the gap between the piston and the bore surface, ideally preventing the flow of gas between the combustion chamber and the sump (blow-by). Furthermore, the rings control the bore surface lubrication, ideally providing an adequate film in these conjunctions, guarding against direct surface interactions and wear, whilst preventing lubricant ingress into the combustion chamber (blow-by). This ingress, if not controlled, would lead to unacceptable emissions and limited life due to lubricant consumption.

**(c) Gudgeon pin:** The gudgeon pin or wrist pin (USA) provides a pivoting connection between the piston and the connecting rod. It permits angular articulation yet restricts the rod’s small-end motion to remain nominally along the bore centreline. The gudgeon pin, depending on design, may be fixed in one of the adjacent components (e.g. shrink-fitted onto the connecting-rod) or it may be free to rotate (fully floating).

**(d) Connecting rod:** The connecting rod is situated between the gudgeon pin and the crankshaft. The upper portion of the connecting rod is referred to as the *small end* and has predominantly a translating motion with small angle oscillatory reversals, which is a tribological unfavourable condition. The lower portion of the connecting rod is referred to as the *big end* and often incorporates suitable bearing elements for the transfer of combustion



thrust into rotational torque applied to the crankshaft. The motion of the big end is predominantly rotational.

**(e) Crankcase:** The crankcase is usually a fairly complex cast structure, at the very minimum containing components above the crank centreline and up to the lowest point of the piston travel. In this minimal case, a cylinder block or barrel is attached on top of this to make a crankcase-cylinder block assembly (thereby containing all the components in figure 1.4). Most commonly in road vehicles the cylinder block is an integral part of the crankcase containing all the oil and water galleries for cooling and lubrication.

**(f) Crankcase / cylinder block with integral liner / bore surface:** Most modern passenger vehicle engines tend to be light alloy constructions. It is quite common to find in such cases that, for tribological reasons, a cast-in cast iron liner or an additional surface treatment to be applied to the crankcase material (parent metal coated / treated crankcase).

**(g) Crankcase / cylinder block with separate liners:** As an alternative to the above, and especially in the case of a limited production volume, the crankcase / cylinder block may be sleeved with a liner of more suitable bore surface material. This 'liner' has two basic versions, a 'dry' version, where the liner sits within the crankcase/cylinder block with full metal contact around its entire surface, or a 'wet' version, where a portion of the liner is in direct contact with the cooling medium employed.

### 1.2.2 Piston assembly sources of friction

When considering parasitic mechanical losses within the piston assembly, the piston assembly creates a resolved force on the cylinder bore due to the inclined reaction from the connecting rod and the connecting rod inertia. An outward thrust due to the sealing rings is also presented to the cylinder bore wall (figure 1.6). These forces produce drag on the cylinder bore during the piston motion relative to the cylinder bore surface.

The forces shown in figure 1.6 are based on several parameters, which are common among the conventional internal combustion engines. These parameters are as follows: Cylinder pressure (which varies with several parameters), component geometry and cyclical position, ring pack static pre-load and dynamic gas loading, mass of components, rotational speed and the gudgeon pin offset (where present).

For the piston assembly to function several factors must be considered: ease of manufacture, cost, low mass, performance at extreme temperatures, etc. This effectively limits the choice of construction materials for individual components and thereby, to some extent, the dry friction between the sliding surfaces.

Early in the IC engine development, (indeed preceding this in external combustion engines and other earlier pumping devices), a lubricant was employed, thereby allowing a nominal separation of the contacting bodies resulting in overall frictional drag some 25% or so of the unlubricated case. This has such a significant influence on the piston assembly's parasitic losses that the piston assembly is now defined to include the lubricant entrained between the contacting bodies. It is known through historical experimentation that the following parameters are amongst those that influence the performance of a given engine piston assembly.

### **1.2.3 Factors influencing piston assembly drag**

The following parameters have been reported as having an influence on the piston assembly's overall parasitic loss:

**(a) Lubricant temperature and method of application:** Different engine configurations employ various methods regarding lubricant delivery to the piston assembly. The usual OEM (original equipment manufacture) method is to splash / big end-bearing spray, where either the rotation of the crankshaft through the lubricant-filled sump drags the lubricant past the crank centre-line and deposits on the upper surfaces of the crankcase (including the bore surfaces) or a small lubricant exit (spray) hole is drilled into the lower half of each connecting rod on the piston assembly's thrust side.

Generally, the temperature of this lubricant is the same as the engine bulk lubricant temperature. However, dual oil feed systems are occasionally used in racing applications, supplying additionally cooled oil into the piston assembly. In highly loaded engines, separate oil spray jets are fitted to each cylinder (shown in figure 1.7). This is primarily to cool the pistons, but with the secondary benefit of further applying lubricant to the cylinder bores. It must be stated that the configuration of lubricant supply to both cylinder bores and pistons is generally fairly empirical, based heavily on previously applied parameters. Overall, there is

little data to truly support the lubricant conditions actually existing on the bore surface during running conditions.

**(b) Bore surface and form:** Sealing ring elements are designed to reciprocate within truly-cylindrical bores. However, for a given cylindrical bore the assembled condition is rarely true to form, due to both thermal and stress-induced parameters. ‘Torque plate honing’ (figure 1.8a) is the de-facto method for practically eliminating assembled displacements due to cylinder head to crankcase bolted construction. Figure 1.8b shows typical ‘cylinder head assembled’ cylindrical bore deformation due to honing with a torque plate (LHS) and without (RHS). The non-torque plate part (RHS) clearly shows the distortion due to 4-off cylinder head bolts resulting in a diamond shape in the upper bore portion.



Figure 1.7 Piston cooling / squirt jets (PCJ)

Methods also exist to negate a large amount of thermal distortion by finish processing the bore surface while assembled in a heated crankcase. However, this ‘match honing’ is a time consuming and laborious method, at the very least duplicating engine-build requirements. Furthermore, ‘taper’ honing of the cylinder bore may be employed in an effort to match the top-to-bottom thermal expansion and to a lesser extent combustion deformation for the most required sealing condition (at the top dead centre during the power stroke).

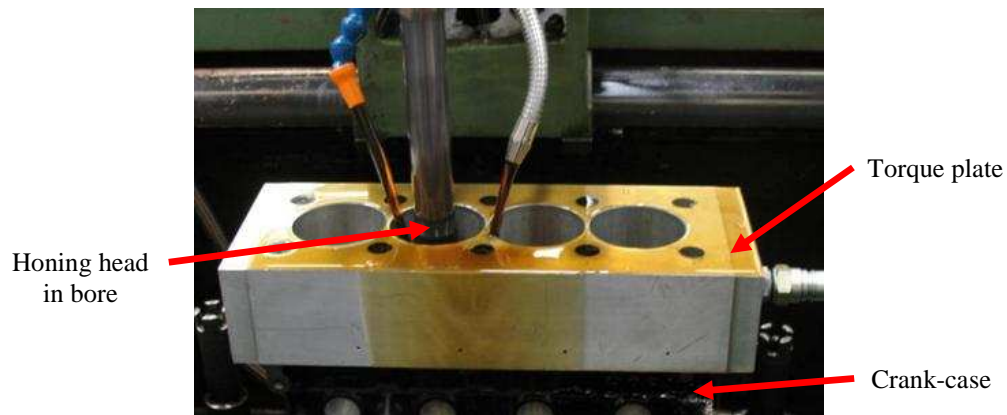


Figure 1.8a Torque plate honing

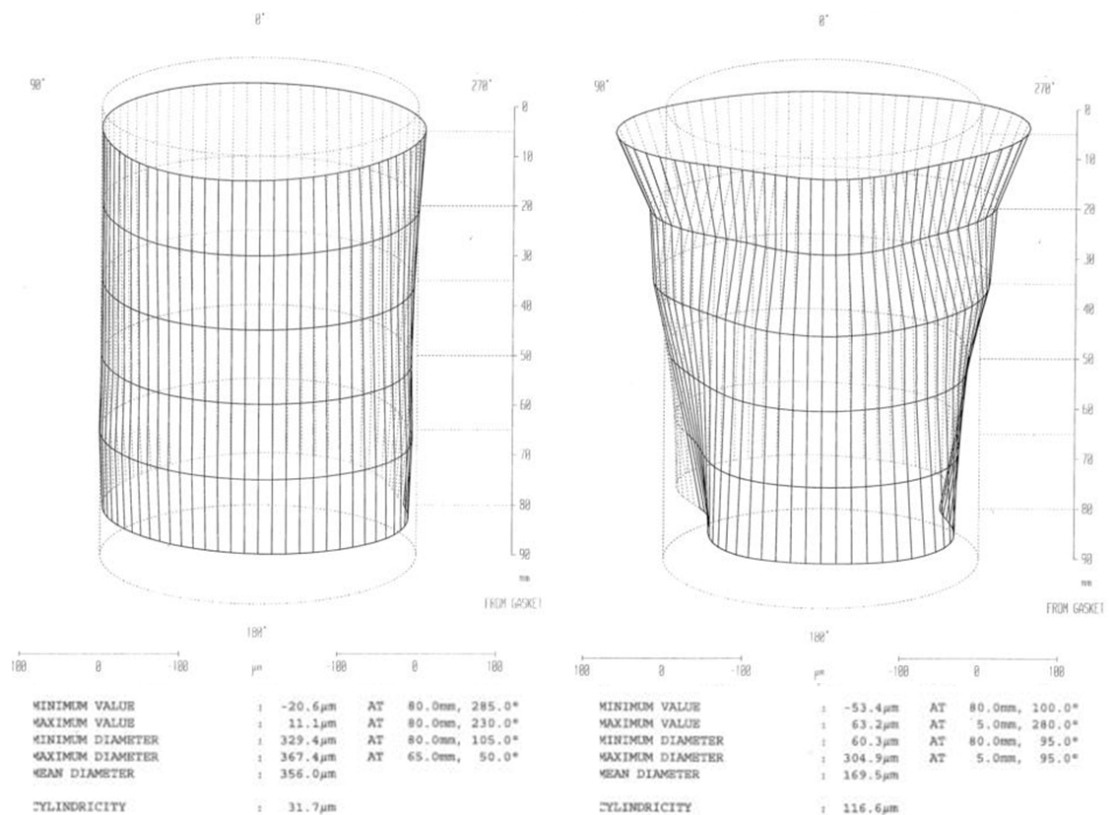


Figure 1.8b Torque plate honing and cylindricity comparison  
 (LHS with torque plate 31.7μm / RHS without torque plate 116.6μm)

The cylinder bore surface is often made of cast iron. However, alternatives such as electroplating and high velocity oxy-fuel deposition exist. These alternatives have various benefits / drawbacks and are often coupled with differing surface finish parameters. The cylinder bore may be integrally part of the cylinder block / crankcase or a separate 'liner'.

The use of cast iron crankcases is in decline due to the high density of this material resulting in an increased vehicle mass. However, the current alternative (aluminium alloy) has poor wear resistance in the bore area. Hence, cast iron liners are often inserted into the mould prior to aluminium casting, resulting in a bimetallic (bi-alloy) crankcase / cylinder block structure. Alternatives for removing the requirement of cast iron altogether exist, such as the application of electroplated nickel-silicon carbide or thermal spraying to the aluminium alloy crankcase directly.

The bore surface texture has logically developed over time, somewhat constrained by production techniques capable of achieving overall geometric shape within a repeatable and cost-effective process. Invariably the process used is internal honing using bonded ceramic abrasives of differing grit size and bond strength. Honing comprises a rotating and axially translating motion within the cylinder bore coupled with a controlled outward radial thrust of the abrasive onto the bore. The resulting surface finish is a combination of the number of honing steps, ratio of rotation to reciprocation (cross-hatch angle), and the abrasive morphology and bond strength. Of tribological interest, the abrasive morphology and process equipment operating range thereby limit the available resulting surface finishes.

**(c) Piston rings:** Piston rings can be broadly subdivided into two groups; compression rings and oil control rings. All IC engines contain at least one compression ring with a primary function to provide sealing between the upper and lower gas volumes (combustion chamber and sump) and conduction of heat away to the liner/bore surface. It is normal to have two oil control rings (a single element ‘scraper’ ring and a multi-element spring energised ‘oil control’ ring) – with the notable exception of 2-stroke engines which may have none. Scraper type oil control rings do offer some gas sealing effect. However, their primary purpose is to maintain a working lubricant film on the bore surface that is adequate for piston assembly operation with the minimum system loss (oil consumption) of lubricant as possible.

Generally, both ring types exert an outward force on the cylinder bore surface. In the case of oil control rings this outward force is similar at operating conditions as during assembly. However, for compression rings this is not the case. Compression ring groove geometry within the piston is designed to allow a portion of combustion gas to pass over the top of the ring and exert pressure horizontally on the back face of the ring. This pressure then directly adds to the pre-existing outward pressure – often by an order of magnitude. It is this gas energized

pressure which provides adequate outward force to ensure ring-bore conformability and hence combustion gas sealing. Therefore, the in-service geometry and resulting gas pressure's outward thrust are important considerations in optimizing the parasitic drag of the compression ring on the cylinder bore. The face geometry and surface treatments (coatings) of ring elements is very important as this, as far as the rings are concerned, is fundamental in dictating the resulting friction in the ring-bore conjunction.

Generally, compression and scraper rings are of rectangular section. Compression rings (due to high load and inevitable wear) are often constructed from steel and hard-faced with treatments / coatings such as chrome or physical vapour deposited titanium nitride, as an example. Generally, the working face is barrelled in the case of compression rings, and scraper rings usually have a tapered or stepped face leading to a sharp initial contact which rapidly wears to give good sealing. The barrel shape also helps entraining action of the lubricant into the contact through the *converging wedge effect*.

Oil control rings are often of multi-piece construction, featuring thin segment rails behind which an expander (spring element) sits forcing the segment rails onto the bore surface. The spring expander can be altered to suit a given application.

**(d) Pistons:** The geometry of a piston is known to influence parasitic drag, especially the outer surface or 'skirt'. The skirt has a complex shape, envisaged to ideally provide close to even wear during operation. The material, design, mass, centre of gravity, structural stiffness, surface treatments, and service requirements are other factors known to alter parasitic drag.

The piston also contains the gudgeon pin bearing (which connects the gudgeon pin, the piston, and the rod to articulate relative to each other during the combustion cycle) and significant loads are transferred from the piston to the connecting rod through this bearing. The loading during articulation inevitably contributes towards frictional losses.

The piston skirt is typically produced by CNC turning utilising single-point diamond tooling. The resulting surface finish is process limited (CNC turning) producing 'ridges' which are nominally parallel to the rings – i.e. a cross-hatch is not possible. Depth of finish ( $R_z$ ) is dictated by the requirement of a radius on the single-point tool of at least 0.1mm, combined

with achieving overall roughness limits. Coatings are often applied on the piston skirts to assist initial scuffing as well as reducing cold ‘piston slap’.

#### **1.2.4 Research focus**

The above preamble states the need to reduce CO<sub>2</sub> in vehicular transport. Power-train mechanical efficiency is identified as a worthwhile area for attention. The piston assembly is cited as the largest contributor to friction, and within this, the piston and the ring-pack interactions with the bore surface induce significant parasitic losses. A literature survey has yielded a bias in research towards ring-bore losses. Therefore, this thesis deals with the piston skirt-bore conjunction, where a relative dearth of investigation still pervades.

### **1.3 Aims and objectives**

The primary aim is:

The reduction of in-cylinder friction by means of optimising the piston skirt to cylinder bore conjunction.

#### **1.3.1 Objectives**

Develop an analytical / numerical predictive model to ascertain tribological conditions, and thus parasitic frictional losses. Furthermore, to use the model to ascertain the effect of influential parameters, outlined in section 1.2.3.

- Develop experimental rigs to determine actual part performance advised by predictions.
- Modify the developed model to ensure that it is representative of piston assembly behaviour, thereby allowing confidence in its future predictions.
- Analyse both the numerical predictions and experimental measurements against standard accepted baselines in an iterative fashion, thereby collating a matrix of practical and ‘optimised’ configurations.
- Effect a reduction in the piston skirt-bore conjunction’s parasitic losses by means of piston skirt geometric and topographical optimisations, thereby increasing specific output and reducing specific IC engine fuel consumption.
- Demonstrate by experimental means the effectiveness of the proposed solution and its robustness.

### 1.3.2 Limitation in research scope

The areas for modification are restricted to the piston and bore surface modifications. These modifications are envisaged to include geometry, materials of construction, coatings and surface treatments, form, and texture.

Changes to the ring elements, lubricant properties and other assembly items are deemed outside the scope of this thesis.

## 1.4 Methodology

The overall methodology is the development of a validated numerical model to direct design of the piston and bore surface based on tribological predictions and pre-existing industrial knowledge base. Central to the methodology is feedback from experimental activities thereby refining the numerical model (figure 1.9). A development loop for pistons and bores results with this combined numerical-experimental approach.

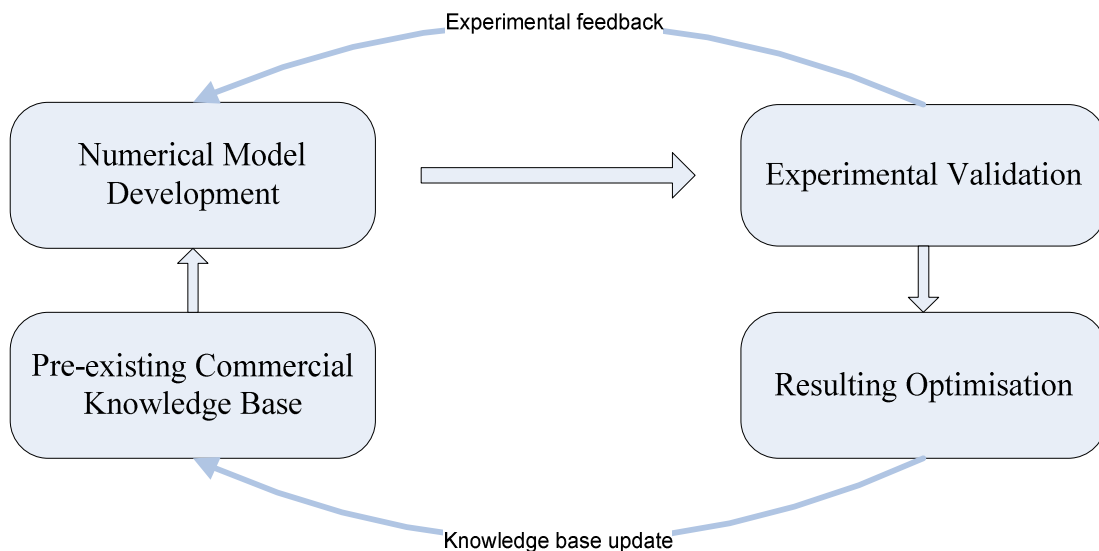


Figure 1.9 Integrated numerical-experimental approach

### 1.4.1 Numerical methodology

The numerical model is developed around mixed thermoelastohydrodynamics of partially conforming piston skirt-to-cylinder bore / liner contact, including primary inertial dynamics of the piston with its secondary motions within the confine of its clearance with the bore surface.



The following parameters are seen as essential:

- The loading regime of the piston to the bore surface and resulting relative velocity.
- Geometry of all parts, including profiles of piston skirts as well as thermo-elastic deformation.
- Microscopic topographical features or surface modifications such as those introduced on the bore surface, and any coatings which may be present.
- Material properties and lubricant rheology including thermal effects.

#### **1.4.2 Experimental methodology**

The experimental validation is conducted on a number of engines / designed rigs due to technical limitations depending on the type of test. These are outlined below.

‘Motorised’ rig. This is a non-IC engine rig, which has high resolution for direct measurement of piston assembly friction. This is anticipated as required because of the relatively small changes in IC engine torque / power that are required to be observed. A motorised engine can offer benefits in terms of instrumentation and ease of conducting tests due to its relative simplicity, when compared with a full ‘fired’ engine.

‘Fired’ single-cylinder engine dynamometer testing. This is required to truly evaluate a numerical model so that compromises made in the motorised stage are verified as not fundamentally unrepresentative of actual engine service. Once complete, this enables confident system development using predictive techniques.

‘Real-world’ engine testing. Testing in an actual road vehicle or independently-calibrated multi-cylinder dynamometer engine is seen as a conclusion to any benefits gained. A single-cylinder engine typically has a relatively low total output and considered benefits may only apply in the tested specific case.

This three stage approach to experimental testing forms a balance of cost, complexity, testing time, and resolution of results at each stage. Figure 1.10 shows a flowchart of undertaken research activities reported in this thesis.

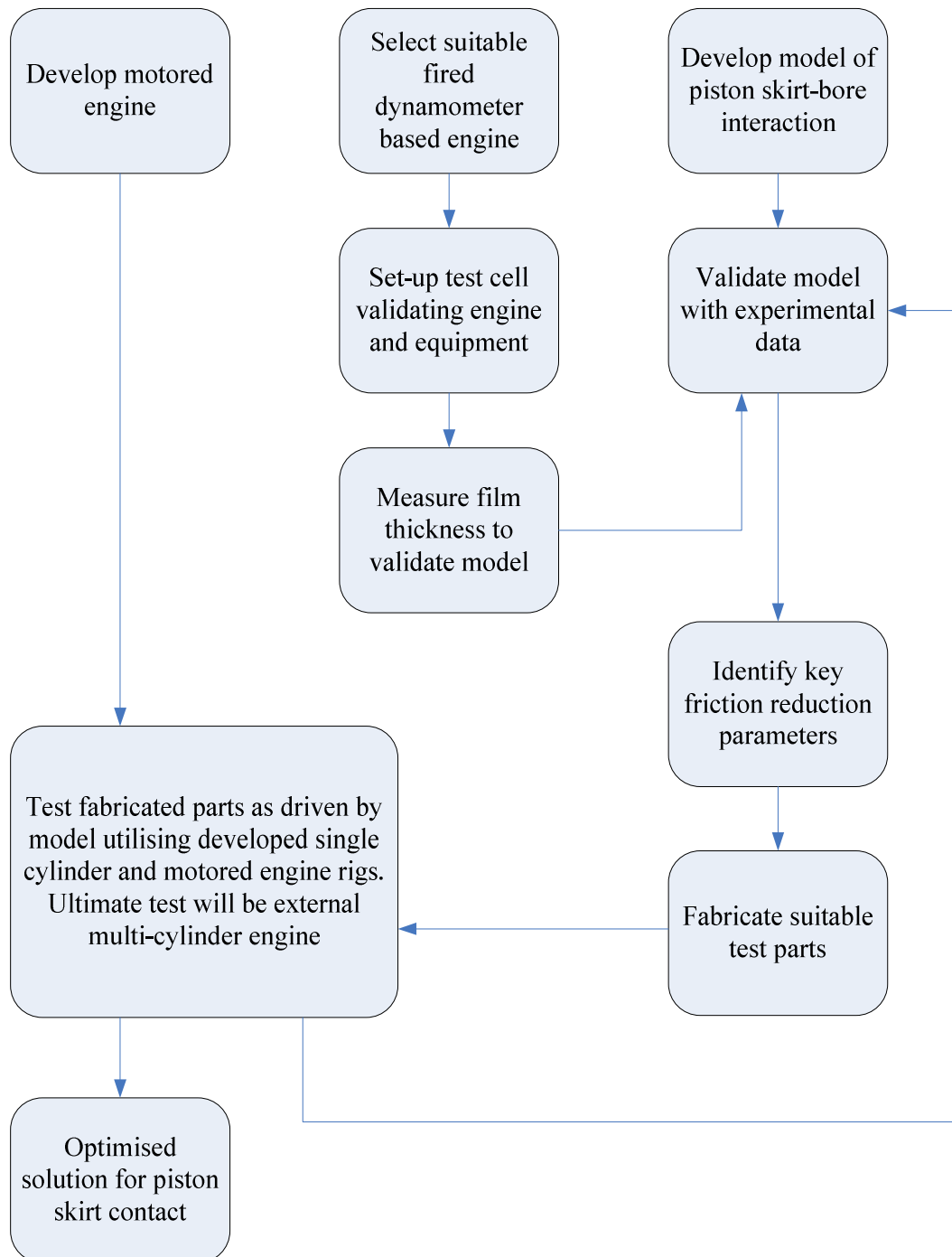


Figure 1.10 Flowchart for planned investigation

## 1.5 Structure of this thesis and third party contributory acknowledgments

This chapter provides an overview and definition of the problem being investigated. The content of subsequent chapters is summarised below, providing a road map to this thesis. Work performed in conjunction with, or by any third parties is also listed below.

Chapter 2 provides a literature review of the relevant material found in literature, with emphasis on piston-to-bore friction, as well as scientific methods to model the piston skirt-to-cylinder bore conjunctional behaviour both analytically and numerically.

Chapter 3 develops the kinematics of the piston crank-slider mechanism and resulting inertial dynamics, thereby providing the required input forces to a numerical model of the piston system.

Chapter 4 develops the tribology of the piston skirt-to-cylinder bore conjunction, utilising the forces from chapter 3 and methods obtained from literature.

Chapter 5 details the design and manufacture of components and testing rigs. Component materials, design, surface finishes, coatings etc. as well as engine choice, engine instrumentation, signal processing, and calibration<sup>1</sup>.

Chapter 6 presents experimental results from fired IC engine and motorised rig testing<sup>2</sup>.

Chapter 7 presents numerical results utilising methods developed in chapters 3 and 4<sup>3</sup>.

Chapter 8 provides an overall conclusion of findings, rationalising experimental and numerical results, achievement of aims, and potential for future work.

---

<sup>1</sup> Conceptual design of components and test rigs was entirely by the Author, however, some drafting assistance was provided by Mr. A. Luther (Capricorn Automotive Ltd.) regarding CRF and ASME components. Dynamometer installation and calibration (CRF, chapter 5.7) was performed by Mr. P. King, Dr. S. Balakrishnan, Mr. M. Gore and the Author. Dynamometer installation and calibration (ASME, chapter 5.8) was performed by Mr. J. Baker and the Author.

<sup>2</sup> Experimental testing which measured oil film thickness was performed by Mr. P. King, Dr. S. Balakrishnan and personnel from the University of Sheffield as well as the Author. Testing of piston and liner combinations (CRF), was performed by Mr. P. King, Dr. S. Balakrishnan, Mr. M. Gore and the Author at Loughborough University. Testing of piston and liner combinations (ASME), was performed by Mr. J. Baker and the Author at Capricorn Automotive Ltd.

<sup>3</sup> Numerical modelling regarding thermo-elastic EHL (chapter 7.5) was performed by Mr. B. Littlefair and the Author. 'Cold' (chapter 7.2), 'Hot' (chapter 7.3) and surface modified (chapter 7.6) numerical analyses were performed by Dr. S. Balakrishnan and the Author. Numerical code in all cases except chapter 7.4 was based on earlier work between Prof. H. Rahnejat and Dr. S. Balakrishnan.

## Chapter 2

### Literature review

---

#### 2.1 Introduction

The following literature review is structured in two parts. The first part (2.2 onwards) presents tribology literature with general scientific applicability, covering such areas as contact mechanics and lubrication. The second part (2.3), presents specific IC engine tribology as well as experimental work found in literature.

#### 2.2 Surface contact and lubrication: A historical perspective

Since the dawn of human civilisation man has acknowledged the importance of overcoming friction (**Dowson, 1979**). Friction results from the interaction of contacting surfaces, and a reduction in its effects reduces required energy input (**Jost (1966)**). One of the greatest technical advances of humans has been the invention of rolling wheels, and historical evidence exists that the Babylonians some 5,500 years ago used animal fat to lubricate wheel axles forming a primitive bearing. The Egyptians rubbed animal fat on logs, essentially linear bearings, to move large stone blocks whilst constructing the great pyramids.

**Gao et al (2003)** catalogues early recorded developments in friction as starting with Leonardo da-Vinci (1452-1519) who measured the force required to move a mass across differing surface combinations, probably iron and wood (**Dowson, (1979)**) making two important observations: frictional force was proportional to the weight and was independent of orientation (area of contact). These observations were later confirmed by **Amontons (1699)** (**Gao, J et al (2003)**) and subsequently refined in terms of velocity independence from force (amongst other parameters) by **Coulomb (1781)** by his seminal paper *Théorie des machines simples* which won him the Grand Prix from the Académie des Sciences.

According to **Barran (1996)** and **Balakrishnan (2002)**, **Boussinesq (1885)** made important contributions to all branches of mathematical physics. His contributions to the study of turbulence were praised by **St Venant (1864)**, and those on theory of elasticity by **Love (1906)**. Although he approached mathematics only in order to apply it practically, he still made important contributions. Notably, in 1880 he came upon non-analytic integrals of hydrodynamic equations. **Hertz (1896)** found an analytical solution defining the contact

stresses for elastic bodies in contact. For a more general case of deformation in two-dimensional elastic half-space, the limits of integral, known as ‘singular integral equation’ (**Johnson, (1985)**) was developed by **Muskhelishvili (1963)**, for which he received the order of Lenin.

### 2.2.1 Body contact and deflection

An approach to solve the deflection of conforming bodies in contact (spherical or cylindrical) was provided by **Paul and Hashemi (1981)**, based on the elastic two-dimensional stress field solution developed by **Ripperger and Davids (1947)** and expanded by **Muskhelishvili (1963)**. An analytical solution for pressures developed, due to a uniform line load along a semi-infinite solid, was given by **Timoshenko and Goodier (1951)**. **Pan et al (2009)** patents a fast method to compute strain within multi-layered solids subjected to arbitrary two-dimensional shaped loading.

Another method to calculate the deflection of bodies in conformal contacts is the finite element approximation (see **Zienkiewicz and Taylor (2000)**, Vol. 1). The finite element method discretises a continuum into elements (figure 2.1) forming strain relationships between adjacent elements by the use of shape functions **Bigelow and Progen (1999)**. **Szabo and Lee (1969)** derived stiffness matrices to express elasticity of a plane using Galerkin’s method (see **Zienkiewicz and Taylor (2000)**, Vol. 1).

**Zienkiewicz and Taylor (2000)** (Vol. 2, pp347) further expand on the use of the finite element method in the solution of body contact stating their inherent non-linear behaviour. Solution of contact problems called the ‘*impenetrability condition*’ involves first identifying which points on boundary will interact and the insertion of appropriate conditions to prevent penetration.

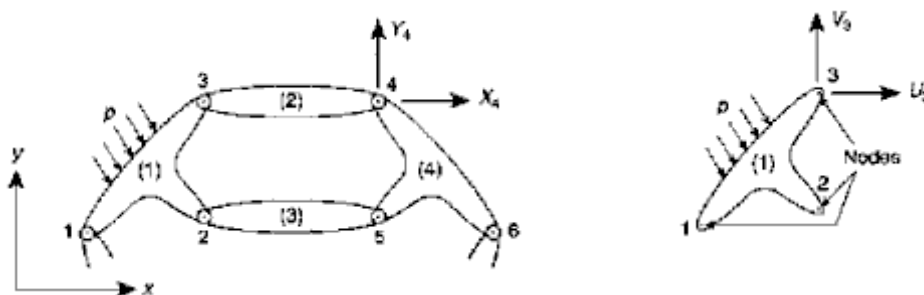


Figure 2.1 A structure discretised into elements  
from **Zienkiewicz and Taylor (2000)**

### 2.2.2 The importance of lubrication in engineering

Mechanical systems often comprise of interacting parts moving relative to each other. This relative movement, such as in the case of transmitting power, often produces high localised stresses between members. Friction (most often in the form of localised heating) results, thereby not only reducing overall system efficiency but also leading to reduced system life, or in the extreme, catastrophic failure. Typical mechanisms are abrasive wear, seizure, fatigue spalling, and pitting.

The introduction of a low shear strength fluid (lubricant) between mating members provides separation of contiguous (otherwise mating) surfaces practically negating any damage to the surfaces as well as overall increased system efficiency (**Forbes and Taylor (1943)**). **Furuhama and Sasaki (1984)** and **Uras and Petterson (1984)** investigated the relative engine motoring efficiencies due to lubricant rheological changes such as viscosity, operating temperature as well as lubricant supply.

**Graddage *et al* (1993)** presented the conclusion that piston (skirt) design features and relative lack of available lubrication at start-up had lead to the catastrophic engine failure of a large marine engine. Failure was ascribed to the lack of adequate (lubricant) wedge formation highlighting the importance of constantly available lubricant.

It is, therefore, critical wherever possible, to minimise solid-solid interaction. Lubricant films can provide this mechanism, however their presence in sufficient thickness throughout the operating cycle must be ensured. Most notably start-up and shut-down conditions present challenges, and in the case of reciprocating (IC) machinery the momentary cessation of relative motion at reversal points (top and bottom dead centres).

Typically mineral oil, or mineral oil derivatives, are employed due to low cost and adequate performance in service conditions. Alternatives to mineral oil are presented in table 2.1 and **Jones and Jansen (2005)**:

Fluid Property	Typ. organic ester	Typ. phosphate ester	Typ. silicone oil	Polyphenyl ether	Mineral oil
Max. operating temp. in air (°C)	240	150	250	350	150
Specific gravity	1.01	1.12	1.06	1.19	0.88
Viscosity index	140	0	175	-60	0-120
Flash point (°C)	255	200	290	275	150-200
Boundary lubrication on steel	Good	Good	Poor	Fair	Good
Rubber seals	Use silicone rubbers	Use butyl rubbers	Use neoprene rubbers	Attacks rubber	Use nitrile rubbers
Corrosion	Can present problems	Can present problems	Non-corrosive	Non-corrosive	Depends on impurities
Particular advantage	High temperature stability	Fire resistance	High temperature stability	High temperature stability	
Approximate cost	10	10	25	250	1

Table 2.1 Characteristic properties of some synthetic lubricants  
(reproduced from **Williams, J. (2005)**)

### 2.2.3 Principles of lubrication

Lubricated surfaces moving relative to each other are not infinitely parallel and discontinuities of separation exist. Large areas of clearance (or infinite clearance) are typical towards the edge of one body, however this clearance constricts due to mechanistic forces, and would ultimately lead to body contact in the absence of lubrication. Lubricant is dragged into the narrowing conjunction during relative sliding motion (**Cameron, (1981)**, pp17-18). As the passage constricts, and the volume of lubricant entering the conjunction remains nominally constant, the fluid generates pressure to force its path through the conjunction (figure 2.2) thereby exiting the conjunction at higher velocity.

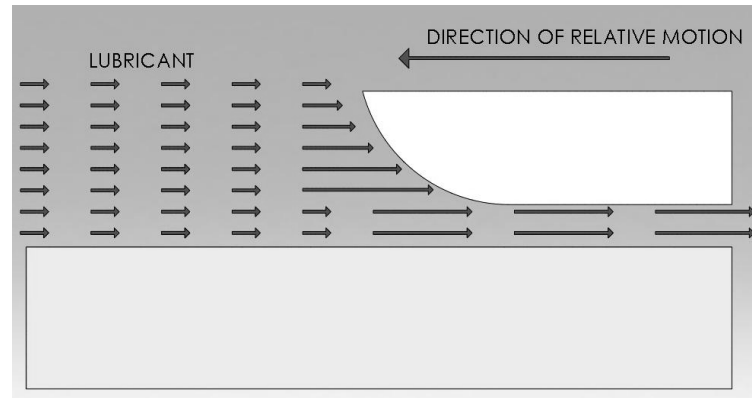


Figure 2.2 Lubricant entrainment in a converging gap

It is known that the early Egyptian and Babylonian civilisations used oils and fats to lubricate moving parts (**Taylor (2003)**). However it was not until the late 19<sup>th</sup> century that a formal scientific understanding of lubrication started. **Tower (1883, 1885)** was commissioned in 1882 to study friction in journal bearings (primarily railroad rolling stock), reporting his findings in 1883 and 1885. He found that lubricant leaked from a hole in the shell of a journal bearing and even more so in the case of a loaded bearing. Efforts to reduce this leakage by plugging all but failed with the realisation that the oil was somehow becoming pressurised in operation.

At a similar time **Petroff (1883)** was studying the variation in frictional characteristics in a journal bearing with different types of oil. He noted that journal bearing friction could be explained as a hydrodynamic phenomenon, when assuming that the lubricant was sheared between a coaxial shaft and a bearing. Petroff evolved the theory that each lubricant application would benefit by selection of optimal lubricant viscosity and was awarded the Lomonosoff Prize from the Imperial Russian Academy. Meanwhile **Reynolds (1886)** published an analytical model showing that lubricant can physically separate contacting bodies in relative motion. He published his landmark work in the Proceedings of the Royal Society. Combining **Newton's (1687)** slow viscous model with **Navier (1821, 1823)** and **Stokes (1845)** equations of motion for a fluid element, Reynolds was able to mathematically describe the phenomenon observed by Tower; when a viscous fluid is drawn into a space of decreasing height by the imposed surface velocities of the bearing elements, load carrying pressures in the oil film would be generated.

As the lubricant in the contact experiences high pressures, its viscosity alters significantly. This was shown by **Barus (1893)** and later modified for high pressures by **Roelands (1966)**.



Lubricant separated bodies are, however, elastic in nature. The combination of high pressure and viscosity leads to deformation of the elastic bodies further preventing body substrate interactions, even with extremely thin lubricant films. This phenomena is sometimes referred to as viscous-elastic behaviour; viscous alluding to the piezo-viscous action of the lubricant and elastic, because of induced localised deformation of the contiguous solid surfaces. This behaviour is often referred to as elastohydrodynamic lubrication (EHL).

The localised deformation of surfaces follows classical Hertzian theory, whilst the piezo-viscous action of the lubricant follows the rheological models developed by **Dowson and Higginson, (1959)**. **Rahnejat *et al* (2009)**, details the development in understanding of EHL first by **Grubin (1949)** based on research work by Ertel further documented by **Ertel and Grubin (1949)**. The absence of wear in moderate-to-high loaded lubricated contacts, which had puzzled Reynolds and the scientific community until this time, was now satisfactorily explained by the mechanism of EHL.

Numerical solutions for EHL began to emerge in the 1950's (**Dowson and Higginson, (1959)**) clearly demonstrating that the lubricant-filled deformed body conjunction gave rise to higher effective film thickness than classical calculations produced. Indeed, in addition to non-linear viscosity behaviour it is now unanimously accepted that lubricant can undergo transformation from liquid state into an amorphous state (**Winer and Sanborn (1978)**, **Alsaad *et al* (1978)**) and the loading and unloading behaviour of the conjunction can show measurable hysteresis (**Seiciu and Pavelescu (2006)**). **Diaconescu *et al* (2007)** have produced AFM images of cooled paraffin after fluid to amorphous transition (figure 2.3) showing (black circle outlined) 20-25Å diameter spherical cluster ordered molecular groupings.

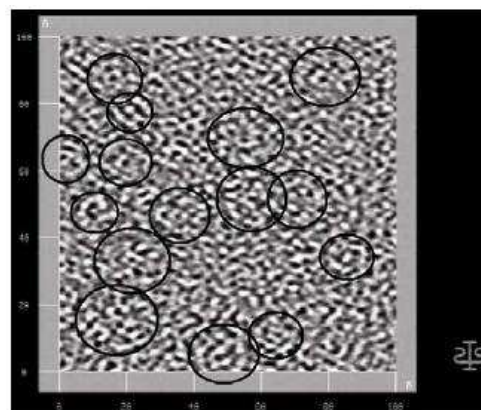


Figure 2.3 Structure of amorphous paraffin reproduced from **Diaconescu *et al* (2007)**

EHL is generally a non-formal contact phenomena such as found in roller bearings to race contact. In applications with pressures below the amount for traditional EHL, bulk structural deformation (as opposed to localised deformation) may still occur. Referred to as iso-viscous elastic or 'soft' EHL (**Hamrock (1980)**), this regime of viscous behaviour is a feature of IC engine piston skirt-to-bore contact.

On the other extreme, micro-EHL is reported where deformation of asperity tips modifies boundary behaviour, resulting in a higher effective body separation. A combination of micro-EHL (running-in) and iso-viscous EHL are likely with the piston skirt-to-cylinder wall conjunction thereby conflicting the pressure and viscosity assumptions of the two models.

#### 2.2.4 Measurements in lubricated contacts

**Kannel *et al* (1965)** using a thin manganin micro-transducer measured pressures in the lubricated contact region of steel rolling discs. **Ioannides and Pareti (1986)** concluded that actual pressures measured in an elastohydrodynamic contact are far higher than their numerically predicted counterparts. **Safa and Gohar (1986)** extended the method of depositing a pressure transducer to study the elastohydrodynamic pressure distribution of rolling line contacts in a disc machine. **Johns-Rahnejat (1988)** and **Johns-Rahnejat and Gohar (1997)** utilising similar technology measured the point contact pressure of a sphere against a flat glass race.

Various methods have been successfully developed to measure and/or visualise the oil film thickness in lubricated contacts, as outlined below.

A mechanical strain gauge method developed by **Meyer and Wilson (1971)** allowed direct measurement in operating machinery.

An electrical resistance method. Electrical resistance approaches zero when metal-to-metal contact takes place and increases in the presence of electrically insulating lubricant films (see **Ninomiya *et al* (1978)**). This method is acknowledged as somewhat unreliable for absolute film measurements, with obvious limitations with non-conductive substrates (**Sherrington (2010)**).

The capacitance method pioneered by **Crook (1958)** measured film thickness between steel rollers. A major difficulty reported with this method is the variation of dielectric constant with temperature and pressure, therefore requiring calibration experimentation (**Dyson *et al*, (1965)**).

Laser induced fluorescence (LIF) is a method useful for optically-transparent substrates. Fluorescence arises when the molecules in the oil film are electronically excited by a laser light source due to photon absorption subsequently returning to their ground state (emitting a photon of a specific wavelength). The timeframe between absorption and subsequent emission is small (in the order nano-seconds). As excitation is in quantum multiples, the laser source is such that it is of lower wavelength (higher energy) than required for excitation, enabling effective filtering of the excitation source (**Greene, (1969)**).

The X-ray method relies on the fact that many lubricants are transparent to X-rays whereas the usually metallic contacting bodies strongly absorb X-rays. This method was developed by **Sibley *et al* (1960)**, (**Sibley and Austin (1962)**).

The use of optical interferometry (**Tolansky (1951)**) allows a great insight into EHL due to the production of three dimensional contact maps, and in its original form utilised a coated glass plate (**Kirk (1962)**, (**Cameron and Gohar (1966)**, (**Wedeven and Cameron (1967, 1968)**, **Wedeven *et al* (1972)**).

The use of ultrasound has also successfully been used. Ultrasound is transmitted through one of the bodies and reflects at the interfaces encountered. Reflection time, coupled with known medium transmission velocity, results in measured gap distances (**Dwyer-Joyce *et al* (2003, 2004)**).

## **2.3 Internal combustion engine tribology**

### **2.3.1 Historical development of the internal combustion engine**

The earliest references to the use of a piston as a machine element concerns water pumps. Philo of Byzantium (2nd century BC) describes the piston pump of Ctesibius (an engineer from Alexandria, Egypt, 3rd century BC) as a force pump totally submerged in water (**Usher (1970)**). **White (1979)** describes the first European equivalent of a piston pump appearing in

the writings of Taccola (c. 1450) and Martini (c. 1475), featuring a suction pipe thereby improving on the basic design.

In the seventeenth century Huygens (1680) and Papin (1690) made some foundation experiments with pistons as a means to utilise heat and pressure (**Usher (1970)**). **Galloway (1828)** discusses how in 1720 Leupold constructed the first high pressure steam engine “previous to this, the only use to which steam had been effectively used was in the formation of a vacuum: true it is, that in the projects of De Caus, Branca and Savery, the elastic force of steam was proposed to be used; but the failure of these plans by waste of steam and other causes, warrant our saying that the plan of Leupold entitles him to the great merit of having invented and constructed the first high pressure engine”. According to **Galloway (1828)**, the design of this engine was a twin cylinder arrangement missing the elements of an articulating connecting rod and a rotating crankshaft.

Some 50 years later James **Watt (1769a)** filed a patent in which the matter of transmitting a linear force to a circular motion was raised, thereby facilitating realistic mechanical work via external combustion. Indeed such was Watt’s prowess that many fundamental and practical issues were experimented on: “We drew the bucket and drove nails into the leather, both to smooth the (cylinder) bore and presently diminish the (piston to cylinder) friction” **Watt (1769b)**.

According to **Usher (1970)**, the patents of Street (1794) and Lebon (1799) mark the start of experimentation into viable internal combustion. Significant practical results did not emerge however until 1860 by ‘combining known elements’. Lenoir produced a practical, though inefficient, flame ignition engine. In 1862 Beau de Rochas invented what in effect is commonly referred to as the 4-stroke cycle although he never made a working example. Nicolaus Otto was the first to practically realise the 4-stroke engine – however his patent was subsequently revoked in 1868 (**Dell and Rand, (2004)**).

Running at slow speed, Otto’s engines were underpowered and therefore unsuitable for automobile use. The high speed spark ignition engine invented by Gottlieb Daimler, and shortly to follow the compression ignition engine of Rudolf Diesel in 1892, made practical automotive transport a reality.

**Dieterichs (1916)** discusses the importance of machine lubrication in the period midway through production of early vehicles such as Ford's Model T and Bugatti's Type 13: "Whenever the surface of one part of machinery in motion is bearing on the surface of another, friction is created and friction creates heat. This heat is evolved and increases with the velocity and continued motion, and if not taken up and carried away by lubrication, will finally increase and accumulate to such an extent that the machinery will have to be stopped to allow the metal to cool off". "...To avoid this we have to keep the revolving parts well lubricated in their bearings, and we have to continue doing this as long as the machinery is kept in motion".

**Robinson (1960, 1961)** reviewed the development of spark ignition (SI) and compression ignition (CI) engine pistons, stating that the pistons used since the inception of the IC engine were heavy and made of cast iron. The performance, economy, and efficiency were developed significantly in the last half century without altering the principle. Gradually the aluminium piston replaced the cast iron design to achieve higher speed.

However in the early days the use of aluminium as a piston material was problematic due to high wear and thermal distortion. It was tackled by alloying aluminium with silicon. Die casting was found to be one of the most convenient methods for making piston from aluminium alloy. "A closely controlled heat treatment is then applied to the die casting to further develop the physical properties and to accelerate the process of age hardening."

**Robinson (1962, 1964)** expanded on earlier work (and that of Rothman, 1936) by producing a parametric database of piston features (gas pressure, section thicknesses, diameter etc.) to enable consistency in design strategy.

### 2.3.2 Numerical predictions of piston-lubricated conjunctions

Most predictive investigations of piston tribology have been directed towards either the piston skirt or piston top compression ring conjunctions. These analyses have been justified based on the significant contributions made by these conjunctions to the overall frictional losses in an engine. Many investigators have noted that the compression ring conjunction accounts for most of the piston assembly parasitic losses, such as **Dowson *et al* (1983)**, **Ma *et al* (1995a, 1995b)** and **Mishra *et al* (2008, 2009)**. However, some claim that frictional losses due to the piston skirt can be even more significant, **Tung and McMillan (2004)** and **Carden (2008)**.

Subjectively the piston compression ring conjunction has received more attention in literature with a larger volume of predictive analysis. Due to the rather large length-to-width ratio when the ring is viewed as a curved beam, a relatively simple one-dimensional solution to Reynolds' equation leads to an analytical solution for pressure distribution and film thickness (for example by **D'Agostino *et al*, (2002)**).

However a one-dimensional solution for the compression ring lubrication pays no regard to side leakage of the lubricant in the circumferential direction of the ring (which would be unsuitable for piston skirt analysis (**Kim *et al* (2009)**)). These approaches have even been included in multi-body models of IC engines, for example by **Boysal and Rahnejat (1997)**, **Offner and Priebisch (2000)** and **Perera *et al* (2007)**.

**Li *et al* (1982)** published one of the earliest papers regarding simulation of piston skirt lubrication of a V8 spark ignition engine. Secondary motion of the piston was solved first without taking lubricant reactions into consideration. The results showed that the location of the gudgeon pin has a critical influence on the secondary dynamics of the piston. A quasi-static analysis was then performed for lubricant behaviour (reaction). The piston-bore clearance and viscosity of the lubricant were also found to be important. The results obtained showed that the location of the gudgeon pin has a direct influence upon the piston skirt-to-cylinder liner friction.

A numerical analysis to compare hydrodynamic lubrication of a conventional piston with that of an articulated piston in a large engine was undertaken by **Dursunkaya and Keribar (1992)**. The articulated skirt piston design was reported to give rise to larger tilt angle of the crown about the gudgeon pin, when compared with that of a conventional piston. The articulated skirt piston was logically less influenced by the piston motion and travelled more parallel to the liner than the rigid skirt. No comments were made on the possibility of impact or contact between the component parts in the articulated piston.

A two-part comprehensive analysis was undertaken by **Zhu *et al* (1992, 1993)** to simulate piston lubrication in an engine at severe operating conditions. The first part of their investigation was focussed on obtaining rigid body piston lubrication analysis and extended to include the piston skirt distortion, including thermal effect in the second part. The conclusions derived are a reaffirmation of the importance of the parameters given in section 2.3.4.

Piston-bore conjunctions are subject to transient changes in many areas: forces, temperature, deformation, relative velocity, etc. The problem may be viewed as both multi-physics and multi-scale where combustion, inertial dynamics, structural (global) deformation, contact mechanics, surface topography, and lubricant rheology all work in an integrative interactive manner. Such transient solutions, to lesser or greater scale, have been attempted by a number of contributors, such as **Mei and Xie (1993)** with respect to IC valve-train and **Balakrishnan and Rahnejat (2002)** with respect to IC pistons.

**Balakrishnan and Rahnejat (2002)** observed that by bringing the misaligned contiguous bodies close together, pressure generated by the lubricant is higher when there is a more abrupt change in profile, thus leading to a higher pressure at the inlet region than at the outlet region. The tilt of the piston about the gudgeon pin had inadvertently caused a smoother profile transition and hence yielded pressure of lower magnitude than that of a non-tilted profile. A repercussion of this finding is that with a reduced clearance the degree of contiguity is enhanced, leading to a reduction in the secondary pressure peaks in addition to reduced impact momentum, which is responsible for slapping noise.

**Duyar *et al* (2005)** shows a new comprehensive piston skirt lubrication model has been developed based on a mass-conserving finite volume algorithm. Piston motion and force results obtained using this finite volume method have been compared with those from an existing finite difference method. The new model allows the user to define the amount of oil supplied to the skirt liner interface which allows more accurate predictions of piston motion. It has been demonstrated that the amount of oil supplied to the interface has a significant effect on lateral motion, and tilt is qualitatively similar for the finite difference and finite volume methods. However, the lateral and friction forces differ between the two methods. Skirt and liner deformations have an effect on piston secondary motions, lateral, and friction forces.

The inherent cyclical reciprocating nature of the piston-bore contact (**Offner and Priebisch, (2000)**) results in rhythmic mechanical losses due to inertial imbalance, component deformation, structural vibration, and frictional losses with respect to cycle position. This means that palliations sought should also suit the varying conditions. For instance, at the reversals (top and bottom dead centres (TDC and BDC)), lubricant entrainment into the contact between the piston skirt and the cylinder by the well-established wedge effect momentarily ceases (**Li *et al*, (1982)** and **Oh *et al*, (1987)**). Under these time-step conditions,

the resulting depletion of a lubricant film leads to excessive friction and wear. In these locations any residual lubricant film would be retained by three possible mechanisms (**Gohar and Rahnejat, (2008)**):

- Lubricant entrapment due to local surface topography.
- Squeeze film action due to localised deformation or lubricant entrapment or both.
- Rapid replenishment as a function of piston velocity.

The last of these is a function of piston stroke and operating (rotational) speed, which improves with higher performance engines. Nevertheless, cessation of entraining motion of lubricant takes place and resulting diminution of lubricating film is a strong possibility. For a given engine configuration (implied duty cycle), the first two mechanisms would account for the remedial actions that can be undertaken.

Squeeze film action is due to the convergence of fluid lubricated contact surfaces under load. This mechanism is now well understood, at least in a theoretical manner (**Kushwaha and Rahnejat (2002)**, **Balakrishnan and Rahnejat (2002)** and **Balakrishnan and Rahnejat, (2005)**). As the bodies approach the lubricant tends to be pushed out of the contact area. However, the rate of approach is usually greater than the viscous flow of the lubricant out of the contact area. Consequently, with sufficient contact load, high enough pressures are generated in the lubricant film to maintain load carrying capacity.

In some cases deformation of the contiguous surfaces may occur, thus inhibiting the interaction of surface asperities. This is particularly true in the non-conformal contacts in rolling element bearings and cam-follower pairs as described by **Kushwaha and Rahnejat (2002)**. However, in partially-conforming contacts such as the piston skirt-to-bore, this phenomenon can only occur at relatively high contact forces because of the prevailing large contact area (compared with Hertzian contact dimensions in concentrated counter-formal contacts). Nevertheless, it is clear that transient inertial dynamics of the system, as well as the elasticity of the bodies in contact, play an important role, yielding a contact / impact force to create the localised deformation (referred to as the squeeze cave) (**Kushwaha and Rahnejat, (2004)**). The problem is the generation of such a contact force at TDC and BDC and its other unwanted implications, such as the slapping action.



To effect squeeze caving, the contact force needs to be of sufficient magnitude in order to cause localised elastic deformation at the positions of reversal. In practice when peak combustion pressure occurs at or very near TDC, excessive and undesirable radiated noise from the cylinder block occurs referred to as ‘pinking’. Pinking was a common problem some four decades ago and was generally considered as an indication of poor quality and performance.

With low side forces, it is also difficult to encourage piezo-viscous action of the lubricant thereby producing a rise in its viscosity. If this was to occur, the lubricant would tend to act as an incompressible amorphous solid maintaining body separation even at low entrainment velocities. Another favoured outcome would be to engineer suitable surface topography so as to encourage lubricant entrapment (**Balakrishnan *et al*, (2003)** and **Rahnejat *et al*, (2006)**). From a tribological viewpoint, in the absence of sufficient contact load, rough contacting surfaces with piezo-viscous lubricant behaviour would be ideal. This is unfortunately the opposite to popular opinion (**Voit *et al*, (1995)**) and also opposite to that found in actuality in IC engines particularly at TDC (where engine operation in the presence of asperity contact has reduced the surface finish to almost ‘smooth’).

The lubrication at both TDC and BDC, and in their immediate vicinities, follows a mixed regime of lubrication, where a very thin hydrodynamic film is interrupted by asperity contacts. The conditions that promote this hydrodynamic film are not favourable, not only due to the reversal effect, but also due to the lack of a sufficient supply of lubricant ahead of the contact (i.e. lack of fully flooded condition).

### 2.3.3 Experimental measurements of piston-skirt oil film thickness

**Dearlove and Cheng (1995)**, using a reciprocating test machine, report minimum oil film thickness (48.7cP to 157.9cP lubricant viscosities) in the region of 0.5-2 microns for relatively low speed (600rpm max), though cite previous work showing a range between 0.2 and 10 microns. Major factors affecting oil film thickness are reported by **Bhatt *et al* (2009)** as piston speed, lubricant viscosity, geometric profiles, boundary conditions, and surface roughness.

**Liu and Tian (2005)** address compression ring lubrication and conclude the necessity to consider the circumferential variation in lubrication thickness which is strongly mitigated by system secondary motions. A successfully implemented tool for visualising and measuring the

lubricant thickness between piston skirt and piston ring with the cylinder bore has been the laser-induced fluorescence (LIF) method. Early qualitative work conducted by **Greene (1969)** and **Ting (1979)** observed the oil film distribution in the lubricated conjunction between a perspex liner and piston. This method was successfully extended by **Brown *et al* (1993)** measuring the oil film thickness by comparing the illumination intensity distribution with that of calibrated data (**Hoult *et al*, (1988)**).

**Dwyer-Joyce, Green, Balakrishnan, Harper, Lewis, Howell-Smith, King, Rahnejat (2006)** used a novel high speed ultrasonic method to measure film thickness in a running engine at realistic speeds and loads, thereby overcoming difficulties with traditional methods. Experimental results (presented in this thesis) measured a minimum thickness of 2 microns for the piston skirt to cylinder liner (2-20 microns total range reported) in a Honda CRF450R single-cylinder engine. The experimentally-measured value correlates with a numerical model (**Balakrishnan and Rahnejat, (2002)**, **Balakrishnan *et al* (2003, 2005)**) and uses methods detailed in **Dwyer-Joyce *et al* (2002)** and **Dwyer-Joyce *et al* (2004)**.

**Saad *et al* (2007)** presents an alternative approach to measure oil film thickness by measuring voltage drop between the bore surface and piston rings on an AVL engine travelling between two tracks that were electrically discharge machined onto the bore surface. This method allows full cycle movement to be measured and reports compression ring film thickness being a maximum at centre stroke reducing at reversal points. Oil ring film thickness is constant throughout the cycle.

**Kim *et al* (2007)** correlates gasoline IC piston skirt friction with lubricating oil film thickness and distribution. Kim concludes that piston (skirt) friction increases where film thickness is relatively low and comprises a good portion of the piston skirt area (thin film area). The thin film area is most prevalent under high engine load immediately after combustion (during the expansion stroke). Thin film area is also large immediately prior to combustion (end of compression stroke). In both of these locations piston friction is relatively high. Detail design of the piston skirt has a strong influence on the minimum piston skirt film and minimum film area **Kim *et al* (2007)**.

**Hooke (1993)** shows that where the direction of entrainment changes the film thickness will fall to zero, while in practice there will always be a finite clearance between the surfaces. This

minimum clearance depends upon the rate of change of entrainment velocity and limit expressions for the film thicknesses in the four regimes of lubrication were developed (**Hooke (1993)**). Similarly **Sato *et al* (2004)** also found that the greatest oil film thickness was measured near mid-stroke, and the oil film appeared thinner near top and bottom dead centre.

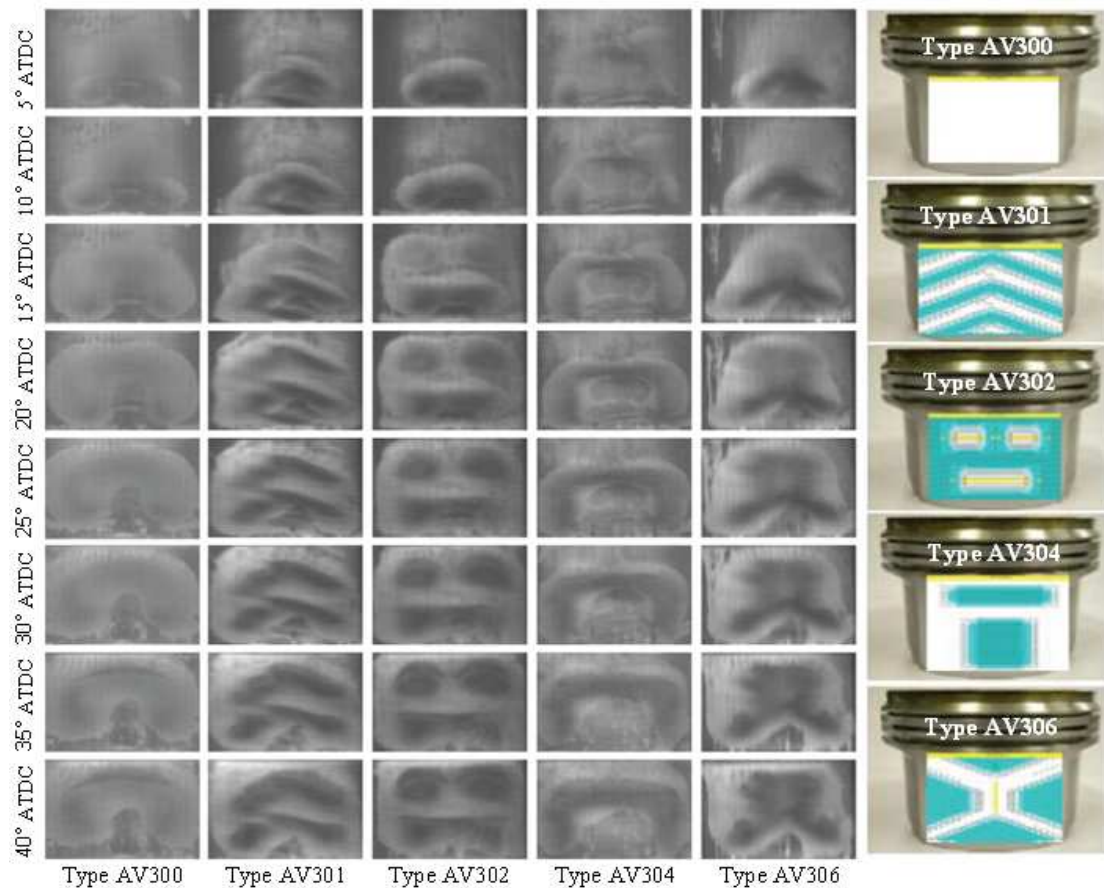


Figure 2.4 Increasing skirt-to-bore contact area for differing skirt types during the expansion cycle (**Kim *et al* (2009)**)

**Kim *et al* (2007)** carried out a study on the effect of lubricating oil film thickness distribution on a gasoline engine piston skirt friction. Dynamic interaction between the lubricating oil, cylinder bore, and piston strongly influences friction behaviour of the piston. A single-cylinder engine was equipped with a floating liner, which enabled real time friction measurements, directly linking the prevailing oil film thickness to friction performance of the piston. It was noted that viscous friction was proportional to the sliding velocity in a contact conjunction. This proportionality was reported as due to asperity (direct surface) interactions. Therefore, under mixed and boundary regimes of lubrication friction does not follow the sliding velocity variation.

A visualization measuring device was also prepared by **Kim *et al* (2007)** for measuring the film thickness using a UV light source and a fluorescent mixed oil (using dye particles). A high-speed video camera coupled with an optical mirror was used to capture the oil film shape/thickness. The piston friction and the corresponding film thickness were plotted for the induction, compression, power, and exhaust strokes respectively. The effect of engine load, skirt width, and skirt ovality on the film thickness and piston friction were also outlined.

It was concluded that the piston friction increases towards the top dead centre (TDC) at the end of compression stroke, where film thickness was found to reduce significantly. Clearly, this is the area where mixed and boundary regimes of lubrication are expected. The piston friction during the expansion stroke increases as the proportion of real contact area occupied by a thin oil film increases (figure 2.4). The thin oil film area also increases with increasing engine load. This can be due to a better defined wedge shape or in some cases due to small localised deflection of the liner surface, giving rise to an elastohydrodynamic regime of lubrication. It was also remarked that piston design features strongly influence observed oil film thickness formation.

**Kim *et al* (2009)** furthers this work presenting very detailed high-speed photography of lubricant flow during engine operation between the piston and an optically transparent (sapphire) cylinder liner. Further, this work is conducted within a floating liner environment allowing in-cycle frictional measurements of the piston and ring elements to be made. **Kim *et al* (2009)** concluded several key factors in reducing piston skirt friction and slap; notably lubricant flow should be stable without starving the central portion of the piston skirt. Various piston skirt designs are proposed coupled with relative performance. Various piston skirt iterations featured localised ‘pockets’ or lubricant reservoirs (refer fig. 2.4), Overall **Kim *et al* (2009)** observed a thinning of lubricant film with increasing speed except in the case of a shallow ‘pocketed’ skirt design (fig. 2.4, type AV302) and that generally the greatest contributor to friction is the thrust portion of the cycle while experiencing combustion load (**Mansouri and Wong (2004)**, **Nakayama *et al* (1997)**).

**Goenka and Meernik (1992)** stated that within reasonable limits skirt lubrication is not necessarily improved with increasing clearance, and that a mixed-lubrication elastohydrodynamic approach is required (for effective automobile piston skirt-liner performance). Progression with this approach is seen as satisfying high reliability and

durability as well as low noise and lowest possible friction. **Oh *et al* (1987)** describe the behaviour of the piston skirt as follows: The pressure deformation of the piston gives the skirt a 'barrel' shape which enables the piston skirt to carry loads during both upward and downward strokes by creating a converging wedge in both directions. **Graddage *et al* (1993)** states that generated lubricant pressures at reversal points (top and bottom dead centre) can be significant.

**Teraguchi *et al* (2001)** conducted novel experimentation with a separate forced (piped) oil feed direct to the piston skirt central area by means of an internal skirt feed on a diesel engine. FMEP reductions in excess of the baseline and solid lubricant versions ( $\text{MoS}_2$ ) resulted, thereby validating the semi-starvation of the piston skirt central portion during operation. It was verified that the supply of a small amount of oil (6mL/min) to the piston skirt reduces about 50% of the block vibration caused by the piston slap motion in idling operation, and about 20% of the piston friction loss in full load operation. Furthermore it was verified that this method did not significantly increase oil consumption.

**Nakayama K., *et al* (1997)** observed a reduction in piston skirt area did not necessarily reduce friction (stating metallic contact area increasing). However, pin offset towards anti-thrust reduces FMEP in the order of 8%. **Parker *et al.* (1989)**, report that reduced skirt area does reduce piston system friction. **Ruddy and Hildyard (1991)** show such a development, the 'X-piston' (AE Piston Products). **Richeiro *et al.* (1995)** further expands on the X-piston as providing increased specific performance (reduced fuel consumption) in the order of 1.5% is cited due to improved hydrodynamic lubrication (figure 2.5).

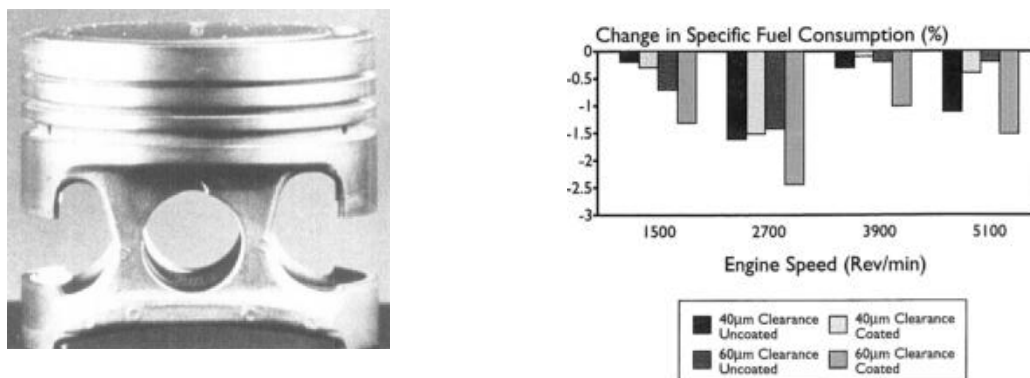


Figure 2.5 AE 'X-Piston' and resulting reduction in fuel consumption  
(**Richeiro *et al.*, (1995)**)

### 2.3.4 Piston slap and dynamics

The secondary motion of the piston (its coupled tilt about the axis of the gudgeon pin and lateral oscillations within the confine of its clearance with the cylinder) is the main source of contact / impact force and moment. Note that the primary motion of the piston is along the axis of the cylinder. The contact / impact forces are generated by the inertia of the system and the combustion gas force.

Piston slap is comprised of clearance, side thrust, component impact, vibration, and excitation (**Cho, Ahn and Kim (2002)**). In-cylinder measurements of piston secondary motion for a large displacement engine are reported by **Graddage *et al* (1993)**.

**Knoll and Peeken (1982)** studied the hydrodynamic lubrication of piston skirts in a motored engine and identified the following parameters to be important parameters influencing secondary dynamics:

- The in-cylinder gas and body inertial forces.
- The piston-to-bore clearance.
- Centre-line off-set of the gudgeon pin offset.
- The hydrodynamic friction acting on the piston skirt and the gudgeon pin.
- The elastic deformation during impact of the piston.

To study structure-borne noise due to piston slap in a 4-stroke, 4-cylinder engine, **Offner and Pribsch (2000)** built an elasto-multi-body model to simulate a piston traversing in a cylinder bore. Extensive finite element analysis was conducted to obtain frequency response from the impact of piston against cylinder bore. Although this analysis was relatively comprehensive, lubrication was not solved for a full cycle of the piston. It was assumed that hydrodynamic reaction action was not significant in all other positions except at TDC (top-dead-centre) and BDC (bottom-dead-centre) in order to minimise computation time.

It is common for the components to be considered rigid when numerically modelled (**Liu *et al* (1998)**, **Yang and Keith Jr. (1996)**). However, **Cho, Ahn and Kim (2002)** utilise a spring damper for the piston-to-bore clearance. Of note the clearance quoted is high (0.05mm radial) and there is no account for thermal expansion.

**Dursunkaya and Keribar (1992)** and **Keribar and Dursunkaya (1992)** present a multi-body solution to piston secondary dynamics (again rigid body), but introduce conventional lubrication analysis of both the skirt and piston pin bore detailing the resulting angular and translated positions of the piston. **Zweiri *et al* (2001)** present a complete non-linear analytical model for a single-cylinder engine, thereby self-generating many required (often assumed) boundary conditions. **Liu *et al* (1998)** conclude that for a conventional rigid analysis piston skirt profile, engine speed, pin offset, and radial clearance are critical factors effecting secondary motion although this drastically reduces with small clearances.

**Kurbet and Malagi (2007)** state the synthesis of the technical contribution in analyzing piston and piston ring motion shows that there is less consideration given to the effect of piston secondary motion namely piston tilt, which has a profound effect on the ring dynamics, which in turn is directly linked to the oil consumption and frictional losses.

**Goenka and Meernik (1992)** elaborate on the relative merits of rigid and thermo-elastic methods stating that, provided the piston and bore have a relatively tight fit, rigid analysis should not be used for predicting piston motion. **Richardson (2000)** concludes that in-cylinder temperature increases measured friction by 0-20% compared to motored testing, having a significant effect on local lubricant viscosity and also reducing secondary motion.

**Mansouri and Wong (2004)** investigate the effects of piston design parameters on secondary piston motion and skirt liner friction by means of a mixed-mode lubrication model utilising impact and resolved forces and structural (piston) deformation. Importantly, the initial as-manufactured piston topography (ovality and taper) is included. However, liner deformation and thermal deformation are not included for both bodies. Conclusions reached are as follows:

- Within limits designed cold clearance has a 20% effect on piston-skirt friction. Oil film thickness has a significant impact on skirt friction loss due to a reduction in boundary contact friction, as opposed to relatively constant hydrodynamic friction.
- Increasing surface waviness radius (radius of curvature from piston skirt top to skirt bottom – in this case a ‘flatter’ profile) of the piston reduces normal contact force and increases normal hydrodynamic force when increased (consequence of conformability).
- Surface finish sensitivity is small compared to waviness.

- Skirt stiffness reduces friction in a similar fashion to increased curvature (conformability), again primarily due to reduced boundary-contact friction.

Overall, **Mansouri and Wong (2004)** state the most significant factor in skirt friction contains only one dimensionless parameter and is directionally proportional to waviness (conformability) and inversely proportional the oil film thickness.

**Nakayama *et al.* (1997)** studied the effect of piston motion on skirt friction for a gasoline engine. The effect of pin offset on the friction force is also determined under this study, as well as the relative frictional contributions to overall friction from different points in the engine cycle.

**Nakayama *et al.* (2000)** observed the friction reduction in piston movement due to the offset positioning of the crankshaft axis with respect to the cylinder axis. It also gave better fuel economy by experimenting with a single-cylinder engine. The piston friction was measured using the floating liner method. The film thickness was measured using laser induced fluorescence (LIF) technique in the piston skirt area. Coil type gap sensors were deployed for measuring piston motion. Introduced crankshaft offset changed piston slap motion. Hence, the condition of piston skirt contact changed thereby affected the friction characteristics overall.

Similar to the findings of **Nakayama *et al.* (1997)**, **Ragot and Rebbert (2007)** observed (analytical) variations in friction (FMEP) due to changes in crank offset from the central plane. Initially starting at 0mm, 6 and 12mm offsets were investigated. In conclusion, FMEP reduction was noted for part-throttle conditions (idling / light duty). However, as load and speed increased the zero offset case gave the greatest reduction (though not in motored engines).

### 2.3.5 Use of finite element analysis

**Knoll and Peeken (1982)** calculated piston skirt deflections using the finite element method. **Oh *et al.* (1987)** referred to the piston design (i.e. the piston's upper and lower end relief radii and ovality) as key factors in reducing friction between the piston skirt and the cylinder liner. Using the finite element package 'Nastran' to compute structural and thermal deformation, simulation was conducted for a motored engine.



**Oh *et al* (1987)** declared that in order to achieve realistic pressures and lubricant films in the contact the profile of the piston has to be modelled accurately. A comparative study between two different piston skirt designs indicated the importance of skirt axial profile in reducing friction.

**Goenka and Meenik (1992)** conducted a sensitivity analysis to study the friction between the cylinder bore and piston skirt of a motored engine (using an in-house computer code developed by General Motors), and by varying the clearance space, the gudgeon pin position and the mass of the piston. Two separate analyses were conducted; one assuming the piston skirt was elastic and the other rigid. Again, a finite element code was used to solve the deformation of the piston skirt (in the case of the elastic piston skirt), assuming the cylinder bore to be rigid.

This study showed the effect of friction behaviour within the contact by varying each of the above parameters in isolation. By comparing the results obtained from the numerical analysis with the experimental data, the authors concluded that a rigid analysis showed a greater deviation from the experimentally measured friction than that obtained from the elastohydrodynamic analysis.

**Abbes *et al* (2004)** developed a thermo-mechanical model for a direct-injection diesel engine piston, citing this as an important start point for an elastohydrodynamic model. In this work the cylinder bore deformation is not included. However, the high significance of thermal contribution (steady state approximation) over structural deformation is noted. Work in producing a transient thermal model is reported by **Dunaevsky and Vick (2004)** thereby extending previous work (**Dunaevsky and Kudish (1988)**) for industrial compressors, though no reference to IC engines was made and these transient effects appear absent from IC engine numerical tribological analysis.

Examples of methods employed to experimentally measure component temperatures can be found from **Rohrle (1994)**, **Furuhama *et al* (1984)** (piston temperature profiling, rpm vs. number of rings), **Hamzehei and Rashidi (2006)**, and **Kumar *et al* (2004)**. **Keribar *et al* (1993)**, in developing a proprietary piston-to-cylinder tribological model state the importance of elastic bodies (vs. rigid) to accurately compute skirt friction, and the consideration of operating geometrical changes due to temperature (thermal expansion).

**Oh *et al* (1987)** produces an EHL model regarding piston skirts. In conclusion they state that the exact operating shape of the piston skirt can only be determined by combined thermal and EHL analysis of the piston containing the barrel shape (of the piston), and that the friction and lubrication characteristics are very sensitive to piston skirt detail geometry. **Zhu *et al* (1993)** provides foundation work on the analysis of piston skirts, with particular attention to deformation. The use of steady state thermal analysis is justified (for piston skirts) and deformation considers both the piston and the cylinder bore. Initial piston shape and thermal effects are considered and presented as important for realistic results.

**Mitchell *et al* (1995)** discuss the use of the finite element analysis method to reduce the overall lead time for new piston designs. **Mitchell *et al* (1995)** presents certain guidelines in piston development and an example of piston skirt-to-cylinder bore contact pressure, (figure 2.6) as below.

- Structural features have to be checked using thermo-mechanical finite element analysis and life analysis.
- Behavioural features have to be checked using various analysis techniques involving engine thermodynamics, kinematics and tribology.

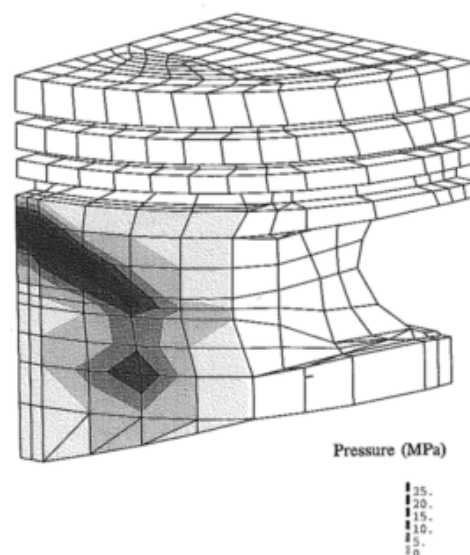


Figure 2.6 Piston skirt-bore contact pressure from **Mitchell *et al*. (1995)**

Work using the finite element method regarding thermal profiling of the piston assembly was performed by **Choi *et al*. (1993)**. **Choi *et al* (1993)** analyzed thermal conduction in the piston ring of a gasoline engine using the boundary element method in three dimensions. Engine

performance simulations were made to obtain the boundary conditions of in-cylinder gas temperature and heat transfer coefficients.

The variation of piston temperature at each point on the piston with respect to engine speed was plotted. The temperature distribution at each part of the piston surface was measured using an L-link mechanism and was compared with the result obtained by the boundary element method. The maximum temperature of the piston crown surface occurred at the centre region of the crown and temperature decreased linearly radially away from the piston centre. The location of the inlet port, exhaust port, and spark plug affected the temperature distribution of the piston crown.

Measures exist to liquid-cool piston crowns by means of integral oil filled gallery features (**Bing *et al.*** US patent 5947065). These measures reduce crown temperatures. However, they are only suitable for cast pistons. A method to incorporate gallery cooling within non-cast pistons is as per **Howell-Smith**, UK patent (pending) 0821761.4.

### 2.3.6 Cylinder finish and wear

Cylinder bore wear and remedial methods are subject to many opinions and qualitative approaches (**Becker and Ludema (1999)**). Indeed, as a bore manufacturer **Capricorn Automotive Ltd (2008)** cites (modifications to the cylinder bore topography) ‘it is as a restless subject for continuous subjective alteration by clients’. **Tian *et al* (1996)** investigated film thickness with regards to conjugating body roughness for multi-grade lubricants. Generally a reduction in cylinder bore roughness decreases lubricant transport to the upper bore region and vice-versa. Logically this is seen as benefitting one region to the detriment of another in the case of constant roughness bore surface, and likely produces the cyclical investigations in bore surface (**Capricorn Automotive Ltd (2008)**).

**Becker and Ludema (1999)** make a distinction between initial wear compared to cylinder average life wear due to the formation of new compounds on the mating components. **Knopf *et al* (1998)** details a hydrodynamic solution for the compression ring-to-bore surface with consideration for cavitation as well as elastic-plastic asperity deformation as per the Greenwood –Williamson model. **Knopf *et al* (1998)** shows that through alterations to the honing angle a good compromise between oil transport and hydrodynamic build-up was found. Further bore surfaces with asymmetrical amplitude density distribution and transversely

orientated topography provided a decisive performance improvement. **Tomanik and Ferrarese (2006)** utilise ‘slide honing’ – a form of extreme plateau honing, itself reducing overall friction compared to traditional plateau honing.

**Xiaoming *et al* (2004)** develop a model predicting EHL for the compression ring-to-cylinder bore conjunction whilst considering bore ellipticity and surface roughness all in a multi-axis fashion. Of note, the surface finish of both the ring face and the bore are identical and the level of ellipticity (radial) is only 1 micron. **Mishra, Balakrishnan and Rahnejat (2008)** increase the level of investigation in the compression ring-bore conjunction, concluding that forces developed (which are far higher than the piston-skirt bore conjunction) are insufficient by themselves to lead to local (micro) deformation or significant lubricant viscosity increase, and a piezo-viscous regime as opposed to EHL dominates.

Logically reductions in lubricant viscosity (to the benefit of skirt viscous shear) as well as thermal effects will further detriment this (compression ring) conjunction. **Mishra, Rahnejat and King (2009)** further expand this investigation confirming the mixed and boundary nature of the transient rheological behaviour at stroke reversals and lubricant ‘reservoirs’ by means of surface modification would encourage piezo-viscous behaviour whilst guarding against undue thixotropic behaviour.

### 2.3.7 Piston and cylinder friction

**Robinson (1959)** classified the basic design and function of the automotive engine piston rings. The piston ring can be classified either as a compression ring or an oil control ring. The compression ring’s main purpose is that of efficient sealing of the combustion chamber, so that maximum possible effort is transferred from the expanding gases to the crankshaft. The cross-section of the compression ring was always designed as rectangular in cross-section. For high-speed applications and performance the ring is designed to be thinner and thinner with the equivalent strength and rigidity. A narrower ring provides more efficient and quicker seal on the peripheral face. An internally-stepped compression ring provides better oil control (through twisting) due to forming an angle to the cylinder wall as it rides over the oil film on the upstroke, yet a scraping action on the cylinder wall during down stroke (where it becomes parallel).

**Sagawa *et al.* (1990)** pointed-out that the axial movement of compression rings in high-speed engines tends to be unstable due to inter-land pressure and inertia force. Hence top ring floatation gives poor sealing function and encourages blow-by. To stabilize piston ring axial movement the most effective method is to reduce ring weight or axial width. The durability of the narrow axial width piston ring is improved by using steel material. Due to the reduced axial width of the piston ring there is a reduction in friction and overall mass. **Thring (1992)** predicts piston rings (especially oil rings) and piston body (skirt) as the greatest contributors to in-cylinder friction (with the exception of windage at very high speed). Successful friction reduction from oil ring modifications is detailed by **Tomanik and Ferrarese (2006)**.

**Toshihide *et al* (1993)** coated piston and valvetrain components with differing radioactive isotopes analysing the sump oil after running. Analysis revealed the highest proportion of removed material originated from the piston system, therefore implying a higher relative contribution to engine friction. It is unclear how these results would compare to direct doping of substrate materials (i.e. valvetrain components are relatively harder than piston cylinder components, and therefore one would expect a coating of same hardness to wear quicker on a valvetrain component than on a piston system component)

**Nakayama *et al* (1997)** studied the effect of piston motion on piston skirt friction in a gasoline engine. The study's aim was to reduce the large contribution of piston skirt friction observed during the power stroke. The analysis predicted the resulting piston skirt wear in various piston skirt shapes and correlated the predictions with actual friction measurements. Piston skirt friction is highest near mid-stroke just after combustion, and skirt frictional contribution towards total cylinder friction is of the order 30% (**Tung McMillan (2004)**).

**Uras and Patterson (1983)** observed that throughout the engine cycle the friction forces were primarily in the mixed or boundary region. Under motoring and firing conditions the friction force was a maximum at TDC (compression stroke end). In tests with no compression the friction was higher when the piston was ascending. This asymmetry is consistent with the scraper profile of the second compression ring.

Several methods exist to measure reciprocating in-cylinder friction (**Kurbet and Malagi (2007)**) falling into three distinct groups: IMEP experimental results, laboratory slider type mechanism and, arguably more representative, though technically challenging modified engine measurements.

Laboratory slider mechanisms invariably involve a split ring or piston element within a split cylinder bore reciprocating at relatively low speeds and estimated normal force (**Dearlove and Cheng (1995)**, **Ting (1993)**, **Akalin and Newaz (1998)**), yet produce accurate resolved friction from relatively simple instrumentation. Much work has been performed in Japan (**Furuhamma and Sasaki, (1983)**) and by General Motors (**Goenka and Meernik (1992)**), utilising the floating liner method, which records total piston ring and skirt friction.

**Furuhamma *et al* (1982)** concludes that although the effects of load and gas pressure were evident, their effect was small compared to other frictional losses. This was due to the short working duration of the gas pressure and that the rubbing surfaces temperature increased under high load. Furuhamma also assumed that the piston generated a large frictional force after combustion due to the effect of the piston slap impulse and, immediately after this, the resolved combustion thrust onto the cylinder wall.

**Goenka *et al* (1992)** further developed a numerical model to parametrically evaluate differing engine configurations for frictional losses as well as piston-to-bore friction. **Taylor *et al* (1994)** used laser induced fluorescence to verify numerical predictions of bore friction showing the strong influence on shear thinning (**Tian *et al* (1996)**). Along with shear thinning, the use of a starved, thermo-viscous model provided good correlation. However, lubricant degradation was not included though considered important for future work. **Sui and Ariga (1993)** similarly develop such a model, but concentrate on the effects of surface topology of the rings verifying with a laboratory moving liner apparatus. The effects of component wear (in-situ re-profiling) results in reduced friction and a deceleration of component wear to a limiting value, and initial values of roughness and form for the ring-pack, skirt, and bore dramatically alter the speed this limiting position is reached and its relative condition (**Taylor (1998)**).

General trends show that friction is linearly proportional to the maximum frictional force found in the mid-stroke (**Stanley *et al* (1999)**) and with certain modifications (geometric) compression rings could be made to operate almost entirely in the hydrodynamic range, with the exception of dead centres where frictional coefficient increases from a minima of 0.03 to 0.14 (**Cho, Choi and Bae (2000)**).

However, the same was not the case for oil rings which operated in mixed mode for the entire stroke and developed higher overall friction than the compression ring (**Cho, Choi and Bae (2002)**). This observation is further supported with acoustic emission experiments conducted on diesel engines by **Douglas *et al* (2006)**, where strong asperity interaction between the oil ring and cylinder bore was measured.

**Kurbet and Malagi (2007)** reviewed frictional losses on both piston skirt and rings, opening with the necessity for a thorough understanding of the lubrication condition at piston-ring-cylinder bore surface. Furthermore, the complexity of the system requires a three-dimensional finite element approach including more engine components than the traditional four decades' worth of primary and secondary piston motion methodology.

**Shayler *et al* (2008)** investigated both ring tangential load and skirt profiles effects on friction. Skirt profile optimisation was undertaken and culminated in approaching a 20% reduction in FMEP. Increasing piston diametric clearance to the largest designed manufacturing limit (max production clearance) produced improvements between 2 and 10%. Further increasing this clearance resulted in a 5-10% improvement relative to baseline and this could be extended by much larger clearances at higher engine speeds. Reducing piston skirt roughness (1.29Ra, 5.75Rz) produced a 4% reduction and a projection for increased benefits at lower oil viscosities.

**Wakabashi *et al* (2009)** utilised a floating liner device to investigate cylinder break-in for differing ring pack types (**Yoshida *et al* (1987, 1990)**). This provides incremental updates and developments to the **Furuhama *et al* (1983)** floating liner (fig 2.7), overcoming gas pressure influence on the liner upper surface, and investigating cylinder surface preparation (single and plateau honing). The oil ring is stated as operating in the mixed lubrication area and physical vapour deposition (PVD) coatings on the compression rings reduce friction, thereby producing an overall reduced FMEP. FMEP was reduced in the case of plateau honing, reaching a low point vs. single honing after one hour of operation. However, this increased (inferred) to a similar level (of friction) as single honed after extended running. Presented surface finishes pre and post engine test show a similar finish for both single honed and plateau honed after 30-60hrs of testing.

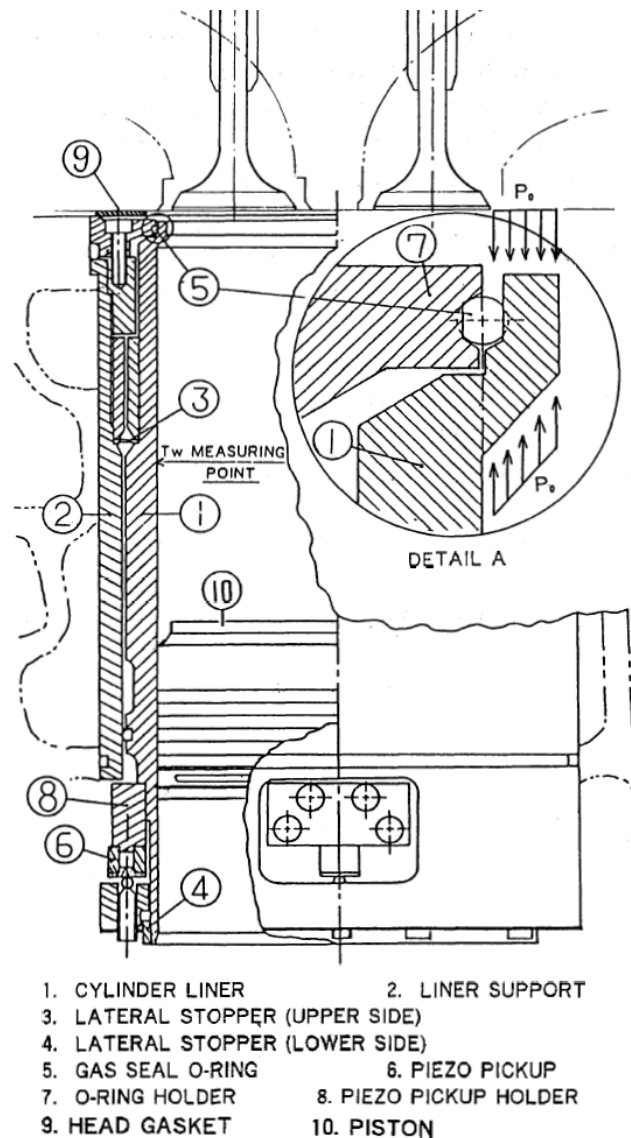


Figure 2.7 'Floating liner' courtesy of **Yoshida *et al* (1990)**

### 2.3.8 Coatings, surface treatments and lubricant additives

**Malaczynski *et al* (1996)** showed that for any piston / bore material couple to survive the engine environment the materials must be evaluated for their cold scuff resistance. "Given enough time, scuffing will always occur under dry conditions, even for the conventional combination of an aluminium piston coupled with a cast iron liner".

For vehicle mass considerations, vehicle engine construction has trended towards light alloy construction. This has seen a general reduction in the sectional stiffness in the bore area. Likewise, increased engine rotational speed (due to downsizing) has seen reduced mass and effective sectional stiffness in the piston assembly. Aluminium (alloys) possesses a lower stiffness than for example cast iron and although this increases contact conformability, it is inherently a poor choice for a bearing surface (**Wang and Tung, 1999**).



“Examination of the worn surfaces suggested that the wear between Al / Al is dominated by an oxidative wear mode. Adhesion between aluminium and aluminium caused scuffing to occur immediately after loading. In order to prevent Al / Al from scuffing when used as piston / bore materials, without cast iron liners one of the aluminium parts has to be treated either by a surface coating or by ion implantation, which would effectively change the surface physical and chemical characteristics through surface alloying.”

**Donnet and Erdemir (2004)** reviewed the almost explosive use of surface treatments and coatings since the 1980's covering soft coatings (lamellar solids, halides, sulphates and polymers such as PTFE and DLC) and hard coatings (carbides, nitrides, borides) produced by diverse processes such as PVD, CVD, etc. resulting in solid lubricant films, duplex, multiplex and nano-structured forms. In combination with 'smart' surface engineering such as micro-texturing, these coatings offer higher tribological performance than conventional uncoated and / or traditionally-textured surfaces.

**Mistry (2008)**, investigated the lubricated performance of DLC coatings with a range of lubricants. **Mistry (2008)** reported that with an optimal lubricant the lubricated friction coefficient of steel is 0.07 whereas as WC-DLC substrate is 0.05. **Shen (1997)** explores emerging coatings and surface treatments for compression rings, stating the requirement to provide low friction in a poorly lubricated environment. Nickel composite coatings (NCC), plasma spray (predominantly molybdenum containing), and PVD / multilayer PVD were amongst those investigated. Likewise **Rohrle (1994)** discussed coating options for pistons and piston skirts in general.

**Prasse *et al.* (1967)** discussed recently specified piston ring materials, face coatings, and designs, (including straight face rectangular compression rings, taper face piston rings, straight face torsion rings, taper face torsion rings, scraper compression rings, reverse torsion compression rings and barrel face piston rings). The constituent face material of piston rings such as hard chromium, molybdenum, etc. are discussed broadly for wear rate and motoring friction vs. engine speed. Future developments of piston ring face coatings are also discussed and suggested to include treatments / coatings such as titanium carbide nickel, boron carbide nickel, mica-nickel, silicon carbide nickel and composite electrolytic coatings.

(**Prasse *et al.* (1968)**) States multiphase hard molybdenum-containing plasma-applied materials are reliable in heavy duty engines. They are relatively unsusceptible to failure such as temporary periods of engine overheating, variations in bore finish, and high-load operating conditions. Oxide growth in molybdenum coatings does not occur at piston ring operating temperatures of heavy duty diesel engines. Improper coating may have low tensile and bond strength, leading to premature failure. The green (as manufactured – i.e. not ‘run-in’) engine friction could be reduced through the use of a graphite-impregnated top compression ring. For a given load output reduced ring friction reduces NO<sub>x</sub> emissions. Metallic oil could also improve piston ring performance (**Prasse *et al.* (1981)**).

**Prasad and Zabinski (1993)** detail the potential of tungsten disulphide (WS<sub>2</sub>) as it has a friction coefficient as low as 0.04, though concedes atmospheric interactions (moisture) can increase this fourfold. **Vadiraj and Kamaraj (2009)** further investigate WS<sub>2</sub> and molybdenum disulphide on a plasma-nitrided spheroidal graphite (SG) iron substrate, stating with reference to IC in-cylinder application ‘a great potential exists to reduce friction especially during initial life’.

Surface modifications / texturing have become an important approach in the reduction of friction. The developments in this field are relatively recent and follow from a fundamental understanding of the mechanisms of fluid film lubrication. Clearly, the hydrodynamic wedge effect which encourages entrainment of lubricant between two contiguous surfaces must also play a similar role between asperities of surfaces as small *bearings*.

Theoretical work of **Salama (1952)** is considered as the fore-running contribution. He studied the effect of what one may consider as macro-roughness from a machining process on the performance of parallel thrust bearings. He showed that with sufficient supply of lubricant, a resulting hydrodynamic micro-wedge would improve friction. This was an interesting finding, noting that surface roughening can improve friction if a supply of lubricant into these micro-wedges can be assured. Prior to such investigations the interaction of surfaces (seen in the context of dry surfaces) itself the root of friction definition, was seen to exhibit increased friction with increased roughness.

The realisation that normally occurring, as manufactured surface topography could lead to enhanced lubrication meant that deliberate texturing of surfaces could be of potential benefit.

An early study was carried out by **Hamilton *et al* (1966)**, who investigated the effect of artificially created asperities by means of photo-etching. They proposed an approximate theoretical analysis of the load support mechanism produced by the asperity/cavities. The study of micro-asperity lubrication was continued later by **Anno *et al* (1968)**. They proposed a theory for load support in the parallel surfaces of a rotary shaft face-seal. One of the parallel surfaces contained cylindrical (protruding) micro-asperities and it was assumed that a tilt mechanism (of the asperity tip) occurred to enable load support.

In another study by **Anno *et al* (1969)** the effect of leakage from seals with modified surfaces was added. They concluded that the *negative features* (cavities) are also capable of producing comparable load support to the *positive features* (protrusions). Load support with almost nil leakage could be achieved by negative asperities.

Surface texturing offers improved load carrying capacity and reduced friction (**Anno *et al* (1969)**). Furthermore side leakage can also be reduced. For these reasons, surface texturing has made in-roads for conjunctions which are largely subject to mixed or even boundary regimes of lubrication. These occur at reversal points such as those experienced by the piston skirt and piston rings to cylinder bore during IC engine reciprocation. The use of this approach has become progressively important in dealing with boundary lubrication, a regime previously improved solely by lubricant rheology (boundary lubricants) and surface coatings.

Since the initial work with photo-etching, many methods for surface modification / texturing were gradually developed. These included indentation, cross-hatch honing and laser surface texturing (LST). **Etsion (2005)** provides a good review of surface texturing developments. With emerging understanding of squeeze film effect as another mechanism of fluid film lubrication, mainly in the 1970s and 80s, the role that micro-cavities play as reservoirs of lubricant is also exploited in the so-called *negative features*.

Detailed numerical analysis by **Rahmani *et al* (2007)** and by **Balakrishnan *et al* (2005)** showed that because of lubricant retention, the *negative features*, perform better than the *positive features*. Experimental analysis performed by **Ohlsson *et al* (2003)** presented frictional reductions in steel strips after micro-texturing with negative features.

Within the IC engine, the cylinder bores are invariably finish processed by means of cross-hatch honing resulting in a characteristic surface texture of inherently negative surface features (**Wong *et al*, 2006**). This process also corrects geometrical errors (straightness, roundness etc.) and combined with relatively low cycle times is therefore the process of choice in finish preparation of IC cylinder bores. **Wong *et al* (2006)** showed that cross-hatched angle plays an important role and alterations to this angle produce differing frictional losses and oil consumption. Where piston to bore contact occurs, lubricant flows into the conjunction from a meniscus ahead of the contact.

Depending on the contact condition and surface features (including cross hatch angle) lubricant tends to skirt around the areas of high pressure caused by discontinuity in contact profile. This is noted by **Balakrishnan *et al* (2003, 2005)**, where pressure raisers occur at the leading and trailing edges of the contact. Therefore, with grooves it is important to follow patterns that encourage the lubricant flow into the contact proper. Process limitations are inherent with honing, and alternative (additional) processing methods facilitate more extreme negative feature pocketing.

**Rahmani *et al* (2007)** evaluated the optimum configuration of introduced micro-texturing (rectangular, triangular etc.) with respect to parallel thrust bearings. **Kligermann *et al* (2004)** presented theoretical benefits of micro-texturing the working face of compression rings. Parameters including pattern depth, pattern diameter, and aspect ratio are presented with resulting friction for a relatively simple linear array of dimples. **Ronen and Etsion (2001)** used a reciprocating slider to correlate minimum friction as a simple ratio of etch pore depth over diameter, thereby showing stability and friction reduction over a surprisingly wide band.

Subsequent work (**Ryk, Kligerman and Etsion (2002)**) using actual piston ring samples found up to 40% reduction in friction for severe starvation with etching performed on ring segment faces. Quoted laser pattern parameters were a diameter of 100 microns with an etch depth of 10 microns for each dimple, with an area density of 20%. Excessive etch depth is reported as (may become) detrimental in excess of 20 microns depth although no depth correlation is given.

**Ryk *et al* (2005)** developed partial ring face etching as opposed to full-face with friction reduction some 60% compared to a fully etched version. **Ergen *et al* (2008)** used linear etched

pockets on the cylinder bore wall in two versions; a) upper reversal point only and b) entire bore area though with reduced density in mid to bottom stroke. Oil consumption by means of a sulphur tracing technique was used to compare against a traditional plateau honed surface. Oil consumption was slightly lower than the traditional plateau surface, especially in the condition where etching was in the upper portion only. **Shayler *et al* (2008)** reports a 10% reduction in FMEP by the use of laser-pocketed cylinder bores.

**Balakrishnan *et al* (2002, 2003, 2005)** developed a numerical technique to predict oil film thickness within an IC engine between the top ring and piston skirt-to-bore conjunctions. Introduced pits at reversal points and increased skirt roughness are shown to increase minimum oil film thickness thereby reducing friction. In chapter 6 the numerical analysis from **Balakrishnan *et al* (2002, 2003, 2005)** is used to advise laser etched patterns which are subsequently tested on some cylinder liners.

Lubricant additives such as molybdenum dithiocarbamate (MoDTC), according to **Glidewell and Korcek (1998)**, during reciprocator testing consistently produce lower friction except in the case of persistent starvation. During persistent starvation the frictional values recorded tend to those of the unmodified lubricant not containing MoDTC. **Kurbet and Malagi (2007)** details a four or five-fold increase in piston cylinder friction for a cold start (20°C) vs. hot running condition (100°C), and result sensitivity to this must be considered when determining the contributing ring friction.

**Rao *et al* (1997)** presents a testing methodology for frictional comparison of piston skirt coatings, comparing four types of solid film lubricants. Observations regarding the oleophobic nature of PTFE (a common piston skirt coating) as well as tungsten disulphide are made versus the oleophillic nature of molybdenum disulphide (MoS<sub>2</sub>) (see also **Sagawa *et al*, (1991)**) as well as the tendency for oleophillic coatings to promote oil film formation. A clear benefit in low-speed friction is made for the four tested types at low engine speeds and loads (3-4%), which decreases with increasing engine speed.

**Shankara *et al* (2008)** adds zirconia and graphite additions to MoS<sub>2</sub>, reporting frictional benefits and also the behaviour of moisture (environmental) which is shown to improve friction as well during reciprocating scratch tests.

## Chapter 3

### Piston assembly dynamics

---

#### 3.1 Overview

To predict piston skirt-to-bore friction it is necessary to ascertain the regime of lubrication as noted in the previous chapters. To determine the prevailing tribological conditions a prediction of film thickness is required at any instant of time. Any film thickness depends on the nominal clearance, global thermo-elastic deformation of the contiguous surfaces, and further localised deformation when a film of lubricant is pressurised in the gap. The procedure to determine any prevailing film thickness is described in detail in chapter 4.

To determine the global thermo-elastic and local contact deformations it is necessary to know the undeformed geometry of the contiguous mating surfaces, the applied load (generated contact pressures), kinematic conditions, and temperature. These conditions are determined by the piston primary and secondary motions, governed by combustion loading and inertial dynamics as well as by the forces and moments generated at the contacts made by the piston skirt with the cylinder bore / liner at the thrust and anti-thrust sides. Therefore, an integrated study of dynamics, combustion loading, thermo-elastic deformation, and elastohydrodynamics is required. Such an analysis spans physical interactions across a broad scale from micro-scale to large displacement inertial dynamics. **Perera *et al* (2007, 2010)** termed such an analysis as *multi-physics, multi-scale analysis*.

This chapter is devoted to the derivation of equations of motion of the piston relative to the cylinder bore, which is considered to be stationary. The primary motion of the piston is its translational motion with respect to the cylinder. This motion is considered to be kinematic, as also noted by other research workers such as **Balakrishnan (2002)**, **Balakrishnan and Rahnejat (2005)**, **Offner and Pribsch (2000)** and **Gohar and Rahnejat (2008)**. However, the geometry of the piston-connecting rod-crank as a slider mechanism causes inertial forces which comprise spectral contributions at multiples of engine speed. Additionally, the repetitive combustion process is also composed of combustion-fundamental frequency and its multiples. This depends on the 2 or 4-stroke nature of the combustion process and is referred to as *combustion signature*. Therefore, the induced inertial forces caused by the slider-crank mechanism contain contributions at various frequencies; those of the combustion process and those of inherent system imbalances. These induced inertial effects are termed *engine order*

*vibrations*. They affect the system kinematics as well, which determine the speed of entraining motion of the lubricant into the piston skirt-to-cylinder conjunctions.

**Rahnejat (1998)** provides a comprehensive analysis of engine order vibrations and the resulting kinematics. There is also secondary piston dynamics. This includes side-to-side lateral motion of the piston as well as its to-and-fro tilting motion, both within the confines of piston-to-bore clearance. Of course, this clearance is affected by thermal distortion of both the piston and the bore, as well as the localised deformation of the surfaces due to the generated lubricant pressures. The secondary dynamics and primary motion kinematics are linked through the lubricant film formation and the corresponding generated contact pressures.

In this chapter traditional kinematic equations are developed for the crank slider mechanism on a relative position basis leading to acceleration of the bodies. In combination with cylinder (pressure) forces, this ultimately derives the required dynamic forces on the bodies.

### 3.2 Piston kinematics

The traditional mechanism employed in IC engines is the crank slider type. Two basic versions are used; one is where the piston centre of rotation remains nominally in line with the crank rotation centroid (zero offset type) and the second version is where there is a lateral offset (offset type). Note that the offset is possible in one of two directions. The general and offset types are shown in figures 3.1 and 3.2:

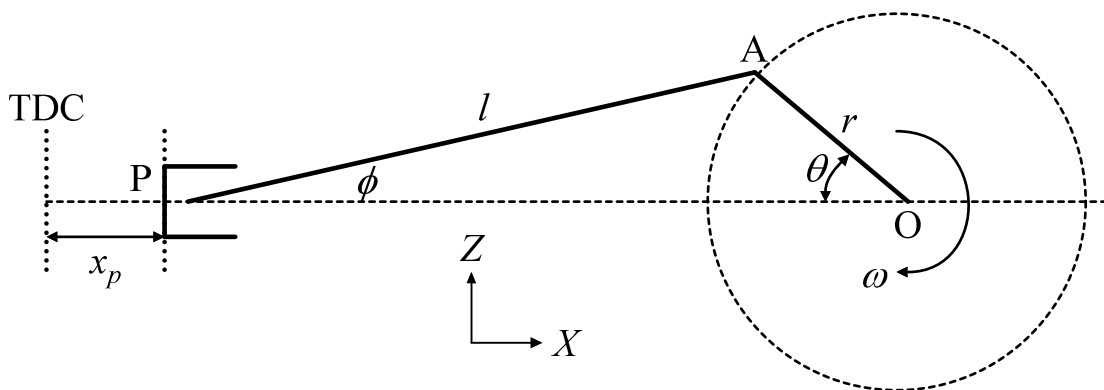


Figure 3.1 Piston assembly mechanism (zero offset)

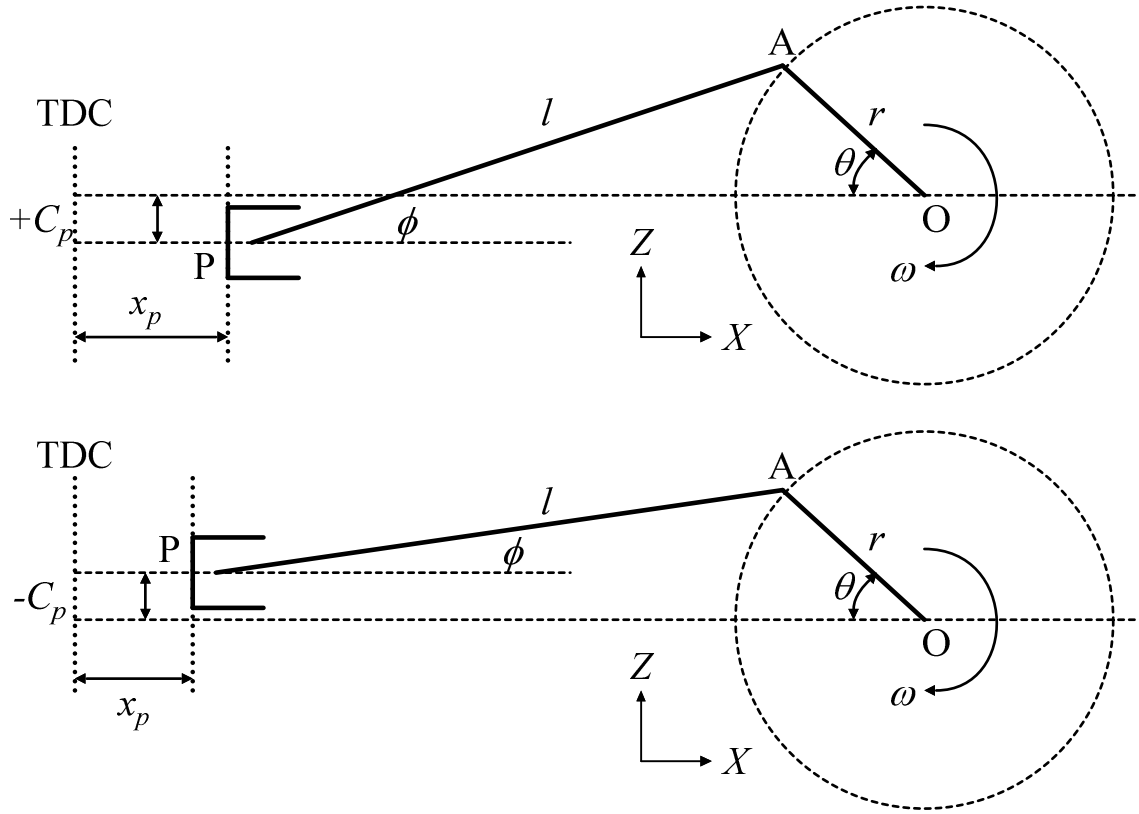


Figure 3.2 Piston assembly mechanism (offset)

The following dimensionless parameters are developed:

$$\Lambda = \frac{r}{l} \quad (3.1)$$

$$\psi = \frac{C_p}{r} \quad (3.2)$$

In the simple mechanism case in figure 3.1 equation 3.2 yields a zero value.

For a constant angular velocity:

$$\omega = \frac{d\theta}{dt} \quad (3.3)$$

Note that this assumption is made for ease of representative derivations here. In fact, as noted in section 3.1, the angular velocity of the engine comprises multiples of the nominal velocity  $\omega$ , known as engine order vibrations. Depending on the number of cylinders in an engine and the flexibility of crankshaft the significant engine orders (multiples of the nominal engine



speed) vary. **Rahnejat (1998)** provides an analytical approach to determine the significant engine order multiples in crankshaft speed and piston motion according to the number of cylinders, the ratio  $\Lambda$ , and flexibility of the crankshaft.

### 3.2.1 Calculation of piston vertical position

Considering the top dead centre (TDC) position as the origin, the piston translates from the TDC position during the crankshaft rotation reaching a maximum displacement from TDC, a position referred to as the bottom dead centre (BDC), before ultimately returning back to the starting point (TDC). These two positions are also referred to as reversal points in tribological parlance, because the entraining motion of the lubricant into the contact changes direction (inlet boundary reversal).

This also means that at these locations momentary cessation of entrainment takes place. This condition can lead to starvation of the contact and a greater chance of boundary interactions. From the general case in figure 3.2:

$$x_p = \sqrt{(r+l)^2 - C_p^2} - (r \cos \theta + l \cos \beta) \quad (3.4)$$

Substituting equations (3.1) and (3.2) into the above equation yields:

$$x_p = r \left[ \sqrt{(1 + 1/\Lambda)^2 - \psi^2} - \left( \cos \theta + \frac{1}{\Lambda} \cos \phi \right) \right] \quad (3.5)$$

Considering both positive and negative offsets in triangle OAP in figure 3.2:

$$\sin \phi = \Lambda \sin \theta \pm \frac{C_p}{l} \frac{r}{r} = \Lambda (\sin \theta \pm \psi) \quad (3.6)$$

And clearly:

$$\cos \phi = \sqrt{1 - \Lambda^2 (\sin \theta \pm \psi)^2} \quad (3.7)$$

Binomial power series expansion of equation (3.7) yields:

$$\cos \phi = 1 - \frac{\Lambda^2}{2}(\sin \theta \pm \psi)^2 - \frac{\Lambda^4}{8}(\sin \theta \pm \psi)^4 - \frac{\Lambda^6}{16}(\sin \theta \pm \psi)^6 - \dots \quad (3.8)$$

The pistons displacement can now be expressed as:

$$x_p = r \left[ A_0 + A_1 \cos \theta + A_2 \cos 2\theta + A_4 \cos 4\theta + A_6 \cos 6\theta + \dots \right] \pm (B_1 \sin \theta + B_3 \sin 3\theta + B_5 \sin 5\theta \dots) \quad (3.9)$$

where the primary (cosine) harmonic coefficients are:

$$\begin{aligned} A_0 &= \sqrt{(1 + 1/\Lambda)^2} - \psi^2 - \frac{1}{\Lambda} + \left( \frac{1}{4}\Lambda + \frac{3}{64}\Lambda^3 + \frac{5}{256}\Lambda^5 + \dots \right) + \\ &\quad + \frac{1}{2}(\Lambda\psi)^2 \left( \frac{1}{\Lambda} + \frac{3}{4}\Lambda + \frac{45}{64}\Lambda^3 + \dots \right) + \frac{1}{8}(\Lambda\psi)^4 \left( \frac{1}{\Lambda} + \frac{15}{4}\Lambda + \dots \right) + \dots \\ A_1 &= -1 \\ A_2 &= -\left( \frac{1}{4}\Lambda + \frac{1}{16}\Lambda^3 + \frac{15}{512}\Lambda^5 + \dots \right) + \frac{3}{8}\Lambda^3\psi^2 \left( 1 + \frac{5}{4}\Lambda^2 + \dots \right) + \frac{15}{32}\Lambda^5\psi^4 + \dots \\ A_4 &= \left( \frac{1}{64}\Lambda^3 + \frac{3}{256}\Lambda^5 + \dots \right) + \frac{15}{128}\Lambda^5\psi^4 + \dots \\ A_6 &= \left( \frac{1}{512}\Lambda^5 + \dots \right) + \dots \end{aligned} \quad (3.10)$$

Further harmonic (sine) coefficients correspond to the presence of pin offset:

$$\begin{aligned} B_1 &= -\left[ (\Lambda\psi) \left( 1 + \frac{3}{8}\Lambda^2 + \frac{15}{64}\Lambda^4 + \dots \right) + \frac{1}{2}(\Lambda\psi)^3 \left( 1 + \frac{15}{8}\Lambda^2 + \dots \right) + \frac{3}{8}(\Lambda\psi)^5 + \dots \right] \\ B_3 &= \frac{1}{8}\Lambda^3\psi \left( 1 + \frac{15}{16}\Lambda^2 + \dots \right) + \frac{5}{16}\Lambda^5\psi^3 + \dots \\ B_5 &= -\left[ \frac{3}{128}\Lambda^5\psi + \dots \right] \end{aligned} \quad (3.11)$$

The pin offset direction is as shown in figure 3.2; positive when it is in the opposite direction as to the tangential motion of the crank pin at the TDC. In the zero offset case (figure 3.1),  $\psi = 0$ . The following simplification occurs from equations (3.8-3.11):

$$\cos \phi = 1 - \frac{\Lambda^2}{2}(\sin \theta)^2 - \frac{\Lambda^4}{8}(\sin \theta)^4 - \frac{\Lambda^6}{16}(\sin \theta)^6 \dots \quad (3.12)$$

$$y_p = r[A_0 + A_1 \cos \theta + A_2 \cos 2\theta + A_4 \cos 4\theta + A_6 \cos 6\theta + \dots] \quad (3.13)$$

$$\begin{aligned} A_0 &= 1 + \left( \frac{1}{4}\Lambda + \frac{3}{64}\Lambda^3 + \frac{5}{256}\Lambda^5 + \dots \right) \\ A_1 &= -1 \\ A_2 &= -\left( \frac{1}{4}\Lambda + \frac{1}{16}\Lambda^3 + \frac{15}{512}\Lambda^5 + \dots \right) \end{aligned} \quad (3.14)$$

$$A_4 = \frac{1}{64}\Lambda^3 + \frac{3}{256}\Lambda^5 + \dots$$

$$A_6 = -\left( \frac{1}{512}\Lambda^5 + \dots \right)$$

Typically values of  $\Lambda$  are less than 0.3. In this case the accuracy lost by ignoring terms above  $A_2 \cos 2\theta$  accounts for less than 0.5% error. This simplifies equation (3.13) to:

$$x_p \cong r \left[ (1 - \cos \theta) + \frac{\Lambda}{4}(1 - \cos 2\theta) \right] \quad (3.15)$$

### 3.2.2 Calculation of piston velocity

From equation (3.15), piston velocity is obtained as:

$$\dot{x}_p = v_p = \frac{dy_p}{dt} = \frac{dy_p}{d\theta} \frac{d\theta}{dt} \cong r\omega \left( \sin \theta + \frac{\Lambda}{2} \sin 2\theta \right) \quad (3.16)$$

The piston velocity is zero for multiples of  $\pi$  radians. These are at reversals; at the TDC and BDC. The maximum velocity is found by differentiation to give the turning point (3.17) and substituted in equation (3.16), leading to expressions for mean piston speed:

$$\frac{dv_p}{d\theta} = r\omega(\cos \theta + \Lambda \cos 2\theta) = r\omega[\cos \theta + \Lambda(2\cos^2 \theta - 1)] = 0 \quad (3.17)$$

$$\theta_{v \max} = \cos^{-1} \left[ \frac{-1 + \sqrt{1 + 8\Lambda^2}}{4\Lambda} \right] \quad (3.18)$$

$$v_{pm} = 2r \frac{2n}{60} = \frac{Sn}{30} \quad (3.19)$$

Note that the instantaneous sliding speed  $\dot{x}_p$ , is used to obtain the speed of entraining motion of the lubricant into the piston skirt-bore / liner conjunction. This is discussed in chapter 4 and is the average speed of the contiguous solids in contact, with the cylinder bore / liner being stationary, thus  $u = \frac{\dot{x}_p}{2}$ .

### 3.2.3 Calculation of piston acceleration

This is required to calculate the inertial force imbalance due to the piston motion. Piston acceleration can be expressed as follows:

$$\ddot{x}_p = a_p = \frac{dv_p}{dt} = \frac{dv_p}{d\theta} \frac{d\theta}{dt} = \omega \frac{dv_p}{d\theta} = r\omega^2 \frac{d^2x_p}{dt^2} \quad (3.20)$$

Substituting equation (3.9) into equation (3.20) and performing differentiation yields:

$$\ddot{x}_p = -r\omega^2 \left[ \begin{aligned} &(A_1 \cos \theta + 4A_2 \cos 2\theta + 16A_4 \cos 4\theta + \dots) \\ &\pm (B_1 \sin \theta + 9B_3 \sin 3\theta + 25B_5 \sin 5\theta + \dots) \end{aligned} \right] \quad (3.21)$$

Disregarding terms above  $4A_2 \cos 2\theta$  (as in equation (3.15)) due to their minimal influence, then:

$$a_p \cong r\omega^2 (\cos \theta + \Lambda \cos 2\theta) \quad (3.22)$$

where in general  $\ddot{x} = a_p = a_g$ , the suffix  $g$  representing the gudgeon pin.

Therefore the inertial forces for the piston and gudgeon pin are:

$$f_{ip} = m_p \ddot{x} \text{ and } f_{ig} = m_g \ddot{x} \quad (3.23)$$

Appendix A1 provides supporting calculations for the inertial contribution of the connecting rod and validation of these calculations by the use of MSC Adams (MSC Software Inc.) multi-body simulation software.

### 3.3 Theoretical analysis

A theoretical analysis and subsequent numerical solution requires a combined solution for dynamics of the piston-connecting rod-crank sub-system, together with tribological interactions between the piston and the cylinder liner at the thrust and anti-thrust sides. This combined analysis is referred to as tribo-dynamics of piston-cylinder interactions and is detailed in references **Balakrishnan and Rahnejat (2002)** and **Balakrishnan, Howell-Smith, Rahnejat and Dowson (2003)**.

The piston assembly comprises of three degrees. The translational motion of the piston (its primary motion in the  $x$  direction) is kinematic. The other two degrees of freedom are in the  $z$  direction (infinitesimal lateral motions of the piston) and  $\beta$  direction (tilting motion of the piston). These two degrees of freedom are referred to as its secondary motions and are governed by the forces and moments from the lubricated conjunctions with the thrust and anti-thrust sides. These are described in chapter 4.

#### 3.3.1 Dynamics of piston axial, lateral, and titling motions

The inertial dynamics of the piston is composed of its primary and secondary motions dependent on the instantaneous kinetic balance, arising from the applied gas force, inertial forces, and the contact forces with the thrust and anti-thrust sides.

Figure 3.3 is a free-body diagram of forces involved in the dynamics of the piston-connecting rod-crank system. The three degrees of freedom are indicated in the figure. The effective combustion gas force  $f_g$  is applied in an eccentric position with respect to the gudgeon pin centre  $C_p$ , and the centre of gravity of the piston assembly is also away from the pin centre, indicated by  $C_g$ .

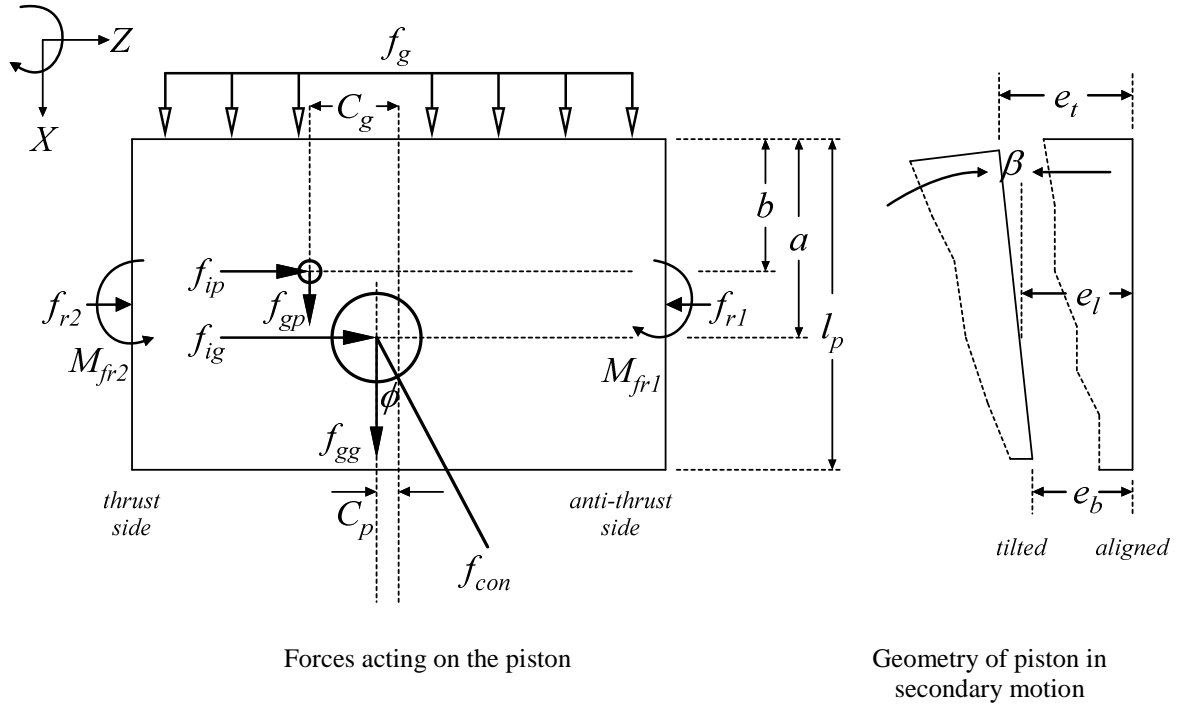


Figure 3.3 Free-body diagram of forces on the piston

The force and moment equations are obtained as (Xie *et al*, (1998), Balakrishnan and Rahnejat, (2005), and Gohar and Rahnejat, (2008)):

$$f_z = f_{ip} + f_{ig} + f_{r2} - f_{r1} - f_{con} \sin \phi \quad (3.24)$$

$$f_x = f_{gp} + f_{gg} + f_g - f_{con} \cos \phi \quad (3.25)$$

$$m_z = f_{ip}(a - b) + (f_g \times C_g) - (f_{gp} \times C_p) + m_c + m_{fr1} + m_{fr2} \quad (3.26)$$

The inertial forces and moment caused by the secondary motion of the piston (Xie *et al*, (1998)) can be expressed as:

$$f_{ip} = m_p \left( \ddot{e}_t + \frac{b}{p_l} (\ddot{e}_t - \ddot{e}_b) \right) \quad (3.27)$$

$$f_{ig} = m_g \left( \ddot{e}_t + \frac{a}{p_l} (\ddot{e}_b - \ddot{e}_t) \right) \quad (3.28)$$

$$m_c = \frac{I_p}{p_l} (\ddot{e}_t - \ddot{e}_b) \quad (3.29)$$

where, referring to figure 3.3, using geometric relationships, the tilt of piston,  $\beta$  and the lateral motion  $e_l$ , expressions for the pistons top edge,  $e_t$ , and bottom edge  $e_b$  lateral displacement are formulated :

$$e_t = e_l + a\beta \quad (3.30)$$

$$e_b = e_l - (p_l - a)\beta \quad (3.31)$$

Equations (3.24) and (3.25) can be used for eliminating the connecting rod force,  $f_{con}$ , and thus the contact force becomes:

$$\begin{aligned} f_z &= f_{ip} + f_{ig} + f_{r2} - f_{r1} \\ &- \tan \phi (f_{gp} + f_{gg} + f_g) \end{aligned} \quad (3.32)$$

The various force components in the vertical direction can be lumped together to simplify the above equation set and yield the following expressions:

$$m_s + m_{fr1} + m_{fr2} = -m_c - f_{ip} (a - b) \quad (3.33)$$

$$f_s = f_{ip} + f_{ig} + f_{r2} - f_{r1} \quad (3.34)$$

where:

$$m_s = (f_g \times C_g) - (f_{gp} \times C_p), \text{ and } f_s = \tan \phi (f_{gp} + f_{gg} + f_g) \quad (3.35)$$

Now substituting for the inertial forces and moment into equations of motion (3.27) and (3.28), the system dynamics can be represented in a matrix form as:

$$\begin{bmatrix} m_g \left(1 - \frac{a}{p_l}\right) + m_p \left(1 - \frac{b}{p_l}\right) & m_g \frac{a}{p_l} + m_p \frac{b}{p_l} \\ \frac{I_p}{p_l} + m_p (a-b) \left(1 - \frac{b}{p_l}\right) & m_p (a-b) \frac{b}{p_l} - \frac{I_p}{p_l} \end{bmatrix} \begin{bmatrix} \ddot{e}_t \\ \ddot{e}_b \end{bmatrix} = \begin{bmatrix} f_{r1} + f_{r2} + f_s \\ m_{fr1} + m_{fr2} + m_s \end{bmatrix} \quad (3.36)$$

It is clear that a solution to this set of equations requires the evaluation of contact forces and moments  $f_{r1}, f_{r2}, m_{fr1}$  and  $m_{fr2}$ . These are discussed in chapter 4. The method of solution for the dynamics equations of motion (3.36) is by the linear acceleration method (**Newmark (1962), Rahnejat (1984)**) obtaining values of the unknowns in each small step of time  $\Delta t$  (of the order of a few micro-seconds). The unknowns are  $\ddot{e}_t$  and  $\ddot{e}_b$ . The step-by-step linear acceleration method then obtains, through integration, values of  $\dot{e}_t$  and  $\dot{e}_b$  and subsequently  $e_t$  and  $e_b$ .

The linear acceleration method is now well established, thus there is no need to detail the approach here (see **Newmark (1962), Rahnejat (1984)**). Once the values of  $e_t$  and  $e_b$  are obtained in each step of time  $\Delta t$ , then the secondary motions of the piston in the  $z$  and  $\beta$  directions are found from equations (3.30) and (3.31). These movements alter the gap between the piston and the cylinder-bore surfaces at the thrust and anti-thrust sides, and are used in the tribological evaluations in the elastic film shape in equation (4.5), chapter 4.



## Chapter 4

### Tribology of the piston skirt conjunction

#### 4.1 The skirt-to-bore contact

**Goenka and Meernik (1992)** analysed piston skirt friction with corresponding opposed piston floating liner tests concluding that a rigid analysis of piston skirts may not always yield representative results. According to **Duyar *et al* (2005)** skirt and liner deformations have an effect on secondary (piston) motions, lateral, and friction forces. **Kim *et al* (2009)** further use the floating liner method to investigate the frictional characteristics of differing skirt profiles. In their work the contribution to friction from differing parts of the 4-stroke cycle are given and reproduced here in figure 4.1.

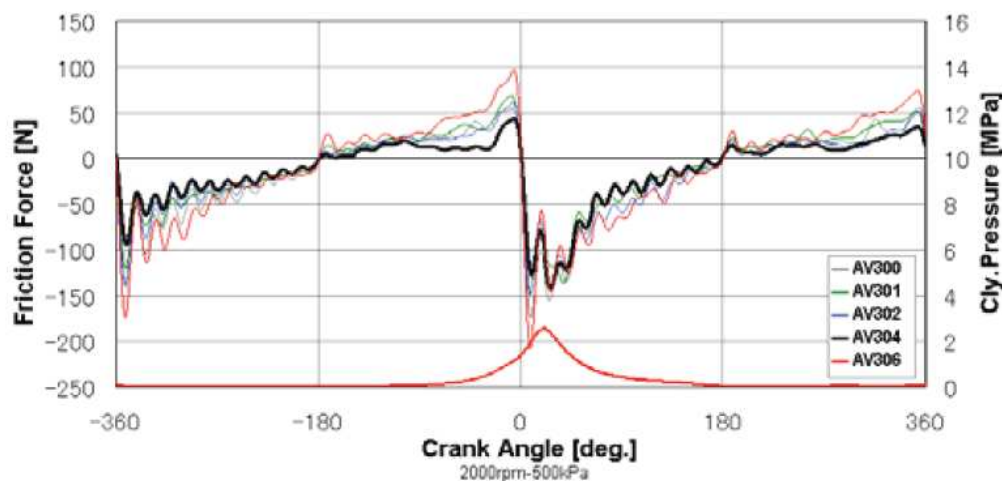


Figure 4.1 Friction force at 2000rpm for differing skirt combinations  
(reproduced from **Kim *et al*, 2009**)

The friction force in the expansion stroke is stated as the highest of the four strokes (induction, compression, expansion, and exhaust). Skirt frictional force increases with increasing load and generally with engine speed, but to a lesser extent. Skirt profile must consider lubricant flow (**Kim *et al*, 2009**), as certain optimisations (contact pressure type) result in excessive lubricant flow away from the contacting area.

## 4.2 Contact geometry

To solve equation 3.36 at any instant of time the forces and moments on the right-hand side of the equation need to be evaluated. For piston skirt contacts the major and minor thrust should be taken into account. Clearly the contact conditions are worst in most instances on the major thrust side due to the higher loads. However, for completeness both contacts have been included in the current analysis.

The solution involves the treatment of contacts with the major or minor thrust sides to include in each case the profile of the piston skirt. The contact of the piston skirt-to-cylinder is categorised as a partially-conforming contact. This means that the contact dimensions are not negligible compared with the principal radii of contact of contiguous solids, as is for ball and rolling-element bearings or a cam-follower pair.

Nor are the contacting radii of solids close enough to cause a fully-conforming contact as in the case of a journal bearing. Partial conformance is due to the fact that one member has a concave radius in its radial plane. Then in figure 4.2 the principal radius  $R_{zy(b)}$  for the bore is considered as negative, whilst that for the piston skirt,  $R_{zy(s)}$  mating with it is positive (convex). The effective radius in this plane is therefore:

$$\frac{1}{R_{zye}} = \frac{1}{R_{zy(s)}} - \frac{1}{R_{zy(b)}} \quad (4.1)$$

The effective radius is, therefore, larger than both the radii of mating bodies and is referred to as the increased radius.

Referring to figure 4.2, in general the principal radii of the contacting bodies in the  $xy$  plane are quite large. It is customary to assume an infinite radius for the bore, thus  $R_{zx(b)} \rightarrow \infty$ . It is also usual in the first instance to assume a parabolic profile for the piston skirt, at least theoretically, to obtain an idea of contact geometry. This parabolic profile will be  $x = \frac{z^2}{2R_{zx(s)}}$

within a specified skirt circumferential domain. Then the effective radius in the  $zx$  plane becomes that of the skirt:  $R_{zxe} = R_{zx(s)}$ .

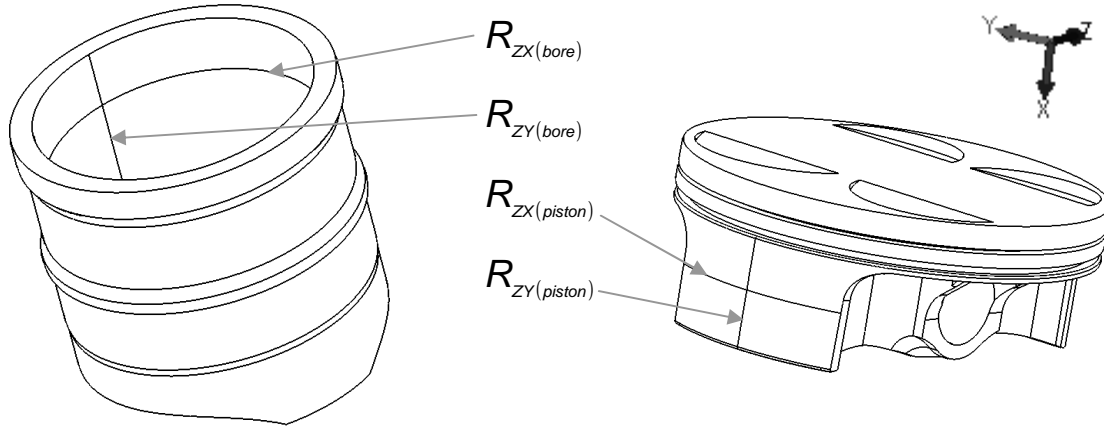


Figure 4.2 Coordinates used for piston to bore analysis

### 4.3 Contact conjunction

It can now be noted that a large footprint area results, whose dimensions are comparable with the principal radii of both the solids the skirt and the bore. This means that use of Hertzian theory is not permissible. This is an important point to note, since for the piston rings often a line contact solution is attempted as an initial analysis, noting that a ring's face-width is much smaller than its unwrapped length, hence a short-width bearing type analysis may be employed, for which analytical solutions exist (**Rahnejat (1984, 1985)**, **Sasaki *et al* (1962)** and **D'Agostino *et al* (2002)**). Such an approach is not permitted for the piston-skirt conjunction.

With the absence of an analytical solution a numerical approach for the solution of Reynolds' equation is required. The most general form of Reynolds' equation is:

$$\frac{\partial}{\partial x} \left( \frac{\rho h^3}{\eta} \frac{\partial p}{\partial x} \right) + \frac{\partial}{\partial y} \left( \frac{\rho h^3}{\eta} \frac{\partial p}{\partial y} \right) = 12 \left( u_{AV} \frac{\partial}{\partial x} (\rho h) + v_{AV} \frac{\partial}{\partial y} (\rho h) + \frac{\partial}{\partial t} (\rho h) \right) \quad (4.2)$$

It is usual, and in fact justifiable, to assume no side-leakage of lubricant into the circumferential direction (i.e.  $v_{av} = 0$ ), denoted here by the  $y$  coordinate, if the contact is viewed as unwrapped. Note that the co-ordinate represents the direction of piston sliding (its primary motion). Therefore the lubricant is entrained into the contact in an opposite sense to piston sliding with an entrainment velocity

$$u_{av} = \frac{1}{2}(u_b + u_p) = \frac{1}{2} \frac{dx}{dt} = \frac{\dot{x}}{2} \quad (4.3)$$

Where:  $u_b = 0$

Pressure builds up in the  $z$  direction.

Hence, Reynolds' equation simplifies to:

$$\frac{\partial}{\partial x} \left( \frac{\rho h^3}{\eta} \frac{\partial p}{\partial x} \right) + \frac{\partial}{\partial y} \left( \frac{\rho h^3}{\eta} \frac{\partial p}{\partial y} \right) = 6 \left( \dot{x} \frac{\partial}{\partial x} (\rho h) + 2 \frac{\partial}{\partial t} (\rho h) \right) \quad (4.4)$$

The ultimate term on the right-hand side of the equation is the squeeze-film effect term. Three reasons give rise to squeeze film effect. Firstly, secondary motion of the piston (laterally in the  $z$  direction, or tilting, indicated by  $\beta$  see figure 3.3, chapter 3) within the confine of its nominal clearance, can cause squeeze and separation effect.

One can refer to this as rigid body squeeze. Secondly, any deformation of the contiguous surfaces due to generated pressures can also lead to squeeze or separation, which is usually termed as elastic squeeze effect. Finally, as the speed of sliding alters the thickness of the entrained film into the contact domain also changes, creating a squeeze or separation effect.

#### 4.4 Elastic film shape

In general one can represent the film shape as:

$$h = h_0 + s \tan \beta + \delta + \Delta \quad (4.5)$$

where  $h_0 + s \tan \beta$  is the rigid gap and  $h_0 = c + e_l$

(Note film thickness is in the  $z$  direction, film profile is along the  $x$  axis)

If one takes the rather simple parabolic piston skirt (chapter 4.2) profile described above then:

$$s = \frac{x^2}{2R_{zxe}} + \frac{y^2}{2R_{zye}} \quad x = 0 \rightarrow \pm \ell/2 \quad \text{and} \quad y = 0 \rightarrow \pm w/2 \quad (4.6)$$

where:  $\ell$  and  $w$  are skirts length and width respectively (figure 4.2).

In equation (4.5)  $\delta$  is the localised deformation of the skirt at any position  $(x, y)$  due to the generated lubricant pressures  $p$ . If such a condition were to occur then elastohydrodynamic lubrication is deemed to have occurred if the viscosity of the lubricant also alters with the same pressures (piezo-viscous behaviour). If the latter condition is not met, then the regime of lubrication is termed as iso-viscous elastic (noting deformation without significant changes in lubricant viscosity due to the generated contact pressures).

Note that elastohydrodynamic lubrication (EHL) requires both a change in viscosity with pressure as well as localised contact deformation, or piezo-viscous elastic behaviour (**Balakrishnan and Rahnejat, (2002)**, **Mei and Xie, (1993)** and **Knoll and Peeken, (1982)**). Previous studies of the piston-skirt conjunction have shown few instances of EHL. However, at the peak combustion pressure with cylinder liners of fairly low elastic modulus, incidence of iso-viscous elastic condition has been noted, for example by **Balakrishnan and Rahnejat (2005)** and **Mei and Xie (1993)**.

#### 4.5 Contact deformation

Localised deflection is obtained by the solution of the generalised elasticity integral, sometimes referred to as the potential equation, because of its similar mathematical form to the electrical potential function (**Gohar and Rahnejat, (2008)**):

$$\delta_{i,j} = \frac{2}{\pi E'} \int_{-\tilde{a}}^{\tilde{a}} \int_{-\tilde{b}}^{\tilde{b}} \left\{ \frac{p_{k,l} dx_1 dy_1}{\left[ (y - y_1)^2 + (x - x_1)^2 \right]^{1/2}} \right\} = \frac{2 p_{k,l}}{\pi E'} D^* \quad (4.7)$$

for a rectangular contact area of  $2\tilde{a}, 2\tilde{b}$ , the influence coefficients (**Balakrishnan, Howell-Smith, Rahnejat and Dowson (2003)**) are found as:

$$\begin{aligned} D^* = & (x + \tilde{b}) \ln \frac{(y + \tilde{a}) + \left[ (y + \tilde{a})^2 + (x + \tilde{b})^2 \right]^{1/2}}{(y - \tilde{a}) + \left[ (y - \tilde{a})^2 + (x + \tilde{b})^2 \right]^{1/2}} + (y + \tilde{a}) \ln \frac{(x + \tilde{b}) + \left[ (y + \tilde{a})^2 + (x + \tilde{b})^2 \right]^{1/2}}{(x - \tilde{b}) + \left[ (y + \tilde{a})^2 + (x - \tilde{b})^2 \right]^{1/2}} \\ & + (x - \tilde{b}) \ln \frac{(y - \tilde{a}) + \left[ (y - \tilde{a})^2 + (x - \tilde{b})^2 \right]^{1/2}}{(y + \tilde{a}) + \left[ (y + \tilde{a})^2 + (x - \tilde{b})^2 \right]^{1/2}} + (y - \tilde{a}) \ln \frac{(x - \tilde{b}) + \left[ (y - \tilde{a})^2 + (x - \tilde{b})^2 \right]^{1/2}}{(x + \tilde{b}) + \left[ (y - \tilde{a})^2 + (x + \tilde{b})^2 \right]^{1/2}} \end{aligned}$$

In fact, the contact footprint resulting from two assumed parabolic profiles as indicated by equation (4.6) with  $R_{zxe} \gg R_{zye}$  tends a rectangular strip. In reality, the axial profile of the skirt is not parabolic at all. A typical profile is shown in figure 4.3. For quite a long time the main (side or radial) profile has been based on a curved beam. It also comprises relief radii or chamfers at either extremities of the skirt (see figure 4.3). These act as hydrodynamic wedges, encouraging the entrainment of the lubricant into the contact. They also reduce the edge stress discontinuity which is more commonly associated with sharp-edge rollers, causing a pressure spike, which inhibits the flow of lubricant into the contact domain. This is the reason why roller bearings are furnished with dub-off or crown edge radii.

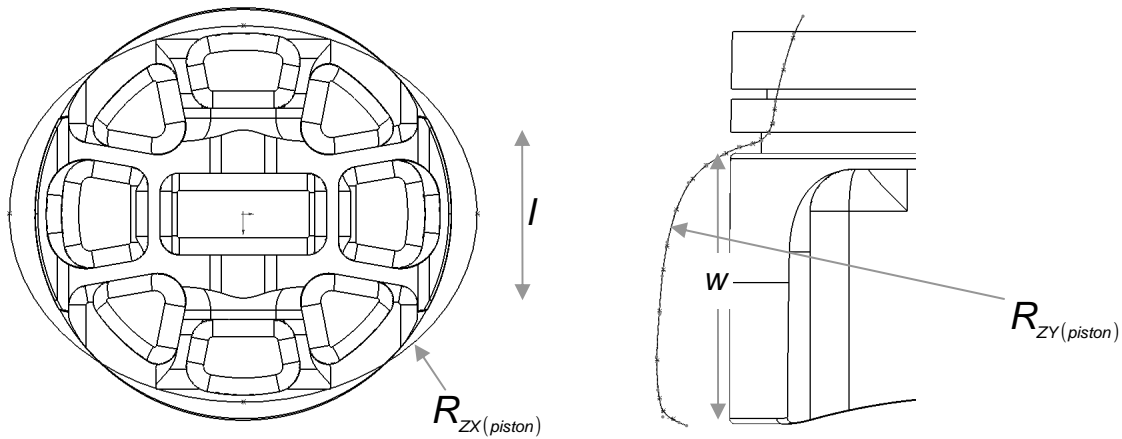


Figure 4.3 Piston profiles (exaggerated diagrammatically)

For the analysis of the actual piston skirt, the real physical profile ( $s = f(x, y)$ ) is either known or can be measured accurately (e.g. using a co-ordinate measuring machine) and imported into equation (4.5), instead of the theoretical parabolic profile used here to simply demonstrate the mathematical procedure.

The difference between roller-raceway contacts and that of piston skirt contact is that the former has a very narrow rectangular or dog-bone shape. Because of the small area of the contact, pressures generated are very high (of the order of GPa for any moderate to high load). The concentrated nature of the contact means that the localised deflection at any point in the footprint area  $(i, j)$  is as the cumulative result of all the pressure elements as in equation (4.7).

The partially-conforming contact of the piston skirt-to-cylinder bore comprises a relatively large area, thus the generated pressures are usually three orders of magnitude smaller (in MPa) compared with concentrated (e.g. counter-formal) contacts. Thus the deflection at any position is dependent almost entirely (in excess of 95%) on the pressure element acting directly above it (column method approach). **Gohar and Rahnejat (2008)** and **Rahnejat (2000)** explain that in such cases the burden of computation reduces significantly. It should be observed that more than 90% of computation time in EHL contacts is due to the evaluation of the contact elasticity potential integral.

Using the column method approach is a simplification of the triaxial state of stress-strain (refer figure 4.3a for co-ordinates), given as:

$$\{\sigma\} = [D]\{\varepsilon\} \quad (4.8)$$

where:  $\{\sigma\} = \{\sigma_{xx}, \sigma_{yy}, \sigma_{zz}, \tau_{xy}, \tau_{yz}, \tau_{zx}\}^T$  is the stress tensor,

$\{\varepsilon\} = \{\varepsilon_{xx}, \varepsilon_{yy}, \varepsilon_{zz}, \gamma_{xy}, \gamma_{yz}, \gamma_{zx}\}^T$  is the vector of direct and shear strains and  $[D]$  is the influence coefficient matrix:

$$[D] = \frac{E(1-\nu)}{(1+\nu)(1-2\nu)} \begin{bmatrix} 1 & \nu/1-\nu & \nu/1-\nu & 0 & 0 & 0 \\ \nu/1-\nu & 1 & \nu/1-\nu & 0 & 0 & 0 \\ \nu/1-\nu & \nu/1-\nu & 1 & 0 & 0 & 0 \\ 0 & 0 & 0 & 1-2\nu/2(1-\nu) & 0 & 0 \\ 0 & 0 & 0 & 0 & 1-2\nu/2(1-\nu) & 0 \\ 0 & 0 & 0 & 0 & 0 & 1-2\nu/2(1-\nu) \end{bmatrix} \quad (4.9)$$

Note that one can make the substitution:  $G = \frac{E}{2(1+\nu)}$  in the above relationships. The influence

coefficient matrix above applies for the case of compressible elastic solids, where  $\nu \neq 0.5$ . In contact mechanics problems the contact pressure distribution is considered as  $|p| = |\sigma_{zz}|$  within

the contact region  $p \geq 0$  and  $\sigma_{zz} \leq 0$  (compressive). Thus only the element (3,3) of the influence coefficient matrix is of interest. Hence:

$$p = -\sigma_{zz} = \frac{E(1-\nu)}{(1+\nu)(1-2\nu)} \epsilon_{zz} \quad (4.10)$$

If the thickness of the shell in this case the liner or piston skirt is considered to be  $d$  and deflection at any location due to the applied contact pressure  $p$  as  $\delta$ , then the deviatoric strain  $\epsilon_{zz}$  through the thickness of the shell is obtained as:

$$\epsilon_{zz} = \frac{\delta}{d} \quad (4.11)$$

Replacing this relationship into equation (4.10), it yields (**Rahnejat, (2000)**):

$$\delta = \frac{(1-2\nu)(1+\nu)d}{E(1-\nu)} p \quad (4.12)$$

This equation applied at every location in the piston skirt-liner conjunction, instead of equation 4.7, reduces the computation burden by a considerable amount. The underlying assumption has been shown to hold valid for contacts which are termed as soft EHL, where the generated pressures are relatively low (in the order of MPa) or when at least one of the contiguous surfaces is of a material of low elastic modulus/sectional stiffness.

**Rahnejat (2000)** introduces this approach for the case of overlay or thin-shell journal bearings, where the pressures do not exceed several tens of MPa. Dowson in chapter 14 of the book by **Gohar and Rahnejat (2008)** suggests the use of the column method for the determination of local deformation of articular cartilage with a modulus of elasticity of 25 MPa. **Balakrishnan (2002)** shows that the generated lubricant pressures in the piston-skirt conjunction fall into this category.

Therefore, equations 4.2, 4.5 and 4.10 can be used to solve the soft EHL or hydrodynamic conjunction of the piston skirt to cylinder bore / liner contact, if no global deformation of the bore or the piston are considered, either due to fitment ( $\Delta=0$ ) or thermal distortion



(isothermal analysis). This has been the approach in most of the reported literature, such as in **Mie and Xie (1993)** and **Balakrishnan and Rahnejat (2005)**, among others. These three equations present 3 unknowns  $p, h$  and  $\delta$  as the lubricant rheological state  $\eta$  and  $\rho$  are functions of pressure in an isothermal solution.

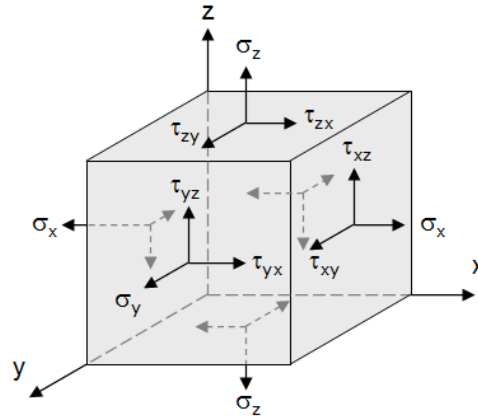


Figure 4.3a Sign conventions for stresses within a solid volume

## 4.6 Lubricant rheological state

For micro-scale tribology the important lubricant properties which should be considered are its dynamic viscosity and density. These are regarded as the bulk properties of the lubricant which alter with pressure and temperature in passage through the contact conjunction. Near the solid surface the behaviour of the lubricant deviates from that in the bulk lubricant film. At the micro-scale, where a continuum is assumed as in hydrodynamic and elastohydrodynamic conjunctions, the lubricant density variation is assumed to be the same as that in the bulk.

This is not the case in lightly-loaded contacts of very smooth surfaces with diminishing gaps. Therefore, in nano-scale, such as contact of lubricant molecules with tips of surface topography and at light load, packing order of lubricant molecules would be different, where clearly quite small shares of the contact load apply. In the micro-scale analysis used in HD or EHD one would ignore such effects, and assume same density distribution through the lubricant film and the same dynamic viscosity. This is also the approach used here, as well as in the works of others in EHD contact conjunction of piston skirt (**Balakrishnan, (2002)**, **Balakrishnan and Rahnejat, (2005)**, **Mie and Xie, (1993)**, **Offner and Pribsch, (2000)**).

The pressures are relatively low in the skirt conjunction, thus both the density and viscosity of the lubricant hardly change. However, for the purpose of generality of the numerical analysis, they are both included in the current study.

For lubricant density the **Dowson and Higginson (1959)** equation is used:

$$\rho = \rho_0 \left( \frac{1 + 2.3p}{1 + 1.7p} \right) \quad (4.13)$$

Lubricant density only increases appreciably as the pressure becomes a few hundred MPa or above. Therefore it generally plays an important role in concentrated counter-formal contacts such as ball and rolling element bearing to races, cam-follower pairs, and gears under medium to high loads. Then the lubricant molecules pack together very closely, such that there is hardly any rate of change of a volume of lubricant with respect to applied pressure. The pressure at which this occurs is known as the solidification pressure (**Hamrock, (1994)**). The lubricant is then regarded to be an amorphous solid (incompressible).

By far the most important lubricant rheological parameter is its viscosity. Under isothermal condition there are two choices to represent it. One is to use Barus Law (**Barus, (1893)**). The other is the more recent Roelands equation (**Roelands, (1966)**). The former was used almost exclusively from its inception up to the early era of EHL analysis (1950s and 1960s). With investigation of higher loaded conjunctions, particularly concentrated counter-formal contacts, it gradually became clear that Barus law yielded values for piezo-viscous lubricant behaviour several orders of magnitude greater than its value under ambient pressure (iso-viscous behaviour). This in turn leads to unexpectedly thicker predicted films, which for given conditions suggest much higher load carrying capacity than that encountered in practice.

**Gohar and Rahnejat (2008)** show that Barus law is only suitable for pressures mostly encountered in conforming and light-to-moderately-loaded counter-forming contacts. It is suggested by them that Barus law is suitable where reasonably high pressures (a few hundred MPa) with the ratio  $\eta/\eta_0$  not exceeding 2 orders of magnitude are found. This means that for higher pressures Roelands equation (**Roelands (1966)**) is a more suitable option returning more sensible values.

The Barus law (1893) is:

$$\eta = \eta_0 e^{\alpha p} \quad (4.14)$$

Roelands (1966) equation is:

$$\eta = \eta_0 \left( \frac{\eta_\infty}{\eta_0} \right)^{1 - (1 + p/c_p)^z} \quad (4.15)$$

Where for most mineral and synthetic engine oils:

$$c_p = 1.962 \times 10^8 \text{ N/m}^2$$

$$\eta_\infty = 6.31 \times 10^{-5} \text{ Ns/m}^2$$

$Z =$  The pressure-viscosity index, which is related to the pressure-viscosity coefficient  $\alpha$  in the Barus law as:

$$Z = \frac{\alpha c_p}{(\ell \ln \eta_0 - \ell \ln \eta_\infty)} \quad (4.16)$$

## 4.7 Contact loads and moments

The contacts and moments acting on the thrust and anti-thrust sides of a piston skirt as the result of conjunctions with cylinder bore / liner can be obtained after the pressure distributions in these contacts are determined.

Thus if  $p(x, y) \in p_{r1}$  and  $p_{r2}$  are the pressure distributions on the thrust and anti-thrust sides then the lubricant reactions in these conjunctions are obtained as:

$$f_{r1} = \int \int_{x \ y} p_{r1}(x, y) dx dy, f_{r2} = \int \int_{x \ y} p_{r2}(x, y) dx dy \quad (4.17)$$

The moments are obtained as:

$$M_1 = r_{p1} \int \int F_1 dx dy \text{ and } M_2 = r_{p2} \int \int F_2 dx dy \quad (4.18)$$

where  $F_1$  and  $F_2$  are the viscous friction on the thrust and anti-thrust sides respectively.  $r_{p1}$  and  $r_{p2}$  are the centres of pressures at these conjunctions. This is because viscous friction for any element of pressure  $p$  with the local film  $h$  is:

$$F = -\frac{h}{2} \frac{\partial p}{\partial x} + \eta \frac{\Delta u}{h} \quad (4.19)$$

where the first term is usually very small compared with the latter.

Now with the applied forces obtained the equations of motion (equation 3.36) in chapter 3 can be solved.

#### 4.8 Method of solution

The solutions provided in this thesis are instructive, not definitive, because certain assumptions are made. These assumptions include the following:

- An isothermal solution is first considered. This means that the predicted lubricant film will be thicker than that encountered in practice.
- Since temperature rise in the conjunction is disregarded there is no need to include friction, which is the source of heat generation in the contact.
- The temperature of contacting surfaces is not included in the ‘cold profile’ models. However, later-on in some simulated cases the thermo-elastic distortion of the bore / liner due to thermal flux is predicted by finite element analysis, given  $\Delta(x, y)$  in equation (4.5). This is carried-out to show changes in the generated pressure distribution (refer chapter 7.5) utilising boundary conditions, loads and lubricant properties given in Appendix 5..
- The predicted films under isothermal conditions have been found to be of sufficient thickness to promote fluid film lubrication, thus direct surface interactions are ignored. In practice, with bore distortion and thermal effect a mixed regime of lubrication is expected in the transition from the compression to the power stroke. In some analyses the viscosity of the lubricant has been adjusted according to the average local temperature of the surface (i.e. the piston). This is regarded as effective viscosity, using Vogel’s equation (**Vogel (1921)**):

$$\ln \eta_e = -1.845 + \left( \frac{700.81}{\Theta_e - 203} \right) \text{ where } \Theta_e = \theta_e + 273 \quad (4.20)$$

- Moment loading as in equation (4.18) is found to be small compared with the effect of direct contact forces, and is thus neglected.
- The predictions are confined to the power stroke and mainly in the vicinity of the maximum combustion pressure (10°-15° of crank angle past TDC, expansion stroke).
- Another assumption concerns the use of **Reynolds (1886)** or Swift-Steiber (**Swift 1932**), (**Stieber 1933**) contact exit boundary condition. This boundary condition is given as:

$$p = \frac{dp}{dx} = 0 \text{ at } x = x_e \quad (4.21)$$

where  $x$  is the direction of sliding of the piston relative to the bore. This condition means that a film of lubricant entrained (drawn) into the contact and pressurised flows towards the contact exit as the pressure gradient is reduced. Somewhere within the vicinity of the contact exit the generated pressures reach ambient condition, denoted by  $p = 0$ . This point is referred to as the film rupture position;  $h = 0$  at  $(x = x_e)$ . Thereafter sub-ambient pressures are encountered in practice.

This region behind the exit boundary is the cavitation region, where flow dynamics is of two phase nature; lubricant and a liberated gas phase from the lubricant. A film of fluid is ideally formed behind this region by a process of film reformation, due to the lubricant surface tension properties. However Reynolds' equation does not deal with lubricant film reformation. The problem with the Swift-Steiber exit boundary condition (1933) is that it is based on film rupture at atmospheric pressure. In reality gasses dissolved in the lubricant are liberated at pressures, not necessarily at ambient value. In most engines suction effect is also present in the crank case, particularly during suction and exhaust strokes. In race engines, in fact, 0.5 atmosphere of suction effect is maintained at all times, which has an advantage of extra cylinder net pressure. All these point to the rather idealistic nature of the Swift-Steiber boundary condition.

- The numerical analysis further assumes a fully-flooded inlet. This condition is certainly not met at the dead centres, where the inlet distances to the top of the skirt in the case of

piston at the TDC and that to the edge of bottom-end relief profile with the piston at the BDC are insufficient to provide a necessary inlet meniscus. Thus starvation is quite likely at the dead centres. However, the extent of starvation depends on the volume of lubricant ahead of contact which would be variable, and difficult to quantify. A scientific study should not be based on any *ad hoc* assumption vis-à-vis the extent of inlet meniscus. A fully-flooded inlet boundary is, therefore, assumed in all the analyses. Since one of the main aims of this research has been comparative studies of various liner / piston surface topography a solid base-line is to assume the same inlet condition for all the analyses.

The following calculation procedure is followed (Figure 4.4 shows a representative flow chart):

**Step 1:** It is convenient to start the simulation process at a location in the piston cycle where pure entraining motion (i.e. insignificant squeeze film action) may be assumed. This is because no prior lubricant film history would be available at the onset of a simulation study.

Therefore squeeze film action;  $\partial h / \partial t = (h^k - h^{k-1}) / \Delta t$  cannot be evaluated.

A convenient position would be at piston mid-span. Thus for the initial time step  $t = \Delta t$ , the squeeze film term in Reynolds' equation is ignored. The speed of entraining motion is given at any time by equation (4.3). The sliding velocity of the piston  $\dot{x}$  is a function of piston-connecting rod-crank kinematics, hence a function of engine order harmonics  $i\omega$  (**Rahnejat, (1998)**). **Balakrishnan (2002)** states the following:

$$\dot{x} = r \sin \omega t - \Psi_i \cos(2i-1)\omega t + \Psi_{i-1} \sin 2i\omega t \quad (4.22)$$

This is obtained in terms of the various engine order response characteristics of the engine, in this case up to and including the 8<sup>th</sup> engine order, where:

$$i = 1 \rightarrow 4 \text{ and } \Psi_i = f(r, l, C_p) \text{ (see } \mathbf{Balakrishnan (2002)})$$

Note that  $\Psi_i$  is a function of various powers of the ratio  $r/l$  according to the chosen Binomial expansion of equation (3.7) in chapter 3. The primary (axial) motion of the piston is

considered to be kinematic. When the piston sliding velocity at any instant of time is determined then the speed of entraining motion of the lubricant is obtained as:

$$\frac{1}{2} \dot{x}.$$

**Step 2:** The next step is to determine the film shape; this being the gap between the piston skirt and the cylinder liner. Equation (4.5) is used to find  $h(x, y)$ . In the simple case described above a parabolic shape was assumed to explain the calculation procedure. However, the piston skirt profile is not parabolic in either  $x$  (axial direction of entraining motion) or  $y$  (the circumferential direction of any side-leakage of lubricant).

The profile,  $s$ , comprises a ‘central’ portion which may be approximated by a parabola under idealised conditions with a large radius in the  $x$  direction and as a circular profile or parabola of a radius similar to that of the bore in the  $y$  direction. The profile in the axial direction has relief radii at its extremities in order to guard against edge stress concentrations developing. This is described above. The key point is that the real piston skirt profile is often idealised in literature to that often represented by a parabola or other such mathematical function (for a typical as manufactured skirt profile refer chapter 5.32 figs. 5.15 and 5.16 as well as fig. 4.3). Therefore it is measured as  $s(x, y)$  and imported into equation (4.5). This was the approach undertaken by **Balakrishnan (2002)**, **Balakrishnan et al (2003, 2005)**, and **Balakrishnan and Rahnejat (2002, 2005)**.

However the profile used in all these analyses was that of a ‘cold’ skirt; one that is not *in situ* under real engine running conditions. In the current work both ‘cold’ and ‘hot’ piston skirt profiles are used in different analyses. In the very initial time step the gap  $h_0 = c + e_t$ . Of course this value changes as the value of  $e_t$  alters; this being a function of  $e_t$  and  $e_b$  (see chapter 3, figure 3.3).

**Step 3:** Once at any instant of time (location of piston) the film shape is known, then the pressure distribution is obtained by solution of Reynolds’ equation 4.4. This means that for the very initial time step where pure entraining motion is assumed, the ultimate term on the right-hand side of Reynolds’ equation is ignored. In the subsequent time steps a previous value for the film thickness is known, thus all the terms in the form of Reynolds’ equation 4.4 are taken

into account. Furthermore, in the initial time step, in the very first iteration the pressure distribution is not known *a priori*.

This is the case in all numerical analyses, where a pressure distribution may be assumed, and which converges to an expected distribution upon use of a suitable iteration process (described below). It is usual to assume a Hertzian pressure distribution or set the pressures to zero at the onset of simulation. The former is usual in the case of concentrated contacts under medium to high loads (**Jalali-Vahid *et al*, (2001)**). In the conforming or partially-conforming contacts such as piston-skirt to the cylinder liner a Hertzian pressure profile is not appropriate, and in general an initial null-pressure distribution is more appropriate.

Because of such initial assumptions the first time step of simulation in a transient analysis is usually much longer than any subsequent steps. However, it has no residual effect upon the analysis as a whole, since tribological problems in numerical approach are not affected by the initial values, owing to the iteration process.

**Step 4:** Prior to the solution of Reynolds' equation, the rheological state of the lubricant in the contact at any location  $(x,y)$  is required. For an isothermal analysis equations 4.13 and 4.15 are used. With a null-pressure distribution these values are considered to be those which would cause under ambient pressure in the very initial iteration of the first time step. For a thermal analysis the lubricant viscosity should be adjusted for temperature.

In this thesis the contact temperature is taken to be that of the liner surface, which has been obtained through a thermo-elastic finite element analysis (described in sections 4.7 and 4.8). A more detailed analysis would use the energy equation (**Gohar and Rahnejat, (2008)**) to obtain the temperature rise of the lubricant in the contact. This approach however would increase the computation burden significantly and is not attempted in this thesis. Thus only the **Vogel (1921)** equation 4.20 is used to adjust for the variation of viscosity with temperature.

**Step 5:** The same procedural considerations also apply to the calculation of contact deflection  $\delta(x,y)$ , using either equation 4.7 or 4.12. As noted above, for relatively low contact pressures equation 4.7 yields values that are only 5% different to those from equation 4.12, but with considerably reduced computation times. **Balakrishnan (2002)** also found the same. Thus equation 4.7 is used throughout this work.



As far as the global deformation  $\Delta$  is concerned this is included in the ‘real’ profile of the skirt,  $s$  as used in equation 4.5. The ‘real’ profile is considered as the *in-situ* shape of the piston skirt in the bore. As already mentioned a ‘cold’ profile refers to the piston shape as manufactured and assumed fitted in the bore without generated heat in a fired engine. This profile can be predicted by finite element analysis. A thermo-elastic finite element analysis, on the other hand, provides the ‘hot’ profile of the piston with thermal and structural deformations. These are described in section 4.8.

**Step 6:** At each step of time corresponding to a particular position of the piston, with known speed of entraining motion and an initial film shape (one based on a converged value from the previous time step) an iterative procedure is followed. The fact that the initial values in a new step of time arise from those of the previous time step means that only very small time steps are permitted. This is in line with the very basis of dynamics analysis as initially established by Newton for changes in evanescent quantities in the calculus of variations (**Newton, (1687)**).

The iterative procedure as shown in the flow chart of figure 4.4 comprises two nested computation loops. These are:

The computation loops:

The outer loop is the ‘dynamics loop’ where the equations of motion (equation 3.36), chapter 3) are solved. It is clear that to solve for the unknown variables  $\ddot{e}_t$  and  $\ddot{e}_b$  the contact forces  $f_{r1}$  and  $f_{r2}$  should be evaluated first. These contact forces are the integrated pressure distributions acting on the piston on the thrust and anti-thrust sides respectively. These are the converged or final outcomes from an inner or the ‘tribology loop’.

The tribology loop comprises the steps 1-5 described above in an iterative process with simultaneous solution of equations 4.4, 4.5, 4.7, 4.13 and 4.14, with the addition of equation (4.20) in the case of a thermal solution. The iterative process continues until the following pressure convergence criterion is satisfied:

$$\sum_{i=1}^{n_x} \sum_{j=1}^{n_y} \left| \frac{p_{i,j}^k - p_{i,j}^{k-1}}{p_{i,j}^k} \right| \leq 0.1 \quad (4.23)$$

where  $(n_x, n_y)$  is the finite difference mesh density and  $k$  represents the iteration index within a time step. If the criterion is not satisfied then an under-relaxation relaxation factor  $\xi < 1$  is used to update the new pressures:

$$p_{i,j}^k = p_{i,j}^{k-1} + \xi \Delta p_{i,j} \quad (4.24)$$

The iteration process is repeated by calculating new values of  $\delta$ , then  $h$  and so on. The numerical procedure used is the same as **Jalali-vahid *et al* (1999)** and **Balakrishnan (2002)**.

If the convergence criterion is satisfied then equation 4.17 is used to find  $f_{r1}$  and  $f_{r2}$ . The computation process for the current time step then proceeds to the outer ‘dynamics loop’ where the equations of motion (3.36) are solved using the linear acceleration method. This is described in detail in **Newmark (1962)** and was used in contact problems by **Rahnejat (1984, 1985)**. The outer loop is satisfied when:

$$\left| \frac{\ddot{e}_t^j - \ddot{e}_t^{j-1}}{\ddot{e}_t^j} \right| \times 100 < 1 \quad \text{and} \quad \left| \frac{\ddot{e}_b^j - \ddot{e}_b^{j-1}}{\ddot{e}_b^j} \right| \times 100 < 1 \quad (4.25)$$

where  $j$  is the iteration counter in the time step  $k$ .

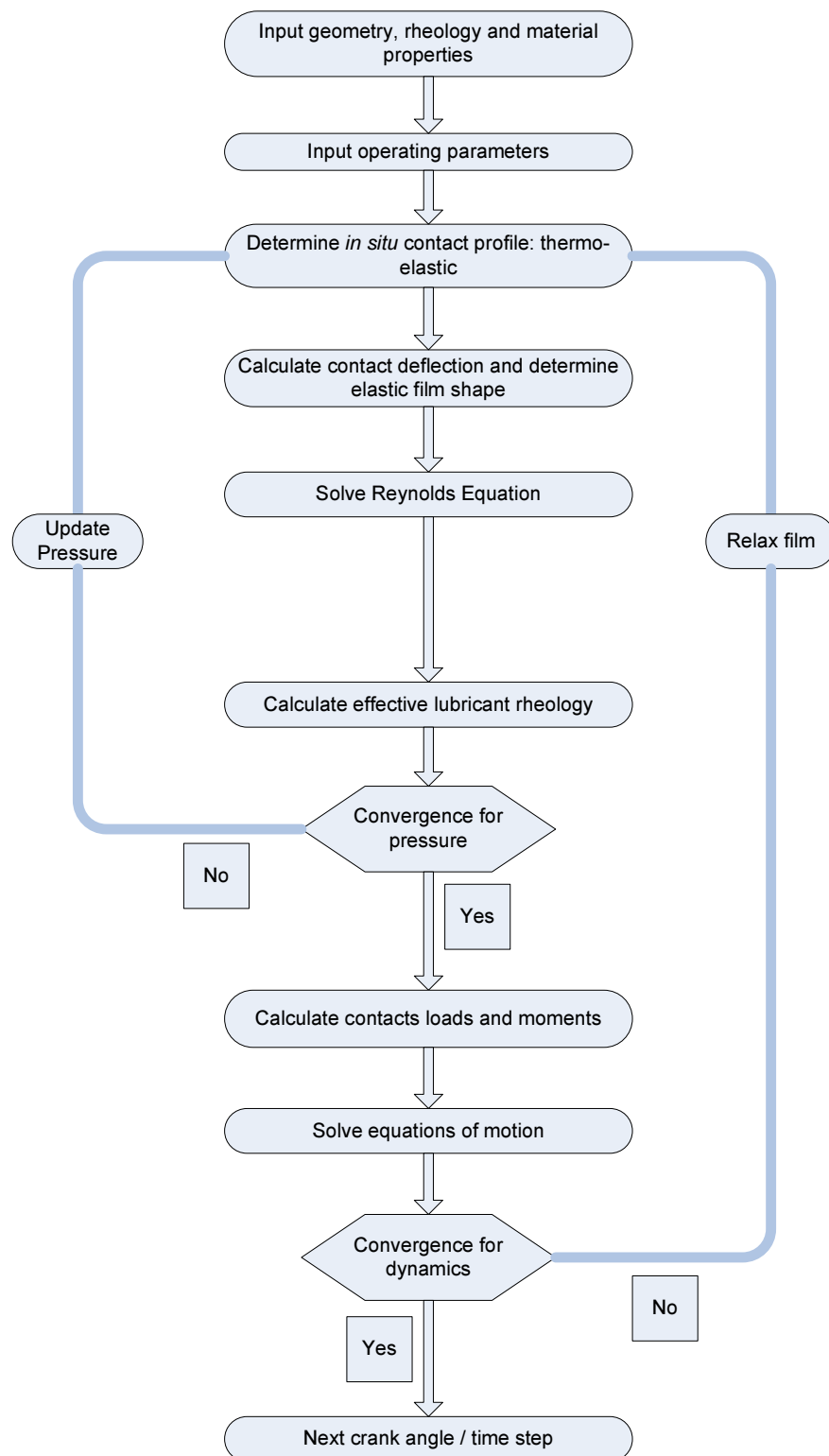


Figure 4.4 Flowchart of numerical procedure

## 4.9 Calculation of thermo-elastic deformation

In the elastic film shape equation 4.5,  $\Delta$  comprises of the global deflection of piston and cylinder liner / bore as the result of thermo-elastic behaviour of the piston. Specifically the piston skirt *in situ* within the bore. This deformation is not often taken into account in many lubrication studies of the piston skirt-bore conjunction. Whilst with older engines heavier pistons initially constructed from cast iron had skirts with appreciable thickness, in more modern vehicles there has been a tendency to reduce component weight to enable higher rotational speeds. Thus modern pistons invariably have thin walls and are made of aluminium. Pistons with such attributes abound in motorsport applications, with many having very short skirt lengths and in some cases they can weigh as little as a few tenths of one kilogramme.

The global thermo-elastic deformation is different to the localised contact deformation, which arises from lubricant pressures generated in the conjunctural gap. This localised deformation is considered to be as the result of small strains, analogous to the Hertzian deflection in concentrated counter-formal contacts. However, as described in section 4.2, the contact between the piston skirt and the bore is partially conforming with relatively low generated pressures when compared with those in concentrated counter-formal Hertzian contacts. Therefore the column method approach was adopted in section 4.4 to calculate  $\delta(x, y)$  for use in equation 4.5. The global deformation  $\Delta(x, y)$  is due to larger strains which are obtained using the finite element method.

### 4.9.1 A brief history of the finite element method

During the 1940's Hrennikoff and Courant developed different domain discretisation methods, resulting in sub-domains commonly referred to as elements (**Clough and Wilson, (1999)**). Courant's method divided a domain into triangular sub-regions utilising 2<sup>nd</sup> order differential equations. The use of these equations allowed the application of previous mathematical methods in this area (e.g. Rayleigh and Galerkin). At that juncture computational available power was rather minimal, although in the late 1950's cold war civil engineering requirements such as dam reinforcements provided an impetus for the development of finite element analysis.

In 1964 NASA reviewed the emerging multi-departmental structural tools, developing and concluding a requirement for a central NASA Structural Analysis (NASTRAN) tool. By the

mid 1970's a mathematical framework (**Strang and Fix, (1973)**) existed, as well as many spin-off software routines to enable complex problems to be benchmarked and solved.

#### 4.9.2 An overview of the finite element method

Finite element analysis is a computational technique obtaining approximate solutions to engineering boundary value or field problems (e.g. force and thermal effects on a structure) (**Hutton, (2004)**). In essence, a boundary value problem is one where one or more dependent variables must satisfy a differential equation everywhere within a known domain of independent variables. Further specific boundary conditions must also be satisfied (**Zienkiewicz and Taylor, (2000)**). Boundary conditions are imposed values encompassing the field domain. The field is typically a closed geometric representation of the problem to be solved (e.g. a piston).

A volume domain of known material / physical properties can be approximately represented as a collection of interconnected points within it. Typically the interconnected points show a finite volume similarity, analogous to a macro-crystalline structure. These sub-structures are often referred to as elements. Topological similarity generally exists between elements for a given field. In its simplest form, a single field variable  $\Phi(x, y, z)$  is required to be determined at all points throughout such a field (**Hutton, (2004)**).

A set of governing (differential) equations exist connecting all the field points throughout the computation domain in a form suitable to satisfy the constrained boundary conditions. In many engineering problems the domain is often complex in both shape and boundary conditions / assumptions. This makes an exact solution practically unachievable. However, with the advent of available computational resources a very close approximation is, however, possible subject to the imposed conditions.

Many forms of finite elements exist (both in geometrical form; triangular, quadrilateral, etc. and in assumed constitutive stress-strain relations). However, typically they all have specific points, referred to as nodes, where the field variable is to be explicitly calculated. The simplest type of solid element is a tetrahedron with 4 nodes – one on each vertex. This type of element is referred to as 'linear' or '1<sup>st</sup> order' and can be visualised as a flat faceted tetrahedron with 4 nodes. A 'parabolic' or 2<sup>nd</sup> order variation introduces mid nodes, totalling 10 nodes (figure 4.5).

Typically, connectivity between elements involves shared nodal positions (external nodes) except for nodal points within elemental volumes, which have no connectivity. Boundary nodes lie on the approximate outer surface of the discretised body and as such usually have no inter-element connectivity except for contact analysis.

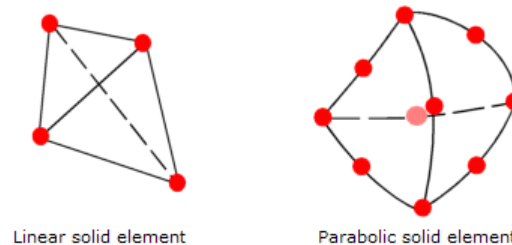


Figure 4.5 Types of tetrahedral element

At any other point within an elemental volume a relationship is constructed between the elemental nodal independent variables (unknown constants) and known functions between the requested positions (this is referred to as constitutive relationship). Typically the form of these interpolation functions are polynomial in form, derived to satisfy nodal criteria, and are referred to as shape functions.

From a computational stand-point a useful measurement of problem complexity is the number of degrees of freedom. Generally this is the product of the total number of nodes multiplied by the number of values in the field variable. A typical displacement analysis would, therefore, have 3 degrees of freedom per element ( $\Phi(x,y,z)$ ) and perhaps 100,000 elements. Due to connectivity of elements (shared nodes) the total number of nodes in the lump component analysis (as opposed to slender bodies) is significantly smaller than the product of element quantity and nodes per element.

Solution quality is an important consideration in finite element analysis. Due to topological connectivity between nodes, the field variable solution ensures that adjacent elements must have a common solution at their shared nodes. However, discontinuity often occurs inter-element, often as a result of poor element shape or inadequate shape function. The first derivative of displacement (strain) allows field discontinuities to be observed, thereby allowing either manual or software assisted automatic remedial attention. Element type (e.g. tetrahedral, hexahedral etc) and higher order polynomial derivatives are well researched

against exact solutions. Choice of element type for a given problem is of prime importance in minimising solution error as noted by **Wang *et al* (2004)** or **Abbey (2004)** (Figure 4.6):

- Never use linear tetrahedron elements. They are much too stiff.
- Quadratic tetrahedral elements are generally very accurate and can always be used.
- Linear hexahedral elements are sensible with respect to a corner angle. One should be careful to avoid large angles in stress concentration regions. Extra shape functions or enhanced strain formulations should be employed for bending dominated problems.
- Quadratic hexahedral elements are very robust, but computationally expensive.
- For thin-walled structures the limit element edge / thickness ratio to use tetrahedral elements is about 2000.

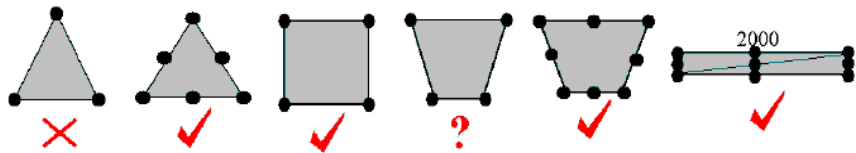


Figure 4.6 General element recommendations (after **Wang *et al*, (2004)**)

The discretisation of a boundary volume with finite elements invariably involves approximation, which leads to certain degree of overall solution inaccuracy. Exact solutions presented by **Roark and Young (1988)** and **Timoshenko and Woinowsky-Krieger (1964)** are compared with finite element approximations using the software package (CosmosWorks, Solidworks Corporation Inc.), which is used in this thesis. The results of such a comparison were presented by **Boissat and Nicolas (2007)**, where 100 of 143 standard test cases stipulated by AFNOR (Association Française de NORmalisation, French Standardization Association) showed typically a 1% error or less.

#### 4.9.3 General applied methodology

Three general stages are involved with a finite element problem; pre-processing, solution, and post-processing. Pre-processing involves the following:

- Definition of the geometric computational domain.
- Model meshing: Definition of element type, geometric properties (overall size, geometric limits / tolerances, local density / refinement, seeding for mesh alignment / mesh efficiency) and the connectivity between the elements.

- Inclusion of material properties for the elements (generally monolithic).
- Apply / define boundary conditions (physical constraints).
- Apply / define loadings such as forces, pressure, temperature to nodal boundary positions.

The solution is generally a software automated procedure. The governing algebraic equations are ordered into matrix form and the primary field variables are calculated. Back substitution is used to arrive at solutions for derived variables such as elemental stresses, heat flow, etc. A checking procedure for pre-processing is often presented as are various convergence checks for the matrix solution. Solution methods are well described in detail by **Raghu (2009)**.

Post-processing, in essence, translates the computed results into useable formats for their interpretation. Typical operations include colour coded plots for stress, thermal profile, and factor of safety (contours). Animated and deformed displacement plots are also normal, allowing insight into structural behaviour, such as various cases demonstrated in this thesis.

#### 4.9.4 Contact analysis

Contact analysis here refers to the calculation of global deformation of a pair of elastic solids due to large thermo-elastic strains encountered as the result of their interactions. This determines the *in-situ* conformance of the two surfaces, before localised deflection within the gap occupied by a film of lubricant is obtained as described in the previous sections.

Several methods exist to compute these large strain contact strains between the bodies. The simplest form creates direct nodal links with a requirement for a ‘mapped’ mesh. A mapped mesh is one where the contacting bodies have matching nodes in the direction of contact. The equation between nodes is sensitive to displacement other than normal to the surfaces, which can lead to inaccuracies. Surface-to-surface contacts are more general and can accommodate some misalignment as shown in figure 4.7. Generally out of plane mismatch should be avoided, if a high degree of accuracy is required. This, of course, is a key requirement for the subsequent hydrodynamic / elastohydrodynamic analysis as outlined previously. A thorough detailing of this subject is provided by **Wriggers (2002)** with extension to include the ‘Mortar’ method. The Mortar method (**Belgacem et al, (1998)**) allows non-matching sub-domain meshes to maintain solution accuracy by means of carefully chosen Lagrange multipliers.



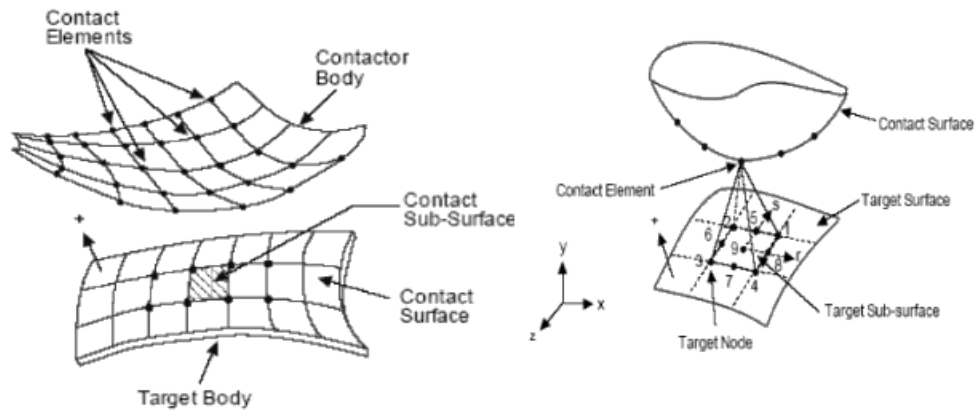
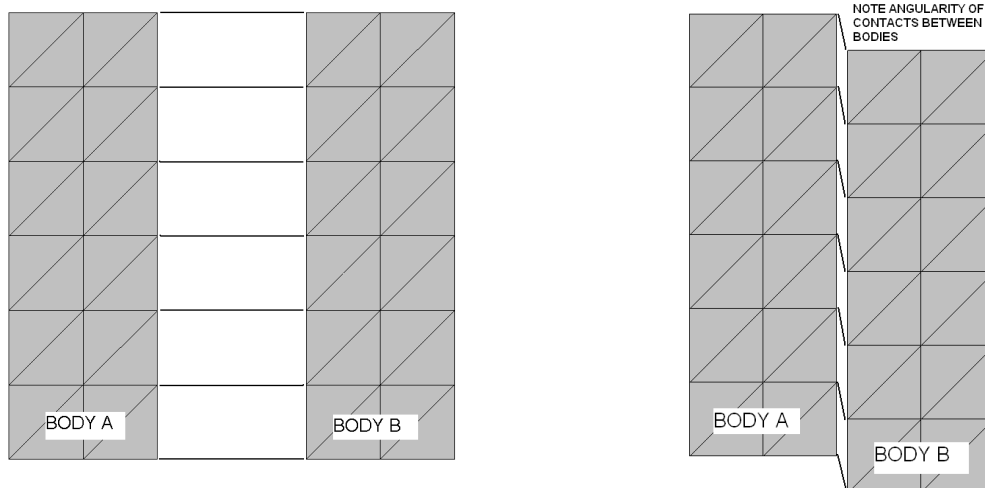


Figure 4.7 Contact elements

In the case of piston skirt-to-bore contact relative body motions due to applied loads and resulting deflections result in a non-matching mesh. Typical skirt-to-bore radial clearance is  $40\mu\text{m}$ , accompanied by a typical vertical displacement (a compressioning effect) 20-30 times the clearance in magnitude (figure 4.8). Thus, when a matched mesh of typically 2mm in length with node to node contacts is used, the resulting contacts will be totally misaligned. Therefore, palliative measures such as the Mortar method are required.



Bodies feature 'mapped mesh' prior to applied loads. Relative movement causes gross misalignment between nodal points with potential inaccuracy in solution

Figure 4.8 Contact skewing due to relative displacement of bodies

Figure 4.9 provides a step-by-step flowchart of activities to solve a thermo-structural analysis of the piston to bore contact. Further details regarding computational methods appear in Appendix 3.

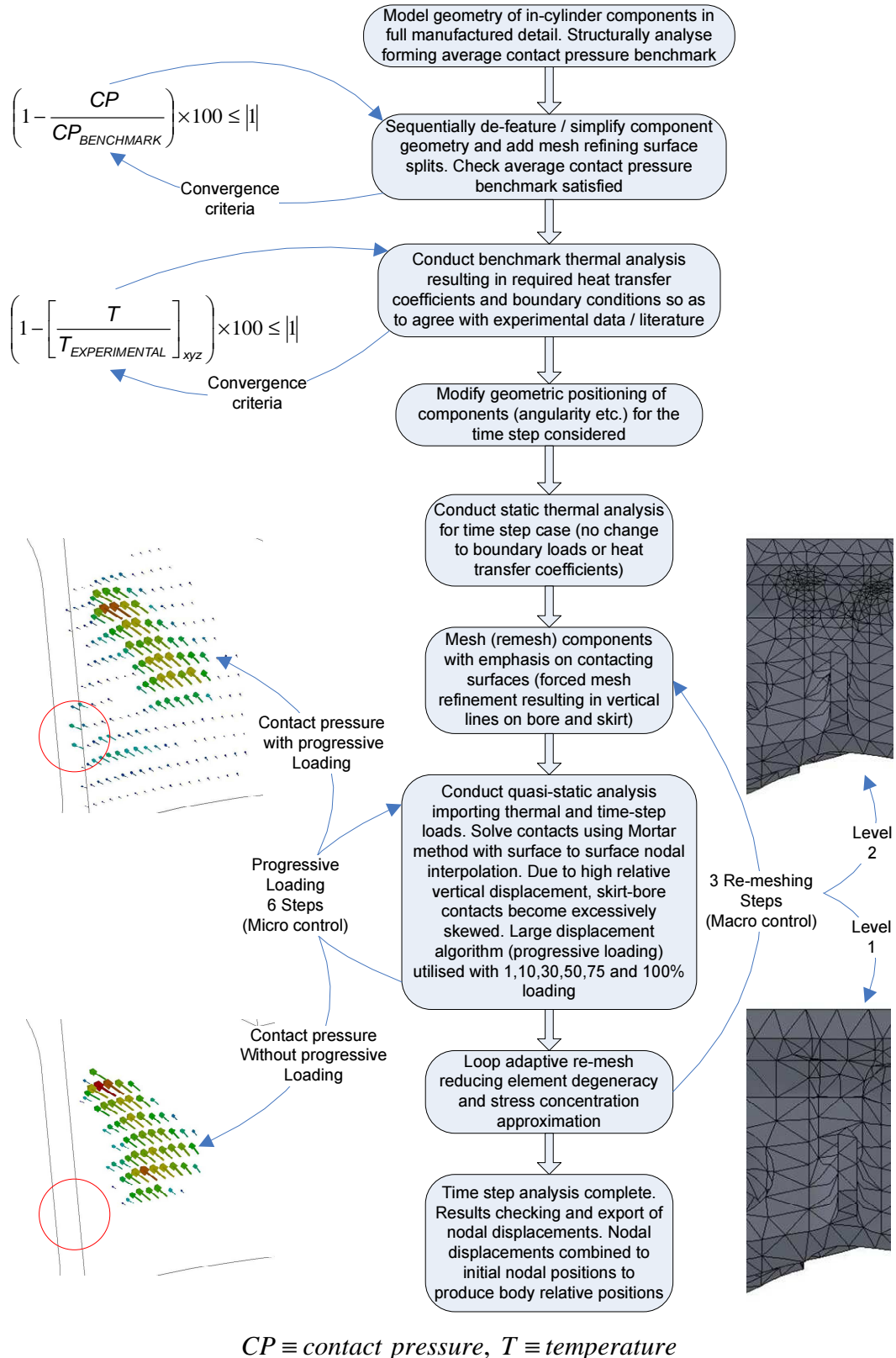


Figure 4.9 FE Flowchart determining thermo-structural global deformation

## Chapter 5

### Development of test rigs and components

#### 5.1 Introduction

This thesis presents a combined numerical and experimental investigation of the piston skirt-cylinder liner tribological conjunction. This chapter deals with the test rigs / the engines used in this study as well as the components designed and manufactured. A suitable test engine was used with appropriate modifications to its standard existing components. This chapter outlines the development of test-beds; the appropriate components as well as the instrumentation and test regime employed.

#### 5.2 Test engine choice

The experimentation is restricted to the in-cylinder region of engines. It was decided to use a commercially existing engine as opposed to developing one from the outset. This decision brought benefits in terms of a sensible way of replacing parts within acceptable times and cost. However, the choice of a base engine had to satisfy certain criteria. These are listed in table 5.1.

Relatively low complexity	To enable highest development-to-cost ratio a single-cylinder engine was sought. Use of multiple cylinders would require multiple test items as well as instrumentation*.
Current market technology	Single-cylinder vehicle engines are typically gasoline fuelled. The highest developed units in terms of specific output are motorcycle-based.
Representative base parameters	<p>The following constraints also applied, namely to allow developed technology to be easily transferred:</p> <p>Gasoline fuel, 4-stroke, normally aspirated spark ignition</p> <p><math>86 &lt; \text{bore size (mm)} &lt; 106</math></p> <p>9,000rpm minimum continuous operation ability</p> <p>Power to be less than 100kW and operating at less than 10,000rpm to be suitable for available dynamometer installation</p>
Engine architecture	The following constraints applied for ease of required modification / testing:.. Separate barrel assembly (as opposed to bore surface incorporated within crank-case). Water-cooled with fully integrated electrical system

Table 5.1 Criteria for engine selection

\*Also measurement sensitivity was an important issue. With single-cylinder engines, the share of frictional losses are different from those of multi-cylinder engines. The usual dominant frictional losses from the piston assembly in the case of latter is not the same for the single-cylinders, where journal bearing (big-end and crankshaft) losses are significant. High-performance motocross motorbike engines employ rolling element bearings with a

considerably smaller share of losses compared with the piston system, thus higher measurement sensitivity would be achieved. Furthermore, making modifications in order to access a cylinder barrel arrangement for measurement of lubricant film thickness is of importance as described later.

The most ideal match to the above was off-road motorcycle engine applications. Several manufacturers are active in this arena, arguably Honda and Yamaha with the greatest market share. Yamaha engines for this class are, however, typically 5 valve per cylinder units, whereas Honda employs 4 valves per cylinder.

The motorcycle power unit chosen was the Honda CRF450R 'CRF'. The basic parameters and performance are listed in table 5.2 and a cut-away of the engine is shown in figure 5.1.

Engine type	Water cooled 4-stroke, 4-valve single-cylinder
Engine displacement	449cm <sup>3</sup>
Bore & Stroke	96mm x 62.1mm
Compression ratio	11.5:1
Max quoted power [specific power]	41kW@9,000min <sup>-1</sup> [91.31kW/dm <sup>3</sup> ]
Max quoted torque [specific torque]	49.8Nm@7,000min <sup>-1</sup> [99.80Nm/dm <sup>3</sup> ]

Table 5.2 Engine characteristics CRF (Honda Motor Co. (2002))

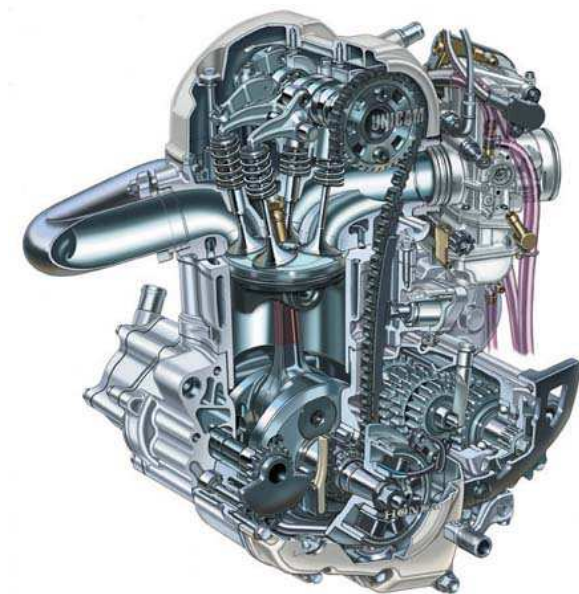


Figure 5.1 Cutaway of CRF450R engine  
(Honda Motor Co. (2002))



Figures 5.2 CRF450R cylinder barrel

## 5.3 Component development CRF450R

### 5.3.1 Cylinder bore / bore surface

The CRF engine as supplied features a cast cylinder block constructed from nominally eutectic aluminium-silicon alloy (LM25/A356). This unit is depicted in figures 5.1 and 5.2 and provides a technical solution to the following:

- Low mass solution due to low density material (aluminium alloy)
- Rigid construction providing bore stability and transfer of cylinder head to crank-case loads
- High thermal conductivity provides efficient thermal transfer from the combustion chamber to the internally cast water jacket.
- Internally cast oil transfer passages thereby minimising external lines (pipe-work) maximises service reliability and controls oil temperature.

The bore surface is furnished with a nickel-silicon-carbide electrolytic coating nominally 6-8% ceramic content. This is a surface treatment providing performance benefits over traditional cast iron and untreated aluminium (**Funatani *et al*, (1994)**). Nickel-silicon-carbide bore coatings are relatively thin; some 50 times thinner than a typically-used cast iron liner, which minimises mass as well as maximising thermal conductivity.

To enable different bore surfaces to be tested a modular replaceable liner unit was designed and manufactured (Figs 5.3 and 5.4). This satisfied all the above listed criteria (with the exception of mass), and allowed good economics in terms of parts produced



Figure 5.3 Replaceable liner



Figure 5.4 Replaceable liner carrier

The replacement liner carrier was machined from wrought (not cast) alloy AA6082 (HE30-TF) (table 5.3) and incorporated nitrile ‘O’ rings to prevent coolant ingress into the crank-case. Alloy AA6082 is a commonly available heat-treatable aluminium alloy which is also suitable for fusion welding. This allowed a fairly simple liner (figure 5.5) to be manufactured in batches so as to ensure dimensional stability across subsequent tests.

Existing top and bottom gaskets were retained as per the Original Equipment Manufacture (OEM) unit. Of key importance was the minimisation of cylinder bore distortion due to thermal and structural loads. Employment of a single-cylinder test engine with a relatively thick wall liner is an approach to minimise this (**Maassen *et al* (2001)**), (**Abe and Suzuki (1995)**). In addition, and different to the OEM component, the replacement liner wall thickness is circumferentially consistent for the vast proportion of its surface area.

Elemental Analysis alloy AA6082 - Data courtesy Alcoa Engineered Products Inc.											
	Si	Fe	Cu	Mn	Mg	Cr	Zn	Ti	Other	Others	Bal
Min wt. %	0.7	0	0	0.4	0.6	0.04	0	0	0	0	Al
Max wt. %	1.3	0.5	0.1	1.0	1.2	0.15	0.2	0.1	0.05	0.15	Al

Table 5.3 % by weight composition replacement water jacket

Elemental Analysis alloy AA2618											
	Si	Fe	Cu	Mg	Ni	Zn	Ti		Other	Others	Bal
Min wt. %	0.1	0.9	1.9	1.3	0.9	0	0.04		0	0	Al
Max wt. %	0.25	1.3	2.7	1.8	1.2	0.1	0.1		0.05	0.15	Al
Elemental Analysis alloy AA4988											
	Si	Fe	Cu	Mn	Mg	Cr	Zn	Ti	Other	Others	Bal
Min wt. %	10.5	0	3.3	0	0.4	0.05	0	0	0	0	Al
Max wt. %	11.8	0.5	4.0	0.1	0.7	0.2	0.05	0.1	0.05	0.15	Al
Elemental Analysis Meehanite 350 / EN-1561-GJL-350 GG35 - Data courtesy United Cast Bar Ltd											
	C	Si	Mn	S	P	Note			Others		Bal
Min wt. %	2.9	1.8	0.4	0	0	Microstructure limits apply			0		Fe
Max wt. %	3.65	2.9	0.7	0.1	0.3				Residual		Fe
Elemental Analysis MW450 / 20MnV6 / BS4360 GR 55 / EN 10294-1											
	C	Si	Mn	V	P	S			Other	Others	Bal
Min wt. %	0.16	0.1	1.3	0.08	0	0.02					Fe
Max wt. %	0.22	0.35	1.6	0.15	0.03	0.04					Fe

Table 5.4 % by weight composition for manufactured CRF liners

Figure 5.5 Detail design for replacement ‘wet’ cylinder liners

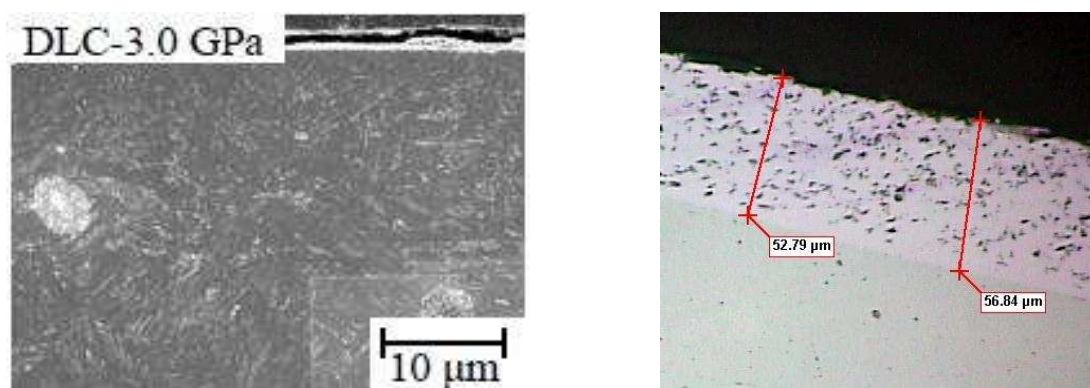
Replacement CRF liners were made from different substrate materials. Two aluminium alloys were used, firstly a 4XXX series alloy AA4988 possessing a similar composition to the OEM barrel and secondly alloy AA2618 (see table 5.4 for composition), a common automotive (motorsport) liner material. Both of these aluminium alloy components were Ni-SiC coated by default whereas the final liner material type, Meehanite GA350 cast iron was not. The following material and surface treatment liner types were manufactured (fig. 5.5):

Material of construction (table 5.4):

- AA2618 aluminium alloy
- AA4988 aluminium alloy
- Meehanite GA350 cast iron
- MW450 low alloy carbon steel

Surface treatments:

- A nickel based electrolytic cylinder bore coating manufactured by Capricorn Automotive Ltd. containing co-deposited silicon carbide (Ni-SiC).
- The vapour deposition of a carbon and hydrogen containing thin film coating referred to as 'diamond like carbon' (DLC). Diamond like carbon is a hard coating (withstanding loads of 3GPa, **Yakabe *et al* (2008)**) coating with a low 0.1-0.2 coefficient of friction.



DLC (LHS) after **Yakabe *et al*** and Ni-SiC (RHS) **Capricorn Automotive Ltd**

Figure 5.6 Bore surface coatings

**Totten and MacKenie (2003)** state that the use of Ni-SiC bore coatings was developed by Mahle GmbH under the trade name Nikasil and has seen extensive and successful use for



cylinder coatings since the 1970s. Since this time additional work has shown the benefit of increased phosphorous levels (**Ishimori *et al* (1977)**), leading to precipitation hardening after thermal treatment. The optimal bath for Ni-P-SiC composite plating is as follows:

Ni(SO <sub>3</sub> NH <sub>2</sub> ) <sub>2</sub> 4H <sub>2</sub> O	(Nickel Sulfamate):	500 gl <sup>-1</sup>
NiCl <sub>2</sub> H <sub>2</sub> O	(Nickel chloride):	15 gl <sup>-1</sup>
H <sub>3</sub> BO <sub>4</sub>	(Boric acid):	45 gl <sup>-1</sup>
H <sub>3</sub> PO <sub>2</sub>	(Hypophosphite):	0.1-4.2 gl <sup>-1</sup>
C <sub>7</sub> H <sub>4</sub> O <sub>3</sub> NSNaH <sub>2</sub> O	(Sodium saccharin):	3 gl <sup>-1</sup>
SiC <sub>p(1-4.5μm)</sub>	(Silicon carbide):	80-150 gl <sup>-1</sup>

Operating conditions (**Ishimori *et al***) are quoted as pH4; 20 Adm<sup>-2</sup>; 54-60°C

### Bore surface finish:

Cylinder bores are invariably finished by the process of honing. The honing process involves a rotating and reciprocating expanding mandrel with abrasive tool inserts placed inside the cylinders nominally, though not constrained to cylinder centre-line. As the tool expands during operation, pressure is generated against the bore surface and a ploughing type action removes material from the cylinder bore until it reaches the required size. The process of honing, although providing exceptional geometric form, does constrain the surface finish resulting in the following characteristics:

- Abrasives suitable for stock removal within reasonable commercial limits produce characteristic roughness profiles typical of 3<sup>rd</sup> body abrasive wear. Abrasive morphology leads to local roughness variation visualised as varying ‘track width’
- The reciprocating motion produces a helical overlay of roughness referred to as ‘cross hatch’ (figure 5.7b). Variation of strokes per minute (S) to mandrel revolutions per minute (R) as well as certain abrasive parameters (F) alters this within limits of mandrel acceleration for a given bore diameter (D) and bore length (L). The resulting cross hatch angle (CHA) is given by (**Sunnen, (1993)**) as  $CHA = 2 \tan^{-1} \left( \frac{(L - F) \times S}{D \times R} \right)$  where F is the ‘stone’ parameter (50-100) and linear dimensions are in mm.

- Some amount of unwanted material folding / smearing and embedding may occur which requires care in processing and subsequent cleaning operations as means of prevention (**Lenhof and Robota, (1997)**)
- Multiple honing steps are common, utilising different abrasive grades thereby leading to one core profile laid over another profile (usually with finer grade abrasive). This is often referred to as ‘plateau honing’ and is considered the norm with cast iron bores

Surface finishes vary by application as a means of optimising in-cylinder performance and longevity (**Lenhof and Robota, (1997)**). Developed finishes are given in table 5.5 as typically measured with a skid type profilometer measuring z axis deviation along the x axis.

Type / Surface parameter
$R_a$
$R_k$
$R_{pk}$
$R_{vk}$
$M_{r1}$
$M_{r2}$
$R_z$
Inc angle (horz)

Notes: As per ISO4288:’96, 4mm evaluation length with Gaussian filter

Table 5.5 Developed bore surface finishes

Where  $R_a$  is the centre-line average of the measured profile as given by the equation:

$$R_a = \frac{1}{L} \int_0^L |z| dx \quad (5.1)$$

Where  $R_z$  is the average minimum valley excursion (v, -z) to maximum peak excursion (p, +z) of a profile as given by the equation:

$$R_z = \frac{p_1 + p_2 + p_3 + p_4 + p_5 + v_1 + v_2 + v_3 + v_4 + v_5}{5} \quad (5.2)$$

The parameters  $R_k$ ,  $R_{pk}$ ,  $R_{vk}$ ,  $M_{r1}$  and  $M_{r2}$  are a means of height characterisation using the linear material ratio curve as per ISO13565-2:’96 as per figure 5.7a.

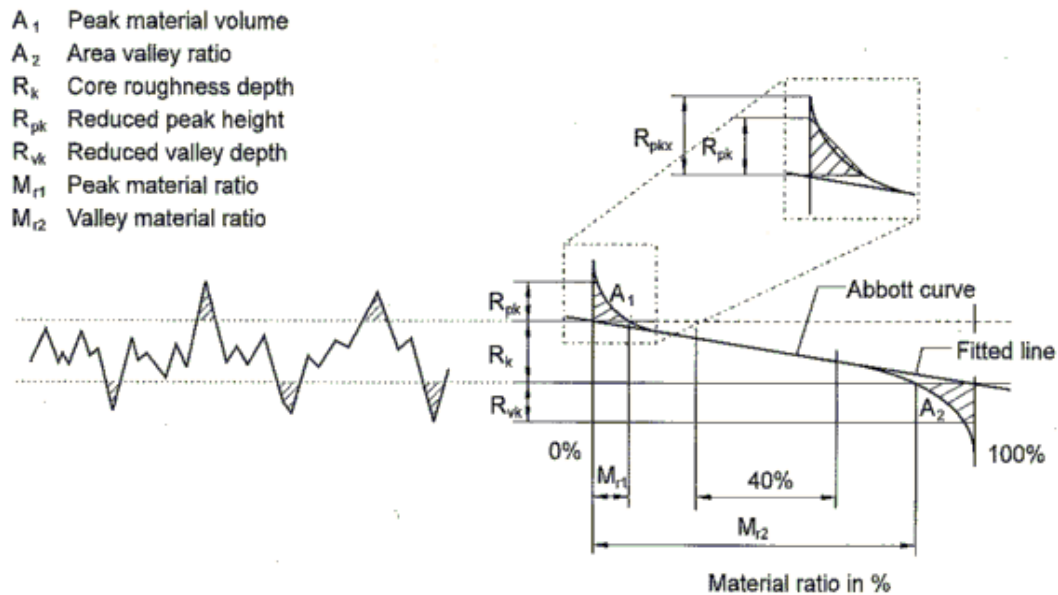
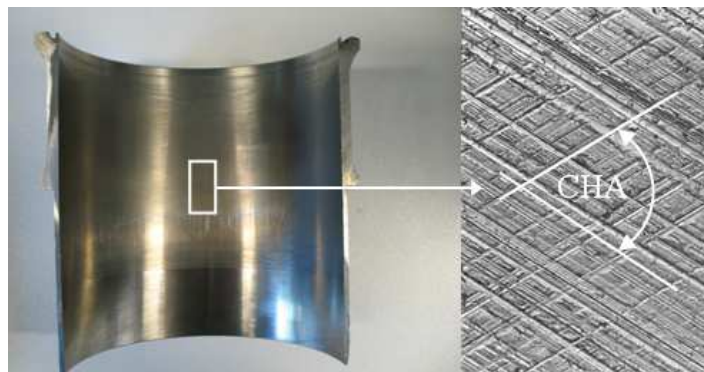
Figure 5.7a Roughness parameters reprinted from **Lehof and Robota (1997)**

Figure 5.7b Definition of cross-hatch angle (CHA)

The  $R_{pk}$  and  $R_{pkx}$  parameters are of key interest with regards to plateau honing. Plateau honing is in essence the reduction of  $R_{pk}$  somewhat similar to the in service reduction of  $R_{pk}$  by the mechanism of wear. By producing a surface with reduced peak height in the manufacturing process, initial asperity interaction is reduced compared to a non-plateau surface. The plateau surface more closely represents a mid-life (worn in) product without the inevitable increase in running clearances (due to asperity tip interaction / wear).

**Ohlsson *et al* (2003)** compare the relative merits of 2D (skid type) surface measurement to 3D (contact / non-contact) measurements, with the aim of isolating the primary parameter influencing friction. Varying surfaces were analysed and 3D analysis of surfaces was shown to be better than 2D analysis with regards to wear assessment. However, with regards to frictional performance, introduced oil trapping reservoirs within the steel strips that produced

best lubricated performance were poorly represented with existing amplitude, spatial, hybrid, and functional parameters. The surface finish of plateau processed parts were compared (figs 5.8 and 5.9) to a standard non-plateau bore surface using a Zygo Newview 5000 non-contact surface analysis machine, with the resulting surface parameters defined as follows:

$S_q$ : Root-Mean-Square Deviation of the Surface. This is a dispersion parameter defined as the root mean square value of the surface departures within the sampling area.

$$S_q = \sqrt{\int \int_a (Z(x, y))^2 dx dy} \quad (5.3)$$

$S_z$ : a parameter defined as the average value of the absolute heights of the five highest peaks and the depths of the five deepest pits or valleys within the sampling area.

$$S_z = \frac{\sum_1^5 |PeakHeights| + \sum_1^5 |ValleyDepths|}{5} \quad (5.4)$$

$S_{sk}$ : Skewness of Topography Height Distribution. This is a measure of asymmetry of surface deviations about the mean plane.

$$S_{sk} = \frac{1}{S_q^3} \int \int_a (Z(x, y))^3 dx dy \quad (5.5)$$

This parameter can effectively be used to describe the shape of the topography height distribution. For a Gaussian surface which has a symmetrical shape for the surface height distribution the skewness is zero. For an asymmetric distribution of surface heights the skewness may be negative if the distribution has a longer tail at the lower side of the mean plane, or positive if the distribution has a longer tail at the upper side of the mean plane. This parameter can give some indication of the existence of ‘spiky’ features. Plateau honed surfaces are characterised as having an  $S_{sk}$  value which is positive.

$S_{ku}$ : Kurtosis of Topography Height Distribution. This is a measure of the peakedness or sharpness of the surface height distribution.

$$S_{ku} = \frac{1}{S_q^4} \iint_a (Z(x, y))^4 dx dy \quad (5.6)$$

This parameter characterizes the spread of the height distribution. A Gaussian surface has a kurtosis value of 3. A centrally-distributed surface has a kurtosis value larger than 3, whereas the kurtosis of a well spread distribution is smaller than 3. By a combination of the skewness and the kurtosis, it may be possible to identify surfaces which have a relatively flat top and deep valleys. Plateau honed surfaces are characterised as having a  $S_{ku} < 3$ .

‘Plateau’ finish



Amplitude Parameters

Sa	= 0.63505 $\mu\text{m}$
Sq	= 0.85801 $\mu\text{m}$
Sp	= 4.5551 $\mu\text{m}$
Sv	= 4.9026 $\mu\text{m}$
St	= 9.4577 $\mu\text{m}$
Ssk	= -0.1024
Sku	= 6.0111
Sz	= 8.8267 $\mu\text{m}$

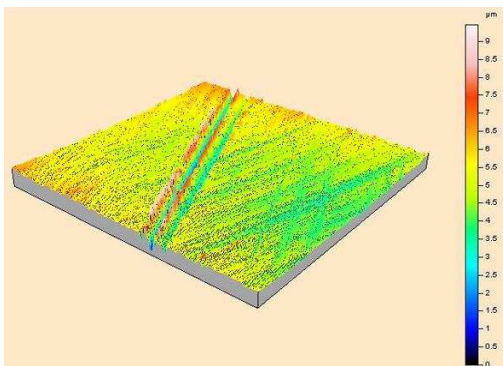
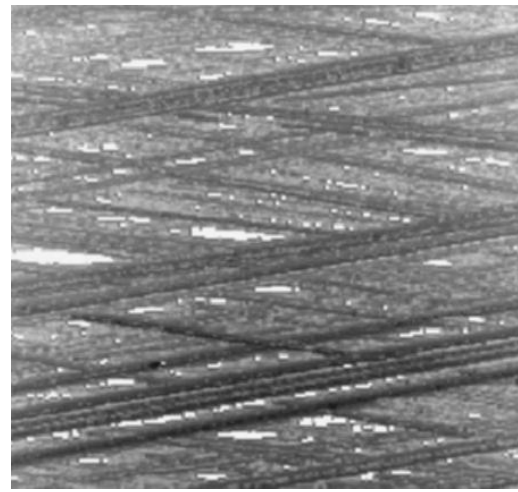


Figure 5.8 ‘Plateau’ finish

‘Standard’ finish



Amplitude Parameters

Sa	= 1.7347 $\mu\text{m}$
Sq	= 2.1211 $\mu\text{m}$
Sp	= 6.687 $\mu\text{m}$
Sv	= 7.537 $\mu\text{m}$
St	= 14.224 $\mu\text{m}$
Ssk	= 0.11434
Sku	= 2.5612
Sz	= 8.5162 $\mu\text{m}$

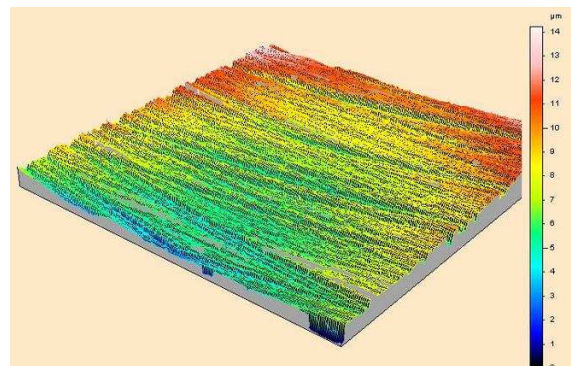


Figure 5.9 ‘Standard’ finish

In the non-plateau case (fig 5.9),  $S_{sk}$  is negative and  $S_{ku}$  is greater than 3. The plateau case (fig 5.8) contrasts this with a positive  $S_{sk}$  and  $S_{ku}$  less than 3.

### 5.3.2 Piston sub-assembly

To enable piston skirt variations to be tested the OEM CRF piston was deemed as unsuitable for modification. The existing part was fully manufactured and certain modifications required alterations to design within the order of manufacture.

As per the interchangeable liner (section 5.3.1) a similar approach resulted in a 'base' part suitable for tribological modification with derived alterations. The piston was designed to be of similar mass to the OEM part thereby negating any requirement to rebalance the rotating assembly. The replacement part was further constrained to be a direct fit with the existing OEM connecting-rod as well as featuring a higher factor of safety than implied by a 30hr rebuild requirement (**Honda Motor Co., (2002)**).

The chosen material was AA2618 (table 5.4), a high-performance alloy used for automotive and aerospace applications (**Luo *et al*, (2002)**). Automotive pistons undergo cyclical loading due to intermittent combustion pressure and inertial loads which at the top dead centre position are in opposite directions. As these forces are of differing magnitudes the regime of operation is therefore cyclical fatigue. Due to aluminium alloys generally not having a fatigue limit it is, therefore, required to ensure any proposed piston is within the (elevated temperature) fatigue envelope (figure 5.10) for a given cyclical life.

Figure 5.10 Fatigue data, AA2618 courtesy of Capricorn Automotive Ltd.

A new higher endurance gudgeon pin was also designed for similar reasons to above. The OEM part is a commercial grade low alloy chrome steel and this was replaced with a VAR (vacuum arc re-melted) ‘GKHW’ nitriding steel produced by Aubert and Duval, France. Post nitriding parts were DLC coated to increase small end bearing reliability.

Elemental Analysis GKHW (AIR 33CrMoV12-9) steel - Data courtesy Aubert et Duval (France)					
	C	Cr	Mo	V	Bal
Nom. wt. %	0.3	3.0	1.0	0.2	Fe

Table 5.6 Developed gudgeon-pin material

A fatigue limit of 950MPa is stipulated with this material based on previous experience (Capricorn Automotive Ltd). To ensure reliability both the proposed piston and pin were analysed for fatigue failure by means of assessing overall thermo-structural stress utilising inertial forces developed in chapter 3 combined with in-cylinder gas pressure. Iterative design ensued to ensure that the components satisfied relevant fatigue limits based on localised temperature field generated. Figure 5.13 details a half model assembly subjected to such loads, with resulting Von-Mises stress results. Secondary assessments of pin bore bearing limits and ring-pack circumferential vertical displacements were also conducted, resulting in the bulk designs presented in figures 5.11 and 5.12. Specialist processing such as surface peening, equiaxial forging, flow-deburring and, micro-finishing were also employed on the produced parts to increase reliability.

Detail design such as that required where assembly mating occurs is performed iteratively based on look up-tables. A key design aspect is that of the piston outside diameter both in terms of clearance size within the bore, topographic form (referred to as barrel and elliptical forms) (**Ejakov (2003)**), surface finish, and applied coatings.

Figures 5.11 Replacement piston showing part variation table



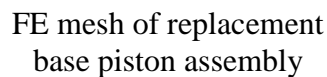
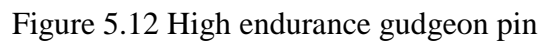


Figure 5.13 Structural analysis of piston assembly

The cold clearance of the piston within the bore is calculated numerically as a function of the following parameters (**Howell-Smith (2002)**):

$$P_{COLDCI} = f(D, P, S, E) \quad (5.7)$$

Where  $P_{COLDCL}$  is the diametrical cold clearance,  $D$  is the nominal bore size,  $P$  is the power per cylinder,  $S$  is measure of the relative skirt stiffness (type of skirt construction), and  $E$  is the differential expansion between bore and piston. The differential expansion and bore size are the most important terms:

$$P_{COLDCL} \approx f(D, E) \quad (5.8)$$

As thermal expansion is itself a function of linear length, and so as to maintain a consistent running clearance when operational for a given application type and method of construction, cold clearance is proportional to bore size (figure 5.14, data courtesy Capricorn Automotive Ltd.):

$$P_{COLDCL} \approx kD \quad (5.9)$$

Where  $k$  is an application / construction constant

The piston maximum radial size is given by:

$$\frac{(D - P_{COLDCL})}{2} \quad (5.10)$$

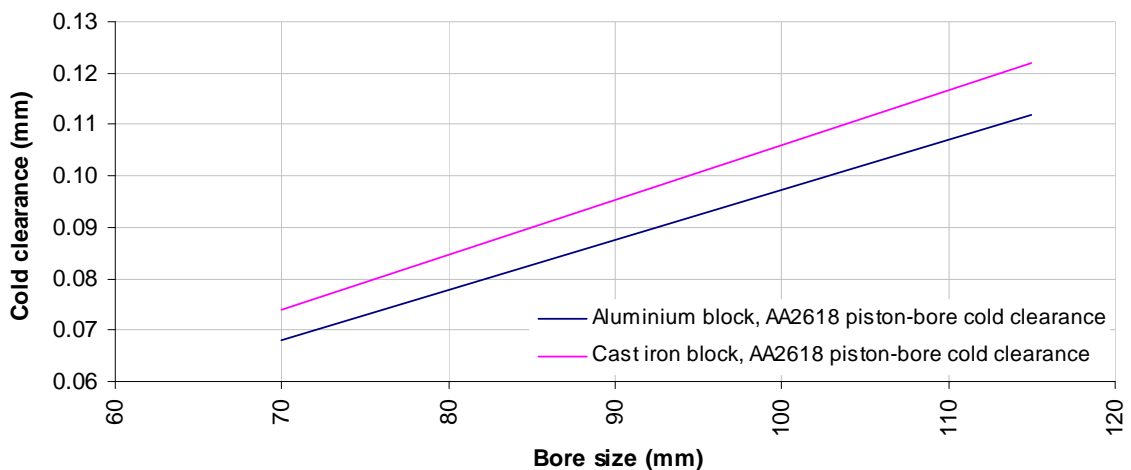


Figure 5.14 Piston to bore clearance for a given application

Once the piston maximum radial size has been defined the side or ‘barrel’ profile is described as a radial reduction from this initial maximum radius (**Ejakov (2003)**). Similar to eqn. 5.7 the required reduction is composed of several parameters, where notably  $S$  and  $E$  varies, due to a

varying temperature field and changing section stiffness of the skirt. This was computed parametrically with results as per figure 5.16 in effect computing eqn. 5.9 with a differing constant based on relative position (and therefore relative sectional stiffness and temperature) within the skirt region.

The land regions above the piston skirt are computed similarly (**Howell-Smith (2002)**). However the  $S$  parameter is removed and replaced with a target gap (clearance) for gas dynamics reasons. The headland (region above the compression ring) is subject to large approximately linear temperature variation, hence the radial drop in this region approaches a fixed angle ( $0.5\text{--}2^\circ$ ) away from the targeted operational clearance. The computed side profile radial drop vs. height coordinates are interconnected by means of a cubic spline. With a cubic spline, the 2<sup>nd</sup> order derivative is of far smoother variation, thereby minimising inertial effects on the machine tool producing the required form (**Takisawa (1998)**).

With a cubic spline expressing a radius for the piston outside diameter from the top of the piston to the skirt end along the skirt centre axis ( $0^\circ$ ) it is possible to section the piston at any vertical position with a now-existing point on the outside edge at the  $0^\circ$  position. On this or a number of similar sections the ‘elliptical profile’ is now seen as a further series of radial drops from the pre-existing  $0^\circ$  position (figure 5.15):

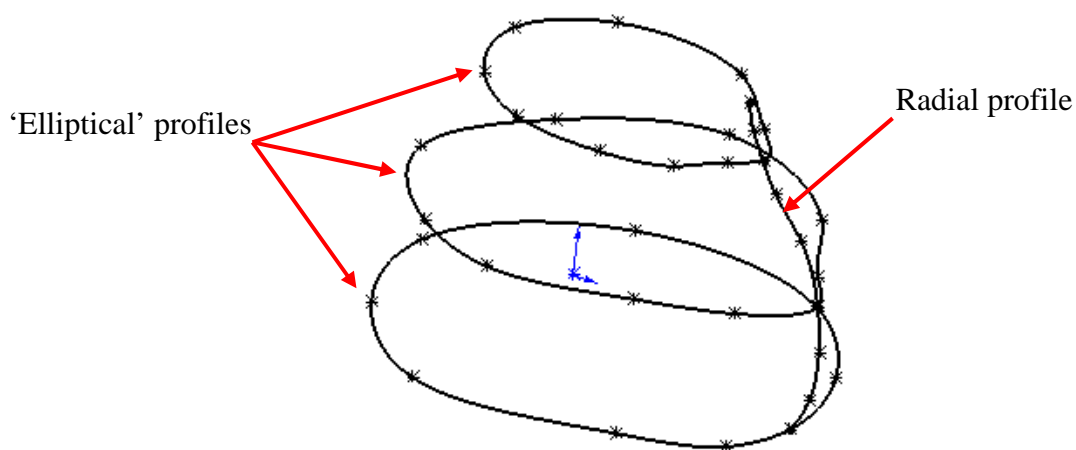
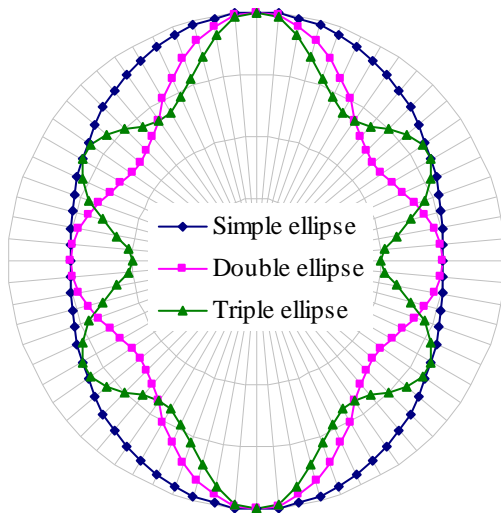


Figure 5.15 Radial and elliptical construction of piston outside form

The elliptical profile is often a simple mathematical ellipse thereby requiring only 1 parameter, an elliptical drop(s) ( $d_1, d_2$ ), to express the OD form at any given vertical position. The elliptical drop is equivalent to  $a - b$  where  $a$  is the major and  $b$  is the minor axis of the chosen ellipse. Both tabular (spline) and equation definitions (ellipse, etc. see table 5.7) are used to

describe the elliptical profile. It is therefore possible, within reason, to define almost any required shape with a combination of radial and elliptical profiles.



Simple ellipse:

$$r_{\min} = r_{\max} - \left( d_1 \frac{1 - \cos 2\theta}{2} \right)$$

Double ellipse:

$$r_{\min} = r_{\max} - \left[ \left( d_1 \frac{1 - \cos 2\theta}{2} \right) + \left( d_2 \frac{1 - \cos 4\theta}{2} \right) \right]$$

Triple ellipse:

$$r_{\min} = r_{\max} - \left[ \left( d_1 \frac{1 - \cos 2\theta}{2} \right) + \left( d_2 \frac{1 - \cos 6\theta}{2} \right) \right]$$

Table 5.7 Equation based elliptic piston OD forms

The developed replacement P1084 piston (Figure 5.11) features a spline side profile (the major profile,  $0^\circ / 180^\circ$ ) and a variable though simple elliptic cross-section. The lands although tapered are nominally round. Within the oil groove region ellipticity is introduced, reaching a constant magnitude for the major proportion of the skirt area. The minor profile is defined as the side profile top to bottom when sectioned along the pin axis ( $90^\circ / 270^\circ$ ) (figure 5.16).

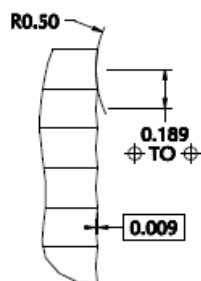
Figure 5.16 Major and minor axis radial drops (P1084)

### Piston turned finish

Piston skirts produced by single point turning (**Takisawa, (1998)**) (figure 5.17), remove material in a helical fashion as typically found on turned parts. The roughness in the axial direction is a function of the tool and feed-rate used. Typical tool geometries produce truncated radii on the surface where the degree of truncation depends on the tool tip nose radius and feed-rate. Figure 5.18 details an industry standard skirt finish, as well as Capricorn Automotive Ltd developed reverse 'saw-tooth' standard and smooth version skirt finishes. Derivative parts based on the baseline P1084 part are shown in figures 5.11 and 5.17.



Figure 5.17 P1084 Selection of manufactured derivative parts



Industry standard

Developed reverse 'saw tooth'

Developed 'smooth'

Figure 5.18 Industry standard and developed skirt finishes

### Piston skirt coating

Two types of piston coating were adopted for testing. The first was fluoropolymer-based, with the trade name Xylan 1010, produced by Whitford plastics Ltd. This coating is sprayed using air atomisation producing a 12-20µm thick coating, and features a high concentration of particulate PTFE. The second coating was 'diamond like carbon' (DLC). DLC was applied all over the piston, although initial testing showed DLC coating of pin bores to be unsuccessful (suffering de-lamination due to low relative modulus substrate). DLC coating was provided by Eltro (GB) Ltd. by a plasma assisted chemical vapour deposition process. Coating thickness

was  $< 4\mu\text{m}$  and, due to an approximate 70%  $\text{sp}^3$  structure the resulting coating is extremely hard (10-40GPa). The coated part is shown in figure 5.17 (RHS)

### **Piston rings and compatibility**

Piston rings in engines have three main functions: to seal the working chamber from the crankcase, to assist in the flow of heat from piston to cylinder wall, and to control oil consumption. To achieve efficient sealing a good fit with both the cylinder wall and the top or bottom of the piston ring groove are required. The radial fit is achieved by the inherent spring force of the ring together with the pressure of the working medium acting from behind the ring. The axial position of the ring within its groove is determined by the gas pressure and the inertia and friction forces, and can alternate between the top and bottom of the groove (figure 5.19).

The ring is forced against the cylinder wall under a contact pressure  $p$ , which depends on the ring dimensions, free gap of the ring and the modulus of elasticity of the material used. A ring can be given a constant or a variable contact pressure; the latter being a function of the angle  $\phi$  and often used to reduce ring flutter. The measurement of  $p$  is extremely difficult and in practice it is therefore calculated from the Tangential Force ( $F_t$ ). The Tangential Force is the force which when applied tangentially to the ends of the ring is sufficient to close the ring to the specified closed gap.

For the case when  $p$  is constant (e.g. ring compressed inside a flexible tension tape), the following expression can be derived for the bending moment  $M$  :

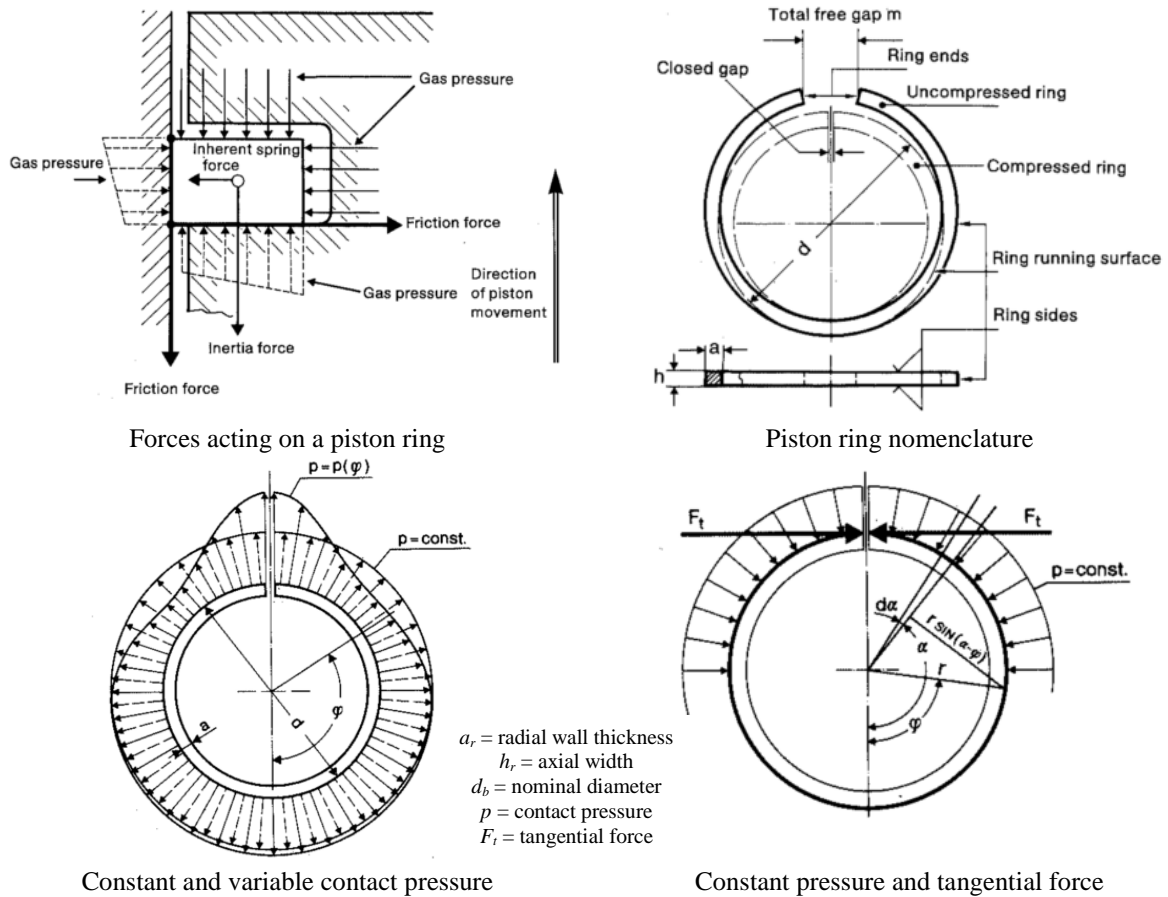
$$dM = phr^2 \sin(\alpha - \phi) d\alpha$$

$$M = phr^2(1 + \cos \phi)$$

Or in terms of tangential force  $F_t$ :

$$M = F_t r(1 + \cos \phi)$$

$$p = \frac{2F_t}{d.h} \quad (5.11)$$

Figure 5.19 Piston ring terminology reprinted from **Goetze (1995)**

Compression ring contact pressure due to inherent tension only lies generally between 0.12 and 0.25 N/mm<sup>2</sup> for rings conforming to relevant DIN/ISO standards. However the actual pressure between ring and cylinder wall is many times greater due to gas pressure (**Goetze (1995)**). To ensure ring to bore compatibility the OEM rings were subjected to SEM analysis. The compression ring nominally 0.94mm thick x 3.1mm radial wall was confirmed as constructed from high chromium steel with a nitrided working face (Table 5.8).

Element	App	Intensity	Weight%	Weight%	Atomic%
	Conc.	Corrn.		Sigma	
Cr K	13.26	1.1534	18.94	0.84	20.06
Fe K	47.44	0.9642	81.06	0.84	79.94
Totals			100.00		

Table 5.8 SEM analysis of OEM compression ring working face

The oil ring is of three-piece construction with an assembly thickness of 1.93mm (compressed) and radial wall of 2.2mm. The oil ring scraper rails are 0.4mm thick each with a 1.9mm radial wall and are chrome nitride face-coated as determined from SEM analysis (Table 5.9):

Element	App	Intensity	Weight%	Weight%	Atomic%
	Conc.	Corrn.		Sigma	
N K	3.19	0.4597	11.09	2.12	29.08
O K	3.77	1.1841	5.09	1.46	11.69
Cr K	50.46	0.9623	83.82	2.38	59.23
Totals			100.00		

Table 5.9 SEM analysis of OEM oil rail working face

## 5.4 Development of etching processes and component modification

Localised etching was performed on the replacement CRF piston, CRF barrel and third party testing partners bore components. The piston etching was produced by laser processing and was restricted to the skirt region only (5.4.1). The liner etching was restricted to the top dead centre (ring pack position) and was produced by laser (5.4.2) as well as mechanical indentation (5.4.3).

### 5.4.1 Piston skirt etching

Increased valley depth (roughness) is a method to improve lubrication performance as discussed in Chapter 2. Localised track-wise removal of material was investigated, and components prepared by means of laser processing and subsequent finishing operations.

Processing was conducted utilising a machine with details as per figure 5.20.

Laser parameters (table 5.10) were optimised so as to produce depth of etch, thereby producing an approximately parabolic track section of width post-polishing. Polishing was required post processing due to ejected base material adhering to the region around the track periphery. Figure 5.21 details the resulting sections pre and post polishing.

Machine:                      Rofin EasyMark/F20



Manufacturer:      Rofin-Sinar GmbH  
 Technology:  
 Output power:  
 Field size:  
 Focal distance:  
 Beam steering:

Figure 5.20 Laser used for piston skirt etching

Etch section prior to polishing

Etch section post polishing

Figure 5.21 Section through skirt etching pre and post polishing

Processing parameter	Value to achieve tracks as per figure 5.21
Current	
Frequency	
Processing speed	
Track width	
Pulse width	

Table 5.10 Skirt laser processing parameters

Three skirt etchings (patterns) were produced with 100% coverage on both skirts. All patterns were nominally at                  track separation however the angle between tracks varied in a

conventional cross-hatch format. The produced patterns had included angles (from the horizontal) of 30°, 90°, and 150° (Type 30, Type 90 and Type 150) (figure 5.22).

Images of the resulting patterns complete with surface measurement visual plots are given in figures 5.22 and 5.23. Table 5.11 presents resolved surface parameters for type 30 travelling in a North-South direction as would be the direction of entrainment, though caution is advised in interpretation due to inherent limitations with sampling methods **Ohlsson *et al* (2003)**.

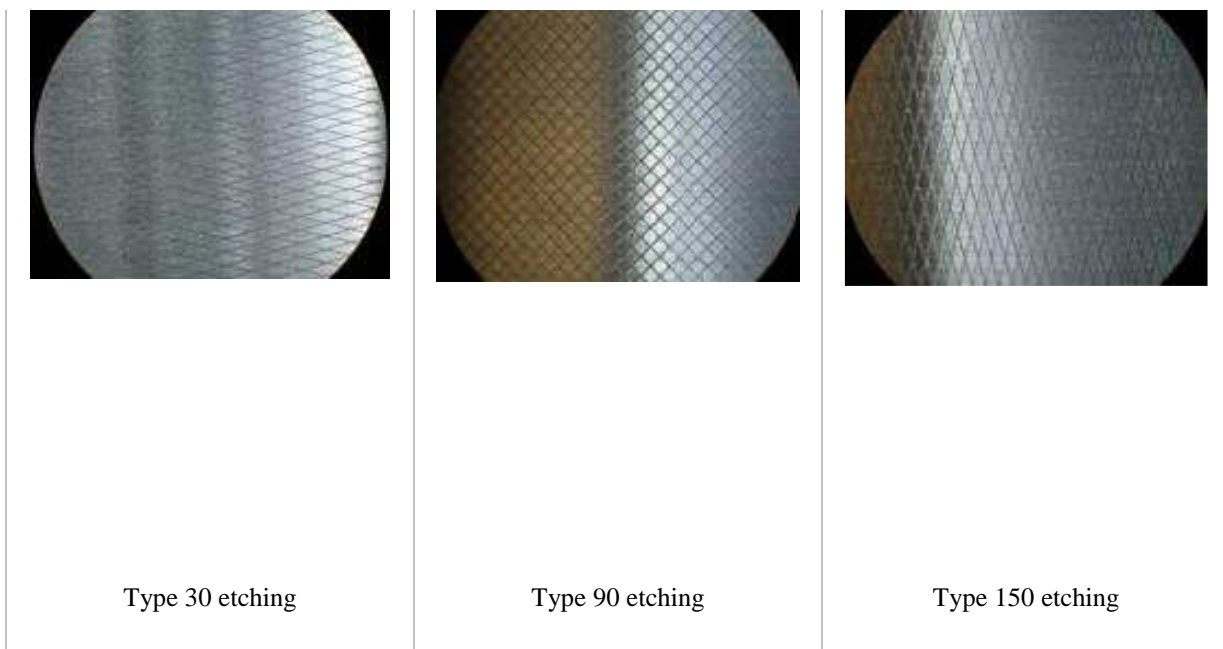


Figure 5.22 Skirt etching after polishing and non-contact surface plot

Figure 5.23 Type 30 etching trace in direction of entrainment

**Calculated parameters from profile shown in figure 5.23 by mean of the first 5 sampling lengths using a micro-roughness filter with ratio of 2.5µm ref 19450\_027/029**

Ra	Arithmetic Mean Deviation of the roughness profile
Rq	Root-Mean-Square (RMS) Deviation of the roughness profile
Rp	Maximum Peak Height of the roughness profile
Rv	Maximum Valley Depth of the roughness profile
Rz	Maximum Height of the roughness profile
RSm	Mean Width of the roughness profile elements

**Roughness Parameters, Gaussian filter 800µm**

Ra	Arithmetic Mean Deviation of the roughness profile
Rq	Root-Mean-Square (RMS) Deviation of the roughness profile
Rp	Maximum Peak Height of the roughness profile
Rv	Maximum Valley Depth of the roughness profile
Rt	Total Height of the roughness profile
Rsk	Skewness of the profile
Rku	Kurtois of the roughness profile
Rz	Maximum Height of the roughness profile

Table 5.11 Calculated roughness parameters (TalyMap Gold)

#### 5.4.2 Bore surface etching using a laser method

To increase roughness in the cylinder bore in a ‘by region’ fashion conventional honing was found to be not suitable. Honing was, however, required to produce the overall geometric shape and bulk surface finish. Local material removal in the size range below 0.3mm is difficult using conventional chip cutting (milling) methods. A Nd:YAG laser source (Control Laser Corporation) of c/w power was used ( ) in combination with galvanometer-driven heads and required optics.

The laser beam exiting the source is galvanometer manipulated (beam steering) passing through a focal length. A rotary table equipped with a Parker Digiplan (Parker Hannifin Corp.) attached to an Alpha Motion S.A. gearbox. Rotational movements are provided in 4° increments. This allowed full flexibility in terms of required geometry in the 0.05-0.2mm width range and depths up to 0.4mm. Table 5.12 details the specification of the laser source utilised.

Laser type:
Wavelength:
Output power:
Laser cooling:
Q-switched frequency range
Beam divergence
Lamp lifetime

Table 5.12 Laser specification for bore surface etching

A silica dielectric mirror with protective gold coating is placed at  $45^\circ$  to the bore centre-line allowing processing to take place normal to the bore surface. Chapters 6 and 7 detail positive performance results indicating that TDC increased roughness by means of tessellated semi-circular features (figure 5.24) will reduce asperity interaction.

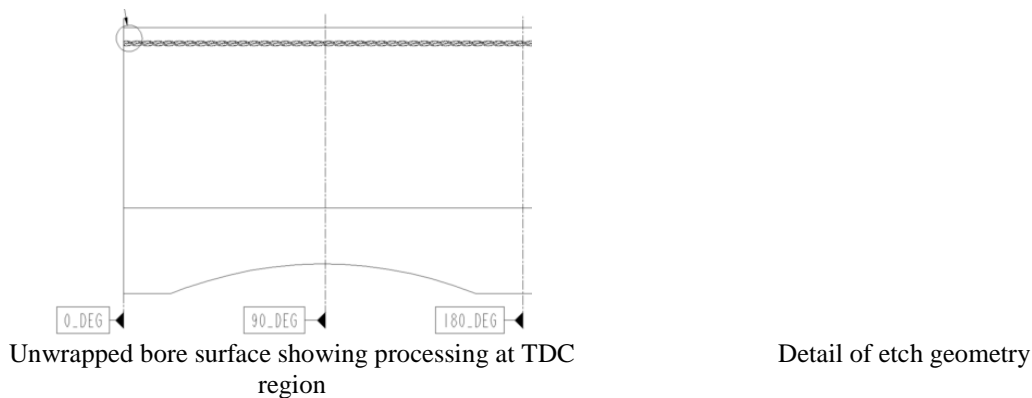


Figure 5.24 Etch pattern and region of application, CRF

Figure 5.25 shows a processed part (post final honing) and a typical section through the processed part. The cross-section shows that the laser etching has extended past the nickel silicon-carbide coating by a factor of into the CRF liner substrate.

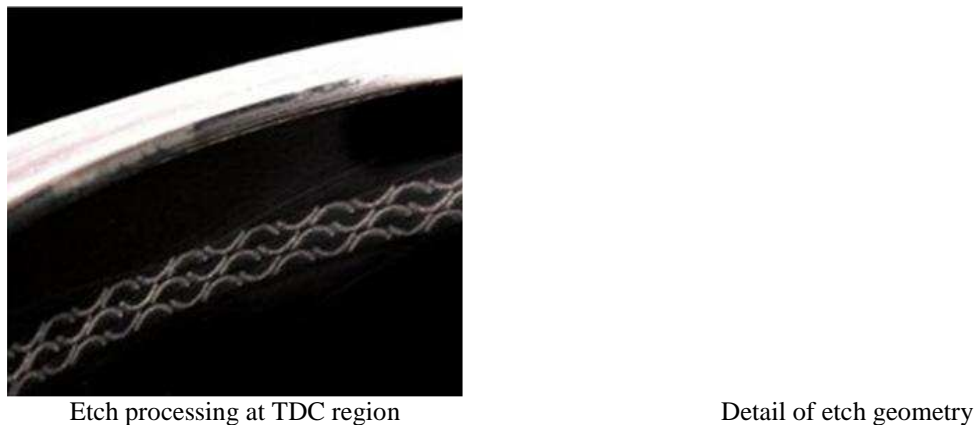


Figure 5.25 Processed etching, CRF

Testing results with the CRF produced positive results (chapter 6) (**Howell-Smith (2006)**), however increased testing utilising other engine configurations revealed variable results in terms of performance. Investigations found that immediately prior to service non-CRF engines featured depth variability of processing due to a number of reasons:

- Variability of etch depth over batch quantities, potentially due to beam focusing issues / in cycle optics degradation.
- Variable stock removal during post processing honing was occurring. In-crankcase final stage honing is a common process on many engines where the cylinder head clamp load is shown to produce bore deformation which may lead to unwelcome effects such as blow-by and oil consumption. In crankcase honing can modify the internal bore centre-line by means of uneven radial stock removal. The CRF liner had no such constraints due to final stage honing being conducted outside of the engine crankcase.

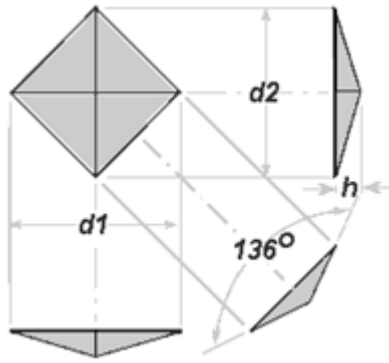
For these reasons an alternative method of local bore roughening was sought, which was processed on the finished bore utilising applied pressure to control etch feature depth.

#### 5.4.3 Impression modification of the cylinder bore surface

An alternative method to introduce localised roughness was direct mechanical impression with diamond indenters. was used as a method of ensuring consistent depth of feature.

Two variations of indenter were used (type A and type B). Indenting was performed on a Matsuura MC-800 VG2 machining centre equipped with a Yasnac J300 control and Kitagawa TT182BE-01 4<sup>th</sup> / 5<sup>th</sup> axis unit. The indenter was placed in a fabricated tool holder presenting the working tip normal to the working face of the bore surface. The fabricated tool holder was introduced using a , thereby limiting applied force.

A CNC programme positioned the tool initially central within the bore and then rotated and vertically positioned the working tip. The tool was driven into the bore surface overshooting slightly to ensure penetration (excessive penetration, positional inaccuracy, and bore shape deviation was compensated-for by the ). Indenter type 'A' was a standard Vickers pyramid diamond and the tessellated pattern form is shown in figure 5.26.



Type 'A' indenter geometry  
(Vickers diamond pyramid)

Type 'A' plan sketch of imprint  
(dimensions in microns)

Figure 5.26 Type 'A' indentation

Indentation depth was dictated by indenter geometry for a target impression width of 150 microns as 30 microns approximately. Numerical analysis directed further increased depth hence an indenter with a  $90^\circ$  inclusive cone was employed (type 'B'). The resulting type A and type B patterns as produced on the bore surface are shown in figure 5.27.

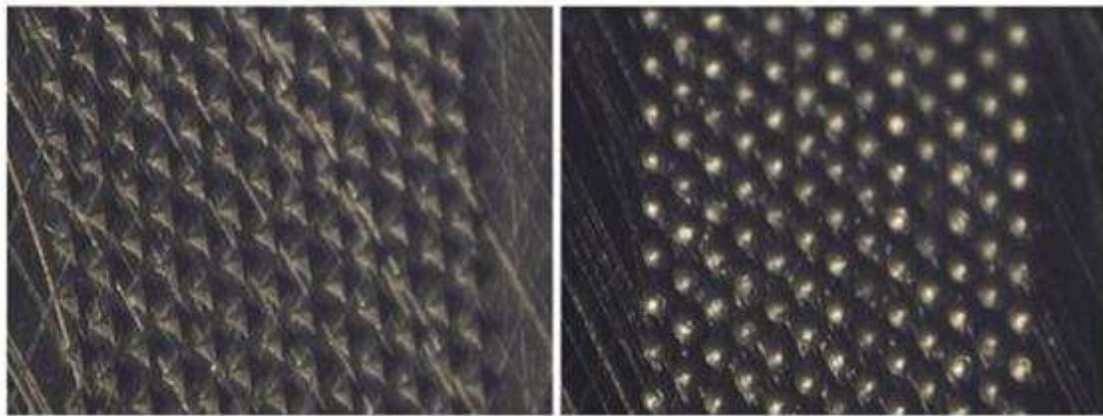


Figure 5.27 Resulting bore surface indentations (Type A, LHS, Type B, RHS)

The type A and type B patterns were applied similarly for full rotational coverage and for a depth corresponding to 1mm either side of the top ring stationary point at top dead centre. A finished etched component (type A) is detailed in figure 5.28. Further detail is given as per **Howell-Smith (2006)**.

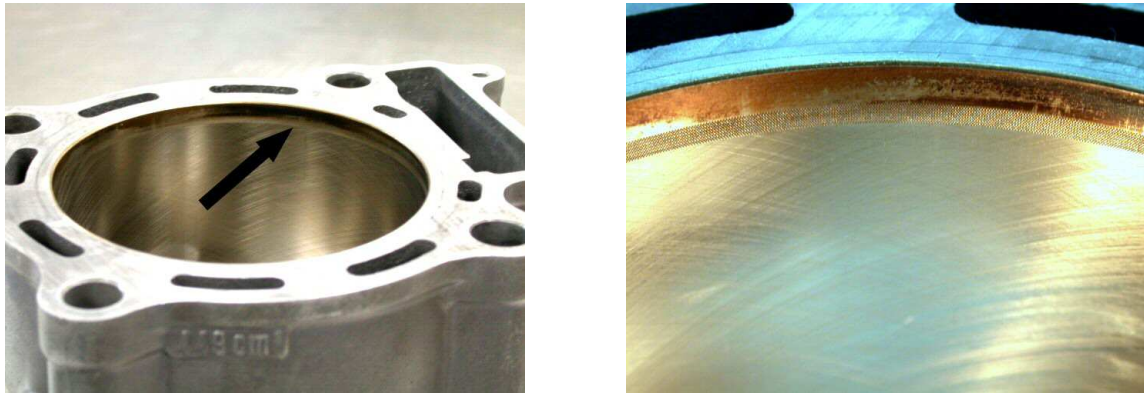


Figure 5.28 Etched and run component (type A). Arrow (LHS) details magnified view (RHS)

### 5.5 Development / instrumentation for film thickness measurement

To ascertain the validity of numerical findings a method to measure film thickness was sought. The ultrasonic method (chapter 2.2.4) utilises a piezoelectric sensor (**Dwyer-Joyce *et al* (2002), Dwyer-Joyce *et al* (2004)**).

The ultrasonic sensor was located such that it was coincident with the piston skirt whilst the piston traversed the top dead centre as shown in figure 5.29. This is at the instant of reversal with momentary cessation of entraining motion, thus representing one of the most undesired tribological conditions. The sensor was tuned to resonate at 10MHz centre frequency, which for planar operation correlates to a piezoelectric sensor thickness of 0.2mm.



Figure 5.29 Piezoelectric sensor bonded to liner outer surface

The sensor was bonded to the exterior wall of the liner using strain gauge adhesive (M-Bond 610 – Vishay Intertechnology Inc.) which has a long term application stability up to 230°C. M-Bond 610 is also low in viscosity and capable of glue-lines down to 0.005mm, free of creep, hysteresis, and linearity problems. The sensor was 7mm in diameter with ‘wrap-around’ electrodes (i.e. the top face has a bonded electrode, whilst the bottom face electrode is wrapped over to the top face).

Two wires were then soldered directly to these electrodes on the top face. The wires were fed out of the replacement liner housing to an ultrasonic pulser-receiver (UPR). The piezoelectric material of the sensor is an atomically-structured crystal such that it is not symmetric, and therefore exhibits a polarity. Applying an electric field causes the material to deform. Application of stress causes a potential difference across the crystal. The application of a voltage pulse therefore causes deformation and initiates the propagation of an elastic wave (in this case longitudinally oriented) into the liner material.

The sensor was pulsed with a rapid-rise narrow duration and high voltage ‘top-hat’ signal approximately half the wavelength of the intended frequency (5.6MHz). The signal pulse results in a 5 kHz ultrasonic pulse which is generated by the piezoelectric crystal. When the ultrasonic pulse emanating from the crystal reaches the liner inner face some of the energy is reflected backwards. When no part of the piston is adjacent to the sensor and there is a gas mixture present the poor acoustic coupling of the liner and gas means that virtually all the energy is reflected back to the sensor (very little energy can be transmitted through gas).

However, when the piston skirt is present in the path of the ultrasonic waves a sandwiched layer is set-up, where a film of oil is positioned between the piston skirt and the liner. Acoustically this is a better coupled system with significantly more energy impinging onto the piston. The stiffness of the contact, and correspondingly its ability to transmit ultrasound through the contact, is dependent upon the thickness of the fluid film. The thinner the sandwiched oil film the stiffer the contact.

Measurement of oil film thickness in the contact is by means of measuring and correlating the reflected ultrasonic energy. System calibration is performed by means of measuring returned energy when the piston is not present and minimal film condition exists (e.g. bottom dead



centre) (figure 5.30). By comparing the measured pulse with the captured pulse in the frequency domain the reflection coefficient can be calculated (figure 5.31).

With the method developed by **Tattersall (1973)**, further developed by **Dwyer-Joyce *et al* (2004)**, it is possible to derive a relationship between reflection and the film thickness.

**From Dwyer-Joyce *et al* (2004)**

Example pulses for different film thicknesses with a steel-oil-air interface. Shell T68 was lubricant employed.

(Due to lower reflection, reflection coefficients are smaller from smaller clearances (gap))

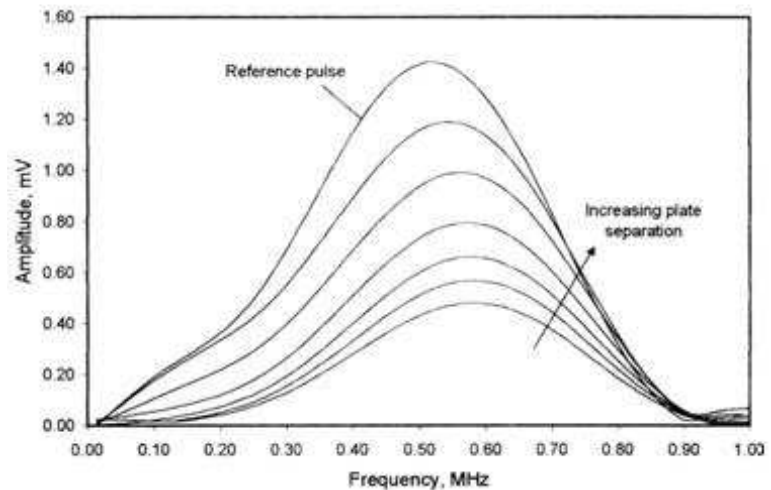


Figure 5.30 Example pulse from steel-oil-air interfaces

**From Dwyer-Joyce *et al* (2004)**

Frequency-wise reflection coefficients for different film thicknesses with a steel-oil-air interface. Shell T68 was lubricant employed.

(Due to lower reflection, reflection coefficients are smaller from smaller clearances (gap))

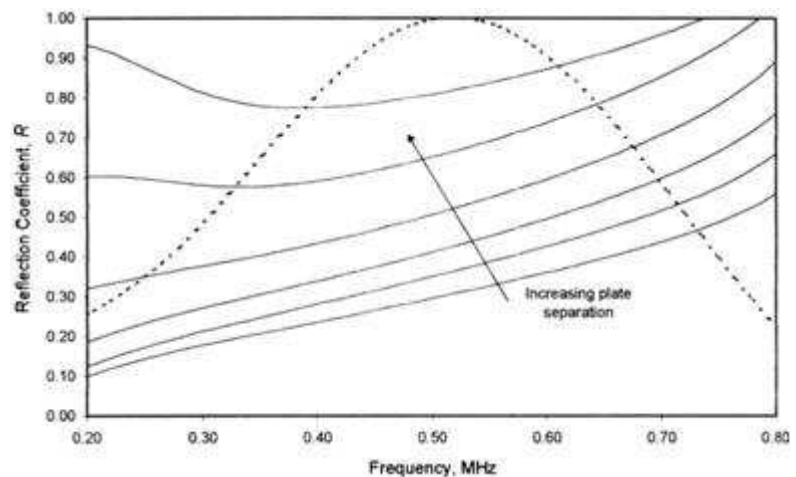


Figure 5.31 Example pulse from steel-oil-air interfaces (FFT)

A schematic of the apparatus used to measure in-cylinder film thickness is shown in figure 5.32. The ultrasonic pulse generator (UPR) emits the excitation pulses as well as receiving and amplifying the reflected pulses. In this manner the transducer acts as both an emitter and receiver (i.e. pulse-echo mode). The reflected signal was digitised on a storage oscilloscope and passed-on to a PC for processing.

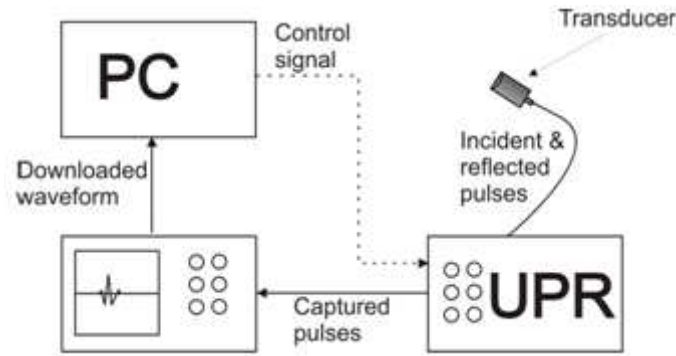


Figure 5.32 Schematic of the ultrasonic pulsing and receiving apparatus

A LeCroy LT342 oscilloscope was used to digitise and capture the received signal. In order to capture the waveforms at a high rate the onboard memory was divided-up into a number of segments. At each trigger event the selected portion of the waveform is written to a segment. The trigger was provided from the UPR, where a signal was sent to the oscilloscope at the same time as a pulse was sent to the sensor. Thus every signal from the pulser is written to the segmented memory. The onboard memory of the oscilloscope was limited to 250k points per channel. Thus the number of data points in each segment determines the number of segments which are possible to capture. During testing the number of points per segment was set at 1000, resulting in 250 pulses acquired per capture cycle.

The sensor was pulsed off with its natural frequency (equivalent to 5.6 MHz rather than 10 MHz) to produce as short a pulse as possible. As a result the maximum pulsing rate was limited to 5 kHz. However, if a higher frequency sensor was used a pulsing rate of up to 10 kHz could be achieved. The oscilloscope has the capability to capture up to 200 kHz. Full details of the procedure is given by **Dwyer-Joyce, Green, Balakrishnan, Harper, Lewis, Howell-Smith, King, Rahnejat, (2006)**.

## 5.6 Development of a floating liner

A floating liner was designed and manufactured towards the end of the research (refer Appendix 4). However, due to the lateness of this development, actual research using this equipment will take place under EPSRC programme ENCYCLOPAEDIC (EP/G012334/1). The floating liner was designed to measure in-cylinder friction directly thereby verifying numerical predictions within this thesis. Verification of numerical predictions for oil film thickness has however occurred by means of ultrasonic sensor measurement as detailed in chapter 5.5.

## 5.7 CRF Engine installation, instrumentation, and test procedure

The aforementioned CRF450R engine performance was evaluated by utilisation of a transient dynamometer cell at Loughborough University (figure 5.33).

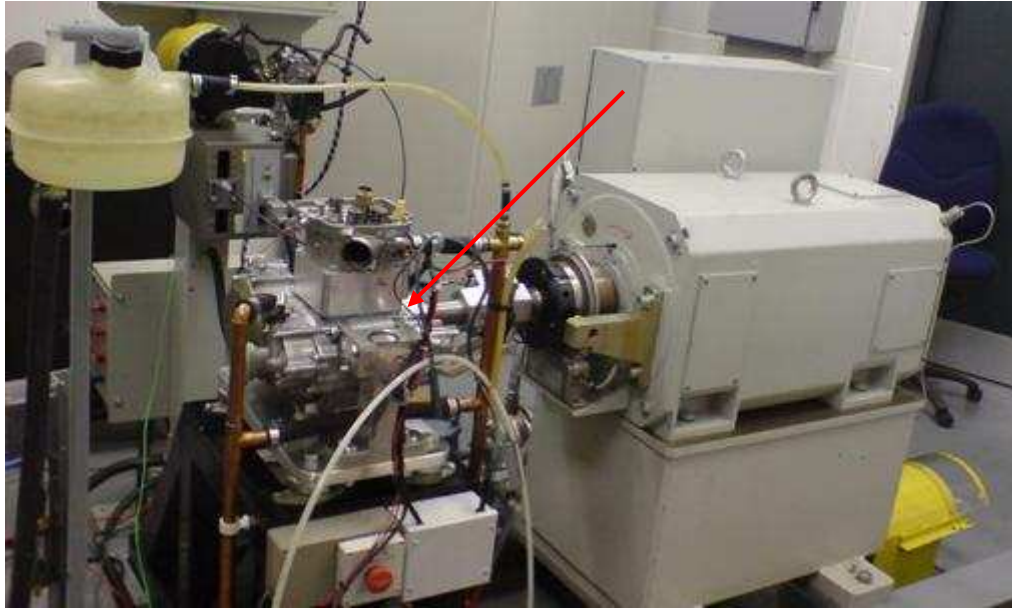


Figure 5.33 Test cell with CRF engine mounted and guarding removed

### 5.7.1 Test cell installation:

The CRF engine was mounted on vibration isolation pads on top of a box section frame. The frame was analysed for modal response similar to that detailed in chapter 5.8.6.

A coupling was manufactured between a 250kW Ricardo S3000/3345 taskmaster transient AC dynamometer (figure 5.33) drive unit and a gearbox drive sprocket on the CRF. The coupling comprised an aluminium centre shaft with Fenner® (Eriks nv.) couplings at either end (see arrow figure 5.33).

Provision was made for 12V electrical supply and remote throttle control for the CRF. Engine cooling was by means of connection to the existing cell cooling system with added pumping and thermostatic control (with data logging output). A custom exhaust system was manufactured by Janspeed UK with an 80L internal capacity, venting vertically upwards into a pre-existing extraction facility. Emergency stop and air monitoring were also facilitated to comply with safety regulations in force.

The CRF power was transmitted through 4<sup>th</sup> gear within its internal gearbox. The compact layout of the CRF and the fact its potential maximum rotational speed was higher than the dynamometer made direct crank coupling unfeasible. Primary reduction to the gearbox was 2.739:1 with subsequent shaft reduction of 1.47:1. Overall the engine rotational speed was reduced by 4.02633:1 with apparent resisting torque four times higher than actual.

### 5.7.2 Test cell instrumentation:

Fuel was supplied from an in-cell 5L tank with an external 12V pump. Fuel flow-rate was monitored by an AVL gravimetric flow-meter (figure 5.35). A fuel chiller unit downstream of the flow meter provided the CRF with constant temperature fuel.

The Ricardo dynamometer was used to pre-acquire engine performance data after calibration (figure 5.34). Data stored within the S3000 control was then transferred and combined with additional data streams from specific sensors all ultimately recorded by a National Instruments PXI data logger (figure A4.5).

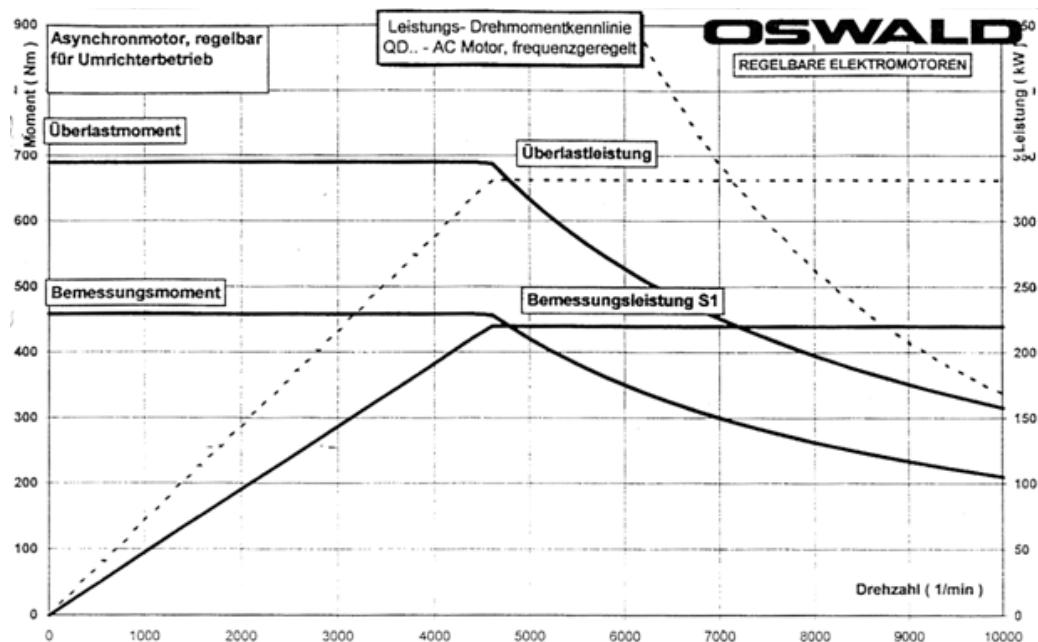


Figure 5.34 S3000 dynamometer performance curve

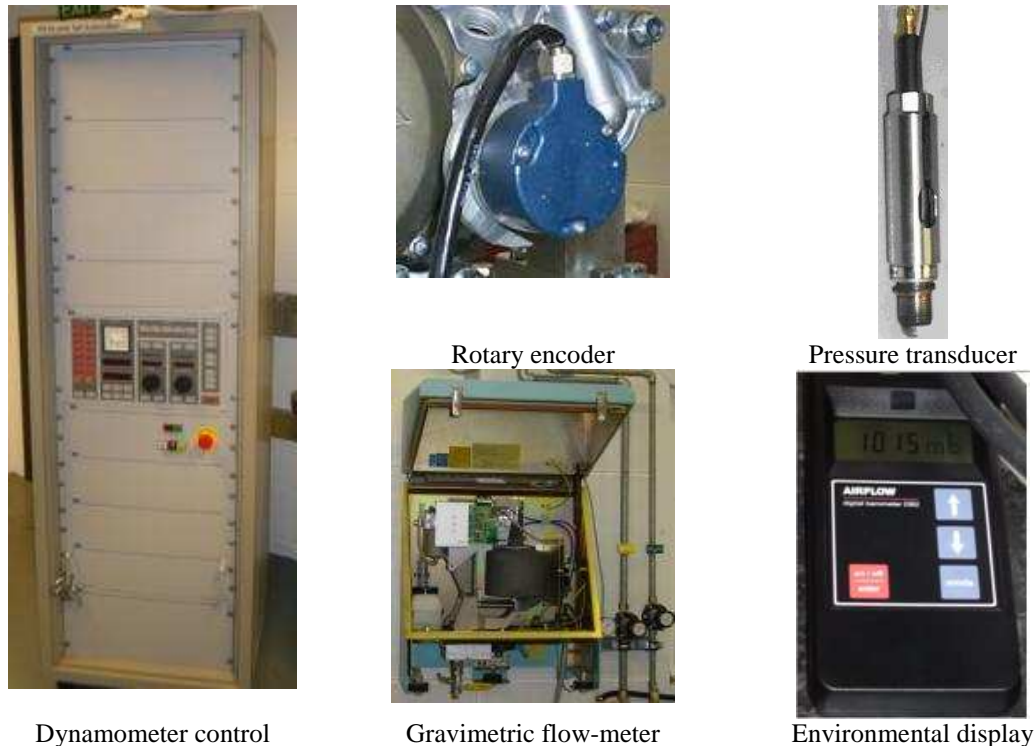


Figure 5.35 Instrumentation used for CRF testing

The additional National instruments PXI recorded sensors comprised of:

- Crank angle by means of a high speed rotary encoder (figure 5.35). This encoder also provided a 'top dead centre' pulse – triggering in-cylinder pressure data acquisition. The encoder was manufactured by Leine and Linde AB (Sweden), part number 632, providing 3600 pulses per revolution output utilising optical technology.
- Combustion pressure was measured, although not during actual component testing, by means of an in-cylinder spark-plug replacement type unit. Manufactured by Kistler AG this sensor utilises a piezo-electric quartz crystal technology and charge amplifier combination (figures 5.35 and A4.5) to provide a voltage output. The sensor was delivered pre-calibrated. Recorded in-cylinder pressure (10 cycle average) is given in figure (5.37).
- Cell temperature, pressure, and humidity were captured by an Airflow Developments Ltd. DB2 digital barometer. The DB2 (figure 5.35) featured RS-232C output, which supplied a further input stream into the PXI data logger.

Data streams incoming to the National Instruments PXI unit were sampled at the frequencies given in table 5.13.

Sensor	Sample
Cylinder Pressure	1 sample / $\mu$ s
Crank angle	1 sample / $\mu$ s
Coolant temperature	1 sample / 10 sec
Cell temperature	1 sample / min
Cell pressure	1 sample / min
Cell humidity	1 sample / min
Throttle position	(triggered as required speed is obtained)
Power output (kW and hp)	(triggered as required speed is obtained)
Torque	(triggered as required speed is obtained)

Table 5.13 Recorded data streams (PXI)

In addition to the above data logging the following variables were manually observed to ensure the CRF was operating within safe limits; CRF water jacket temperature, air-to-fuel ratio with respect to stoichiometric (AFR), and exhaust gas temperature (EGT).

Water jacket temperature was visually observed to ensure that at no time a temperature of 120°C would be exceeded. It also provided a pump relay start and a parameter for testing to begin (80°C minimum).

Air-fuel ratio was monitored visually by means of a DynoJet Wide Band Commander (Dynojet Research Inc., USA). This sensor comprises a Bosch GmbH LSU4 wide band residual oxygen (Lambda) sensor and a digital display (figure 5.36). The sensor is mounted onto the exhaust pipe near the cylinder head exhaust exit and allows the sensor tip to penetrate into the exhaust gas stream.



LSU4 sensor



Sensor installed



DynoJet display

Figure 5.36 Lambda sensor installation

**Bosch (2007)** states that for SI engines using gasoline fuel a stoichiometric ratio of 14.7:1 of air-to-fuel by mass is the ideal for wide open throttle running, though generally not achievable due to incomplete combustion. The excess air factor  $\lambda$  (Lambda) is expressed as:

$$\lambda = \frac{air_{actual}}{air_{required}} \quad (5.12)$$

For intake manifold fuel delivery increasing the amount of fuel, thereby making the mixture slightly rich, has the benefit of reducing inlet charge temperature and thereby increasing charge (air) density. Ideal Lambda ratio varies for a given engine type and operating conditions. However, for maximum power  $0.85 < \lambda < 0.95$  is quoted (**Bosch, (2007)** pp 625). This corresponds to an air-fuel ratio (AFR) range of:  $12.5 < AF < 13.2$ . The CRF was found in operation to be within this range, and readings from this sensor were primarily used to ensure fuel supply consistency. A change to this would indicate operating changes outside of the in-cylinder modifications, thereby leading to inconsistent results comparisons.

An Inconel 600 sheathed K type thermocouple was inserted into the exhaust system to record exhaust gas temperatures with a Digitron 2029T (Elektron Instruments Ltd.) hand held digital thermometer. Exhaust gas temperature analysis by this method was for indication only and maintained below 900°C. Temperature, pressure, and humidity data was used to compensate recorded power as per SAE J1349 JUN90 correction factor (equation 5.13). Error is quoted as less than 0.2% for  $-10^{\circ}\text{C} > T_c > 50^{\circ}\text{C}$  not including instrumentation error.

$$\text{Dynamometer correction factor, } cf = 1.180 \left[ \left( \frac{990}{P_d} \right) \left( \frac{T_c + 273}{298} \right)^{0.5} \right] - 0.18 \quad (5.13)$$

where:  $P_d$  = the pressure of the dry air, (mb) and  $T_c$  = ambient temperature, ( $^{\circ}\text{C}$ )

Examples of resulting correction factors are given in table 5.14:

$T_c$	$P$	$\chi (\times 10^2)$	$P_{sat}$	$P_v$	$P_d$	$\rho$	$cf$
19.04	998	0.5038	22.03	11.10	986.90	0.0118	0.9921
19.08	1000	0.5025	22.08	11.10	988.90	0.0119	0.9898
19.11	1001	0.5010	22.12	11.08	989.92	0.0119	0.9887
19.13	999	0.4997	22.15	11.07	987.93	0.0119	0.9911

Table 5.14 Typical spread-sheet output to calculate correction factor

The pressure of dry air ( $P_d$ ) required for equation 5.13 is derived as follows:

$$P_{sat} = 6.1078 \cdot 10^{\frac{7.5T_K - 2048.625}{T_K - 35.85}} \quad (5.14)$$

$$P_v = \chi \cdot P_{sat} \quad (5.15)$$

$$P_d = P - P_v \quad (5.16)$$

where:

$P_{sat}$  = the saturation vapour pressure of water, (mbar)

$T_K$  = ambient temperature (K)

$\chi$  = the relative humidity

$P_v$  = vapour pressure of water vapour (mbar)

$P$  = absolute measured pressure (mbar)

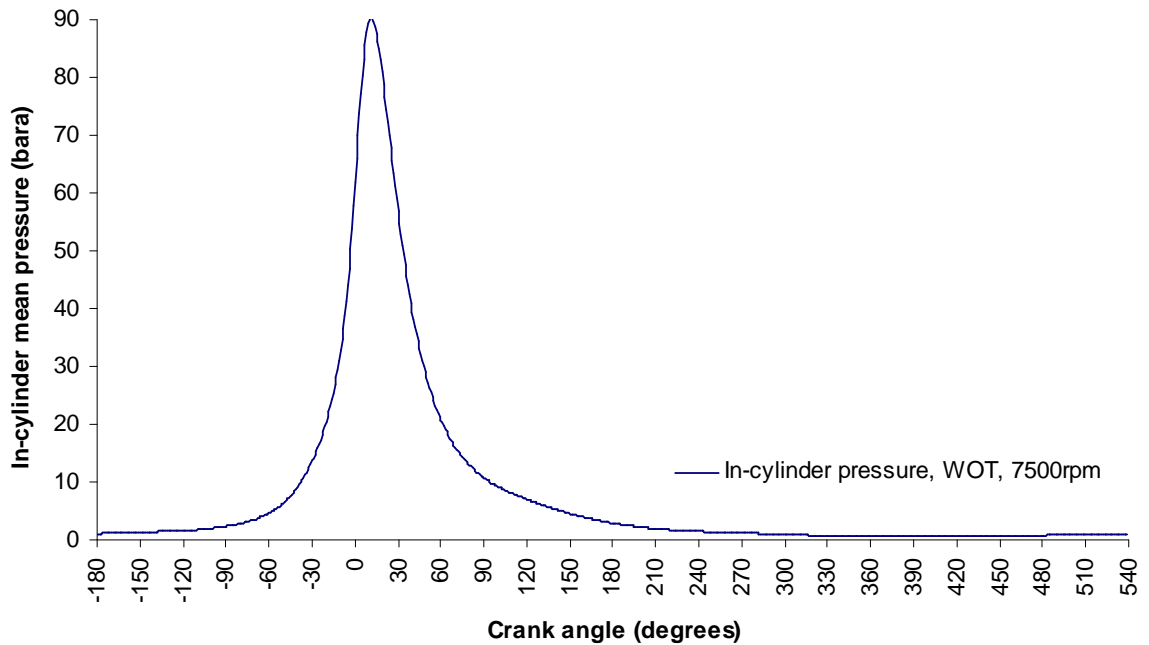


Figure 5.37 10 cycle average recorded CRF in-cylinder pressure



### 5.7.3 CRF test procedure

All testing was conducted using same grade lubricant Castrol Magnatec ACEA A3/B4, API SL/CF of viscosity recommended by the manufacturer (10W-40). BP unleaded fuel to BS EN 228:2004 was used for all tests. Testing followed a basic A-B-A-B method (table 5.15), where test A was the control set up and test B was a modified test. For 'B' tests, where the cylinder liner was changed, new rings and pistons were used. For 'A' tests the exact same components were used through to end of life, thereby reducing overall test time through a reduction of 'bedding-in' time.

Control 'A' Test (1st and 3rd builds)	'B' (new component) Test (2nd and 4th builds)
<p>N/A</p> <p>Start engine, run to 4000rpm checking status. Progressively increase load over a 10 min. period to 50% WOT maximum.</p> <p>Check water temperature reaches and maintains 80°C.</p> <p>Further bedding-in not required unless other engine component / overhaul has been conducted.</p> <p>Engine oil drained and replaced.</p> <p>Engine started by dynamometer. Proceed to 4000rpm and 50% WOT till water temperature reaches 80°C.</p> <p>WOT 'stepped' power tests recording data previously detailed at 4500, 5000, 5500, 6000, 6500, 7000, 7500, 8000, 8500 and 9000rpm load sites. Testing is ascending and each data recording step is of about 10s duration.</p> <p>One power test results in uncorrected raw torque data for each of the rpm intervals listed. Once stepped acquisition run is complete return to 4000rpm and repeat for a total of 4 times.</p> <p>Inspect recorded data for consistency (e.g. 10s sample average pull 1 @ 5000rpm vs. 10s sample average pulls 2, 3, 4 @ 5000rpm) – if results are inconsistent repeat until consistent sets achieved (discarding 1st set, 2nd set etc).</p> <p>Replace spark plug with Kistler unit and perform one-off test as above recording data. Re-replace with standard plug. This data is not part of performance data listed above.</p> <p>N.B. (oil from this control test can be re-used as build oil)</p>	<p>Components prepared, inspected, and data recorded. Engine rebuilt with new oil.</p> <p>Start engine, run to 4000rpm checking status. Progressively increase load over a 10 min. period to 50% WOT maximum.</p> <p>Check water temperature reaches and maintains 80°C over an additional 30 min. of 'bedding in'. Note all sensor streams for value as deviation may indicate fault / imminent failure.</p> <p>In the case of new liner (liner testing) or ring replacement double the shown times</p> <p>Engine oil drained and replaced.</p> <p>Engine started by dynamometer. Proceed to 4000rpm and 50% WOT till water temperature reaches 80°C.</p> <p>WOT 'stepped' power tests recording data previously detailed at 4500, 5000, 5500, 6000, 6500, 7000, 7500, 8000, 8500 and 9000rpm load sites. Testing is ascending and each data recording step is of about 10s duration.</p> <p>One power test results in uncorrected raw torque data for each of the rpm intervals listed. Once stepped acquisition run is complete return to 4000rpm and repeat for a total of 4 times.</p> <p>Inspect recorded data for consistency (e.g. 10s sample average pull 1 @ 5000rpm vs. 10s sample average pulls 2, 3, 4 @ 5000rpm) – if results are inconsistent repeat until consistent sets achieved (discarding 1st set, 2nd set etc).</p> <p>Replace spark plug with Kistler unit and perform one-off test as above recording data. Re-replace with standard plug. This data is not part of performance data listed above.</p> <p>Engine oil drained and sample collected. Component surface measurements in same physical location.</p>

Table 5.15 CRF test procedure

Corrected performance data for the four data runs is averaged at each load site. Subsequent tests with same components were similarly averaged within their own data sets. This produces corrected output curves for Test A run 1, Test B run 1, Test A run 2, and Test B run 2 (4 curves in total). If a significant difference between type A or type B performance curves is noted testing continues until stability is reached.

## 5.8 Development of motored engine tester

### 5.8.1 Discussion

Experimental testing with the CRF indicated several shortcomings. A primary instrumentation concern was the inherent vibration from a single-cylinder 4-stroke. Furthermore changes in engine friction yielded only small changes in shaft output (due to the relatively small contribution of in-cylinder mechanical to other engine losses). An assessment of overall measurement sensitivity versus a not insignificant 10% reduction in piston-bore friction (of which total in-cylinder friction is 5-10% of shaft output), would produce an indicated torque increase of only 0.5-1.0% (figure 5.38). Concerns existed that small in-cylinder frictional reductions would not be adequately resolved. A test facility with reduced vibration and increased output resolution was therefore sought.

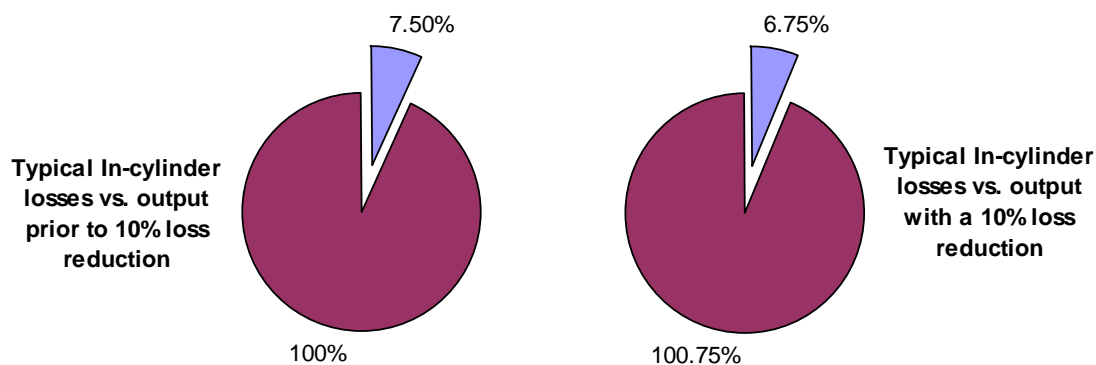


Figure 5.38 Illustration of fired engine frictional reduction resolution

### 5.8.2 Motored engine concept

Capital cost precluded the use of a full-scale multi-cylinder instrumented engine. However, from a tribological point it was necessary to ensure that representative relative velocity, lubricant rheology, applied forces, and ring gas pressures were representative of a real engine so as to ensure the prevailing regime of lubrication was maintained. Laboratory type reciprocating machines were assessed e.g. Plint TE77 (Phoenix Tribology Ltd.) as having insufficient load capability and speed range. Furthermore, laboratory slider machines do not

produce similar bulk deformation due to gas pressure, therefore not producing the same skirt-bore conformability results. On this basis a gas pressurised design was formulated, working on an air-spring principle (figure 5.39) based around an existing IC engine architecture. An existing engine would provide the required surface velocity and inertial forces as well as a proven base design. Gas pressure acting on top of the piston, if correctly configured, can replicate an in-cylinder IC engine pressures and therefore produce representative piston-bore and ring-to-bore forces. Driven by an electric motor, the predominant losses would be mechanical and almost directly indicated by reduced input torque requirement for a given rotational speed.

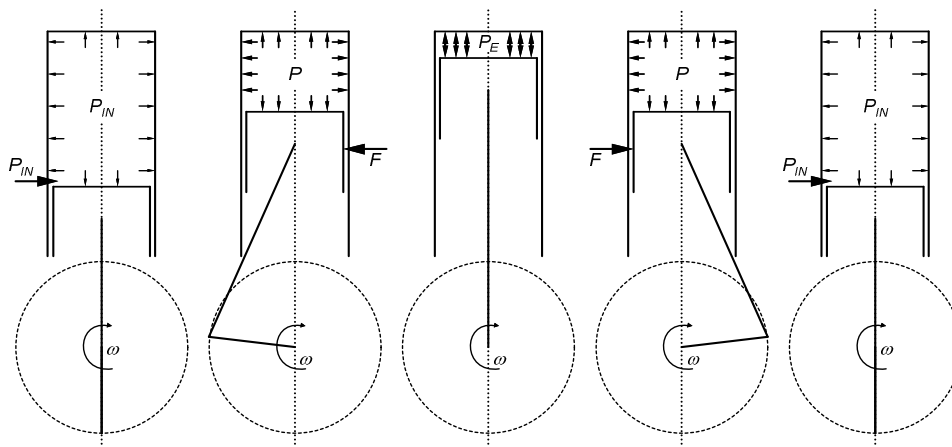


Figure 5.39 Air spring principal for pressure generation

The configuration of such a driven engine in terms of cylinder number, orientation, and crank phasing produces free forces and moments. A configuration which minimised these as much as possible was preferred. Free forces and moments up to the 2<sup>nd</sup> order are given in table 5.16:

Cylinder arrangement	1 <sup>st</sup> order free forces	2 <sup>nd</sup> order free forces	1 <sup>st</sup> order free moments	2 <sup>nd</sup> order free moments
3 cylinders in line, 3 throws	0	0	$\sqrt{3} \cdot F_1 \cdot a$	$\sqrt{3} \cdot F_2 \cdot a$
4 cylinders in line, 4 throws	0	$4 \cdot F_2$	0	0
4 cylinders flat 'boxer', 4 throws	0	0	0	$2 \cdot F_2 \cdot b$
5 cylinders in line, 5 throws	0	0	$0.449 \cdot F_1 \cdot a$	$4.98 \cdot F_2 \cdot a$
6 cylinders in line, 6 throws	0	0	0	0
6 cylinders V 90°, 3 throws	0	0	$\sqrt{3} \cdot F_1 \cdot a^2$	$\sqrt{6} \cdot F_2 \cdot a$
6 cylinders flat 'boxer', 6 throws	0	0	0	0
6 cylinders V 60°, 6 throws	0	0	$3 \cdot F_1 \cdot a/2$	$3 \cdot F_2 \cdot a/2$
8 cylinders, V 90°, 4 throws, 'X-plane'	0	0	$\sqrt{10} \cdot F_1 \cdot a^2$	0
12 cylinders V 60°, 6 throws	0	0	0	0

Table 5.16 Free forces and moments (Bosch 2007)

### 5.8.3 Choice of base motored engine

From table 5.16 the configurations with zero 1<sup>st</sup> and 2<sup>nd</sup> order free forces and moments are in-line 6-cylinder, flat boxer 6-cylinder, and 60° (V12) 12-cylinder. Utilisation of one of these configurations in effect leaves only combustion imbalance to be considered for low vibration operation. Due to the relatively long length of in-line 6 cylinder and V12 engines bore spacing is generally close to the bore size, leaving minimal space for alterations and instrumentation. For this reason a flat-6 cylinder engine was chosen as a base part.

A flat-6 engine manufactured by Porsche AG was chosen due to its relative simplicity in air-cooled form (no water cooling). The exact model was a 1992 911 (964) Carrera RS engine type M64/03 as per table 5.17:

Engine Designation	M64/03
Layout / type	6 cylinder 'Boxer', normally aspirated
Displacement	3600cm <sup>3</sup>
Bore [turbo]	100mm [100mm]
Stroke	76.4mm
Rod length	127mm
Bore spacing	118mm
Compression ratio	11.3:1
Max engine power	191kW (EC 80/1269)
Max torque [turbo]	325Nm (EC 80/1269) [520Nm]
Max engine speed	6720rpm
Cooling	Air / oil cooled
Lubrication	Dry sump with piston cooling jets
Crankshaft	Forged, 8 main bearings
Block construction	Vertically split light alloy crank-case with individual cylinder barrels

Table 5.17 Motored engine details

The M64 engine is 'over-square', as is often typical with flat IC engine applications. The standard bore / stroke ratio was 1.309 and it was decided to reduce bore / stroke to be more representative of mass-market gasoline automotive engines (typically 'square'). A reduction in bore size would also reduce overall crank loading as well.

The M64 crankshaft features 6 individual journals, and in the case of pseudo-2-stroke operation (chapter 5.8.2 'air spring') journal shear stress is approximately twice that of a 4-

stroke with similar piston force. The same crankshaft is also used within the M64/50 turbocharged engine, providing an indication of journal strength based on engine torque (table 5.17):

$$2 \cdot T_{NA} \cdot D_2^2 \leq T_T \cdot D_1^2 \quad (5.16a)$$

$$D_2 \leq \left( \frac{T_T \cdot D_1^2}{2 \cdot T_{NA}} \right)^{\frac{1}{2}} \quad (5.16b)$$

Where  $T_{NA}$  and  $T_T$  are the peak quoted torques for the normally aspirated and turbocharged versions respectively,  $D_1$  and  $D_2$  are the turbocharged bore size and new bore size respectively. This effectively limits the bore size to 89mm or less. A bore size of 86mm was chosen, resulting in a bore / stroke ratio of 1.126. Lastly, the use of a flat-6 configuration does allow cylinder de-coupling to provide flat-4 and flat-2 configurations, the latter enabling transient torque to be investigated.

#### 5.8.4 Development of representative in-cylinder pressure and side force

Figure 5.37 provides a reference cylinder pressure. If the working medium within the air-spring motored engine ‘ASME’ (5.8.2) is assumed to be an ideal gas and isothermal in operation, then the in-cylinder pressure  $P_{CYL}$  is simply calculated by the rearranged ideal gas law:

$$P_{CYL} = \frac{P_{IN}}{\left( \frac{V_{CYL}}{V_{IN}} \right)} \quad \text{where } P_{IN} \text{ is the pressure at BDC where the cylinder volume is } V_{IN}.$$

The ASME was configured to produce representative in-cylinder pressure and side force by means of introducing pressurised air at the BDC and modifying the operational compression ratio to suit. Figures 5.40 and 5.41 depict the in-cylinder pressure and the resulting side force  $F_N$  due to gas pressure alone for the ASME compared with the CRF. The ASME configuration in figures 5.40 and 5.41 is a  $P_{IN}$  of 10.0barg with a compression ratio of 9.5:1, facilitated by the introduction of compressed air at BDC and physical modification of cylinder head volume / piston compression height respectively. Modification of these two parameters allows for a reasonable correlation of in-cylinder combustion pressures for the expansion portion of the

cycle, not only for the CRF case but also for others. The reduction of  $P_{IN}$  logically provides reduced in-cylinder pressure and side force, allowing part-throttle performance evaluation.

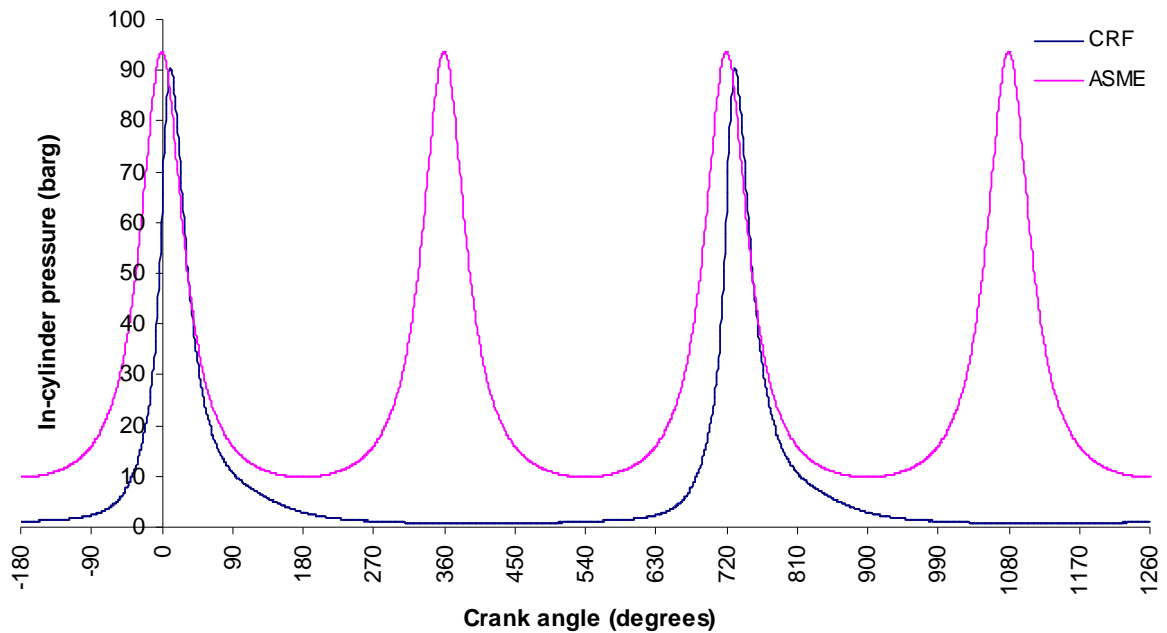


Figure 5.40 In-cylinder pressure CRF vs. ASME

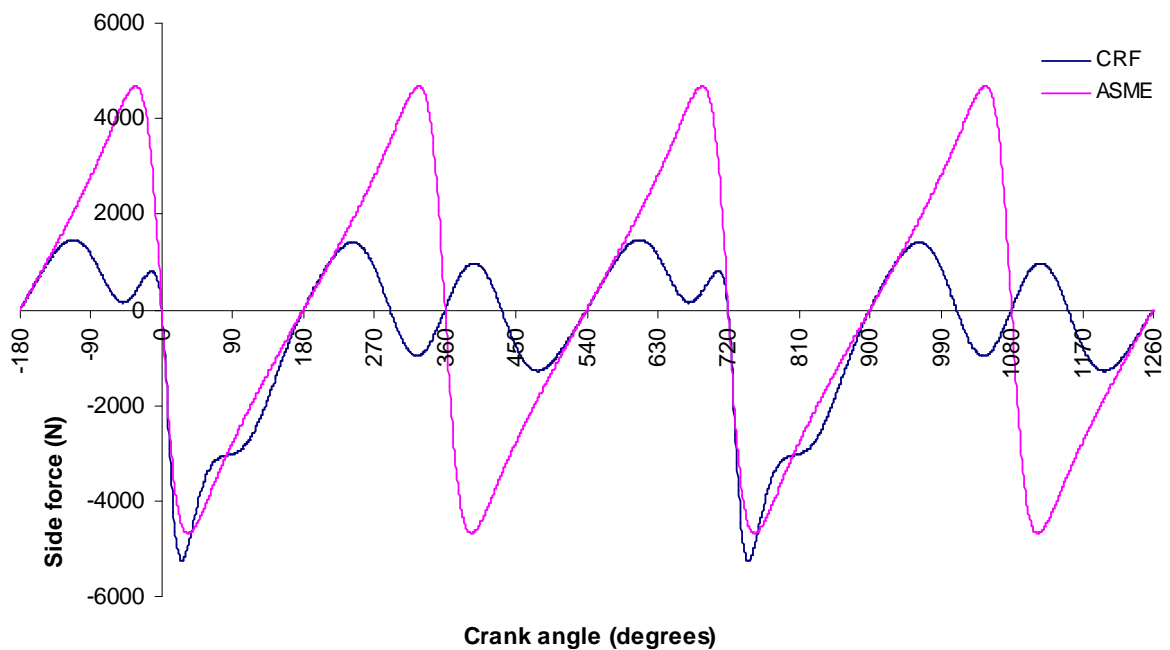


Figure 5.41 Side force due to gas pressure CRF vs. ASME

From figure 5.40 it can clearly be seen that the ASME is operating in the 2-stroke mode ( $360^\circ$  periodicity), whilst reasonably representing the CRF combustion pressure curve just after

combustion. The pressures in other areas of the cycle are generally higher and symmetrical around TDC. Overall the ASME has a higher average side force per cylinder, 2447.0N vs. 1236.1N (1.98:1).

With 6 cylinders compared with a single-cylinder (e.g. CRF), the total side force is some 11.88 (~12) times higher than in the single-cylinder case.

### 5.8.5 Calculation of crank-shaft torque due to gas pressure

For satisfactory operation it is necessary to evaluate the impact on crankshaft torque due to gas pressure (figure 5.40). From chapter 3.2 the total force  $f_g$  decomposes into  $f_{con}$  along the rod axis and  $f_r$  towards the cylinder wall (skirt direction).

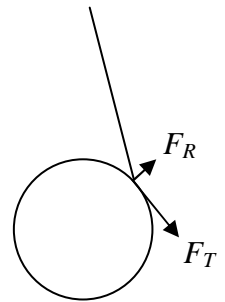
$$f_{con} = f_g \frac{1}{\cos \phi} \quad (5.17)$$

$$f_r = f_g \tan \phi \quad (5.18)$$

The force transmitted by the connecting rod  $f_{con}$  decomposes at the big end articulation point into tangential ( $F_T$ ) and radial ( $F_R$ ) components as:

$$F_T = f_{con} \sin(\theta + \phi) = f_g \frac{\sin(\theta + \phi)}{\cos \phi} \quad (5.19)$$

$$\text{Resulting in torque (T): } T = rF_T \quad (5.20)$$



From figure 5.42 the inclusion of an additional 2 cylinder pairs (6 cylinders vs. 2 cylinders) reduces peak torque. However, the level of attenuation is such that three distinct torque swings of circa  $\pm 1\text{kNm}$ . In consideration of this, it was decided to retain the M64 flywheel to aid smooth operation.

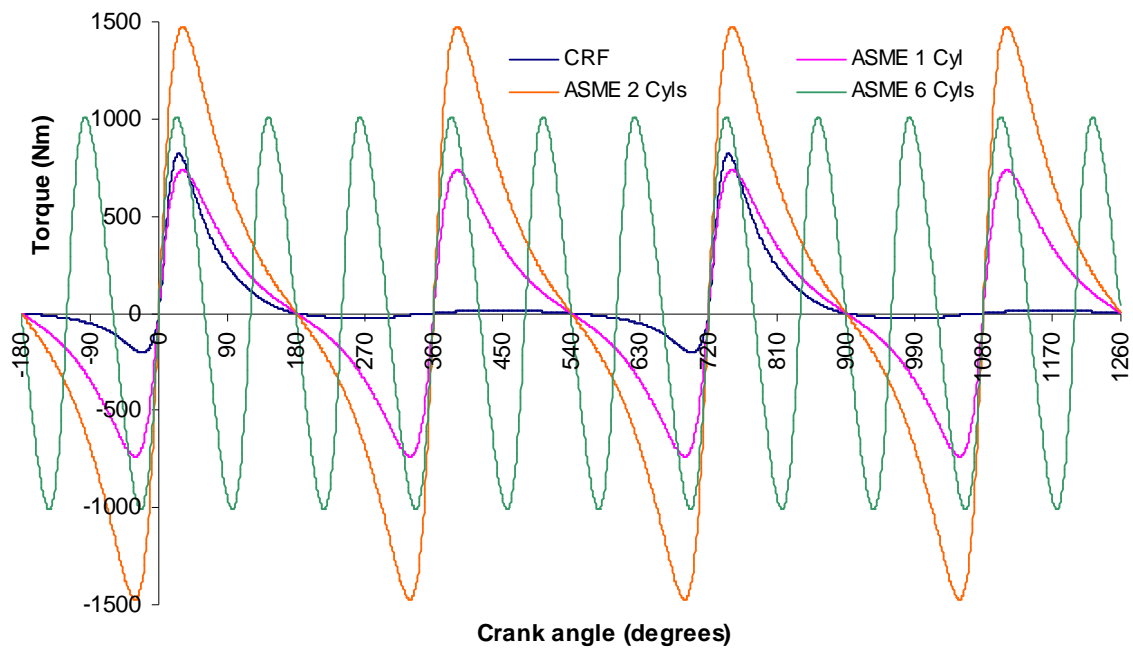
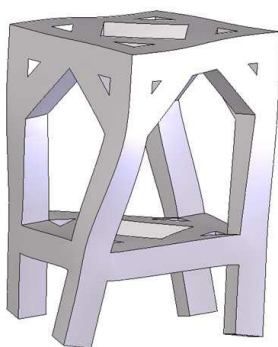


Figure 5.42 Contribution to crank torque due to gas pressure

### 5.8.6 Development of an air-spring motored engine

From the original M64/03 engine only the engine cases, shell bearings, crankshaft, and bolting hardware were retained. Table 5.16 shows no free 1<sup>st</sup> and 2<sup>nd</sup> order forces and moments due to inertia. However figure 5.42 depicts a strong forcing frequency of  $\frac{3 \cdot rpm}{60}$  Hz. Maximum operational rpm (table 5.17) is 6720rpm, equating to a forcing frequency of 336Hz. A stable platform (mounting base) (figures 5.43, 5.44 item B) was required and modal analysis was undertaken with a resulting first resonant frequency (ignoring rigid body modes) of 20% higher than 336Hz.



Mode No.	Frequency ( $\omega$ )	Frequency (Hz)	Period (s)
1	0	0	1.000000033e+032
2	0	0	1.000000033e+032
3	0.001149782096	0.0001829935063	5464.674805
4	0.005670078099	0.0009024209576	1108.130249
5	0.008422283456	0.001340448041	746.0192261
6	0.009673342109	0.001539560268	649.5361328
7	2546.661133	405.3136902	0.00246722484
8	2956.908936	470.6066589	0.002124916762

Figure 5.43 ASME base frame and modal analysis results



Machine mounts (Fabreeka, VSC2-15-C-S-M10) with a critical frequency range of 23-28Hz (460-560rpm equivalent) were attached to the frame top to allow the engine assembly to be attached (figure 5.44 item A).



Figure 5.44 ASME test rig key components

The M64 crank-cases featured integral flow shut-off for six piston oil cooling jets during low-speed running. This was not required and, therefore removed, as was the in-sump scavenge pump. Modifications to the casing lubrication circuit produced a relatively simple system (figure 5.45).

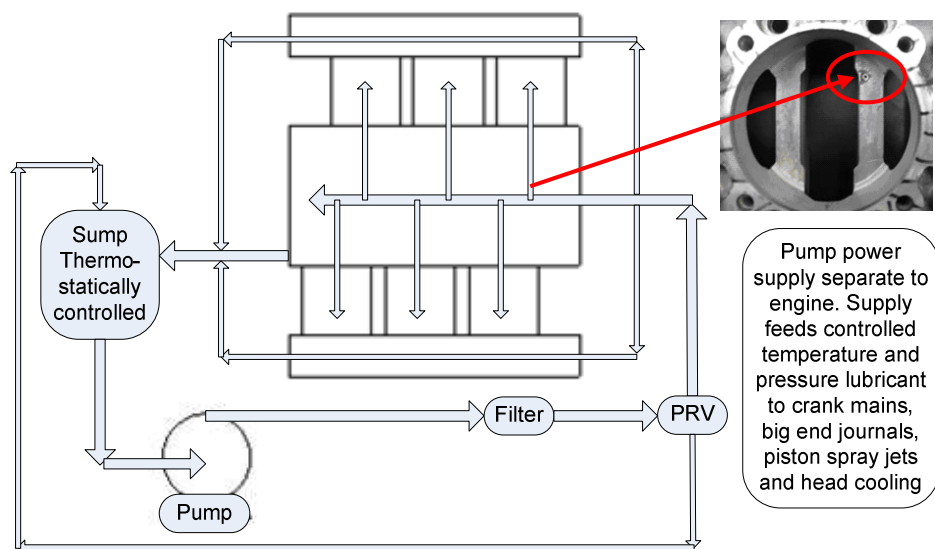


Figure 5.45 ASME test rig lubrication system schematic diagram

An external temperature-controlled sump tank gravity feeds a 0.75kW 3-phase gear pump (Tuthill Corp., USA model 1012). A gear pump was chosen as these are recognised as having low delivery pulsation and minimal variation in volume delivery per revolution over a wide range of fluid viscosity (**Bolegoh, (2001)**).

The gear pump (figure 5.44 item C) features a preset internal pressure relief set at 7barg with a rated delivery of  $14.55\text{lmin}^{-1}$  at 3.45barg. A full-flow 50 micron screen oil filter is placed downstream of the pump ahead of a pressure-reducing valve with an over-pressure return back to the external sump. Controlled pressure and temperature lubricant is delivered to the M64 crankcase main oil gallery, with secondary feeds for cylinder head cooling (figures 5.45, 5.44 item D).

Lubricant entering the crankcase main gallery provides lubrication to the crankshaft main bearings, and by means of internal crank oil passage drillings, ultimately the big end journals. Both of these bearings are of the plain shell type.

Lubricant also exits through 6 piston cooling jets (PCJ) These orifices are arranged so as to direct lubricant onto the upper portion of the piston / connecting rod assembly (figure 5.45). In operation lubricant drains into the lower portion of the crankcase and is returned, along with the cooling stream provided to the cylinder heads, back to the external sump.

The sump oil is temperature-controlled through an external loop, with indirect heat exchange within a Regoplas chiller unit (figure 5.46).


	Supplier	Regoplas, Switzerland
	Model	RC2E30/Z
	Cooling capacity	28.0kW
	Refrigerant	R407C
	Efficiency (COP)	5.1
	Compressor power	5.5kW
	Fan flow rate	$15500\text{m}^3/\text{hr}$
	Pump flow rate @3barg	$80\text{lmin}^{-1}$
	Operating voltage	400V/50Hz
	Power consumption	<11.9kW

Figure 5.46 Specification of sump cooling system

The pressurised air requirement detailed in section 5.8.4 requires controlled air pressure of up to 10barg to be entered into the cylinder at the BDC position. Shop air was below this pressure

and measured to vary between 5.4 and 7.3 barg. Mass flow of the available air was however high, allowing the use of an air amplifier as opposed to a dedicated high pressure compressor installation. An SMC VBA4100 booster regulator was specified, as the air amplifier uses an existing air supply to produce compressed air at up to twice supply pressure (SMC Corporation, Japan). The air preparation circuit used is shown in figure 5.47 (LHS), detailing the use of a high pressure storage chamber and a secondary lower pressure pre-delivery chamber (cascade system).

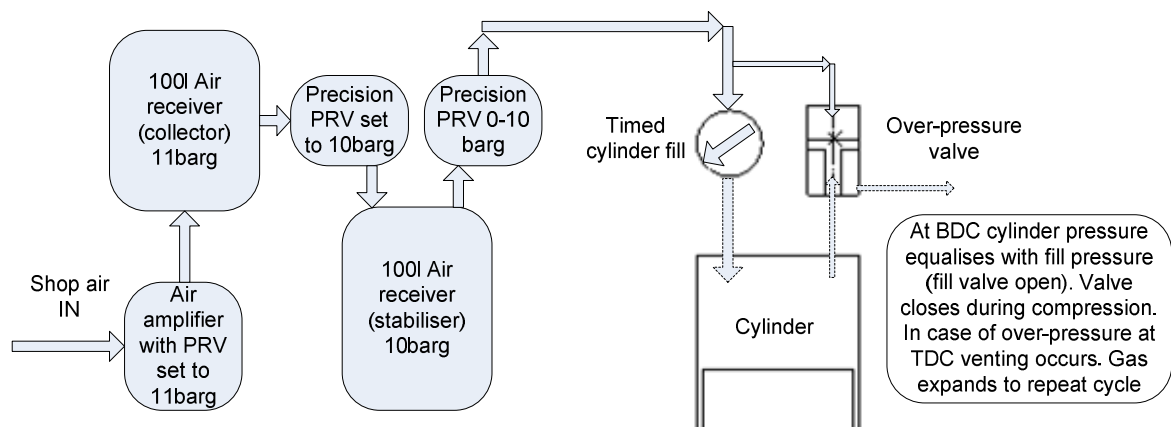


Figure 5.47 ASME pneumatic supply and in-cylinder control schematic

The method to provide in-cylinder compressed air is by means of timed delivery at the BDC. Referring to figure 5.47 compressed air with controlled pressure is introduced by means of a ‘timed cylinder fill’ control valve. A rotary method of operation was chosen, where a hollow rotating shaft (one per bank of 3 cylinders, supported on rolling element bearings) was maintained at the operating pressure required. Along the length of each shaft 3 holes were drilled at 120° phase separation in a linear position corresponding to the individual cylinder centre position. These shafts rotated within specially fabricated cylinder heads with through holes in the cylinder centre position. As each shaft rotates there is only one position (BDC) where the hole in the cylinder head is in line with the through hole in the hollow shaft (figure 5.48).

Over-pressurisation and protection from in-cylinder lubricant ingress was made by means of an air-over-air pressure relief system (figures 5.47, 5.49). This system provided a mechanism to de-pressurise each cylinder to atmospheric at start up, as well as providing a safe route to vent excess gas pressure (e.g. PRV failure) or guard against lubricant ingress (extended running / ring failure).

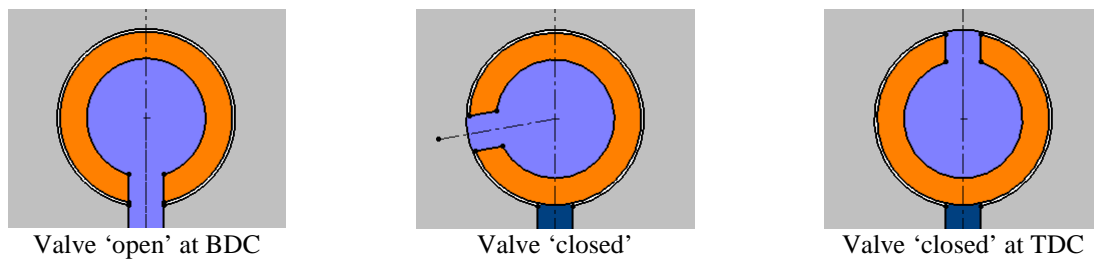


Figure 5.48 Rotary valve operation

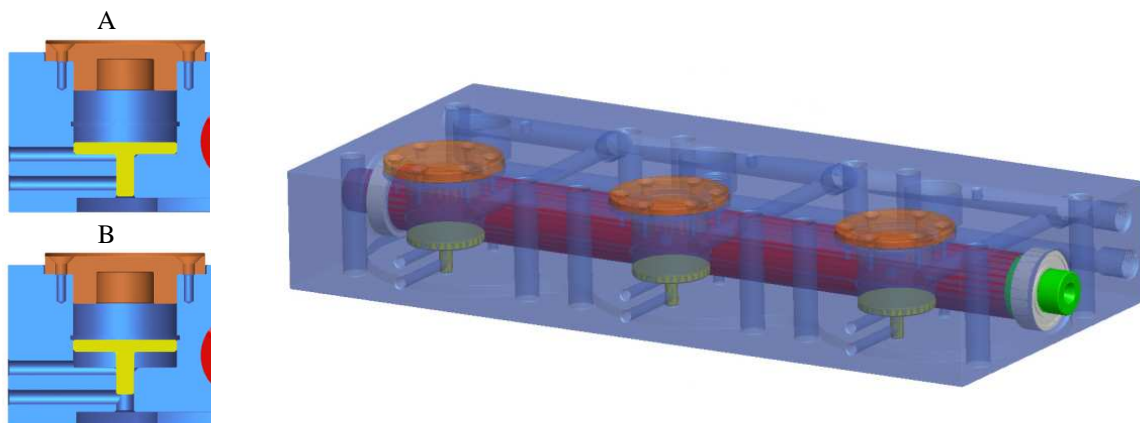


Figure 5.49 Over-pressurisation valve and cylinder head cut-away

From figure 5.49 the over-pressurisation valve is typically in position 'A', effectively restricting gas exchange between the working chamber below and atmosphere. The upper portion of the valve is pressurised with gas at pressure  $P_{IN}$  and has a surface area ratio, when compared with the lower plunger, in excess of the compression ratio. This effectively ensures the valve remains closed in normal operation. 'B' details the case of over-pressurisation, providing a fluid exit stream to atmosphere. The replacement cylinder head was constructed from AA6082-T6 (Table 5.18), featuring internal pneumatic and oil cooling lines. Valve components were manufactured from C86700 manganese bronze due to recommended suitability (**ASM Handbook (1992)** Vol. 2, 1992, p. 370) for valve applications and closely matched thermal expansion.

Drive power requirements were simply estimated by means of base engine frictional losses due to the piston assembly (section 5.8.1, 5-10% of the shaft output power). Engine power was measured by means of a dynamometer (figure 5.50, courtesy of Ninemeister Ltd.) to be

approximately 279Hp (208.1kW). Using the mid-to-upper 7.5-10% estimation for piston assembly frictional losses, an electric drive of 15.1-21kW was required

Elemental Analysis alloy AA6082											
	Si	Fe	Cu	Mn	Mg	Cr	Zn	Ti	Other	Others	Bal
Min wt. %	0.7	-	-	0.4	0.6	-	-	-	0	0	Al
Max wt. %	1.3	0.5	0.1	1.0	1.2	0.25	0.2	0.1	0.05	0.15	Al
Elemental Analysis alloy C86700 (Manganese Bronze)											
	Cu	Al	Pb	Mn	Ni	Sn	-	-	-	-	Bal
Min wt. %	55.0	1.0	0.5	1.0	-	-	-	-	-	-	Zn
Max wt. %	60.0	3.0	1.5	3.5	1.0	1.5	-	-	-	-	Zn
Selected properties AA6082						Selected properties C86700					
C.T.E., 20-200°C			24µm/m			C.T.E., 20-200°C			19µm/m		
Elastic modulus			70GPa (tension)			Elastic modulus			105GPa (tension)		
Tensile strength			310MPa (T6)			Tensile strength			585MPa (M01)		
Yield Strength			260MPa (T6, 0.2%)			Yield Strength			295MPa (M01, 0.2%)		

Table 5.18 Material properties, ASME cylinder heads

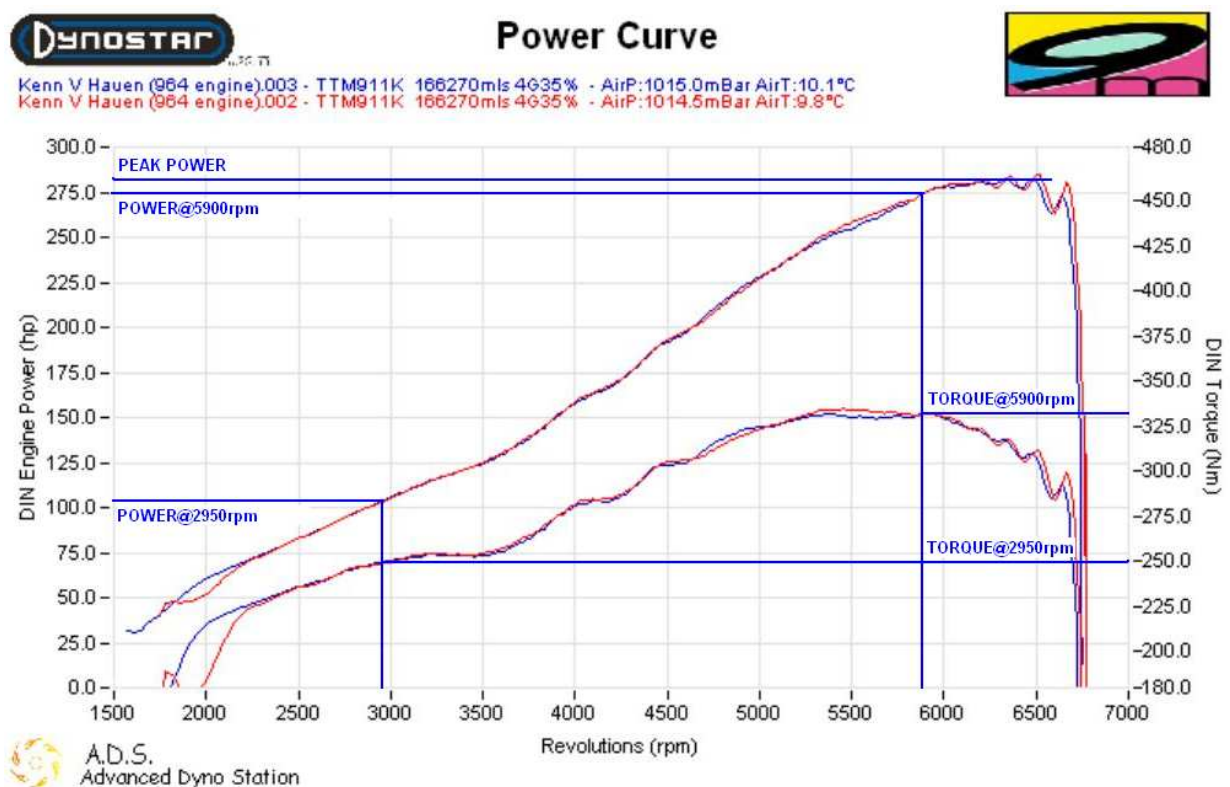


Figure 5.50 ASME 964 base engine dynamometer results (WOT)

An 18.5kW Parker (Parker Hannifin, USA) 690+ inverter drive unit was paired with an ABB Ltd. (Switzerland) 18.5kW 2-pole electric motor as in figure 5.44. To ensure stable driven speed the encoder feedback was provided from the electric motor to the drive unit, providing closed loop operation (Figure 5.44 item E).

Native speed of the ABB motor was 2950rpm. Due to the effective 2-stroke operation frictional up-scaling estimated in section 5.8.4 was a ratio of 1.98, which dictated two gear ratios to be accommodated. From figure 5.50 a 2:1 upscale in motor speed would result in a crankshaft speed close to the actual engine peak power speed (5900rpm vs. 6100rpm). A 1:1 drive would result in a maximum crank-shaft speed of 2950rpm, with the reduction in speed compensating for the frictional up-scaling ( $2 \approx 1.98$ ).

Figure 5.44 item F details the belt drive arrangement employed. Torque from the base-mounted motor is transferred through an Eriks 30mm wide 8mm pitch toothed belt. Differing combinations of pulley diameters and belt lengths maintained belt centre-centre length whilst providing the two required maximum speeds of operation. Speeds between start up and the maximum speeds (2950rpm and 5900rpm) were by means of operational controls on the Parker inverter drive unit.

Compression ratio and bore size changes necessitated the development of replacement in-cylinder components. Methods detailed in chapters 5.3.1-5.3.2 were utilised again. However, several additional changes were made. The connecting rods were replaced with ones constructed from AISI 4330V. (Carrillo Industries, CA). The original finned aluminium cast alloy barrels were substituted for forged AA2618 (Table 5.4) units with 102mm nominal bore size, with secondary liners of 102mm outside diameter and 86mm nominal internal bore size inserted inside. Piston clearances were reduced due to the semi-isothermal mode of operation. The resulting components are shown in figure 5.44 (items F, RHS).

Calibration of in-cylinder pressure was by means of an in-cylinder pressure transducer detailed in section 5.7.2. Access for the Kistler pressure transducer is through 3 ports in the cylinder head (figure 5.44 item G).

## Chapter 6

### Experimental results

#### 6.1 Oil film thickness results

Oil film thickness was measured (fig 6.1) as detailed in chapter 5 for the CR450F engine. Further details are as per **Dwyer-Joyce, Green, Balakrishnan, Harper, Lewis, Howell-Smith, King, Rahnejat, (2006)**.

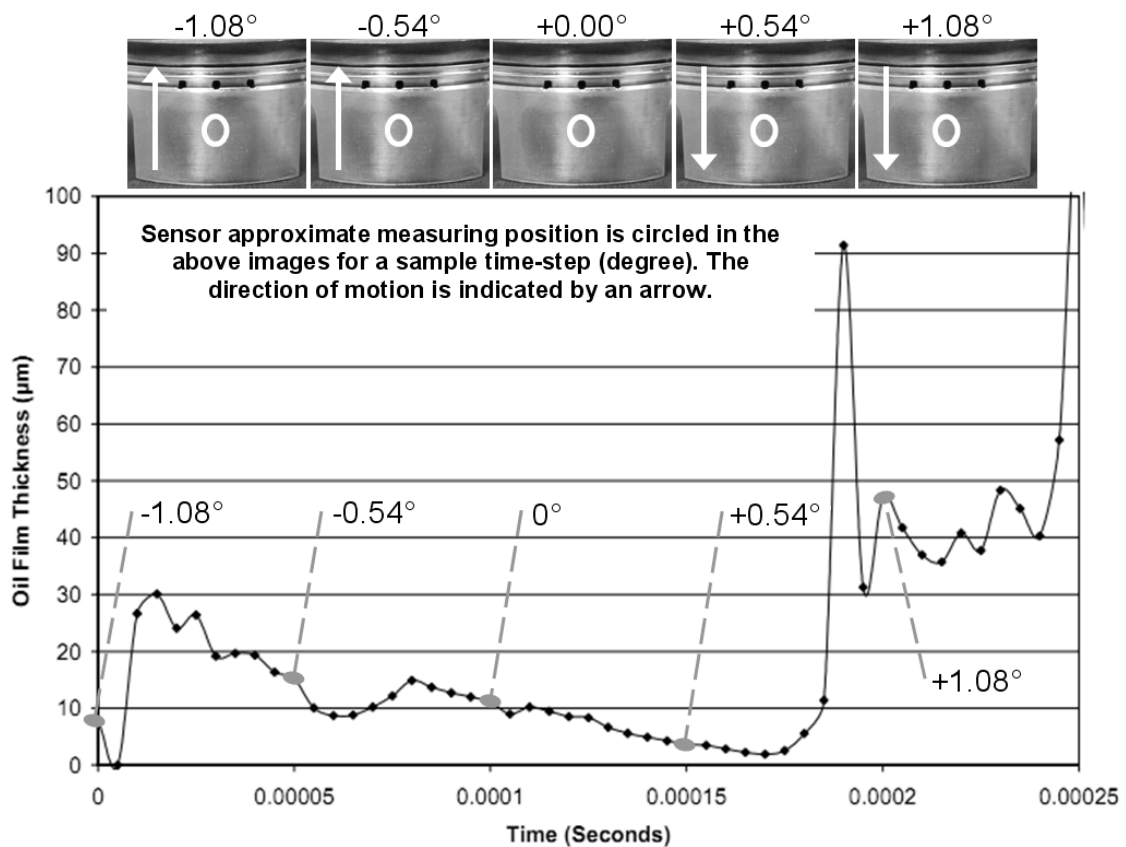


Figure 6.1 in-cylinder film thickness measurement (1,800rpm)

#### 6.2 Cylinder bore experimental results

As already mentioned in chapters 2 and 5, coating and texturing of contacting surfaces can improve the tribological performance of a conjunction. Additionally, material of construction also plays an important role influencing the available gap for film formation to occur.

As described later in chapter 7, both the piston and the liner are subject to thermo-mechanical distortion. Furthermore, surface finish of the contiguous surfaces is an important factor in the



prevailing regime of lubrication, and dependent on the material of construction, the use of coatings, and surface modifications. To ascertain the effect of these parameters, engine testing with different liner and piston derivatives was undertaken as part of a benchmarking exercise. Such an exercise was focused on:

- Surface finish
- Bore (liner) material of construction.
- Bore surface (coating)
- Localised etching / surface roughening

A baseline standard liner (L2017-LINER-C) made of eutectic aluminium alloy grade AA4988 (table 5.4) was used. This liner and all tested derivatives were cross-hatch honed as described in chapter 5.3.1. The surface roughness of the baseline liner is 0.2-0.3 $\mu\text{m}$   $R_a$ . Two other liners with different materials of construction were benchmarked against this standard liner.

The first variation was a 1CB15B cast iron liner (L2017-LINER-G) which was plateau honed to nominal 0.3-0.4 $\mu\text{m}$   $R_a$ . Cast iron was used because it is the traditional material for cylinder liners and therefore also produces a logical comparison for results reported in literature. Figure 5.14 shows that in the cold condition a cast iron liner typically features a larger running clearance than an aluminium liner. However due to the low thermal expansion of cast iron, thinner conjunctions often result when the engine is operating at high temperature. High-temperature operation further affects the lubricant viscosity and therefore the film thickness within the conjunctions.

The second liner variation, L2017-LINER-A (figure 5.5) was constructed from a low silicon, aluminium-copper alloy AA2618 (table 5.4). This part being surface coated on the working bore surface with electrolytic Ni-SiC (chapter 5.3.1), and then subsequently honed with a resulting surface finish of 0.2-0.3 $\mu\text{m}$   $R_a$ .

The derivative parts along with the baseline wet liner were all tested on the CRF single cylinder engine (chapter 5). Component performance was assessed by means of measuring dynamometer resisting torque for a given test rpm. This measured torque was converted into uncorrected power (chapter 5.7.2) and ultimately corrected power after atmospheric compensation. Baseline testing was conducted at the beginning and interspersed with



component derivative tests as per table 5.15. The derivative results were divided by those of the baseline for each rpm load site resulting in a percentage gain or loss comparison (equation 6.1).

$$\text{Percentage power differential} = \left[ 100 \frac{T_{\text{derivative}}}{T_{\text{baseline}}} \right]_{\text{rpm}} \quad (6.1)$$

The percentage performance deviation for different wet liners constructed from differing materials is given in figure 6.2.

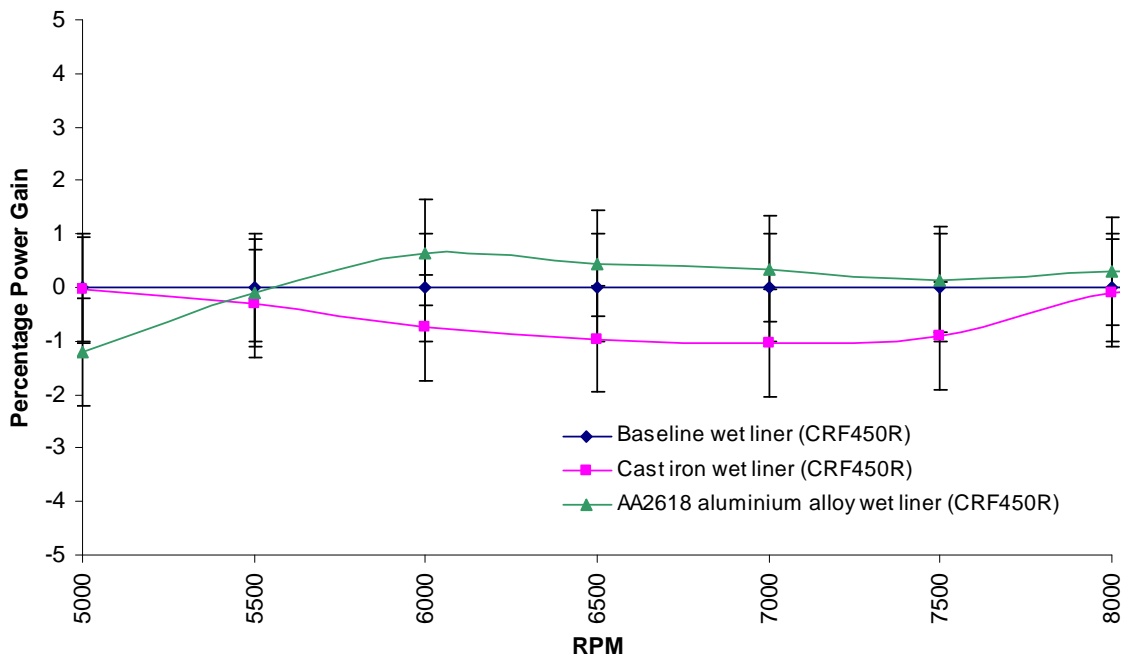


Figure 6.2 AA2618 and cast iron liner types vs. baseline wet liner

It can be seen from figure 6.2 that the cast iron liner performs consistently worse than the baseline liner, whilst the opposite is generally true for the AA2618 aluminium alloy variant. Aluminium and its alloys typically have far higher thermal conductivity and expansion than ferrous materials including cast irons. Therefore one conclusion that can be drawn from this result is that generated conjunctional heat is conducted through the cylinder wall more readily in the aluminium cases, hence reducing the temperature of the fluid film on the cylinder surface. Furthermore, due to increased thermal expansion in the aluminium alloy cases, average separation between conjunctional bodies increases (increased gap). In combination these phenomena result in a thicker, higher viscosity film between the piston and cylinder liner

wall. Generally thicker, higher viscosity films have increased load carrying capacity and a reduced likelihood of asperity interaction.

Surface interactions do still take place in the piston skirt – cylinder bore conjunction. For much of the expansion (power) stroke, particularly at high combustion pressures and during reversals, one would expect mixed or boundary regimes of lubrication. It is also often the case that a coherent meniscus is not attained to supply the conjunction. Therefore, to limit component wear, hard wear-resistant coatings are often used. In preparation for hard surface coating, smoother substrate surfaces are often required.

Smoother surfaces generally assist required cleaning processes and prevent the hard coating cracking due to residual stress. Hard coatings (with a higher modulus than the substrate material) retain the sub-surface stress field, thereby protecting the substrate from their (crack) inward propagation. A major drawback with high elastic modulus coatings is a greatly reduced tendency to locally deform within the conjunction, thus minimising the occurrence of EHL. Nevertheless, for the piston skirt, the global (bulk) deformation accounts for the main gap generating mechanism (chapter 7.5).

Tests were conducted with differing internal bore coatings. The results are benchmarked against the aforementioned baseline liner as in the previous tests. Note that the baseline liner is Ni-SiC coated (figure 5.6). The other tested liner L2017-LINER-B was Diamond-Like Carbon (DLC) coated with a coating thickness of approximately  $2\mu\text{m}$ , and surface roughness of  $R_a$  of  $0.04\text{--}0.06\mu\text{m}$  (chapter 5.3.1). This is a much smoother surface than the baseline liner. Figure 6.3 shows the relative performance of this smooth DLC coated component vs. the baseline Ni-SiC part. Note that the DLC coated liner produces inferior power than the baseline liner irrespective of its enhanced surface finish for lower engine speeds. The performance of the two liners merges at higher engine speeds.

The relatively poor performance of the DLC-treated component can be explained as being due to lower retained lubricant (due to the smoother surfaces) within the conjunction. At, or close to, the stroke reversal positions a boundary regime of lubrication is expected with asperity interaction, as previously discussed. An increase in adhesive friction occurs due to the large quantity of low amplitude, broad asperities found in smooth surfaces such as the smooth, DLC-coated bore surface. It should be noted that the DLC-coated liner is only honed prior to

the coating process, not post-coating. This creates a very fine cross-hatched structure with quite shallow grooves and therefore relatively low lubricant-carrying capacity (refer table 5.5 parameter  $R_{vk}$ ). Process limitations in DLC deposition require the use of such a fine finish and, due to high deposited hardness, effectively prevents post-process honing. Therefore, Ni-SiC without these surface finish limitations performs better, as one would expect.

DLC does however have a reduced possibility of scuffing in operation. This can provide additional benefits, though the main reason for choosing it is the protection of substrate material at high pressures. Such applications are more prevalent in cam-tappet contact at high speed and high load than in the piston skirt – bore conjunction.

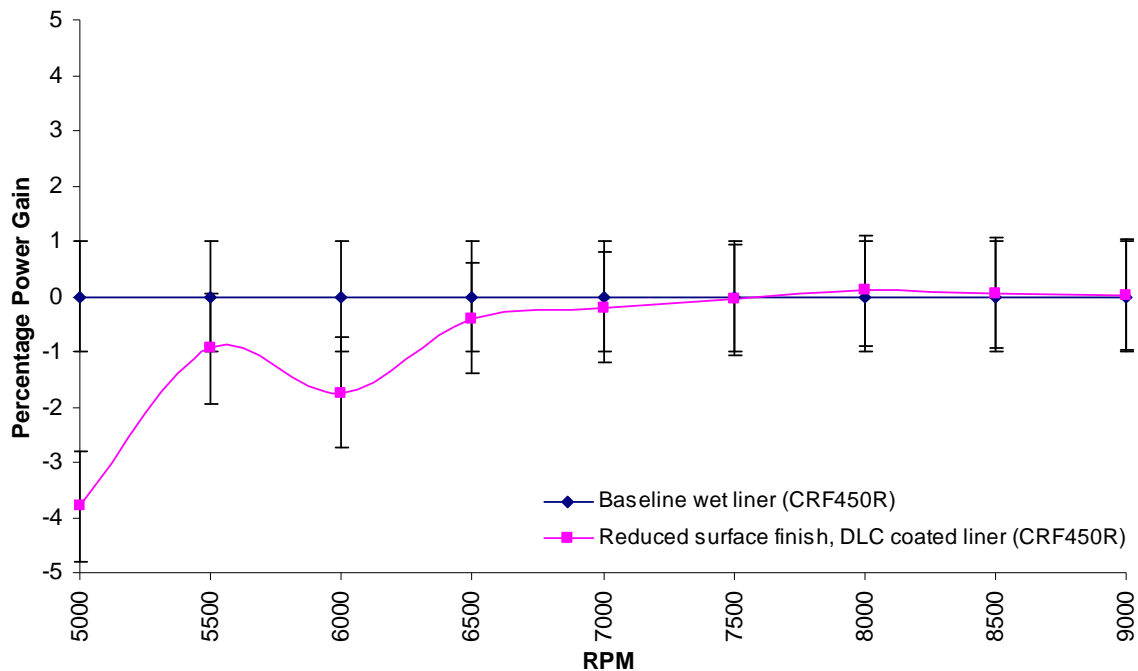


Figure 6.3 A DLC coated liner vs. baseline wet liner

These results are consistent with the expectation that some degree of surface roughening introduces lubricant reservoirs and leads to the micro-wedge effect (see chapter 2). To investigate this, a series of liners were textured and benchmarked against the baseline component.

Figure 6.4 shows the relative performance of liner L2017-LINER-D constructed from the same 4988 alloy as the standard (baseline) liner but with a surface finish 1/5th that of the baseline part (0.04-0.06 vs. 0.2-0.3  $\mu\text{m}$  Ra). Also included in the figure is the same smooth

finished liner, but with laser surface texturing as shown in figure 5.25. The location of the texturing is such that the compression ring working face is coincident upon the etched bore surface at and just below the TDC position. The reasoning for the choice of etched feature geometry / form is provided later in this chapter.

From figure 6.4 one can observe that improving surface finish by a factor of 5 on the Ra value results in improved power output. A power increase of 1-2% for engine speeds in excess of 7000rpm results and somewhat less, though still positive, down to 6000rpm. At even lower rpm speeds the performance of the liner with improved surface roughness (no etching) deteriorates in comparison to the rougher baseline liner. The interpretation here is that thinner films are generated at lower speeds and when mixed and boundary regimes of lubrication occur (for instance at or in the vicinity of the reversals) where there is increased adhesion for smoother surfaces. This surface interaction is far reduced at higher speeds of entraining motion.

In contrast, when laser surface texturing is employed the improvement is mostly noted at the lower engine speeds, with up to 4% improvement in power at 5000rpm relative to the baseline liner. Thereafter, the percentage improvement in power reduces to the extent that at speeds in excess of 6500rpm the non-textured liner with similar surface finish shows better output power. This suggests that whilst the laser-etched grooves retain lubricant their presence may also lead to increased viscous friction, where an excess supply of lubricant entrains into the ring pack and the skirt conjunctions after reversal. A thicker film can also affect sealing performance of the ring elements, resulting in loss of power as well as blow-by. In fact field experience using the same texturing form on engines operating at higher speeds, such as in NASCAR, (usually in excess of 9000rpm) indicated increased oil loss at high speeds (**ECR (2008)**).

Therefore, whilst surface texturing has been found to aid lubrication and reduce friction in an assortment of conjunctions (see chapter 2), texture optimisation in terms of form (dimples, grooves, indentations, etc), size (feature depth, height, shape, pattern, etc) and distribution are important. Furthermore the control and repeatability of processing these textures is also of importance as this can pose some problems as discussed in section 5.4.2. **Rahmani et al (2010)** discuss various features and the optimisation process.

Figure 6.4 Effects of improved surface roughness and laser texturing

Figure 6.5 is the inlet part of the isobar chart shown in figure 7.5 (chapter 7). The pattern of lubricant flow into the conjunction is shown by black arrows on the figure. It can be seen that the horizontal arrows ahead of the conjunction (LHS) flow outwards and around the island of high pressure where the piston skirt relief radius commences. The discontinuous nature of the skirt profile causes a pressure spike. The curved arrows on the top and bottom of the figure are drawn for visualisation purposes to clarify the overall trend of lubricant flow. Thus only a small portion of flow actually enters the contact proper as shown in the figure. The remainder of flow is directed outward and around the contact. The flow in the contact also avoids the other pressure spike at the outlet (see figure 7.5) as shown by **Balakrishnan, Howell-Smith and Rahnejat (2005)**. Hence, corresponding thin films occur in the areas of pressure spikes as well as in the contact proper.

In chapter 7 a case of diamond-turned piston skirts is analysed, showing significant improvement in the retained film of lubricant in the contact. This surface modification encourages greater inward-bound flow of lubricant. Two approaches were undertaken to encourage this behaviour, due to modifications of the cylinder bore surface. One was to create dimples through physical indentation to retain a reservoir of lubricant as well as encourage micro-wedge effect. The other method employed was to introduce curved laser etchings at the top dead centre in order to inhibit the flow of lubricant outwards from the contact region.

The results of analysis reported by **Balakrishnan, Howell-Smith and Rahnejat (2005)** indicated significant improvements in lubricant film thickness for the compression ring to cylinder liner conjunction for the laser pattern in figure 5.25 (chapter 5). The pattern lends itself to laser ablation where beam steering is available (chapter 5.4.2). The consecutive rows of inward and outward curved features inhibit outward lubricant flow during reversal of the ring as well as encouraging micro-wedge effects. Figure 6.6(a) shows a model of the ablated texture shown in figure 5.25. Note that the textured features are introduced in the area where maximum pressure isobars are predicted to occur (maximum gas pressure behind the ring).

The resulting pressure isobars at the inlet to the conjunction, analogous to figure 6.5, are shown in figure 6.6(b). The texture pattern can be seen to act like a multitude of micro-wedges directing lubricant into the conjunction rather than it skirting around the leading edge of the contact. Furthermore, wherever a feature exists a reservoir of lubricant is maintained. These predictions were seen as favourable and advised laser ablation at appropriate locations at the TDC and in its vicinity. The improvements in power have already been discussed in figure 6.4.

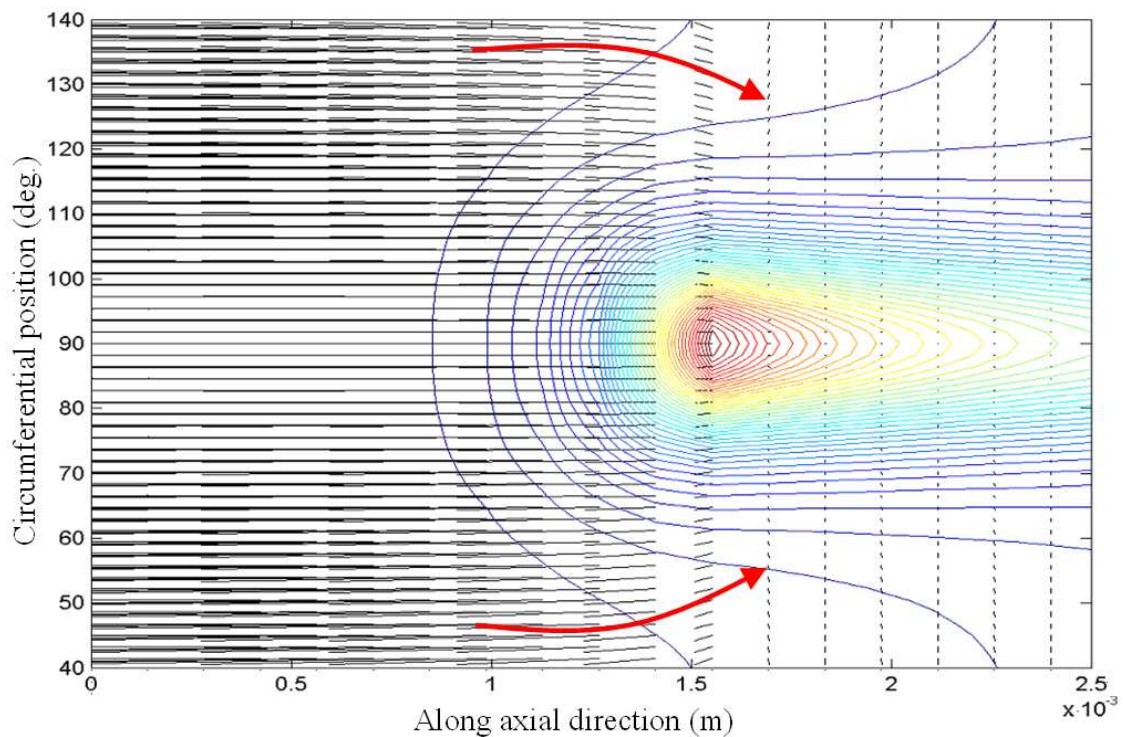


Figure 6.5 Flow around high pressure regions



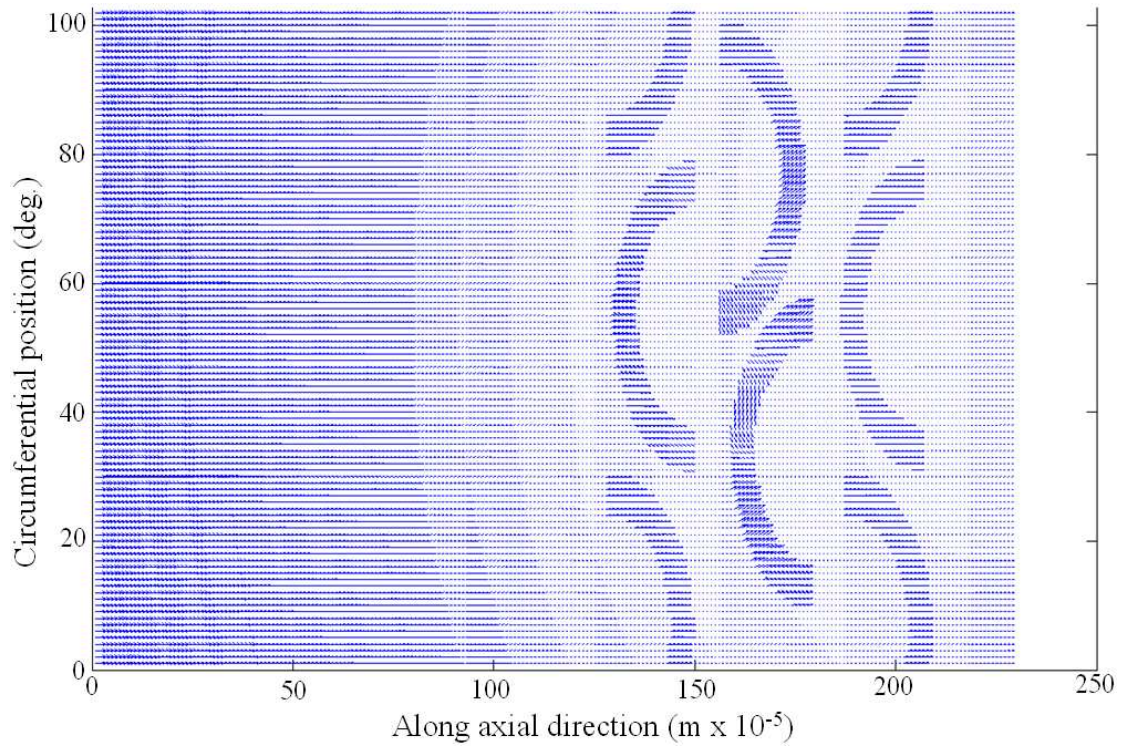


Figure 6.6(a) Model of laser ablated textures at the TDC position

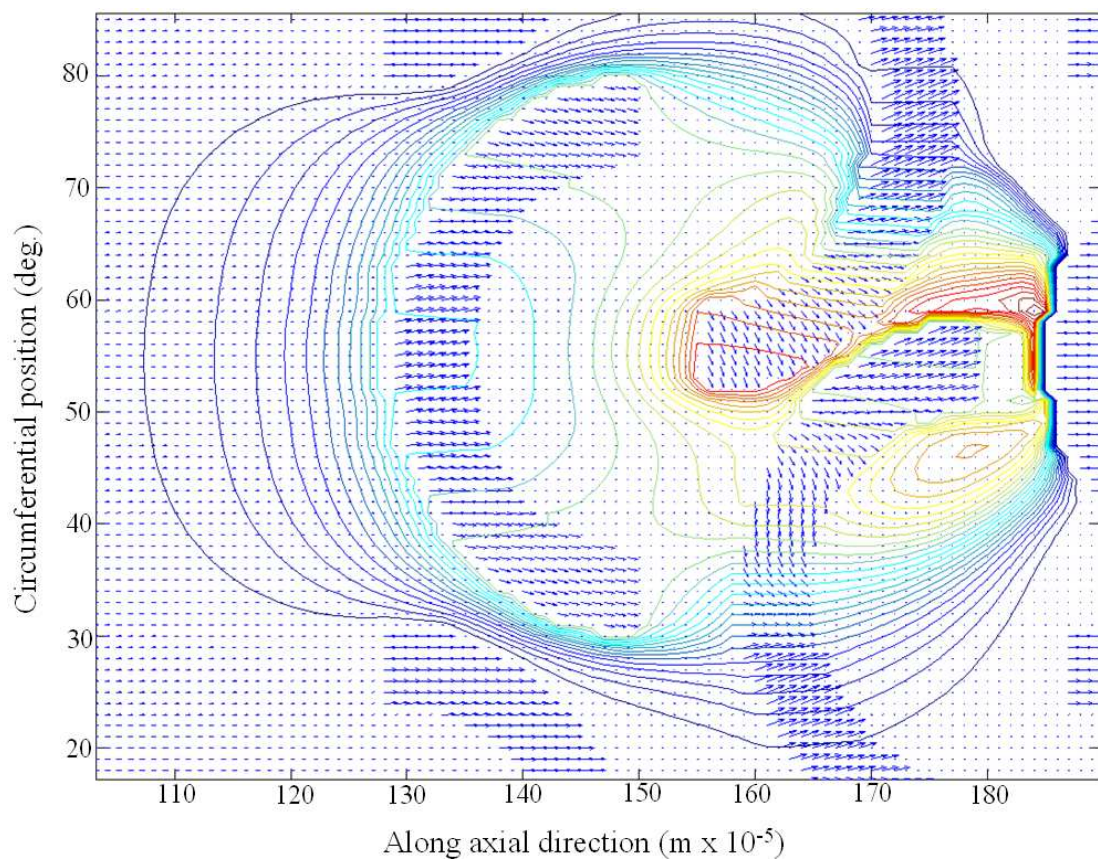


Figure 6.6(b) Flow pattern with laser textured bore surface

The above engine tests were with the baseline wet cylinder liner. Some tests were also carried out with the *dry* OEM standard Honda mono-cylinder (figure 5.2). This is a eutectic Al-Si casting with an integral cooling jacket and a nominal surface finish of  $0.2\text{--}0.3\mu\text{m } R_a$ . Figure 6.7 shows results for this mono-cylinder in comparison with the standard baseline wet liner (previously described), as well as a wet liner with indented textures.

This textured surface was limited to the upper bore surface so that the top ring would be in contact at and around TDC. The type discussed here was the Vickers type (fig. 5.28) and the development of this component and the required processing is detailed in chapter 5. It is interesting to note that the mono-cylinder Honda liner showed improvement against the wet standard liner across almost all engine speeds exceeding 5500rpm. This would indicate either a lower running clearance in the case of the wet liner at the reversal points, particularly at or in the vicinity of the TDC, or otherwise a thicker film giving greater viscous friction throughout the cycle.

An explanation is found when the indented OEM mono-block liner is compared with the standard OEM (non-indented) mono-block liner. These results are shown side-by-side in figure 6.7. It is shown that the indented liner has improved power for all speeds relative to the otherwise identical standard baseline wet liner ((L2017-LINER-C). This, therefore, indicates two significant findings. Firstly, that the standard wet liner performs worse than the mono-cylinder Honda barrel because of reduced clearance. Secondly, that this reduced clearance causes increased boundary friction at the TDC reversal position.

A major find of the experimentation, advised by numerical analysis (see chapter 7), is that most of the power losses are due to boundary friction at the TDC position and during the expansion (power) stroke down to regions where insufficient speed of entraining motion and conjunctional force are experienced. It is also noteworthy that the wet barrel arrangement will be subject to greater thermo-mechanical distortion than a solid mono-block. Hence, surface modifications performed on the OEM mono-block would arguably benefit the wet liner barrel arrangement more.

Significantly, improved power is noted for the indented liner relative to the baseline variant across all tested engine speeds from 5000rpm to 9000rpm (figure 6.7). Interestingly **Rahmani et al (2010)**, in bench-marking of various texture types, predicted that conical textured patterns show the highest load carrying capacity and the lowest friction. The tests here also indicate the



same. The indentations not only act as reservoirs of lubricant, but also induce a micro-wedge effect.

Figure 6.7 Comparison between bore construction and localised indentation

It is more usual to introduce surface modification onto the cylinder bore as opposed to the piston skirt. The bore surface is typically static relative to the engine, whereas the piston assembly is continually translating along the cylinder axis. For a given rotational speed, and translating point on the piston assembly, entrainment speed on the bore surface coincident with the piston assembly point will be constant. Therefore, the regime of lubrication will be consistent at this position, allowing *targeted* application of any surface modification. For example, texturing may be introduced at the TDC and BDC positions to reduce the effect of boundary interactions due to unfavourable kinematic conditions inhibiting the formation of a coherent lubricant film. Furthermore, at other locations in the piston cycle where speed of sliding is sufficient to entrain a film of lubricant into the conjunctions no modification may be necessary to enhance the formation of a film, as long as a good supply of lubricant can be assured. In fact any dimples, indentations, and cavities at locations where hydrodynamic conditions already prevail may result in leakage of lubricant. Aside from the now fairly usual cross-hatch honing, the introduction of surface texturing onto cylinder liners requires time intensive and fairly expensive processes such as laser ablation, where the depth of grooves or features remains a control issue as discussed in chapter 5.

### 6.3 Experimental results for differing piston configurations

Surface modifications can alternatively be conducted on the piston skirt itself. There may be a variety of reasons for this e.g. capital cost of equipment and smaller processing area thereby reducing cycle time (cost). Furthermore, the piston skirt surface is naturally more suited to laser processing due to its convex surface. The processing of the internal bore surface (concave) requires internal beam steering equipment such as specialist optics not required for external convex piston skirt processing.

A further reason for piston skirt processing is due to cylinder bore thermal and mechanical distortion. Component distortion can modify the conjunctional gap such that it is not necessarily at its minimum in the vicinity of the reversal points. These distortions are often due to structural design of the cylinder liner and piston, e.g. local stiffening, localised ‘hot spots’, or shrink-fit insertion. These ‘additional’ distortions can modify the position of the minimum resulting gap such that it is some distance away from the originally considered minima (TDC). In such circumstances the perceived *targeted* modification at the TDC position on the liner surface would not suffice. Hence a number of variously-textured piston skirts were tested against a nominally plateau-worn and embedded cylinder liner.

Additionally the piston skirt can be coated much more readily than the cylinder liner with many types of coating materials. Example processes to deposit hard wear-resistant coatings are PVD (physical vapour deposition) or PECVD (Plasma-enhanced chemical vapour deposition at room temperature) resulting in DLC with fairly smooth topography.

Due to their smoother topography some surface coatings are an alternative way of reducing friction and inhibiting wear. DLC coatings are a family of carbon chains in an amorphous structure, comprising of primarily  $sp^2$  (trigonal) or  $sp^3$  (tetrahedral) bonds. The hydrogenated PECVD DLC coating used in this thesis has a very low coefficient of friction, typically 0.01-0.2 depending on its exact structure. Furthermore, the hydrogenated DLC with diamond-like structure, a-C:H, has quite a low surface energy, which further reduces the chance of adhesion with a counter-face (Yan *et al* (2004)). The surface energy of DLC coatings depends on the contacting fluid used. Measurements have generally been made for the contact angle of different types of DLC with water.

**Gohar and Rahnejat (2008)** give the value of  $60^\circ$ , whilst a value between  $57^\circ$  -  $77^\circ$  is often quoted by many researchers (**Tao et al (2008)**, **Tagawa et al (2004)**). These contact angles are relatively large, making the untreated DLC coatings rather hydrophobic. In fact **Kiuru and Alakoski (2004)** suggest that untreated DLC coatings are essentially hydrophobic as well as oleophobic. For example **Tao et al (2008)** give the contact angle of ethylene glycol hydrogenated with *untreated* hydrogenated DLC as  $52.5^\circ$ .

A typical DLC coating has a relatively soft  $sp^2$  structure top surface and a thicker inner harder layer of  $sp^3$  structure. The upper layer can form a transfer film which reduces the surface energy and thus adhesion, whilst the lower layer provides hardness. During sliding contact temperature increases. As DLC is oleophobic and not easily wetted with high sliding velocity / shear this transfer film is worn / sheared away and friction increases. This can be seen in figure 6.8 as declining performance of a DLC coated piston (P1084-K, fig. 5.11) vs. a standard baseline AA2618 alloy piston (P1084-A, fig. 5.11).

During testing the DLC coated piston consistently under-performed compared to the standard piston due to its oleophobicity and smoother surface. Surface retaining pockets of lubricant are greatly reduced because of these factors. The transfer film is more likely to form in concentrated high stress contacts as found in cam-tappet or rolling element bearings. Both of these contacts are with thinner film and a mixed regime of lubrication, where application of DLC has been reported to be beneficial. **Podgornik et al (2008)** note that a thin transfer film is formed by DLC. This is very beneficial in the boundary regime of lubrication. However, they noted that such films are not usually evident under elastohydrodynamic or hydrodynamic regimes of lubrication. With the piston-skirt-to-bore surface predominantly operating in a hydrodynamic regime this poor performance is therefore to be expected and in agreement with literature.

Another tested coating was tungsten disulphide,  $WS_2$ .  $WS_2$  possesses low friction and a typical coating thickness of  $0.5\text{-}1\mu\text{m}$ . Coefficients of friction as low as 0.03 have been reported, making this coating suitable for space applications in the absence of any liquid lubricant.  $WS_2$  is oleophobic with a thin lamellar structure which inhibits molecules of lubricant residing on its surface. The weak sulphur - sulphur bonds make the lamellar structure rather like stacks of easily floating plates, which have practically no shear strength, thus reducing friction. This makes  $WS_2$  one of the lowest friction materials known to science. With thin lubricating films containing extreme pressure (EP) sulphur-based additives, tungsten reacts with the sulphur

forming thin tribo-chemical films as reported by **Podgornik *et al* (2006)**. This film acts as a thin boundary lubricant and similar to the DLC case above it is not observed with thicker hydrodynamic conjunctions. Tungsten disulphide is in fact super-hydrophobic. On contact with water a contact angle in excess of  $120^\circ$  results. Note as the contact angle increases the free surface energy is reduced, thus the likelihood of viscous friction. As in the DLC skirt coated case, a lack of a tribo-chemical layer or its depletion at higher shear rates (engine speed) deteriorates the performance of the  $WS_2$  coated piston skirt. This is also observed and presented in figure 6.8.

Figure 6.8 also includes the test results for a piston featuring spray-coated skirts (figure 5.17, 3<sup>rd</sup> component from the LHS). The coating used was designated Xylan 1010 (refer chapter 5.3.2) applied at a thickness of 12-20 $\mu$ m creating part P1084-B (fig. 5.15). This coating too is also oleophobic, hydrophobic (producing a contact angle of  $126^\circ$  with water, measured by **Critchlow *et al* (2006)**), and with a low free surface energy of 9mJ/m<sup>2</sup> (far less than that of DLC, between 30-50 mJ/m<sup>2</sup>) as measured by **Tao *et al* (2008)**.

Xylan coatings are primarily used as release coatings in resin transfer mouldings due in part to their oleophobic properties. **Critchlow *et al* (2006)** refer to this class of fluoro-polymer and metal-PTFE coatings as abhesive, this being a term used initially by **Zisman (1962)** as an antithesis of adhesion. Xylan 1010 has a proprietary composition containing a high proportion of polytetrafluoroethylene (PTFE) within a binder matrix. Some Xylan grades also contain molybdenum disulphide and other low friction dry lubricants. The active ingredient within the 1010 grade however is only PTFE. In practice Xylan is routinely used in the development phase of a new piston, where the in-service running clearances (and therefore required cold clearance) are not known. Wear patterns created in the relatively soft and easily abraded Xylan-coated skirts gives an indication of the actual operating clearances.

From figure 6.8 it can be seen that overall the Xylan-coated piston performs better than the other oleophobic coatings;  $WS_2$  and DLC. However, due to its soft nature it wears quite rapidly. There is an indication that at higher rates of shear a low shear strength film of PTFE forms over the surface such that some power gain over the baseline piston is noted. The same characteristic is often noted of  $MoS_2$ . The solid Xylan coating has begun to act as a polymeric additive within the lubricant proper. However, the piston eventually tends to an uncoated surface and emerging clearances can lead to excessive oil loss and blow-by.

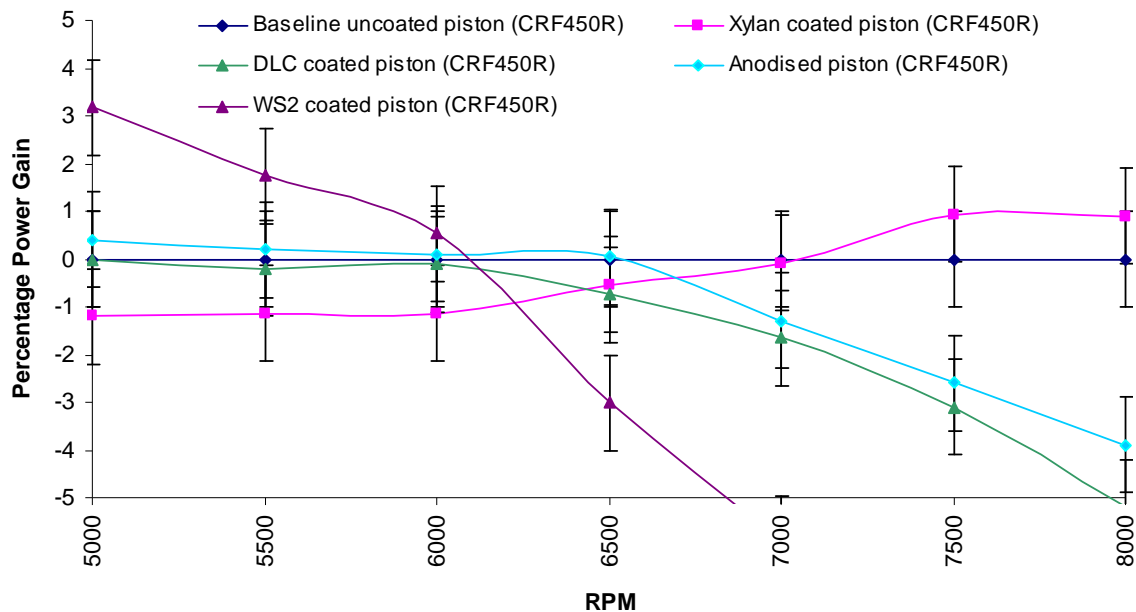


Figure 6.8 The effect of various piston coatings / surface treatments

Figure 6.8 also includes the results of CRF engine testing with an anodised aluminium piston. The piston was hard-anodised by immersing it into a bath of cold (circa 8°C) sulphuric acid. Initially a low voltage is applied (due to the high conductivity of the metallic piston surface) thereby controlling the current per unit area of the component. The exposed surface rapidly oxidises increasing the surface hardness from approximately 100-150VPN to 350-500VPN. As the process progresses the potential difference (applied voltage) is increased so as to maintain the optimal current with increasing internal resistance.

The much harder anodised surface is dramatically improved in terms of scratch resistance and corrosion resistance. However, one problem with anodising is an increased surface roughness. This roughness increase can exceed double that of the untreated aluminium substrate. For round bores honing of the anodised surface is often undertaken (**Mistry *et al* (2010)**).

The results for the anodised piston show hardly any improvement compared with the baseline piston for lower engine speeds, with quickly deteriorating performance at speeds exceeding 6500rpm. Increased NVH was noted with this piston, particularly at higher engine speeds.

The surface-coated piston skirts previously discussed are hydrophobic, unlike the anodised surface which has a contact angle with water of around 30° (as measured by **Bolanca and Hladnik (2000)**) and are therefore hydrophilic. The anodised surface is also rough (0.5-1µm  $R_a$ ), thereby facilitating lubricant retention within the valleys of its topography. When an

insufficient film thickness occurs friction is increased relative to the baseline piston due to the rougher surface. Significant wear was noted on the counter-face area on the liner compared with the baseline piston. This wear can be explained by the plasticity index,  $\Psi$  (**Greenwood and Williamson (1966)**) from equation 6.2.

$$\Psi = \left( \frac{E'}{H} \right) \left( \frac{\sigma}{r} \right)^{1/2} \quad (6.2)$$

where:

$\left( \frac{E'}{H} \right)$  is the effective contact modulus over the hardness of the anodised surface.

$\left( \frac{\sigma}{r} \right)$  is a measure of average asperity slope.

$\sigma$  is the surface roughness ( $R_a$ ), and  $r$  is average asperity tip radius.

The anodised surface has an effective contact modulus over the hardness of the anodised surface some one quarter that of the baseline aluminium alloy piston ( $E^*$  being unaffected by the anodising process). The asperity slope is changed by a somewhat smaller ratio. Hence, a lower plasticity index means that more of a pronounced ploughing action (frictional increase) on the softer counter-face occurs. This increased friction is dependent on the relative sliding speed of the surfaces as shown by **Gohar and Rahnejat (2008)**. This explains the progressively decreasing performance of the anodised piston relative to the baseline piston.

As for the cylinder bore surface through honing, it is also possible to introduce cross-hatched texture features into the piston skirts. Such introduced grooves can again aid retention of lubricant in the contact, similar to the laser-etched features described above. Key parameters of cross-hatched surfaces include the cross-hatch angle (figure 5.7b), groove depth, and spacing. Reasonable process control over each of these parameters exists. Clearly these parameters play a role in the load-carrying capacity and film formation, and therefore one can strive to find an optimal solution. There have been a few such attempts to predict the effect of cross-hatched honing angle.

One of the first attempts was reported by **Michail and Barber (1995)**, solving the Reynolds equation in its average flow form, proposed by **Patir and Cheng (1978)**. They represented the honed surface by a combination of cosine terms. This is analogous to a cross-hatched, honed

surface with removed peaks at the edges of the grooves, thus forming a plateau. These plateau surfaces are non-Gaussian and a better representation was provided by **Spencer *et al* (2010)**, in a semi-deterministic manner, based on an average groove width and cross-hatch angle. *Spencer et al* showed that for their investigation a maximum film thickness is achieved with a honing angle of  $35^\circ$ . Their findings agree well with those of **Michail and Barber (1995)**, who noted that a thicker film is obtained with shallower honing angles near the dead centres. At the TDC and BDC positions there is a tendency towards a mixed regime of lubrication. Away from the TDC and BDC positions the beneficial effect was seen as marginal, as a coherent thick hydrodynamic film was predicted. Based on the above findings a number of engine tests were carried out with three cross-hatched piston variants. These cross-hatch angles were  $30^\circ$ ,  $90^\circ$ , and  $150^\circ$  (figure 5.22). Prior to cross-hatching the base finish of these parts was far smoother than the compared-against baseline piston (chapter 5.4.1). To allow the influence of base finish vs. added cross-hatching to be understood a 5<sup>th</sup> piston with smooth finish but no cross-hatching was also tested.

Figure 6.9 shows the test results of these four types (three-off cross-hatched and one-off smooth) of piston compared against the baseline P1084-A component. Of note, the piston with the produces the maximum power gain over the standard part. This result is in line with the predictions of the aforementioned research workers.

Figure 6.9: Benchmarking of pistons with different honing angle

Figure 5.22 shows diamond-shaped (rhomboid) plateaus created by the cross-hatching process. Each diamond shape plateau is due to the introduction of overlapping grooves onto the surface. The angle of these grooves is dependent on cross-hatch process parameters where the shallow included angle produces grooves more orthogonal to the entrainment flow (i.e. RFE30 is more orthogonal to flow than RSFE150). Due to this ordered groove orientation the shallow cross-hatchings act very similarly to the laser ablated features discussed earlier. Conversely, steeper cross-hatch angles divert the flow away from the rhomboidal plateaus. This is the reason for relatively poorer performance of RSFE150, even compared with the baseline *untreated* piston, as the grooves are almost along the direction of lubricant entrainment thus leaving the rhomboidal plateaus somewhat parched.

Finally one should note that lubricant temperature plays a critical role in the lubricants' interaction with conjunctural surfaces. In the above tests carried-out on the CRF engine no specific control of lubricant temperature is possible. The CRF engine features a self-contained internal lubrication system. The lubricant is indirectly cooled by heat transfer to the water cooling circuit or external atmosphere by means of conduction through the predominantly aluminium engine structure. Heat transfer coefficients would be unlikely to increase in value proportional to engine output (fixed section thicknesses etc.) and therefore, in the case of a nominally constant water circuit (sink) temperature, oil temperature (source) varies depending on engine load.

The ASME engine test rig described in chapter 5 enables control of bulk oil temperature without any appreciable thermo-elastic distortion of the cylinder. This allows the study of lubricant effect at different temperature, with the hypothesis that control of lubricant temperature in the bulk can have a significant effect upon viscous frictional power losses. These losses dominate in the hydrodynamic regime of lubrication which prevails for most of the piston cycle, even during the power stroke. Figure 6.10 shows results for identical pistons where bulk oil temperature was controlled during various rotational speed testing.

From figure 6.10 it can be seen that the higher oil temperature with lower effective viscosity (the standard case) performs better than all other tested temperatures. This is a rather expected result. However, it shows the reasons behind the drive for use of lower viscosity lubricants in engines. The same may not be the case for highly-loaded concentrated contacts such as the cam-tappet pair. Herein lies the conundrum.



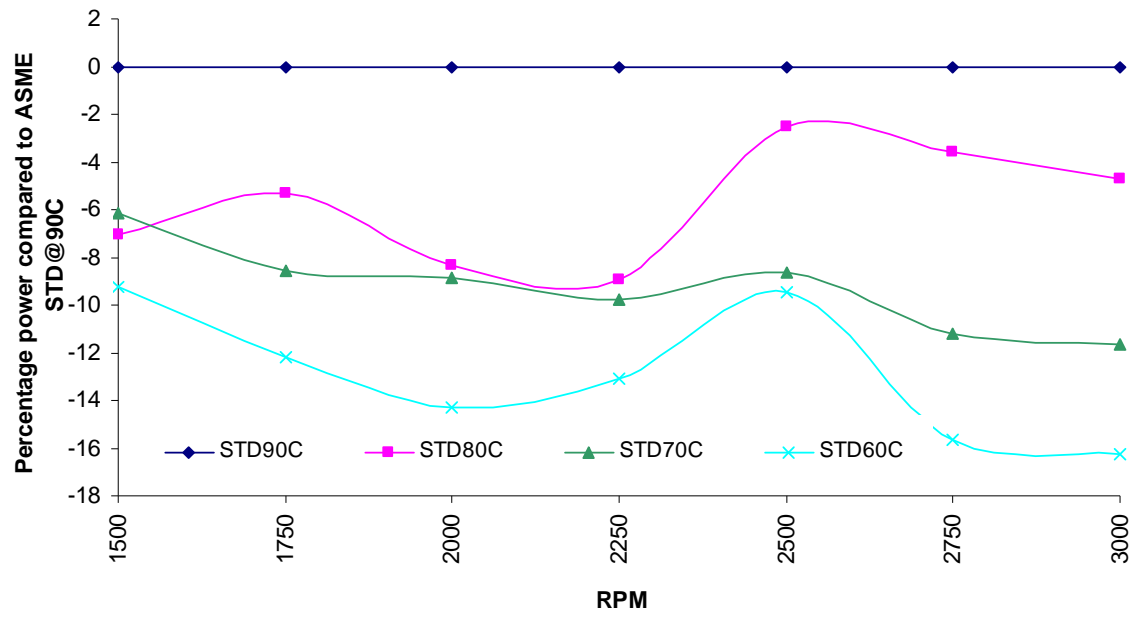


Figure 6.10 ASME: Baseline part (STD) vs. oil temperature

## Chapter 7

### Numerical results

---

#### 7.1 Preamble

This chapter provides simulation studies of tribological conditions predicted using the methods outlined in chapter 4. The analyses reported in literature often correspond to ‘cold’ piston skirt profiles, such as those reported by **Li *et al* (1983)**, **Knoll and Peeken (1982)**, **Oh *et al* (1987)**, **Balakrishnan, Howell-Smith, Rahnejat, and Dowson, (2003)**, **Balakrishnan and Rahnejat (2002)**, and **Rahnejat, Balakrishnan, King, and Howell-Smith, (2006)**. In some of these analyses isothermal contact conditions are assumed, whereas some others have adjusted the lubricant viscosity according to measured or assumed contact temperatures.

In practice and under fired engine conditions both the contiguous surfaces (i.e. cylinder liner and the piston skirt) are subject to thermo-elastic distortion as described in chapter 4. Some analyses, notably by **Offner and Priebisch (2000)** and **McClure (2007)**, have taken the distorted shapes into account. The former uses finite element analysis to incorporate global elastic distortion, whilst the latter includes the thermal effect as well. Although the numbers of studies including thermo-elastic effects are small, they do show that the ‘hot’ skirt conjunction renders a contact footprint shape which is quite dissimilar to that generally used in most (cold / rigid body) tribological studies.

The skirt-to-bore contact ‘footprint’ shape, as shown in chapter 4 figure 4.9, in fact points to a much smaller contact area than that of the entire skirt (figures 7.1 & 7.2). This means that the skirt-to-bore contact is of differing conformability than that assumed in the case of ‘cold’ skirt profiles. Nevertheless the predictions made with the ‘cold’ skirt analysis, in some cases, agree quite well with the measured film thickness using ultrasonic sensors as reported by **Dwyer-Joyce, Green, Balakrishnan, Harper, Lewis, Howell-Smith, King, Rahnejat (2006)**, and **Gohar and Rahnejat (2008)**. Note that these studies have used motorised engine tests.

This chapter presents a series of simulation studies of both ‘cold’ and ‘hot’ piston skirt conjunctions and combines these with the experimental findings of chapter 6 to make some key conclusions. In all cases the analyses include adjustment to the lubricant dynamic viscosity with pressure and temperature (i.e. the use of effective viscosity).



Figure 7.1 Localised piston skirt contact



Figure 7.2 Localised bore thrust wear

These analyses are purely hydrodynamic / elastohydrodynamic studies (i.e. a fluid film regime of lubrication is assumed). In reality some of the predictions yield lubricant film thickness which are insufficient to guard against direct surface interactions, although an asperity interaction model is not included.

## 7.2 EHL of ‘cold’ skirt profile

There are a number of prime positions of interest in any tribo-dynamic analysis of piston skirt or ring pack to cylinder liner contact. Two such positions are the reversals at the TDC and the BDC positions. At these reversal positions the primary mechanism of film formation (entraining motion) ceases resulting in film depletion. The positions of the inlet menisci are fortunately relatively close to the contact proper thereby providing an immediate lubricant reservoir once relative motion reoccurs. From these reservoirs, lubricant is entrained into the contact depending on the direction of motion. This action takes place 4 times in each cycle of a 4-stroke engine (twice per crank revolution).

The main mechanism of lubrication at TDC and BDC positions is the squeeze film effect. This is any film of lubricant which may be entrapped in the contact in a formed *dimple* (an elastic locally deformed cavity on the contiguous surfaces) or retained between the asperity pairs of the contiguous surfaces. The first mentioned mechanism plays an important role in reciprocating rolling element bearing applications or in cam-tappet contacts whilst transitioning from the cam flank to the cam nose region (*wind-up*,) and returning back to the flank *wind-down* (**Kushwaha and Rahnejat, (2004)**).

However, unlike the aforementioned concentrated counter-forming contacts in the valve train, the piston-bore contact presents a large area of partially conforming contact resulting in

generated pressures which are considerably lower (in tens of MPa) and thus insufficient to cause any significant localised deformation. Therefore, any mechanism of squeeze is by rigid body approach, and hence there is a low chance of fluid film retention. Thus lubricant entrapment is the only potential mechanism during instances of reversal or low speed of entraining motion. Hence, as far as lubrication is concerned, suitably rough surfaces can act as sources of lubricant retention. However, any ensuing asperity interactions also act equally well as the main contribution to friction, both by adhesive friction as well as ploughing (deformation) friction (**Gohar and Rahnejat, (2008)**). These contradictory effects have been a source of empirical action in practice for many years. Therefore, for these positions (i.e. TDC and BDC), an asperity model would be essential as a mixed regime of lubrication is expected at best. Hence this thesis does not concentrate on these positions, but at the positions of maximum combustion pressure / maximum horizontal side force where the speed of entraining motion is still quite low. This combination often accounts for the worst tribological outcome, especially when thermo-elastic effects are included.

The cylinder bore / liner surface topography is carefully developed depending on the application type. Very generally it is smoother for high-speed race vehicles ( $<0.1 \mu\text{m Ra}$ ) than the niche OEM ( $0.25 \mu\text{m Ra}$ ), and coarser still for the OEM ( $0.35 \mu\text{m Ra}$ ). This trend is driven by the relatively short life of race engines coupled with the use of low viscosity lubricants (reduced viscous drag), where some wear at reversal points (and ensuing asperity friction) is accepted and offset by reduced viscous drag. High-cost palliative actions are, however, required to ensure even limited acceptable service operation ranging from high cost surface coatings through to extreme geometric tolerances.

Ideally bore roughness would be variable with respect to the entraining speed. This is, however, difficult to achieve whilst maintaining other parameters such as geometric form and manufacturing efficiency. Bore roughening to increase reliability in service is practically well known, with evidence of this even in the early steam engines (if not much earlier), and certainly before the fundamental understandings emerged from the works of **Tower (1883 and 1885)** and **Reynolds (1886)**. It seems that the engineers had appreciated, almost by intuition, that there is less chance of a lubricant film at reversals and some may be entrapped between rough surface topography.

A further position of interest is where the maximum combustion pressure and maximum side force occur. The piston instantaneous position, corresponding to the peak combustion

pressure, occurs shortly after TDC due to the fact that combustion is not an instantaneous process. For net work to result this does not symmetrically coincide with the position of highest efficiency with a crank-slider mechanism. Highest efficiency in case of instantaneous combustion would be at TDC ( $0^\circ$ ). In practice,  $11\text{--}13^\circ$  is a typical crank angle after top dead centre for this to occur (Figures 7.23 & A1.5). Peak side force is dictated by the combustion process and the geometric arrangement of the crank slider mechanism. Figures 7.23 and A1.12 show this occurs shortly after the peak combustion event. Although the side force is increasing from the point of combustion the sliding velocity is also rapidly increasing. Therefore, from a tribological consideration, a combination of high load and relatively low speed of entraining motion usually accounts for some of the most severe tribological conditions prevailing around the peak combustion time.

This is particularly true if elastohydrodynamic condition is not achieved. For this to occur, as originally proposed by **Grubin (1949)** and now generally predicted and observed, the contiguous solids should undergo some local deformation and the lubricant viscous action should also take place. **Balakrishnan, Howell-Smith, Rahnejat, and Dowson, (2003)** noted that in the piston skirt conjunction the generated pressures were only sufficient to cause elastic deformation at the maximum combustion pressure in the case of a race engine, which is also investigated in this thesis (Honda CRF 450). However, no appreciable piezo-viscous action of the lubricant was noted throughout the engine cycle (**Balakrishnan, Howell-Smith, Rahnejat, (2005)** and **Rahnejat, Balakrishnan, King and Howell-Smith (2006)**).

All these analyses were for a ‘cold’ skirt profile. The cylinder bore was assumed to be a perfect right circular cylinder and the piston profile as shown in figure 7.3. Of note are the relief radii at the top and bottom of the piston skirt, a feature used to create a hydrodynamic wedge in order to entrain a film of lubricant into the contact. Although these are common features of all modern pistons, minimal detailed tribological studies have been reported as to what constitutes an optimum piston skirt relief radius.

It is clear that a sharper inlet wedge results in a higher pressure gradient (increased Poiseuille flow). This would suit higher speeds of entraining motion, usually encountered in high-performance engines. However, large relief radii can also result in thicker films that can extend further towards the exit and breach any desired sealing effect, as in the case of compression rings. Large relief radii can also inhibit the formation of an inlet meniscus where the lubricant should be able to wet both of the contiguous solids and cling / adhere to them by

forming a bridge. Figure 7.3 shows the relief radii used in the case of the piston skirts used in this thesis (In this and the accompanying figures, ' $\psi$ ' indicates the skirt lower edge on the skirt centreline). These radii have been used by Capricorn Automotive, based on many years of in-field and engine testing experience, for maximum reliability and performance.

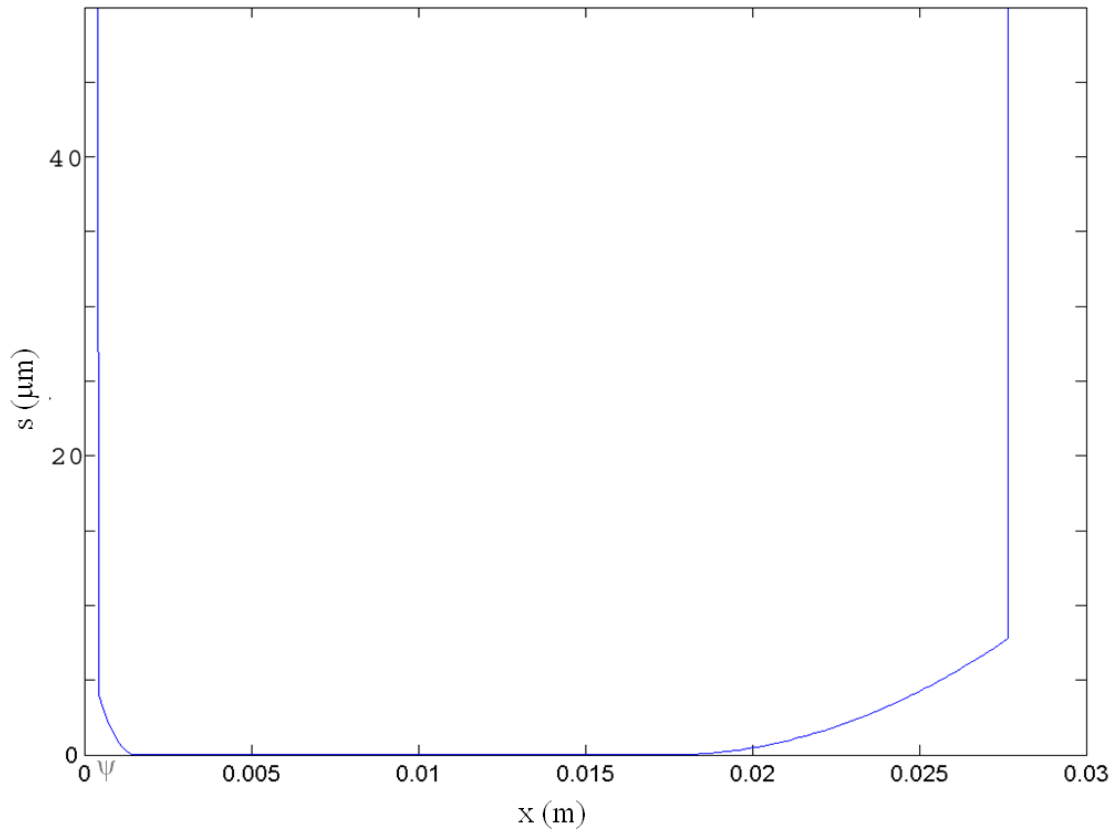


Figure 7.3 The undeformed CRF 'cold' piston skirt axial profile  
(courtesy of Capricorn Automotive Ltd)

The analysis for a 'cold' skirt was carried out by Balakrishnan and the author (**Balakrishnan *et al*, (2003, 2005)**) and **Rahnejat *et al*, (2006)**). Here some of the salient points of the results reported in the above mentioned work and the underlying reasons for those are highlighted. Detailed description of this earlier work is reported in **Balakrishnan, Howell-Smith, Rahnejat and Dowson (2003)**.

The very initial numerical analysis was motivated by the early investigations of Perfect Bore Ltd. (now Capricorn Automotive Ltd) regarding increased piston skirt roughness. The aim of the investigation was to ascertain any improvements arising from designed roughness in the form of an increased lubricant film thickness. In line with other numerical models at the time,

the ‘cold’ piston skirt profile was used as well as an assumption of a perfectly round cylinder liner. The chosen case examples were a contemporary F1 engine (**Balakrishnan, Howell-Smith and Rahnejat (2005)**) and for the case of previously detailed (Chapter 5) Honda CRF450R. The skirt profile given in figure 7.3 corresponds to this Honda case. A nominal piston-bore / liner clearance of  $47\mu\text{m}$  (radial) was used for the analysis, and contact load of 3220N was obtained at the instant of maximum combustion pressure of 9.03MPa (Figure 5.37).

Figure 7.4 shows the predicted pressure distribution for a standard piston skirt against a cross-hatched and honed Ni-SiC coated cylinder liner. Note that the CRF piston system considered here is the modified wet-liner barrel (Chapter 5) designed and developed by the author to modify the standard Honda CRF piston-bore configuration. In this figure the direction of entraining motion is from right to left as the piston is sliding downwards on the power stroke (left to right). There are two pressure spikes in the pressure distribution; one at the inlet wedge and the other at the outlet, prior to the divergent gap created by the relief radius at the top of the piston skirt.

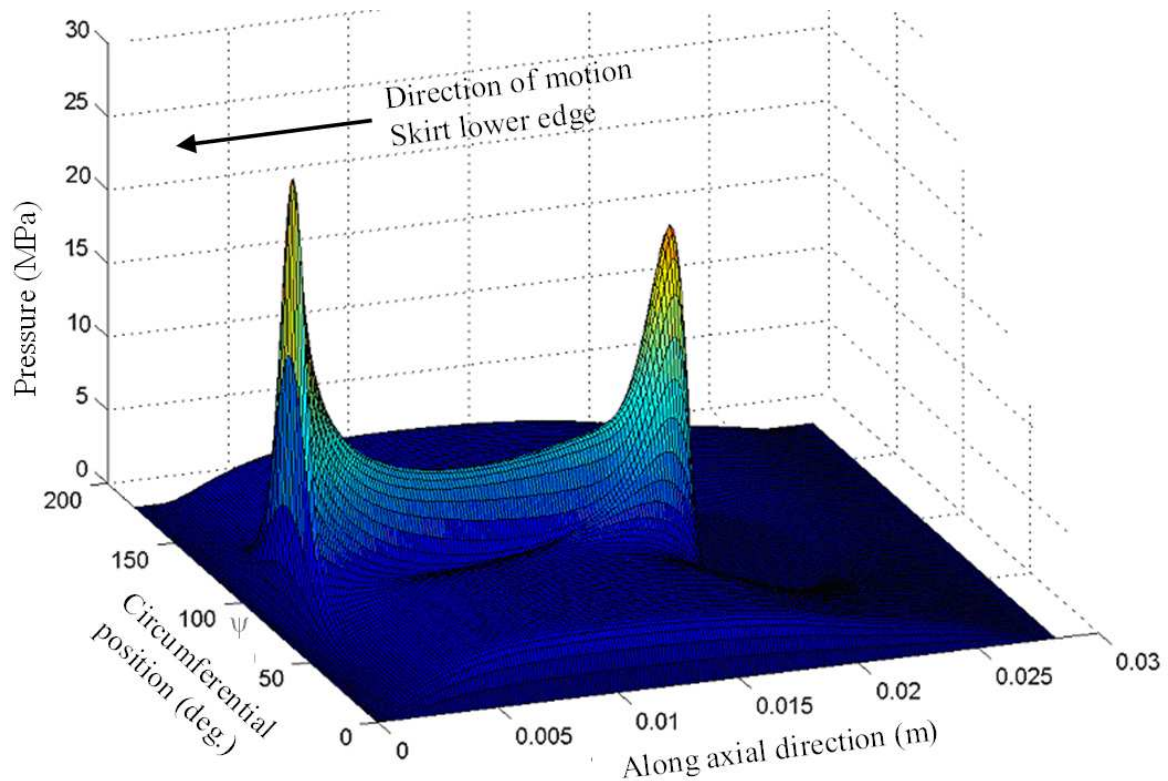


Figure 7.4 Hydrodynamic pressure distribution at  $P_{\text{max}}$  ( $11^\circ$ )

These pressure spikes may be conceived as edge stress discontinuities, where an abrupt change in the profile causes a corresponding sharp rise in the generated pressures. **Balakrishnan, Howell-Smith, Rahnejat and Dowson (2003)**, and **Gohar and Rahnejat (2008)** present the generated pressure distribution in isobaric form as shown in figure 7.5. The figure key refers to regions of pressure as indicated in MPa. This shows an elongated contact footprint deviating from a rectangular shape. It somewhat resembles a dog-bone or dumbbell shape contact footprint, more commonly encountered as the 90° rotated footprint shape of a roller indenting a semi-infinite elastic half-space (**Mostofi, (1981)**, **Mostofi and Gohar, (1983)**, and **Kushwaha, Rahnejat and Gohar, (2002)**).

Similar footprints are also noted for cam-tappet contact (**Kushwaha and Rahnejat, (2002)**). However the similarity between these finite concentrated line contacts and the current footprint ends in shape only. Whilst finite line contacts have a relatively large aspect ratio (much longer than the width of contact, the latter being the direction of entraining motion), the footprint shape here has a much lower aspect ratio and the direction of entraining motion is along the length of the contact (axial direction of the piston skirt).

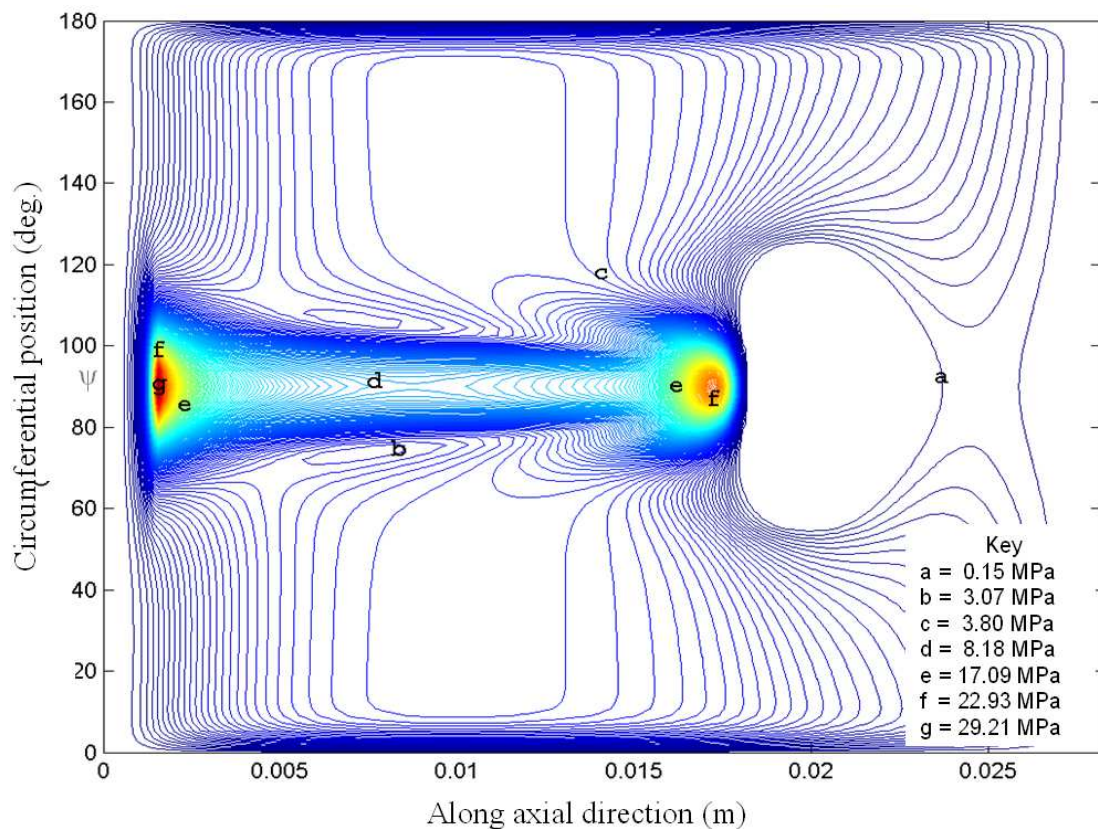


Figure 7.5 Cold skit isobaric pressures ( $P_{max}$ ,  $11^\circ$ )



In all tribological conjunctions, including that of the piston skirt, any pressure spike inhibits the flow of the lubricant into the contact. Most of the lubricant flows around the contact, like in nature where water takes the path of least resistance as noted by **Gohar and Rahnejat (2008)**.

The corresponding predicted oil film thickness contour for the pressure isobars of figure 7.5 is shown in figure 7.6. The piston skirt for this case is referred to as that of *standard OEM* which is considered to be *smooth* (i.e. with no surface roughening modification). The actual surface roughness ( $R_a$ ) for this type of skirt was measured to be nominally in the range 0.1-0.3 $\mu\text{m}$ . The contour levels in the figure are in micrometres of lubricant film thickness. A more detailed picture emerges by a cut through the centre of the contact in the axial direction, as shown in figure 7.7.

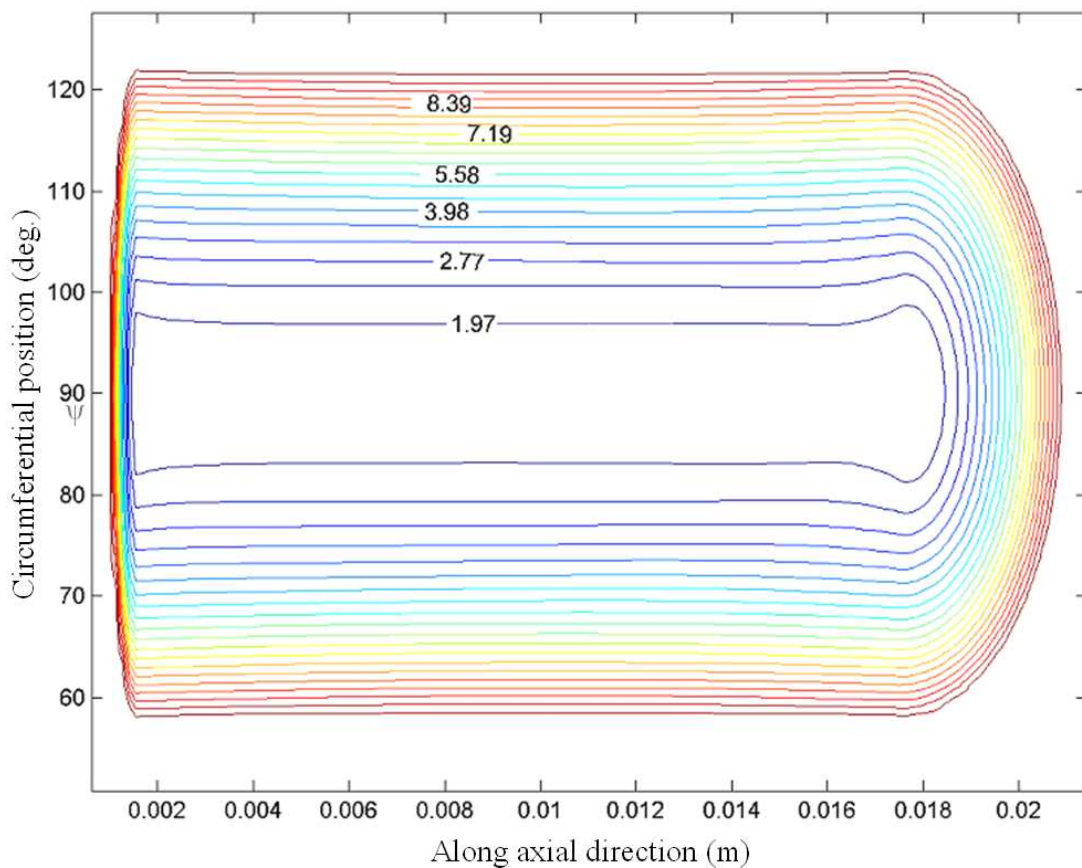


Figure 7.6 Oil film thickness contour for case in fig. 7.5  
(after **Balakrishnan, Howell-Smith, Rahnejat and Dowson (2003)**)

The thinnest films actually occur in the areas corresponding to the generated pressure spikes. These are along the flat portion of the piston skirt axial profile, immediately before the change in profile introduced by the relief radii. The film shape indicates local deformation of the piston skirt which is reminiscent of an elastohydrodynamic regime of lubrication, except that lubricant viscosity hardly alters, given maximum pressures of the order of 29MPa.

It is clear that for typical engine oils of pressure viscosity coefficient  $\alpha = 10^{-8} \text{ Pa}^{-1}$ ,  $\alpha p = 0.029$ , an almost iso-viscous condition results. Using Barus's law (4.14), for example:  $\eta = \eta_0 e^{\alpha p}$ ,  $\eta \approx \eta_0$ . Hence no piezo-viscous action of the lubricant is noted. Therefore, as **Balakrishnan, Howell-Smith, Rahnejat and Dowson (2003)** have also noted, the contact condition may be regarded as iso-viscous elastic. Some refer to such conditions as *soft EHL*.

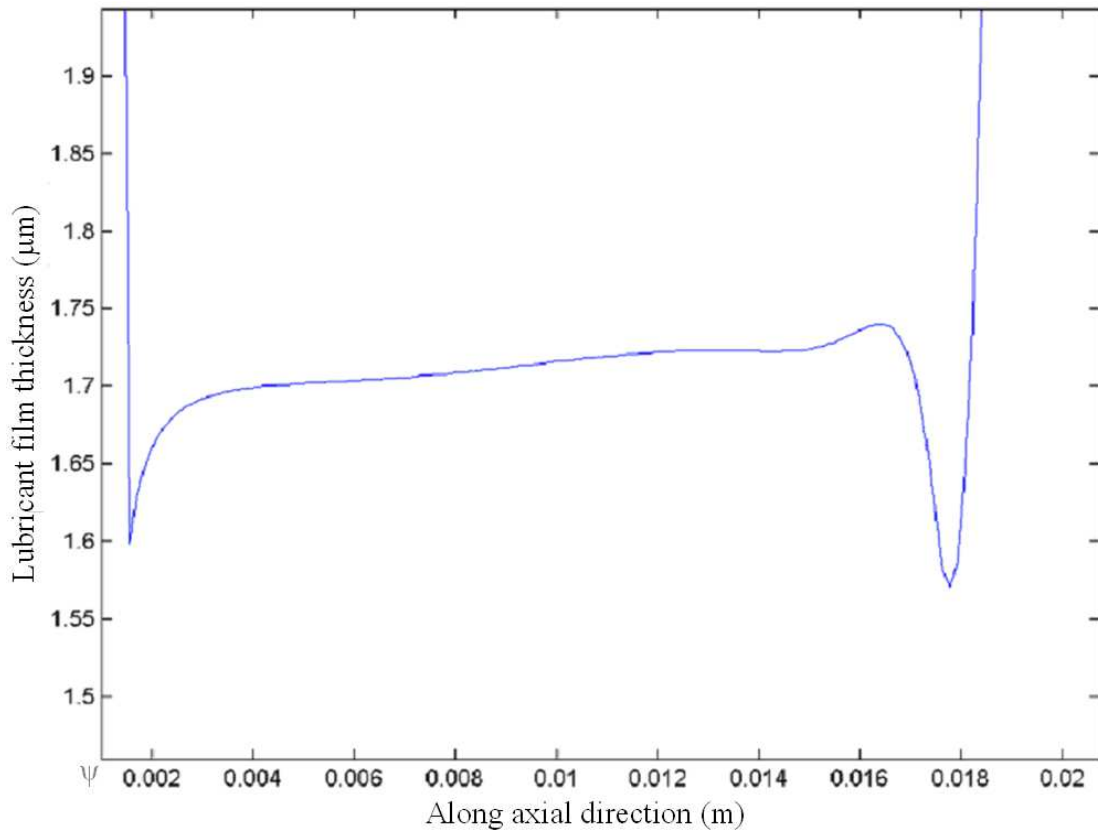


Figure 7.7 Centre line (90°) lubricant film thickness from fig. 7.6

From figure 7.7 and where the RMS surface roughness of the counter-faces is  $\sigma_{\text{RMS}} = 0.56 \mu\text{m}$ , then the Stribeck oil film parameter is:  $\frac{h}{\sigma_{\text{RMS}}} = 1.6 / 0.56 \approx 2.86$ , which indicates full fluid film lubrication, potentially under elastohydrodynamic conditions. Similar analysis carried out

in different locations other than at reversal points yield similar results. However, these are mostly under a hydrodynamic regime of lubrication. These results do not support the in-field observations, where wear scars are evident not only at the dead centres, but often at other locations (Figure 7.2).

It is clear that a salient practical feature is not included in the above analysis. This is the global thermo-elastic deformation of the piston. The distortion of the piston under operating temperatures changes its shape and thus the footprint contact area that it would make with the cylinder bore / liner. This deformation also depends on the construction of the cylinder barrel and the way it is restrained. Therefore it is important to predict the shape of the contact footprint prior to any tribological assessment. The global *in situ* shape of the contacting solids would tend to change significantly from the case of the ‘cold’ skirt analysed thus far. Their thermal expansion would reduce the clearance gap and can result in better conformance of the counter-faces. Chapter 5 and Figure 6.1 detail motored experimental work performed on the CRF engine to measure oil film thickness. A good correlation resulted between predicted and measured values, thereby somewhat verifying the numerical approach employed. For further details refer to **Dwyer-Joyce, Green, Balakrishnan, Harper, Lewis, Howell-Smith, King, Rahnejat, 2006**).

### 7.3 EHL of ‘hot’ thermally deformed piston skirt conjunction

When the effect of thermal expansion of the piston is taken into account the contact conformity is enhanced and a larger contact footprint area is expected. To obtain this deformed shape of the piston skirt *in situ* it is necessary to compute both global thermal loading as well as the localised deformation due to generated conjunctional pressures (Chapter 4).

The local deformed profile of the piston skirt after thermal analysis is referred to as the ‘hot’ skirt profile. This is imported into a subsequent EHL analysis as the initial profile which determines the gap at a particular location in the piston cycle (i.e. at a given crank-angle). Therefore, it may be regarded as the initial conjunction which is subjected to further localised analysis to obtain the pressure distribution (from Reynolds’s equation) and the corresponding lubricant film thickness.

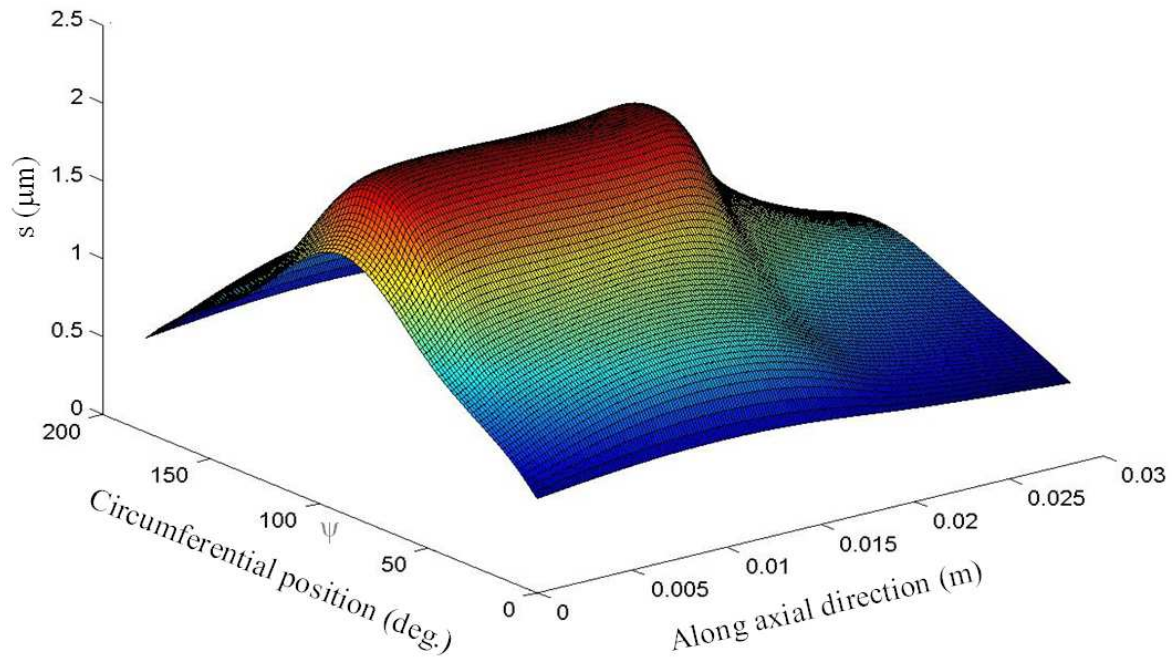


Figure 7.8 Skirt profile after 'hot' thermal analysis (Pmax)

After the thermal analysis has been performed the deformed piston skirt for the same conditions (position and load) as that for the 'cold' skirt is shown in figure 7.8. In this instance the thermal expansion of the bore / liner is assumed to also yield a right circular cylindrical profile. The three-dimensional lubricated contact pressure distribution resulting from this condition is shown in figure 7.9. There are two noteworthy points.

Firstly, a better degree of contact conformity is observed (a larger contact area), which is best noted by comparing the high pressure regions of the isobaric pressure plots of figures 7.10 and 7.5. Note that at maximum combustion pressure the piston adheres to the thrust side. In the case of the former ('hot' skirt) nearly  $100^\circ$  of the circumferential profile constitutes the contact footprint, whilst this is only  $50^\circ$  in the case of the 'cold' skirt (compare fig. 7.9 with fig. 7.4).

Secondly, with improved conformity the generated pressures including the pressure spikes at the inlet and outlet positions have reduced, which heralds improved tribological conditions. However, this initial analysis lacks the important point of not taking the barrel constraints into consideration. This affects the distortion of the liner and hence the proper contact footprint shape. This is remedied by a detailed thermo-elastic FEA for *in situ* conditions.

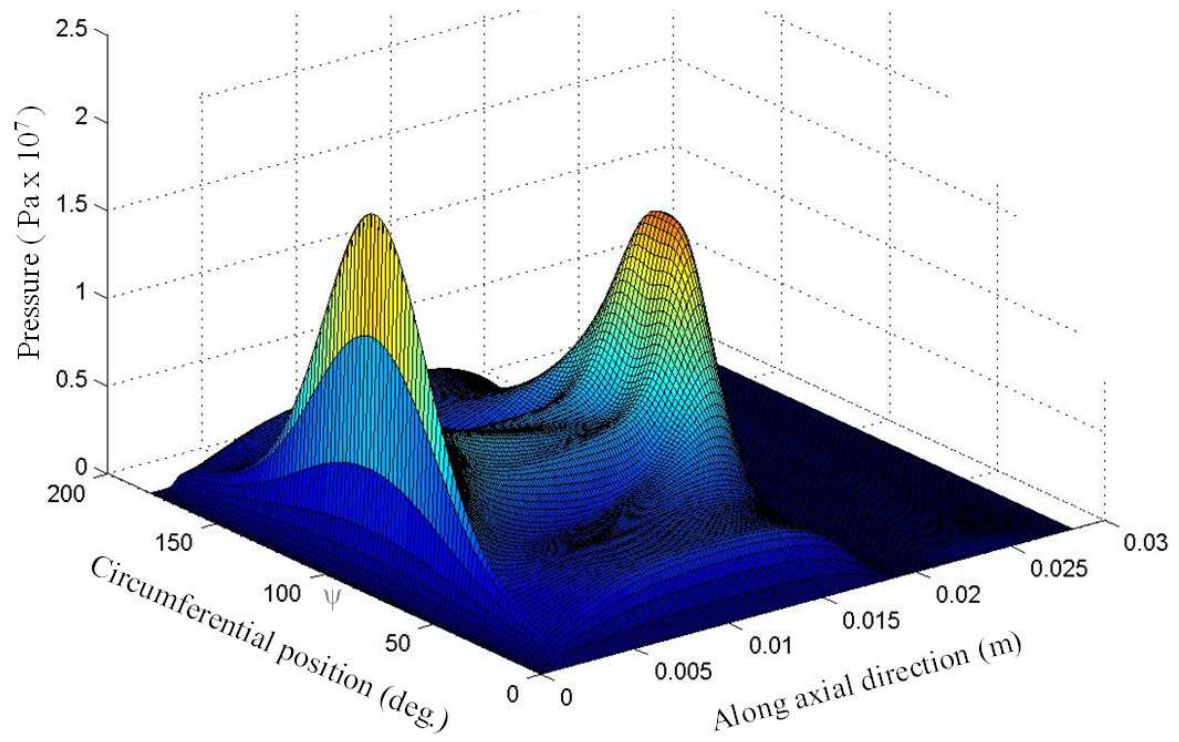
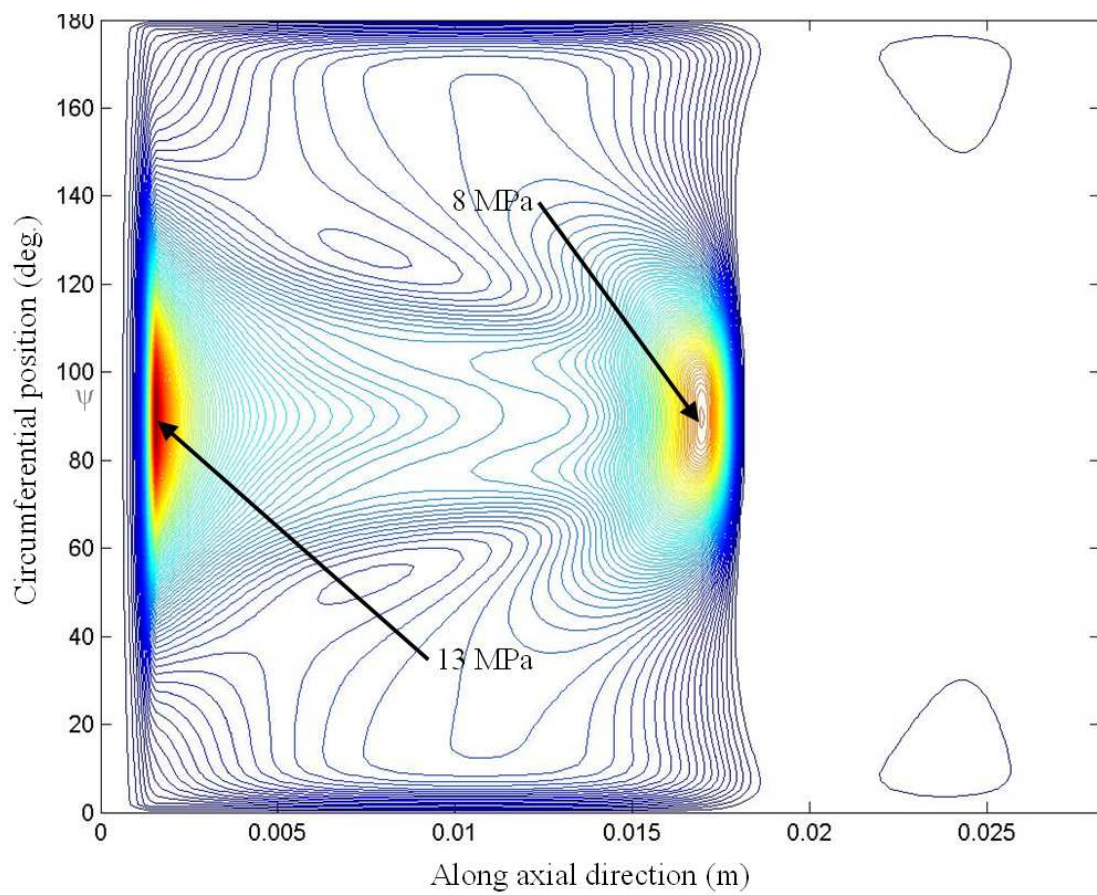


Figure 7.9 Lubricant generated pressure (iso-viscous 'hot')

Figure 7.10 Isobaric pressure for 'hot' skirt profile ( $P_{\max}$ )



## 7.4 Thermo-elastic distortion

The modified Honda CRF barrel described in chapter 6 is not unconstrained. It is held within the block by means of a transition fit and nitrile ‘o’ rings (figs 5.3 & 5.4). The outside of the liner is subject to differing thermal parameters (water jacket, etc.) and the horizontal surfaces are subject to cylinder clamping loads. Thus its thermo-elastic deformation does not yield a right circular cylindrical shape as assumed in the previous case in Section 7.3.

The method of thermo-elastic finite element analysis is described in chapter 4. Here, examples of piston skirt and liner global deformation are given for the various key angular positions. More in-depth results are provided in Appendix 3. The conjunctural footprint results from piston skirt and liner conformance reached *in situ* when subject to calculated forces and thermal influences. Calculation of piston and liner thermal and structural deformation is based on their initial undeformed geometry, material properties, loading (chapter 3), and an initial gap (real world clearance, figuratively shown in figure 7.11).

### 7.4.1 Procedure for evaluation of thermo-structural deformation

During operation, the IC piston is subjected to both thermal and structural loads. Tribological analysis critically requires the correct curvature and separation for the contiguous bodies to be considered, as well as the reaction forces and the speed of entraining motion of the lubricant (chapter 3 & 4). The form of the piston and, to a lesser extent, the cylinder bore are non-trivial as manufactured and as discussed in chapter 6, and are further influenced by the presence of thermal gradients throughout the components. The overall effect of thermal influence in this case is that of drastically reducing the ‘as-manufactured cold’ clearance. This reduction in cold clearance logically affects the tip and translation assumptions made earlier.

To calculate lubricant reaction acting upon the piston skirt the following steps are required:

1. Calculation of correct part clearances due to thermal effects (thermal analysis).
2. Calculation of relevant forces (chapter 3) which act upon the piston exerting a contact load onto the cylinder bore.
3. Calculation of piston and liner structural deformation based on thermally deformed geometry and material properties, resulting in an initial conjunction lubricant ‘gap’ and the overall liner reaction force.

4. Calculation of lubricant reaction based on the relative sliding velocity of the contiguous solids in contact and the lubricant rheology utilising representative starting geometry (1-3) shown diagrammatically in figure 7.11:

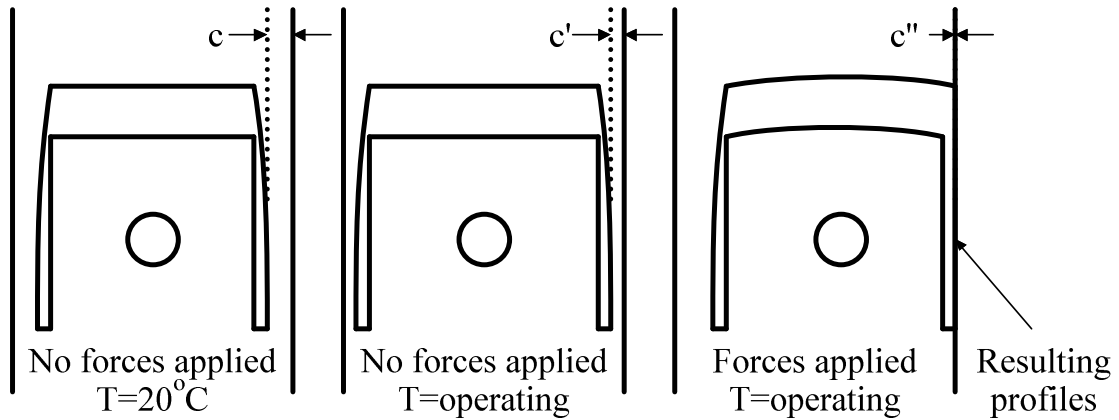


Figure 7.11 Diagrammatic representation of skirt deformation

For steps 1 through 4 a developed part detailed in chapter 5 was used with defeaturing as per the accepted norm for FEA (**Mobley *et al*, (1998)**). The exact component references are:

Part	Reference
Piston	P1084-06
Liner	L2017-07
Gudgeon pin	PN3035-01
Connecting rod	OEM

#### 7.4.2 Calculation of thermal distortion

Differential temperature within the IC cylinder yields differential growth of the components **Bosch (2007)** and **Abbes *et al* (2004)**. Figure 7.12 shows a thermal profile for a 53kWl<sup>-1</sup> spark ignition engine with 7.3MPa peak cylinder pressure and figure 7.13 shows the resulting differential expansion for a diesel piston.

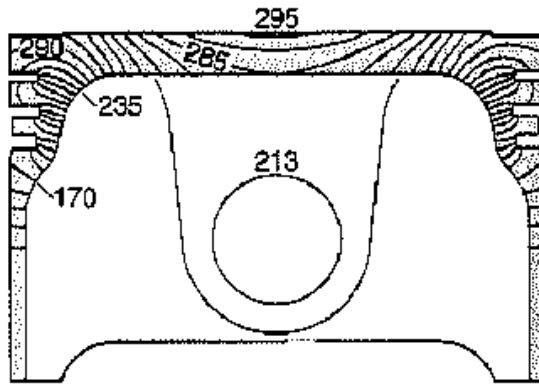


Figure 7.12 Temperature gradient within a spark ignition piston (**Bosch, (2007)**)

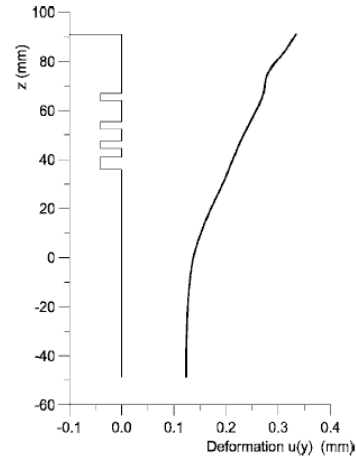


Figure 7.13 Piston thrust axis thermal deformation (**Abbes *et al*, (2004)**)

Analysis of the thermal expansion of the piston in the bore at the instantaneous operating temperature is based on the residual hardness correlation of components against a known part history (annealing time). This yields the average temperature at a given point, which is then used as a positional temperature target for the analytical calculation (interpolation of unmeasured areas and calculation of thermal stresses and strains).

**Abbes *et al* (2004)** presents a largely convective approach to in-cylinder thermal analysis of components, listing suitable bulk convective transfer coefficients as noted in table 7.1. Bulk temperatures are given as the average cylinder gas temperature throughout its cycle.

$h_1=310\text{W/m}^2\text{K}$	$h_2=490\text{W/m}^2\text{K}$	$h_3=240\text{W/m}^2\text{K}$
$h_4=490\text{W/m}^2\text{K}$	$h_5=350\text{W/m}^2\text{K}$	$h_6=90\text{W/m}^2\text{K}$
$h_7=1880\text{W/m}^2\text{K}$	$h_8=320\text{W/m}^2\text{K}$	$h_9=200\text{W/m}^2\text{K}$
$h_{10}=800\text{W/m}^2\text{K}$	$h_{11}=700\text{W/m}^2\text{K}$	$h_{12}=200\text{W/m}^2\text{K}$
$h_{13}=50\text{W/m}^2\text{K}$	$h_{14}=320\text{W/m}^2\text{K}$	$h_{15}=2500\text{W/m}^2\text{K}$
$h_{16}=50\text{W/m}^2\text{K}$	$h_{17}=50\text{W/m}^2\text{K}$	

Table 7.1 Mean heat transfer coefficients used in diesel piston analysis  
(**Abbes *et al*, (2004)**)

Table 7.1 shows a range of heat transfer coefficients ranging from 50 to 2500W/m<sup>2</sup>K. By means of altering the regional bulk temperature (combustion chamber, piston under-crown, water jacket, etc.) this results in a close fit to the measured data, and by extrapolation to the physically unmeasured areas. Appendix 5.4 details the methods used to calculate physical part



running temperatures. In accordance with Newton's law of cooling this method involves two unknowns in steady state approximation a) bulk temperatures and b) the relevant heat transfer coefficients (HTC). As HTC's vary widely and are in effect a composite of heat flow phenomena (**Coulson and Richardson, (1999)**), the chosen method is to fix the bulk temperatures at an experimentally averaged value and modify the starting transfer coefficients until the resulting analytical temperature agrees with the temperature values from the hardness measurements.

The finite element method was used on a suitably de-featured half model due to one axis of symmetry. The correct outer 'barrel' and 'elliptical' forms were applied to the piston and the maximum diameter was set as 95.911mm. The resulting thermal distribution and displacement are given in figures 7.14 and 7.15.

Actual heat transfer coefficients and fixed boundary temperature values utilised to produce figs 7.14, 7.15, 7.18 and 7.19 are detailed in Appendix 5.1.

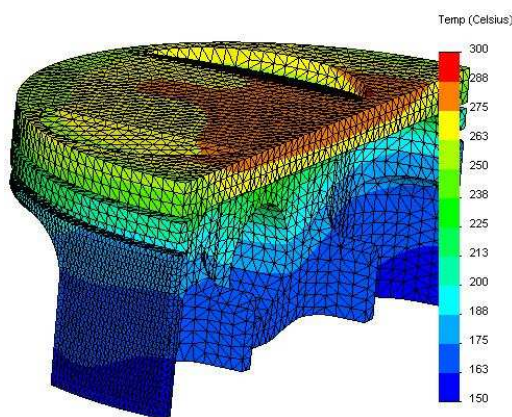


Figure 7.14 P1084 Predicted temperature

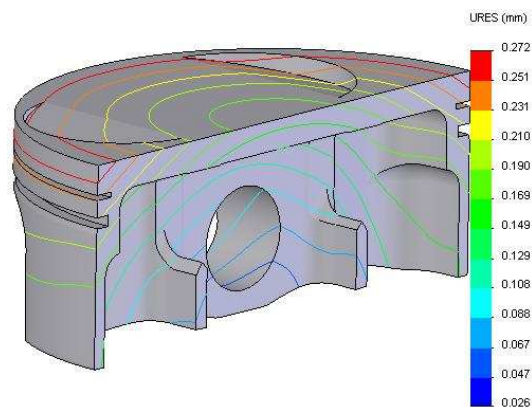


Figure 7.15 P1084 Thermal displacement

For the cylinder liner service temperature is typically below that resolvable by annealed hardness correlation. **Kumar *et al* (2004)** report that the internal surface temperature profile decreases from 155°C at the cylinder top to 110°C at its base. Research conducted at Capricorn Automotive Ltd (fig 7.16), cross-referenced by (fig. 7.17), yields a general trend for wet aluminium liners in 4-stroke high performance engines of 25°C above the mean coolant temperature in the working contact area of the piston skirt. For this work the experimental coolant temperature was set at 95°C. The resulting temperature distribution and thermal displacement of the L2017 liners are given in figures 7.18 and 7.19.

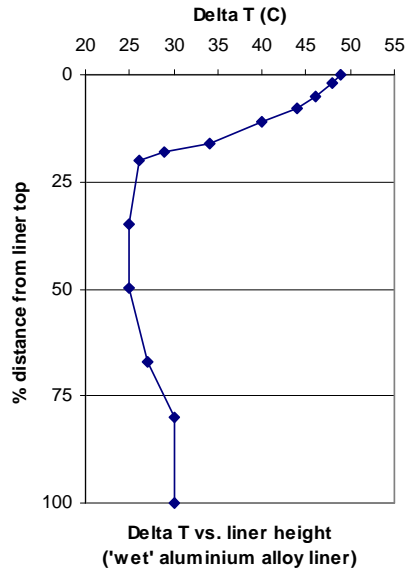


Figure 7.16 'Wet' liner surface temperature differential

Figure 7.17 'Wet' liner surface temperature profile

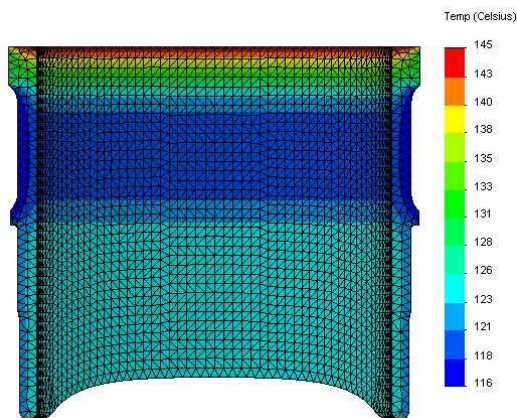


Figure 7.18 Thermal distribution in liner

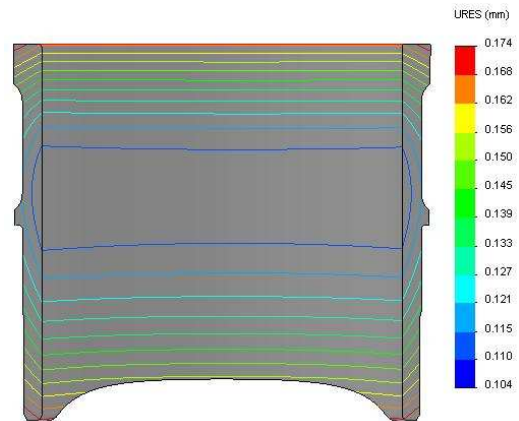


Figure 7.19 Resulting thermal displacement (x,y,z)

Figure 7.22 shows side by side the absolute thermal displacement of the piston and the liner as well as structural effects discussed below.

#### 7.4.3 Calculation of thermo-structural distortion

Differential temperature within the IC cylinder combined with varying loads results in a complex multi-physics load set. A quasi-static thermo-structural (QSTS) FEA model is constructed containing the cylinder bore, the piston, and a representative gudgeon pin / connecting-rod small end. Loads from chapter 3 (verified and expanded in appendix 1) are then applied and suitable contacts are made between the contiguous bodies. Boundary constraints (appendix 5) are so chosen in order to least influence the results and achieve

correlation to the actual engine parts, requiring the use of an artificial cylinder head. Figures 7.20 and 7.21 show the model developed for QSTS analysis.

Figure 7.20 shows the constraints used in the QSTS analysis. A half-model is used with a symmetrical constraint on all the cut body faces. An idealised cylinder head is used to join this to the cylinder liner, whose inner surface is subjected to the same thermal loading as the piston crown. This allows the upper portion of the cylinder liner to expand due to any temperature rise in the radial direction, whilst it ensures that the top liner surface remains nominally horizontal as in a typical gasket sealed cylinder head-to-liner interface.

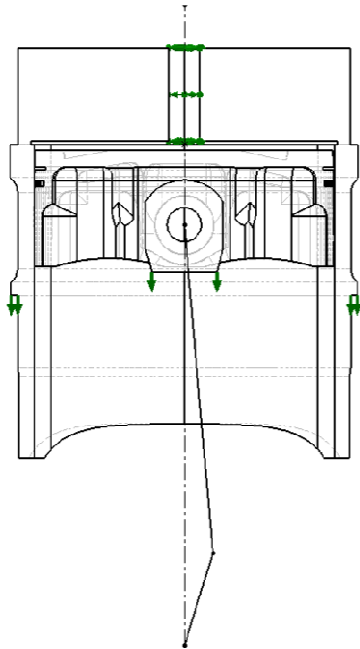


Figure 7.20 QSTS constraints

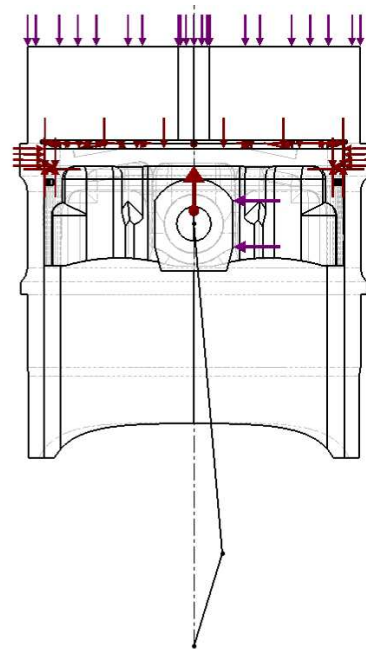


Figure 7.21 QSTS loads

A force is applied to the upper surface of the idealised head to represent the cylinder head bolt torque loads and a vertical hole in the centre of the idealised head ensures global restraining of the liner assembly. The lower flange on the liner's outside diameter is constrained vertically, as is the lower face of the idealised gudgeon-pin / connecting rod small end. The piston is only constrained by the symmetrical cut face and contacts formed between the idealised gudgeon pin and the liner's internal surface. Therefore, the piston is able to tip and translate towards the cylinder bore, as well as deform due to pin bending. This constrained system remains common for all the load cases considered in this thesis.

Figure 7.21 displays the forces applied to the assembly (refer to Appendix 5 for exact values). Thermal deformation (fig. 7.22) is calculated first by a subroutine, and the forces and pressures are then applied. Figure 4.9 provides a flowchart for the steps required to calculate deformed piston and liner profiles at any instant of time (crank-angle position). Appendix 3 provides additional details and the resulting contact ‘footprints’.

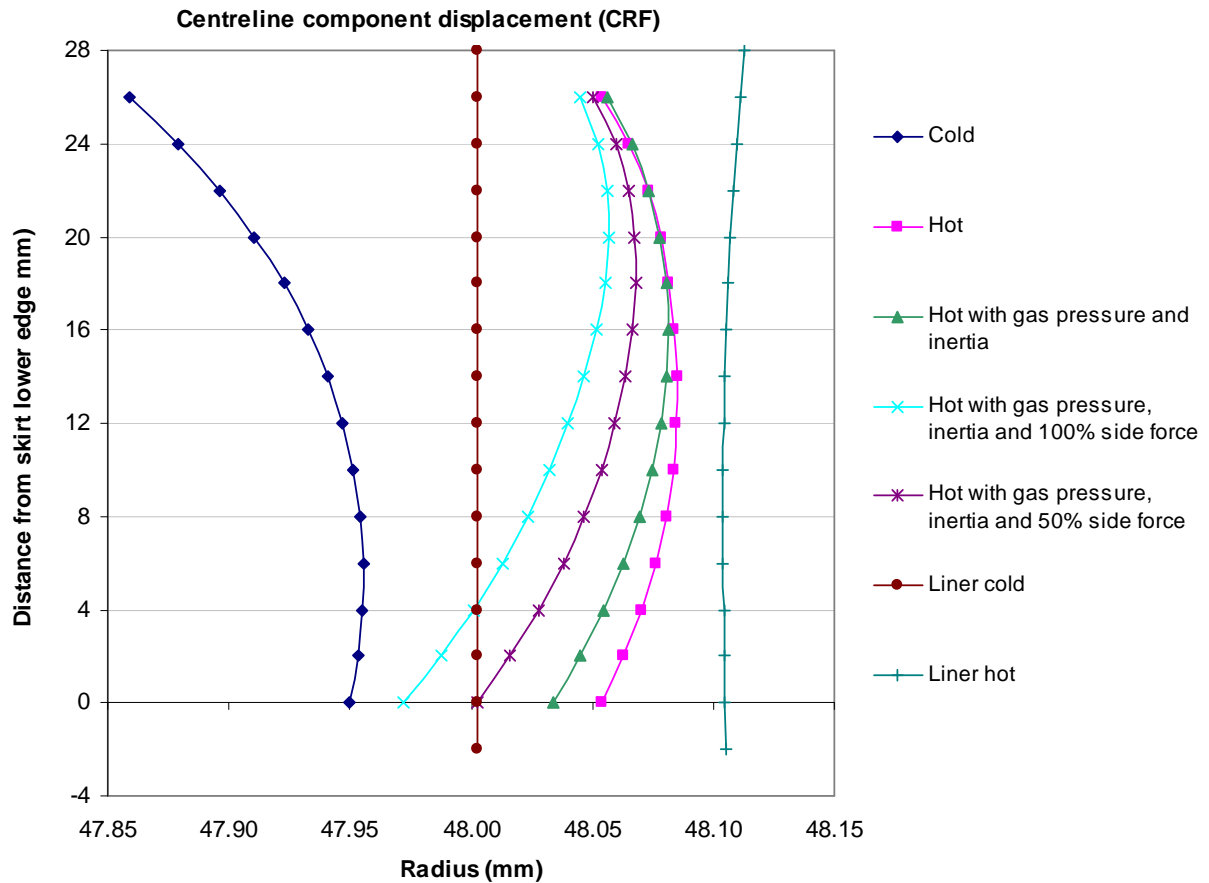


Figure 7.22 CRF skirt and bore distortion

From figure 7.23 several key crank angular positions with high resulting contact pressure can be noted. These are in line with **Kim *et al* (2009)**, noting their occurrence over a large portion of the thrust part of the cycle. Combustion starts immediately prior to the top dead centre in the power stroke. However, the in-cylinder pressure does not reach a maximum until  $11^\circ$  crank-angle (figure 7.24a) after the top dead centre. Although the vertical force is a maximum, overall side force is not a maximum due to the relatively low connecting rod obliquity. In fact the actual side force continues to increase, (maximum at  $26^\circ$  ATDC) though it maintains a similar footprint (figure 7.24c).

The peak side force occurs at  $26^\circ$  after top dead centre (figure 7.24c). After this position side and combustion forces begin to or are in decline. However, due to the geometric behaviour of the cylinder structure, contact pressures actually increase. This is due to the relative lack of conformability in the liner central portion, where a stiffening rib is present in the case investigated here. Figure 7.24d details this phenomena and figures 7.1 and 7.2 show actual physical examples of this (high position piston skirt wear and mid-span wear on the cylinder bore (fig. 7.24e)). This finding, although in practice realised, is somewhat absent as an observation in literature.

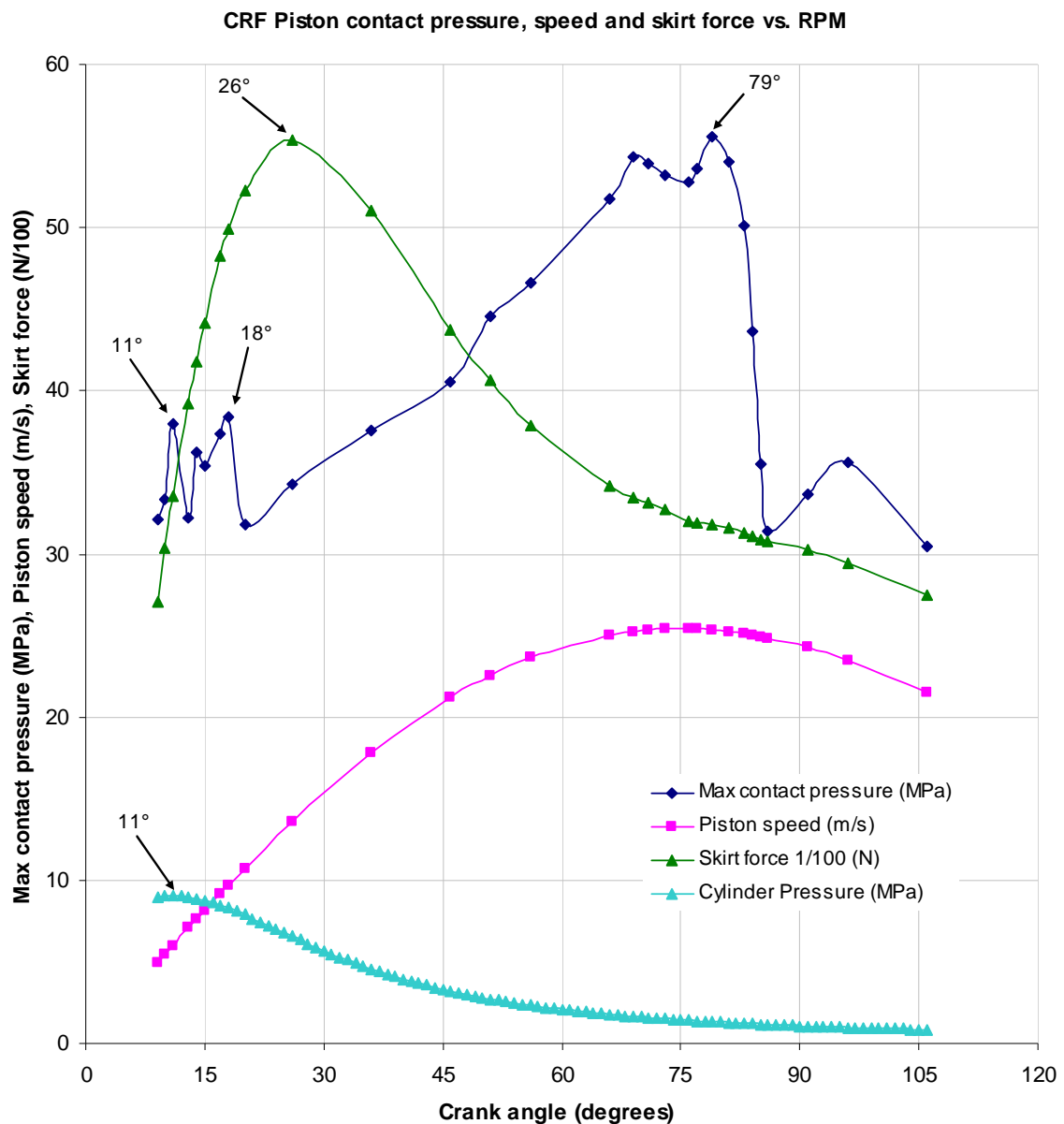


Figure 7.23 CRF analysis parameters vs. rpm.

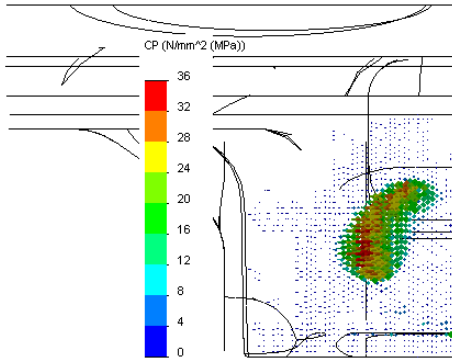


Figure 7.24a ATDC 11° footprint

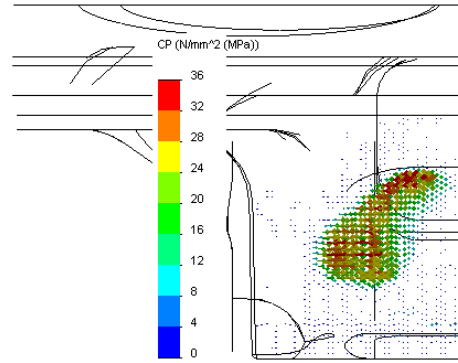


Figure 7.24b ATDC 18° footprint

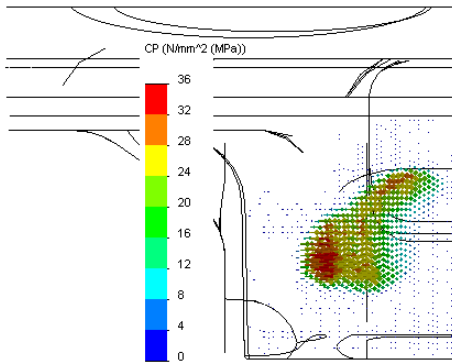


Figure 7.24c ATDC 26° footprint

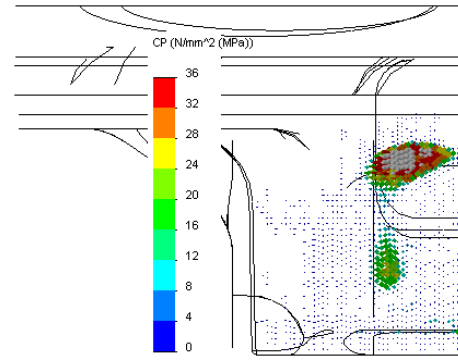


Figure 7.24d ATDC 79° footprint

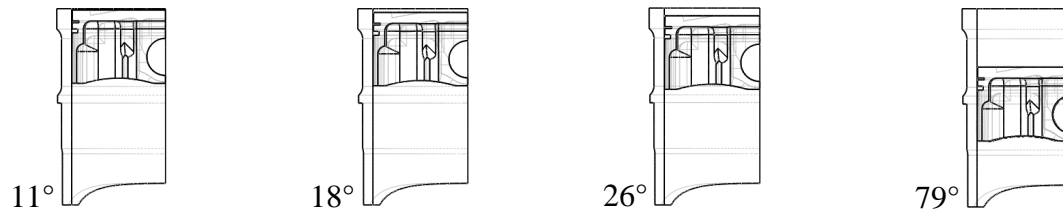


Figure 7.24e Relative footprint position of piston within liner

## 7.5 Thermo-elastic EHL

Chapter 4 and sections above describe the method used to generate deformed piston skirt and cylinder wall geometry. The resulting geometry is due to the combined effects of system forces, as well as thermal and differential thermal effects. Chapter 4.8 details the numerical solution procedure used to calculate lubricant reaction pressure and film thickness for these deformed geometries and operating conditions.

Figure 7.25 provides lubricant pressure distribution for the CRF P1084 piston to L2017 liner for the initial starting conditions dictated by an angular position of 18° ATDC (approx midway



between peak combustion pressure and peak side force). The lubricant properties used are given in Appendix 5.

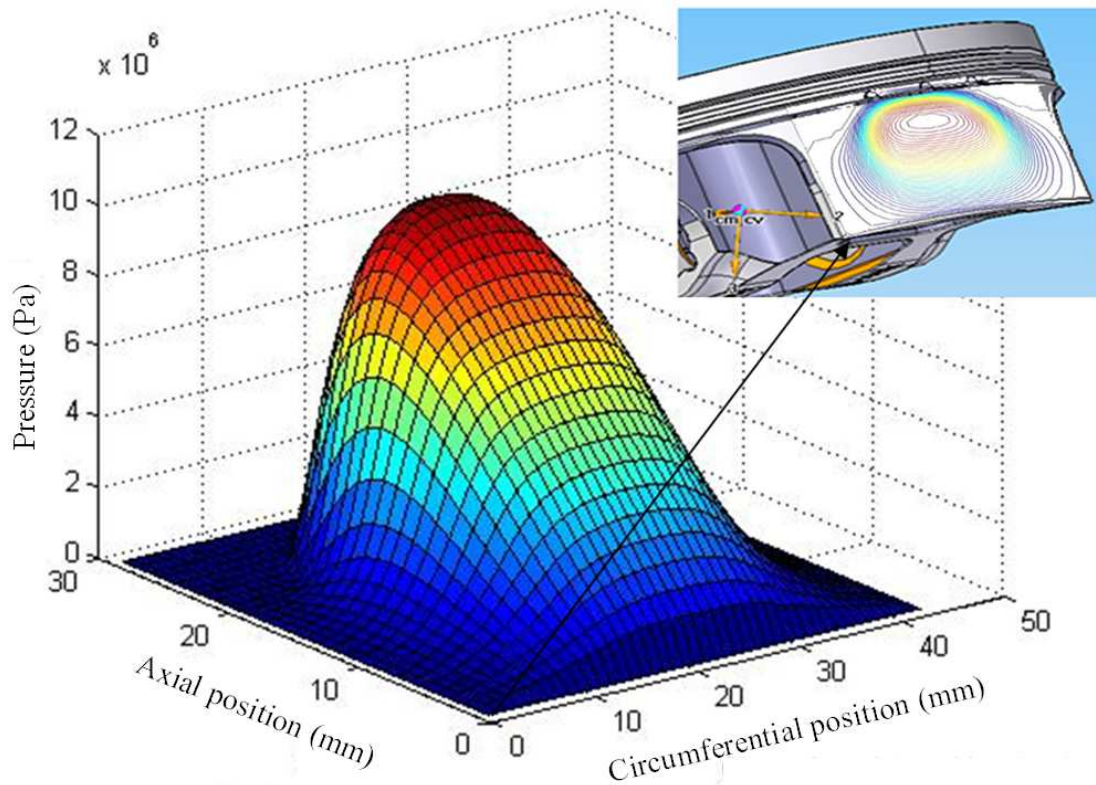


Figure 7.25 Lubricant pressure distribution (hot constrained skirt)

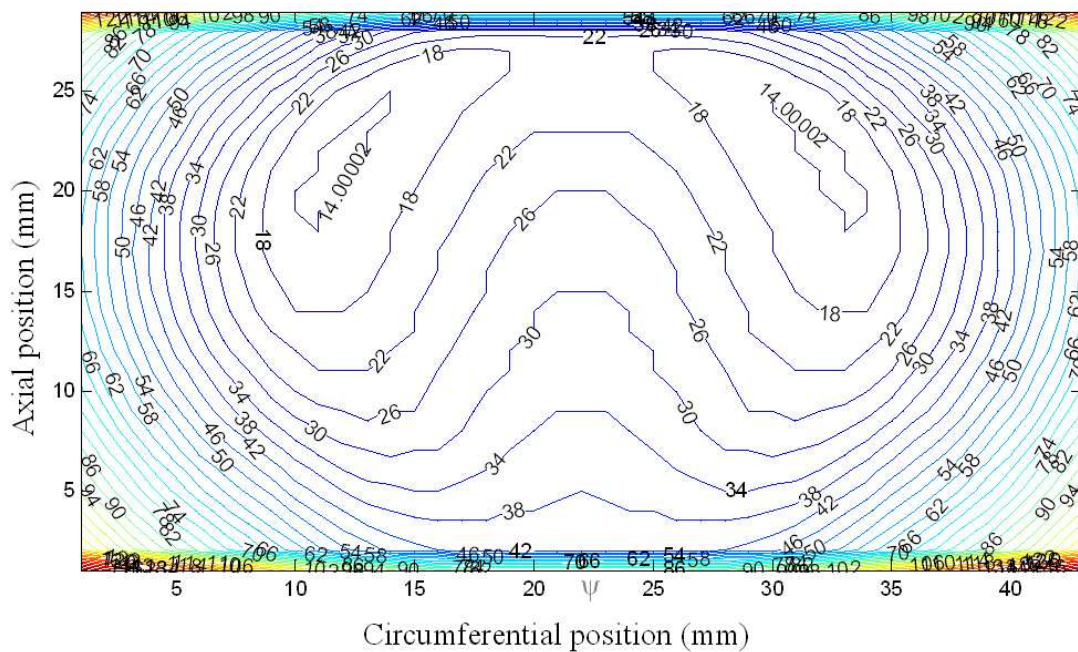


Figure 7.26a Film thickness ( $\mu\text{m}$ ) contour (hot constraint skirt)

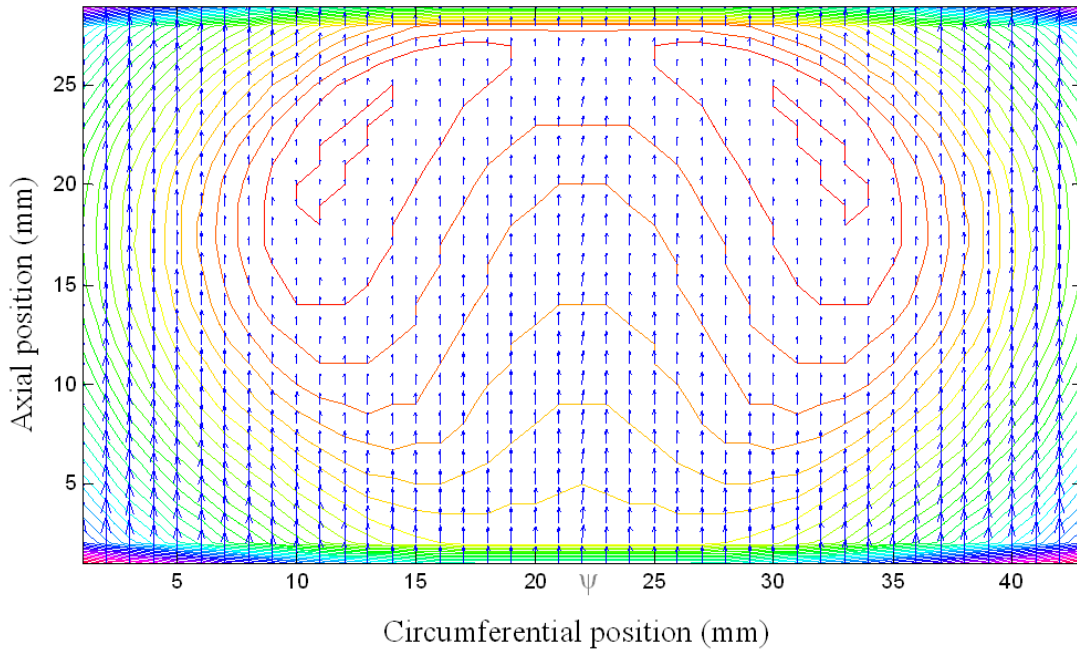


Figure 7.26b Lubricant mass flow vector plot (hot constraint skirt)

Figure 7.26a shows the resulting film thickness contours in micrometres and figure 7.26b figuratively displays lubricant mass flow. Although thicker than those previously reported for other cases, excluding those of thermo-structural (bulk) distortion, it can be seen that the film thickness minima occur in a similar position to that reported by structural contact calculation alone (fig. 7.24b).

Figure 7.27a superimposes the resulting film thickness from figure 7.26a over the actual run piston skirt (CRF with an assumed ‘smooth’ skirt). The regions of minimum film can be seen to clearly translate to regions of actual wear found, thereby validating the predictive methods used in this thesis.

Figure 7.27b provides a cut through the central skirt plane of figure 7.26a. It can be seen that oil film thickness reduces from the skirt lower edge towards a point below the oil ring position. Likewise, skirt structural stiffness also increases from the open edge to the oil ring position.

Both localised deformation due to lubricant reaction pressure and reaction pressure reaches a maximum mid-span along the skirt similarly, though in slightly differing positions; most likely due to the bottom-top variation in skirt stiffness.





Figure 7.27a Film thickness prediction overlay and actual run part

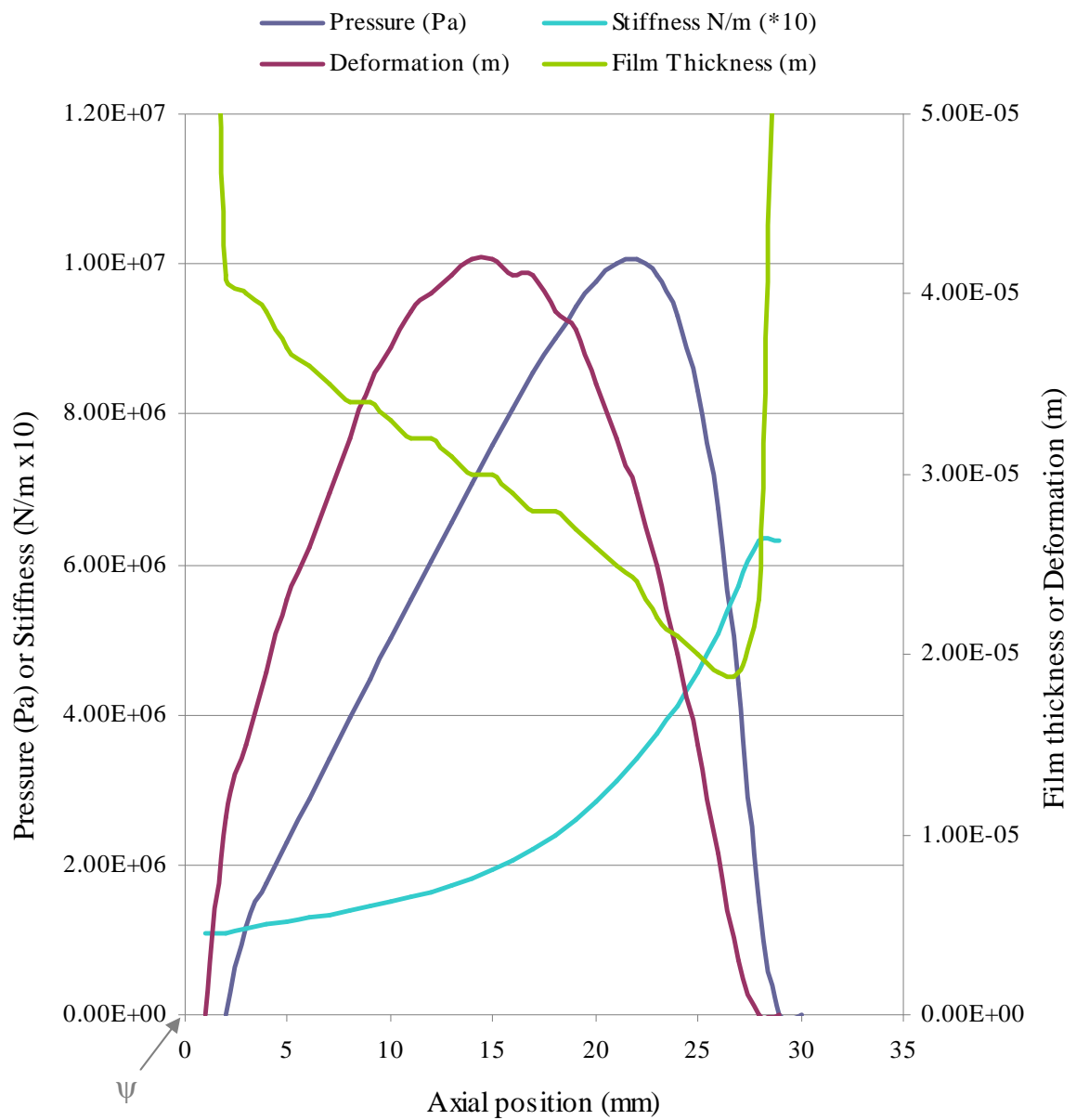


Figure 7.27b Parameter variation through skirt centre

## 7.6 Surface modification

The analysis carried-out here and in fact reported elsewhere (**Oh *et al* (1987)**, **Balakrishnan, Howell-Smith, Rahnejat, and Dowson (2003)**, **Balakrishnan, Howell-Smith, Rahnejat, (2005)** and **Offner and Pribsch (2000)**), show that in parts of the engine cycle fairly thin films of the order of a couple micrometres are predicted. With thermo-elastic deformation of the piston and increased conformity these thin films can alter. The situation is also exacerbated at the reversals, with cessation of entraining motion. Therefore, as already shown in this thesis, gradual wear of the surfaces can result with an inadequate film of lubricant. This situation is not uniquely applicable to the piston skirt conjunction, but to a host of tribological conjunctions at low speeds of entraining motion and insufficient pressures to induce piezo-viscous behaviour of the lubricant. This is particularly true of conforming or partially-conforming surfaces. They include various journal bearings and even hip joint arthroplasty. Of note, component wear has been noted by the author as a time-dependent phenomena. This is generally reported in automotive engineering as ‘breaking-in’, often resulting in rapid initial wear, thereby intimately modifying the contiguous surfaces. Once this initial wear has taken place a relatively long period of stability ensues, thereby requiring careful timeline (part life) analysis to be conducted before concluding geometric or surface suitability / degradation mechanisms.

A number of solutions have been used to either improve the load-carrying capacity of such contacts (increase the film thickness) or reduce the chance of ensuing wear where a sufficient lubricant film thickness cannot be assured. One solution is to introduce surface modifications. These include a number of distributed surface feature types (**Rahmani *et al*, (2007)**). **Rahmani *et al* (2007)** provide a review of various distributed surface feature forms. They classify these into two overall categories; *positive* or *negative* surface features.

Positive surface features are those that stand proud of the contact surface. The most common of these used by **Etsion (2010)** are hemispherical dimples. **Etsion** and **Sher (2009)** advocate the use of dimples, noting that such modified surfaces have shown improvements of the order of 3-4% in power output (attributed to reduced friction). Positive features improve lubricant film formation by a combination of lubricant retention through formation of menisci and creation of micro-wedges.

**Rahmani *et al* (2010)** refer to features that are cut into a contacting surface as a negative feature. Negative features are typically either etched, usually by laser, or are as the result of micro-indentation. The authors show through numerical analysis that distributed conical negative features lead to highest load carrying capacity, thus resulting in thicker lubricant films and consequently lower friction. Lubricant film formation with negative features is through micro-wedge effect as well as lubricant retention in the form of reservoirs / pockets of oil. Micro-indentation, although tried in this thesis (see chapters 5 & 6), can be a long fabrication process with difficulties in repeatability and control of depth of indentation, as well as plastic deformation of edges of the indentations requiring a further honing operation.

Laser etching is a far quicker process and, in combination with subsequent honing, results in a reasonably commercially economic method. Accurate control of the laser beam is required to create the required grooves on a concave surface (e.g. a cylinder liner) at a controlled depth. Issues with depth control and generated fume / weld splatter are the main drawbacks.

This problem is reduced considerably when laser ablation is carried out on convex surfaces such as on the piston skirt rather than on the liner's concave surface. However, surface 'roughening' is not necessary at all piston to bore / liner contact positions. This is desired where mixed or boundary regimes of lubrication are expected such as at the dead centres. Therefore introduction of laser-etched or turned features on the piston may lead to oil loss in parts of the piston cycle where a sufficient film of lubricant already exists, such as at mid-span and at high sliding speeds. This problem may also be viewed as an evolutionary one due to progressive industry reduction in crank case lubricant viscosity, where such issues become prevalent unless remedial actions are undertaken.

Nevertheless, problems of additional cost and slight oil loss are not viewed in the motorsport industry as critical as they might be regarded by the OEM market. Hence in this thesis negative features introduced by laser-etching and physical indentation have been used on the liner surface and for the piston skirt, laser etching and single point turning (Chapter 6). The numerical analysis is carried-out for the case of the single point turned piston skirts and is computationally very time and memory intensive.

**Rahnejat, Balakrishnan, King, and Howell-Smith (2006)** report on a case where curved shaped cavities (negative features) were cut into the surface of the liner (see chapter 6). These

appear in a pattern at the TDC position (figure 5.25 and **Howell-Smith, 2006**). In an alternative approach, features resembling an almost saw-tooth sinusoidal profile were turned onto the surface of a piston skirt, utilising a specially shaped polycrystalline diamond insert (figures 7.28 and 5.18) by the author after numerical predictions carried out by **Balakrishnan, Howell-Smith and Rahnejat (2005)** predicted potential significant improvement in the conjunctural oil film thickness. The saw-tooth nature of the modification pattern is as the result of sharp edges of the grooves cut by single point turning. Alternative methods are detailed in chapter 5, including physical roughening of the liner surface by indentation and laser milling of piston skirts.

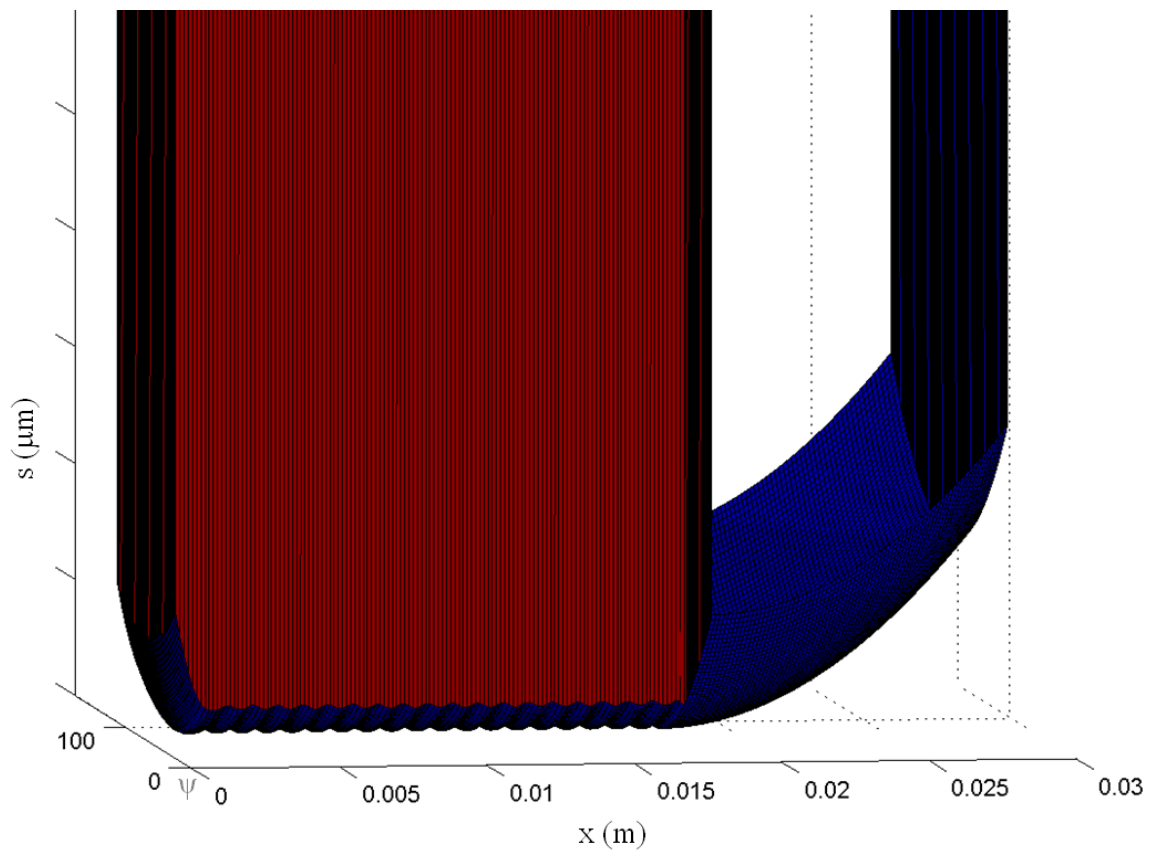


Figure 7.28 Modified skirt surface featuring an introduced sinusoidal waveform

This ‘skirt roughened by turning’ variation was analysed at the same position within the 4-stroke cycle as the previous macro-rigid skirt cases (nominally smooth ‘cold’ (chapter 7.2) and nominally smooth ‘hot’ (chapter 7.3)). This variation was analysed as isothermal ‘cold’ and due to analysing at the same crank angle, the contact kinematics and forces remain unaltered as per the previous smooth ‘cold’ skirt case.

Figures 7.29 and 7.30 show the generated pressure distributions. They detail the overall hydrodynamic pressure profile, rather similar in shape to that for the case of the nominally smooth ‘cold’ skirt in figure 7.4 except that the largest pressure spike occurs at the exit side of the contact (the right-hand spike in the figure). The magnitude of the pressure spike at the leading edge of the contact has reduced from that in figure 7.4 (see figure 7.31 for orientation). It can be seen that the overall mid-span pressure has increased, though exit pressure has also increased to a higher level than shown in figure 7.4. The reduction in inlet pressure is consistent with the increased film thickness in the lower to mid-skirt regions (figure 7.31). The exit side however shows a large length of film thickness reduction, thereby resulting in high exit pressures.

With this case the introduced surface features at right angles to the direction of entrainment produce a characteristic fluctuation in both the pressure profile and, to a lesser extent, film thickness. The overall hydrodynamic pressure profile is superimposed by small amplitude pressure fluctuations (referred to as pressure perturbations). These perturbations, superimposed on the hydrodynamic / elastohydrodynamic pressure distribution, are termed micro-hydrodynamic / micro-elastohydrodynamics.

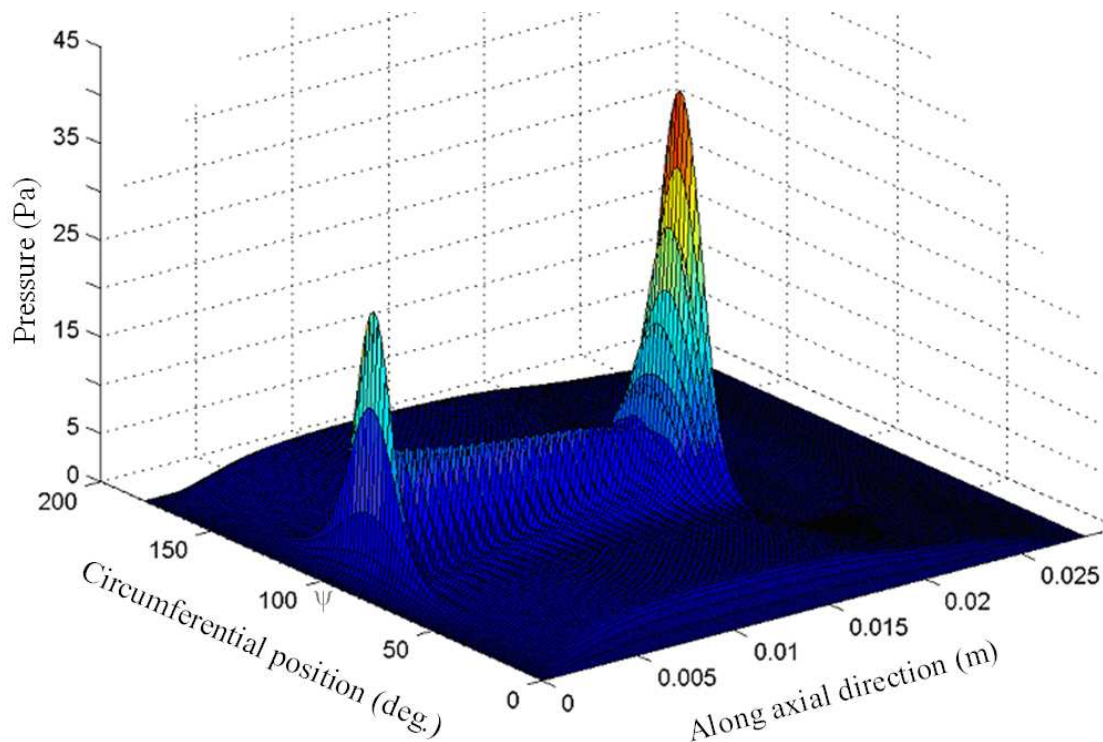


Figure 7.29 Lubricant reaction pressure vs. position on piston skirt

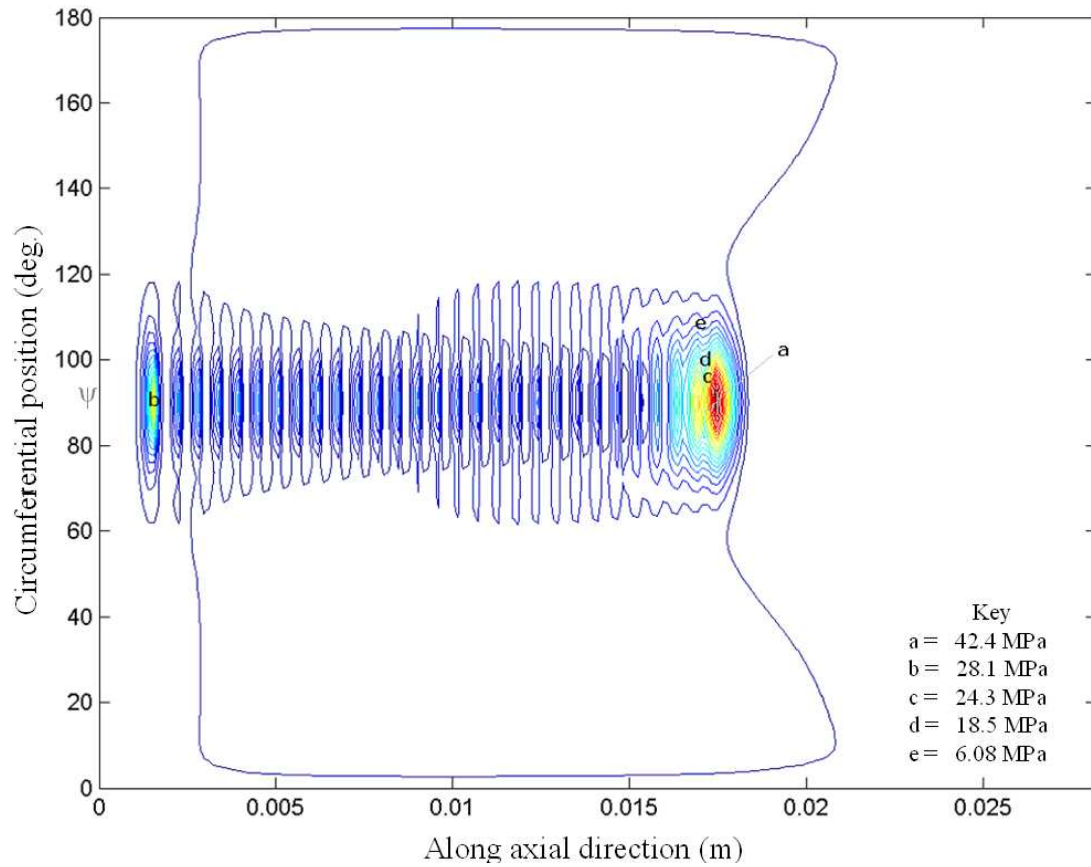


Figure 7.30 Lubricant reaction pressure vs. position on piston skirt

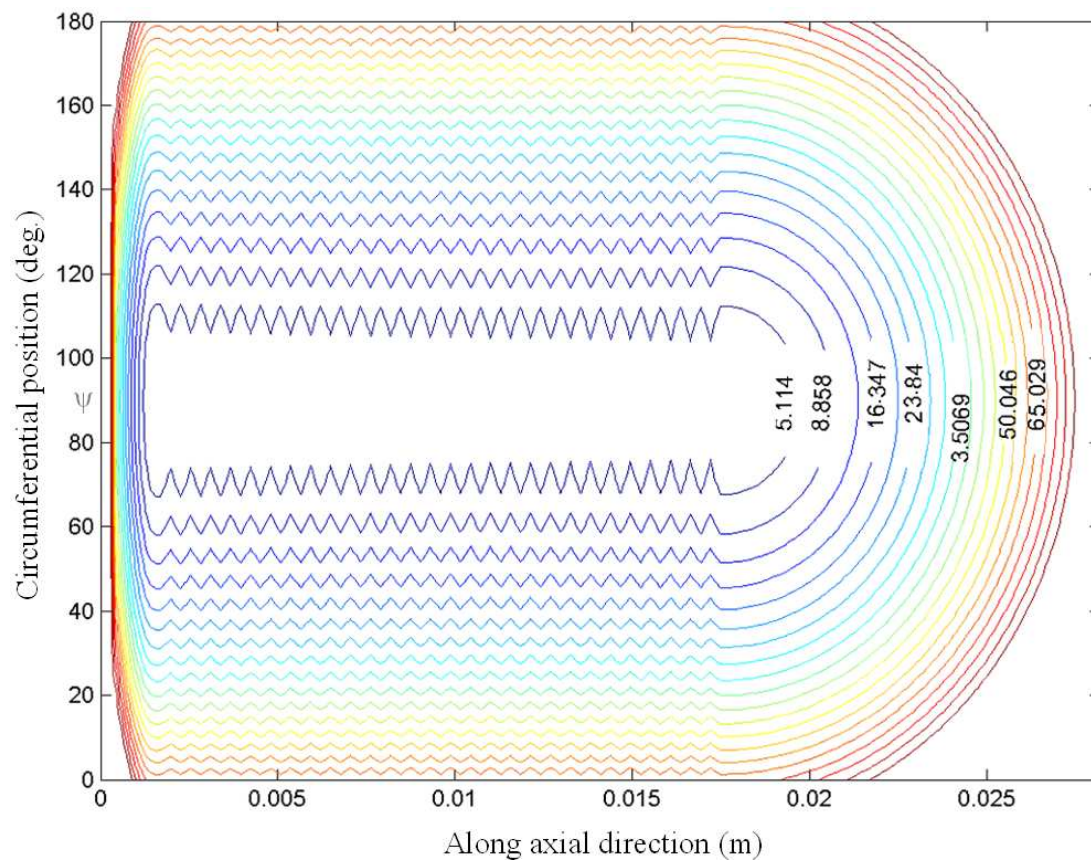


Figure 7.31 Unwrapped film thickness on piston skirt



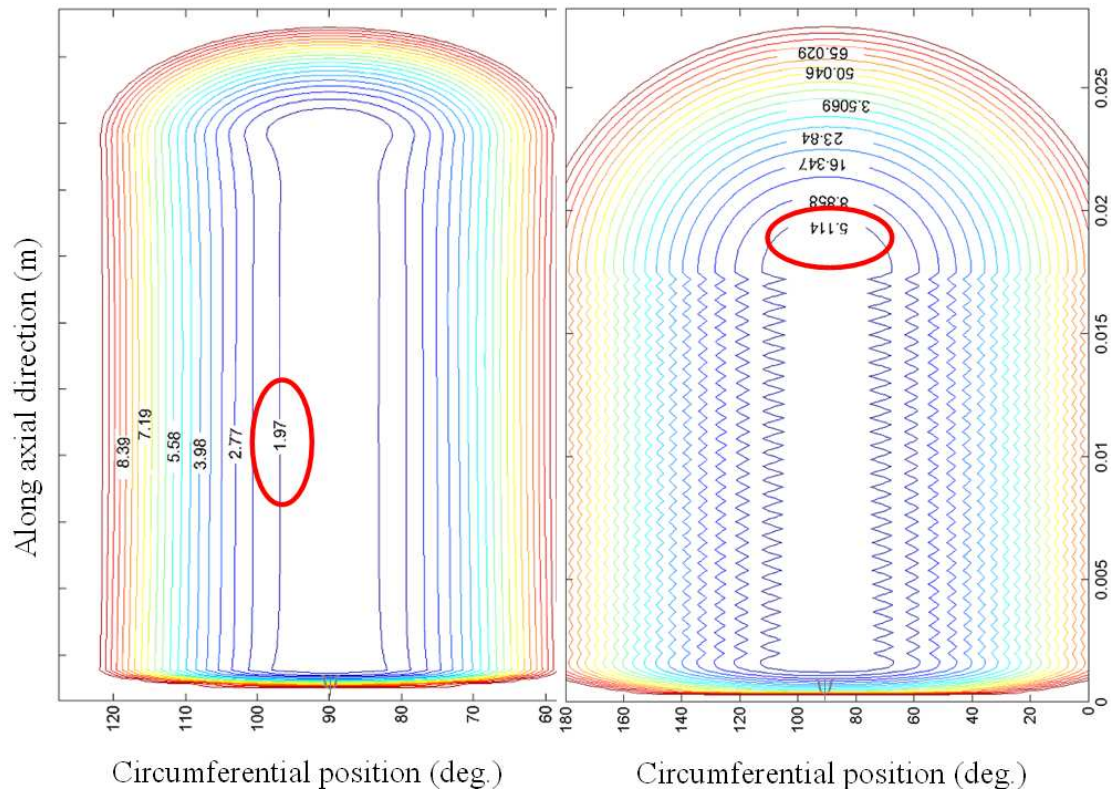


Figure 7.32 Comparison of predicted film thicknesses

Figure 7.32 shows a side-by-side comparison of the predicted film thickness between the ‘cold smooth’ (LHS) and ‘cold rough’ (RHS) skirt profiles. The images are rotated to represent in cylinder orientation and the differences in minimum film thickness ( $\sim 2 \mu\text{m}$  versus  $\sim 5 \mu\text{m}$ ) is clearly observed.

In conclusion, the combined numerical predictions and experimental results show the importance of constrained global thermo-elastic deformation of both the piston and the liner. These play an important role in piston skirt tribology which should not be ignored via use of isothermal analysis. Good agreement is found between the experimental findings and the numerical predictions throughout the thesis. This means that further improvements in piston skirt design, geometry, surface topography, and structural constraints should be motivated by in-depth numerical analysis. Although quite time-consuming this approach would significantly reduce the rather *ad hoc* trial-and-error basis of piston detail design which is currently prevalent in the industry.

## Chapter 8

### Overall conclusion & suggestions for future work

---

#### 8.1 Overall conclusions

Most traditional tribological solutions of the piston skirt-cylinder bore conjunction, may be regarded as of the ‘cold’ skirt type. In reality these isothermal solutions are a simplification as the *in situ* shape of the piston at any instant of time is governed by its thermo-elastic global deformation. This thermo-elastic global deformation also affects the shape of the liner thereby modifying the contact area or ‘footprint’ between the two bodies. This footprint is also affected by any localised stiffening of the piston, which causes a gradient in the skirt stiffness. The analyses presented in this thesis take into account such effects, leading to a true contact profile and the corresponding footprint.

The piston skirt-to-cylinder conjunction is generally considered as partially conforming. This conformance is greatly influenced by thermo-elastic influences on the bodies, as already noted. This also creates an opportunity to introduce localised structural stiffness alterations, to modify the contact area, which would directly benefit friction. Reduced stiffness regions within the footprint area would yield large deflections, thus enhanced film thickness (gap). However such modifications must not be to the detriment of other areas with symptoms such as stress concentrations and insufficient crown support. Therefore, the work reported here shows how piston skirt design can be extended to achieve the aims of reducing friction through improved skirt compliance. Note that generated pressures are usually insufficient to encourage piezo-viscous action of the lubricant, thus maintenance of the iso-viscous elastic regime of lubrication would be the aim.

Contrary to the common belief in practice, smooth piston skirts are not wholly the optimal solution. Indeed it has been shown that ‘rough’ surfaces with appropriate roughness amplitude can enhance the load carrying capacity of the contact. Thus for a given contact load, rough surfaces would exhibit higher lubricant film thickness and thus reduced friction. The proviso for this is to ensure that the right shape and dimensions are adhered to for rough profiles. This calls for the approach discussed in this thesis. A noteworthy point is that unintended consequences for surface modification must be mitigated, such as oil loss and blow-by.

This thesis has incorporated a variety of methods for engineering the conjunctural surfaces, including use of various coatings, cross hatching and plateau honing, diamond turning and



laser etching, as well as indentation of surfaces, all of which have been linked to the numerical predictions and fundamental tribological knowledge. This reduces the trial-and-error based developments. A point of caution is that the numerical analysis itself can be a long and arduous process. Therefore, an intimate mix of experimentation / measurement and numerical predictions is ideal; an approach which is highlighted in this thesis.

## 8.2 Achievement of aims

The following were the main objectives of this research and a brief record of achievement of the same:

- Develop experimental rigs to determine actual part performance advised by predictions.

This has been achieved by devising and developing a motored engine test rig and a fired engine test-bed. These are described in detail in the body of this thesis. Additionally, fired engine tests were conducted by 3<sup>rd</sup> parties.

- Develop realistic thermo-elastic, thermo-elastohydrodynamic numerical codes / procedures and undertake simulation studies. These should direct a programme of experimentation. Both the numerical predictions and experimental measurements against standard accepted baselines should be carried-out in an iterative fashion, thereby collating a matrix of practical and ‘optimised’ configurations. Some of these configurations will be tested.

A combined thermo-elastic global deformation procedure using FEA and thermo-elastohydrodynamic finite difference method is used to carry out realistic analysis, of what is termed as the ‘hot’ skirt conjunction. Additionally, isothermal ‘cold’ skirt conjunction analysis has been carried-out with and without certain surface modifications. The former analysis is elastohydrodynamic, whilst the latter includes the pressure perturbations induced by surface modification features pertaining to micro-elastohydrodynamic analysis.

- Effect a reduction in the piston skirt-bore conjunction’s parasitic losses by means of piston skirt geometric and topographical optimisations, thereby increasing specific output and reducing specific IC engine fuel consumption for *in situ* geometry.

Various piston skirt profiles, pertaining to ‘cold’ skirt, unconstrained ‘hot’ skirt and constrained ‘hot’ skirt due to structural stiffening, are reported in the thesis.

- Demonstrate by experimental means the effectiveness of the proposed solution and its robustness.

Experimental work carried out on motored and fired engines have confirmed numerical predictions with remarkable agreement in film thickness prediction and measurement using an ultrasonic sensor for the ‘cold’ skirt condition.

### 8.3 Contributions to knowledge

The approach in the analysis of the piston skirt conjunction, referred to as ‘hot’ is new, unlike the ‘cold’ isothermal elastohydrodynamic analysis employed by most authors such as **Balakrishnan and Rahnejat (2005)**, **Balakrishnan, Howell-Smith and Rahnejat (2005)**, **Dowson *et al* (1983)**, and **Knoll and Peeken (1982)**, among others. This approach is only reported by **McClure (2007)**. This thesis provides a methodology for the quantitative design of the piston skirt-cylinder wall through combined thermo-structural and lubrication analysis.

Micro-elastohydrodynamic analysis is reported here as previously reported by **Balakrishnan, Howell-Smith and Rahnejat (2005)** for an isothermal nominally ‘smooth cold’ skirt elastohydrodynamic analysis. The results agree remarkably well with the measured film thickness using an ultrasonic sensor (**Dwyer-Joyce, Green, Balakrishnan, Harper, Lewis, Howell-Smith, King, Rahnejat, 2006**).

Various laser etched, indented, or diamond turned surface modified liners, cross hatched and honed, were tested under fired engine conditions and they were bench-marked against the standard OEM liner. Gains in power of the order of 2-4% are reported. This work is cited by the leading researchers in the field such as **Etsion and Sher (2009)** and **Etsion (2010)**.

### 8.4 Critical assessment and suggestions for future work.

Combining micro-elastohydrodynamic analysis with a thermo-elastically deformed skirt and liner is the ultimate goal of analysis. This is likely to pose problems in computation times and long-duration model development. Whilst thermo-elastohydrodynamics is a generic

methodology thermo-elastic global deformation would depend on piston construction. It is this latter issue which contributes to protracted model building times.

In terms of both experimentation and analysis, whilst surface feature optimisation is a key issue for enhanced load carrying capacity and reduced friction, the drawback may be oil loss and blow-by at high speeds and under flooded conditions. Controlled experiments would still be required to ascertain / establish exact feature geometry and distribution, as well as their location on the cylinder liner or piston.

This thesis has treated surface coating as semi-infinite solids of fairly high elastic modulus. The implication is that the pressures generated are mainly due to the lubricant and global deformation of contiguous surfaces. This may not be the case if footprint areas are reduced significantly and coating thickness is small enough to cause small localised elastic deformation. Under such conditions increased pressures can lead to exfoliation of coatings.

This thesis presents results for the position of maximum combustion pressure whereas problems at the reversal points (lack of entraining motion) have also been highlighted. The analysis at these locations should also extend beyond the detailed work reported by **Balakrishnan, Howell-Smith, Rahnejat and Dowson (2003)**.

## References

- Abbes, M.T., Maspeyrot, P., Bounif, A. and Frene, J.** (2004): A thermomechanical model of a direct injection diesel engine piston, Proc. Instn Mechanical Engineers Vol. 218 Part D.
- Abbey, T.** (2004): Elements of Finite Element Analysis, Desktop Engineering, Dublin, New Hampshire, December 2004.
- Abe, S. and Suzuki, M.** (1995): Analysis of Cylinder Bore Distortion During Engine Operation, International Congress and Exposition Detroit Michigan, SAE 1995.
- Akalin, O. Newaz, G.M.** (1998): A new experimental technique for friction simulation in Automotive Piston Ring and Cylinder Liners, SAE Powertrain Tribology SP-1372, Dearborn, Michigan (981407).
- Alsaad, M., Bair, S., Sanborn, D.M. and Winer, W.O.** (1978): Glass Transitions in Lubricants: Its Relation to EHD Lubrication, ASME Paper No. 77-Lub-3 (to be published in Trans. ASME, Journal of Lubrication Technology).
- Amontons, G.** (1699): Mémoires de l'Académie Royale A, pp257-282.
- Andersson, B.S.** (1991): 'Company's Perspective in Vehicle Tribology.' Leeds-Lyon Symposium on tribology, pp503-506.
- Anno, J.N., Walowit, J.A. and Allen, C.M.** (1968): Microasperity Lubrication, ASME Journal of Lubrication Technology, Vol. 90, pp351-355
- Anno, J.N., Walowit, J.A. and Allen, C.M.** (1969): Load Support and Leakage from Microasperity-Lubricated Face Seals, ASME Journal of Lubrication Technology, Vol. 91, pp726-731
- ASM Handbook Volume 2** (1992): Properties and Selection – Nonferrous alloys and special purpose materials, ASM International.
- Balakrishnan, S.** (2002): Transient elastohydrodynamic analysis of piston skirt lubricated contact under combined axial, lateral and tilting motion PhD Thesis Loughborough University, Loughborough, UK.
- Balakrishnan, S. and Rahnejat, H.** (2002): Transient elastohydrodynamic lubrication of piston skirt to cylinder wall. 3<sup>rd</sup> Aimeta International Tribology Conference.
- Balakrishnan, S. and Rahnejat, H.** (2005): Isothermal Transient Analysis of Piston Skirt-to Cylinder Wall Contacts under Combined Axial, Lateral and Tilting Motion, J. of Phys., D: Appl. Phys., 38, pp787-799.
- Balakrishnan, S., Howell-Smith, S., Rahnejat, H.** (2005): Investigation of reciprocating conformal contact of piston skirt to surface modified cylinder liner in high performance engine. IMechE Vol.219 Part C.
- Balakrishnan, S., Howell-Smith, S., Rahnejat, H. and Dowson, D.** (2003): Investigation of reciprocating conformal contact of piston skirt and ring pack to cylinder liner under transient condition, 30<sup>th</sup> Leeds-Lyon Symposium.
- Barran, M.** (1996): Eric Weisstein's World of Biography, <http://scienceworld.wolfram.com/biography/Boussinesq.html>.
- Barus, C.** (1893): Isothermals, Isopiestic and Isometrics Relative to Viscosity, Am. J. Sci.,

- 45, 87.
- Becker, E.P. and Ludema, K.C.** (1999): A qualitative empirical model of cylinder bore wear, *Wear* 225-229 (1999) 387-404.
- Belgacem, F.B., Hild, P., Laborde, P.** (1998): The mortar finite element method for contact problems, *Mathematical and Computer Modelling*, volume 28 (4-8), pp263-271.
- Bhatt, D.V, Bulsara, M.A. and Mistry, K.N.** (2009): Prediction of oil film thickness in piston ring-cylinder assembly in an IC Engine: A review, *Proceedings of the World Congress on Engineering 2009 Vol, 2, WCE July 1-3, London, UK.*
- Bigelow, R., and Progen, J.** (1999): *Mathematica Structural Mechanics Documentation*, Wolfram Research Inc. [www.reference.wolfram.com/applications/structural/FiniteElementMethod](http://www.reference.wolfram.com/applications/structural/FiniteElementMethod).
- Boissat and Nicolas** (2007): *Validation CosmosWorks 2008*, Solidworks Corporation Inc, Concord, MA.
- Bolanca, Z. and Hladnik, A.** (2000): Some Properties of the Anodized Aluminium Surface, 15<sup>th</sup> World Conference on NDT, Rome, Italy.
- Bolegoh, G. S.** (2001): *Pumps Reference Guide*, 3<sup>rd</sup> Edition, Ontario Power Generation, Canada.
- Bosch** (2007): *Automotive Handbook*, 7th Edition, John Wiley and Sons.
- Boussinesq, J.** (1885): *Essai théorique sur l'équilibre des massifs pulvérulents comparé à celui des massifs solides, et sur la poussée des terres sans cohésion*. 2nd ed. Brussels.
- Boysal, A. and Rahnejat, H.** (1997): Torsional vibration analysis of a multi-body single-cylinder internal combustion engine model. *Journal of Applied Mathematical Modelling*, 21, pp. 481-493.
- Brett, P.** (2009): Personal communication between P. Brett (Castrol, UK) and the author regarding in service lubricant properties.
- Brown, M.A., McCann, H. and Thompson, D.M.** (1993): Characterization of the oil film behaviour between the liner and piston of a heavy duty diesel engine. *Tribological Insights and Performance Characteristics of Modern Engine Lubricants*, SAE/SP-93/996/932784.
- Cameron, A.** (1981): *Basic Lubrication* 3<sup>rd</sup> Edition, Ellis Harwood Ltd., John Wiley & Sons.
- Cameron, A., and Gohar, R.** (1966): Theoretical and Experimental Studies of the Oil Film in Lubricate Point Contacts, *Proc. Roy. Soc., London, Series A*, Vol. 291, pp520-536.
- Capricorn Automotive Ltd (2008)**: Market observations made by Mr R Burggy 2008.
- Carden, P.** (2008): *Tribology in Motorsport*, IMechE/IOP Conference, Castrol UK, Pangbourne UK.
- Cho, S., Choi, S. and Bae, C.** (2000): Frictional modes of barrel shaped piston rings under flooded lubrication, *Tribology International* 33 545-551.
- Cho, S., Choi, S. and Bae, C.** (2002): An Experimental measurement of lubrication behaviour of piston rings in a spark ignited engine.
- Cho, S.H., Ahn, S.T. and Kim, Y.H.** (2002): A simple model to estimate the impact force

- induced by piston slap, *Journal of sound and vibration* 255(2), 229-242.
- Choi, Y., Jeong, P., Kim, D. and Hong, J.** (1993): Analysis of thermal conduction in piston of Gasoline engine by boundary element method, SAE technical paper-931907, pp1-9.
- Clough, R.W. and Wilson, E.L.** (1999): Early finite element research at Berkeley, the 5<sup>th</sup> US National Conference on Computational Mechanics, 4<sup>th</sup>-6<sup>th</sup> August, 1999.
- Cook, A.W.** (1958): The Lubrication of Rollers, Part 1, *Phil. Trans. Roy. Soc., London, Series A*, Vol. 250, pp387-409.
- Coulomb** (1781): *Théorie des machines simples*. Par C.A. Coulomb, nouvelle edition (1821), Bachelier, Libraire, quai des Augustins.
- Coulson, J. and Richardson, J.** (1999): *Chemical Engineering, volume 1: Fluid flow, heat transfer and mass transfer*, Butterworth-Heinemann, sixth edition, pp382.
- Critchlow, G.W., Litchfield, R.E., Sutherland, I., Grandy, D.B. and Wilson, S.** (2006): A review and comparative study of release coatings for optimised abhesion in resin transfer moulding applications, *Int. Journal of Adhesion and Adhesives*, Vol. 26, Iss. 8, pp577-599.
- D'Agostino, L., della Valle, S., Ruggiero, A. and Senatore, A.** (2002): A study on the piston top ring lubrication using the open-end boundary condition, *Proc. 3rd AIMETA International Tribology Conference*, Salerno, Italy 18-20 September 2002.
- Dearlove, J and Cheng, W.K.** (1995): Simultaneous piston ring friction and oil film thickness measurements in a reciprocating test rig, *Recent snapshots and insights into Lubricant technology SAE (SP-1116)*, (952470).
- Dell and Rand** (2004): *Clean Energy*, The Royal Society of Chemistry, 2004.
- Diaconescu, E., Zegrean, V. and Miron-Onciul, O.** (2007): Viscosity of amorphous molecular substances, *Proceedings of 10th International Conference on Tribology, ROTRIB'07*, Bucharest, November 2007, RO097-1-RO097-6, ISBN 978-973-78-38-49-0.
- Dieterichs, E.F.** (1916): *A Practical Treatise On Friction, Lubrication, Fats And Oils*, Henry Carey Baird & Co.
- Donnet, C. and Erdemir, A.** (2004): Solid lubricant coatings: recent developments and future trends, *Tribology Letters* Vol. 17, No. 3, October 2004.
- Douglas, R.M., Steel, J.A. and Reuben, R.L.** (2006): A study of the tribological behaviour of piston ring/cylinder liner interaction in diesel engines using acoustic emission, *Tribology International* 39 (2006) 1634-1642.
- Dowson, D.** (1979): *History of Tribology*. Longman Group Limited, London.
- Dowson, D. and Higginson, G.R.** (1959): A numerical solution to the elastohydrodynamic problem. *Journal of Mechanical Eng. Science*, Part 1, Volume 6.
- Dowson, D., Ruddy, B.L. and Economou, P.N.** (1983): The Elastohydrodynamic Lubrication of Piston Rings. *Proc. R. Soc. Lond. A*, April 8, 1983 386:409-430; doi:10.1098/rspa.1983.0043.
- Dowson, D., Taylor, C.M. and Godet, C.M.** (1983): *Tribology of Reciprocating Engines*. 9th Leeds-Lyon Symposium on Tribology (Butterworth, Oxford), pp. 348.

- Dunaevsky, V. and Kudish, I.** (1988): Friction temperature generated by piston ring in a reciprocating oil-less compressor, SAE 982827.
- Dunaevsky, V. and Vick, B.** (2004): Friction temperature of the piston rings with consideration of the cylinder wall thickness, SAE Compression Ignition and spark ignition power cylinder systems (SP-1820), Detroit Michigan (2004-01-0612).
- Dursunkaya, Z. and Keribar, R.** (1992): Simulation of Secondary Dynamics of Articulated and Conventional piston assemblies, SAE Engine Tribology (SP-919), Detroit Michigan (920484).
- Duyar, M., Bell, D. and Perchanok, M.** (2005): A comprehensive piston skirt lubrication model using a mass conserving EHL algorithm. SAE International Paper, (SP-1964) Detroit, Michigan (2005-01-1640).
- Dwyer-Joyce, R.S., Drinkwater, B.W. and Donohoe, C.J.** (2002): The measurement of lubricant-film thickness using ultrasound, The Royal Society, London, 459, 957-976.
- Dwyer-Joyce, R.S., Green, D.A., Balakrishnan, S., Harper, P., Lewis, R., Howell-Smith, S., King, P.D. and Rahnejat, H.** (2006): The measurement of liner –Piston skirt oil film thickness by an ultrasonic means, SAE technical paper P5-06P-596 (2006-01-0648).
- Dwyer-Joyce, R.S., Harper, P. and Drinkwater, B.W.** (2004): A method for the measurement of hydrodynamic oil films using ultrasonic reflection, Tribology Letters, Vol. 17, No. 2, August 2004.
- Dyson, A., Naylor, H. and Wilson, A.R.** (1965): The measurement of oil film thickness in Elastohydrodynamic Contacts, Proc. Inst. Mech. Engrs., Vol. 180, Pt. 3B, pp119-134.
- ECR (Earnhardt Childress Racing) Ltd.** (2008), Personal correspondence between N. Hayes and S. Howell-Smith.
- Ejakov, M.A.** (2003): Piston and ring dynamics CAE, Analytical Powertrain Department, Ford Motor Company
- Ergen, O., Kurnaz, G., Soydemir, N., and Akalin, O.** (2008): Reduced oil consumption by laser surface texturing on cylinders, SAE International, Journal of Commercial Vehicles, Vol. 1, Issue 1 pp446-452 (2008-01-2688).
- Ertel, A.M. and Grubin, A.N.** (1949): Investigation of Scientific and industrial research. Book 30, Central Scientific Research Institute for Technology and Mechanical Engineering, Moscow.
- Etsion, I.** (2005): State of the art in Laser Surface Texturing, Journal of Tribology, 127(1), pp248-253
- Etsion, I.** (2010): Surface Texturing for In-Cylinder Friction Reduction, in Rahnejat (Ed.) Tribology and Dynamics of Engine and Powertrain, Woodhead Publications, London/New York.
- Etsion, I. and Sher, E.** (2009): Improving fuel efficiency with laser surface textured rings, Tribology Int., 42(4), pp. 542-547.
- Forbes, J.E. and Taylor, E.S.** (1943): A method for studying piston friction. NACA Wartime Report W-37.
- Fox, I.E.** (2005): Numerical evaluation of the potential for fuel economy improvement due to boundary friction reduction within heavy-duty diesel engines, J. Tribology

- International 38, pp265-275.
- Funatani, K., Kurosawa, K., Fabiyi, P.A. and Puz, M.F.** (1994): Improved Engine Performance Via Use of Nickel Ceramic Composite Coatings, International Congress and Exposition, Detroit Michigan, SAE 1994.
- Furuhashi S., Takiguchi M. and Tomizawa K.** (1982): Effect of piston and piston ring designs on the piston friction forces in diesel engines. SAE Technical Paper 810977.
- Furuhashi, S. and Sasaki, S.** (1983): New device for the Measurement of Piston Friction force in small engines, SAE paper 831284.
- Furuhashi, S. and Sasaki, S.** (1984): Effect of oil properties on piston frictional forces. JSAE Rev., November 1984, 15, 68-76.
- Furuhashi, S., Kojima, M., Enomoto, Y. and Yamaguchi, Y.** (1984): Some studies on two-ring pistons in Automobile Turbocharged gasoline engine, SAE technical paper 8401183.
- Galloway, E.** (1828): History of the Steam Engine from its earliest invention to the present time, 2nd edition, B Steill, Paternoster Row.
- Gao, J., Luedtke, W.D., Gourdon, D., Ruths, M., Israelachvili, J.N. and Landman, U.** (2003): Frictional forces and Amonton's law: From molecular to the macroscopic scale. J.Phys.Chem. B Vol 108 No.11. P3410-3425.
- Glideswell, J. and Korcek, S.** (1998): Piston ring/cylinder bore friction under flooded and starved lubrication using fresh and aged engine oils, SAE international (SP-1390), San Francisco California (982659).
- Goenka, P. and Meernik, P.** (1992): Lubrication Analysis of piston skirts, SAE international (SP-919), Detroit, Michigan (920490).
- Goenka, P.K., Paranjpe, R.S. and Jeng, Y.** (1992): FLARE: An integrated software package for friction and lubrication analysis of automotive engines – Part 1: Overview and applications, SAE international (SP-919), Detroit, Michigan (920487).
- Goetze** (1995): Piston Ring Manual 5<sup>th</sup> edition, AE Goetze GmbH, Burscheid, Germany.
- Gohar, R. and Rahnejat, R.** (2008): Fundamentals of Tribology, Imperial College Press, Covent Garden, London.
- Graddage, M.J., Czysz, F.J. and Killinger, A.** (1993): Field Testing to Validate Models Used in Explaining a Piston Problem in a Large Diesel Engine, J. Eng. Gas Turbines Power, Volume 115, Issue 4, pp721-782.
- Greene, A.B.** (1969): Initial visualization studies of piston-cylinder dynamic oil film behaviour. Wear, Volume 13, pp345.
- Greenwood, J.A. and Williamson, J.B.P.,** (1966): Contact of nominally flat surfaces, Proceedings of the Royal Society of London. Series A, Mathematical and Physical Sciences, vol. 295, pp300-319.
- Grubin, A.N.** (1949): Fundamentals of the Hydrodynamic Theory of Lubrication of Heavily Loaded Cylindrical Surfaces, in Investigation of the Contact Machine Components, Kh.F. Ketova, ed. Translation of Russian Book No. 30, Central Scientific Research Institute for Technology and Mechanical Engineering, Moscow.
- Hamilton, D.B., Walowit, J.A. and Allen, C.M.** (1966): A theory of Lubrication by



- Micro-irregularities, ASME Journal of Basic Engineering, Vol. 88 part D, pp177-185
- Hamrock, B.J.** (1980): Film Thickness for different regimes of fluid-film lubrication, NASA Technical Memorandum 81550
- Hamrock, B.J.** (1994): Fundamentals of fluid film lubrication, McGraw-Hill.
- Hamzehei, M. and Rashidi, M.** (2006): Determination of piston and cylinder head temperature distribution in a 4-cylinder gasoline engine at actual process, Proceedings of the 4<sup>th</sup> WSEAS Int. Conf. on heat transfer, thermal engineering and environment, Elounda, Greece, August 2006 (pp153-158).
- Hertz** (1896): Miscellaneous papers by H. Hertz. translated Jones and Schott, Macmillan, London pp146-162.
- Honda Motor Company** (2002): Owners Manual, CRF450R, Part number 69MEB510 00X69-MEB-6101.
- Hooke, C.J.** (1993): The minimum film thickness in line contacts during reversal of entrainment. Trans. ASME, J. Tribology, 1993, 115, 191-199.
- Hoult, D.P., Lux, J.P., Wong, V.W. and Billian, S.A.** (1988): Calibration of laser fluorescence measurements of lubricant film thickness in engines. SAE 881587.
- Howell-Smith, S.** (2002): Piston skirt profile computation. Internal design procedures, Capricorn Automotive Ltd.
- Howell-Smith, S.** (2006): 'Lose to Win', Race Engine Technology Summit, Motorsport World Expo, Cologne, 2006.
- Hutttton, D.V.** (2004): Fundamentals of Finite Element Analysis, The McGraw-Hill Companies.
- Inoue, T., Maeda, Y., Takeda, M. and Nakada, M.** (1989): Study of transient oil consumption of automotive engine. SAE 892110.
- Ioannides, E. and Pareti, G.** (1986): Fatigue life predictions in line contacts with and without edge stresses. Proc. International Conference on Fatigue of Engineering Materials and Structures, Proc. Institution of Mechanical Engineers, Volume 1.
- Ishimori, S., Shimizu, M., Honda, S., Otsuka, S. and Toyoda M.** (1977): The Metal Finishing Society Japan, 1977, 28(10), pp419-424.
- Jalali-Vahid, D., Rahnejat, H., and Jin, Z.M.** (1999): Elastohydrodynamic Solution for Concentrated Elliptical Contact of Machine Elements under Combined Entraining and Squeeze Film Motion. Journal of Engineering Tribology, Proceedings of the Institution of Mechanical Engineers, 212, 401-411.
- Jalali-Vahid, D., Rahnejat, H., Jin, Z.M. and Dowson, D.** (2001): Transient analysis of isothermal elastohydrodynamic circular point contacts, Proc. Instn. Mech. Eng., Vol. 215, Part C: J. Mech. Eng. Sci., pp 1159-1173.
- Johnson, K.L.** (1985): Contact Mechanics. Cambridge University Press, ISBN 0521-34796-3.
- Johns-Rahnejat and Gohar, R.** (1997): Point Contact Elastohydrodynamic Pressure Distribution and Sub-Surface Stress Field. in H Rahnejat and R Whalley (eds), Multi-Body Dynamics: Monitoring and Simulation Techniques-II, Mechanical Engineering Publications, London, ISBN 1-86058-064-5.

- Johns-Rahnejat, P.M.** (1988): Pressure and Stress Distribution Under Elastohydrodynamic Point Contacts. Ph.D. Thesis, Imperial College of Science and Technology, University of London.
- Jones, W. and Jansen, M.** (2005): Lubrication for Space Applications, NASA report CR-2005-213424.
- Jost, P.** (1966): The Jost Report, Lubrication (Tribology) – Education and Research. A report on the present position and industry needs, Department of Education and Science, HMSO, London.
- Kannel, J.W., Bell, J.C. and Allen, C.M.** (1965): 'Methods for Determining Pressure Distributions in Lubricated Rolling Contact,' ASLE Trans., 8, pp 250-270.
- Keribar, R. and Dursunkaya, Z.** (1992): A comprehensive model of piston skirt lubrication, SAE Engine Tribology (SP-919), Detroit Michigan (920483).
- Keribar, R., Dursunkaya, Z. and Venkatesh, G.** (1993): An integrated design analysis methodology to address piston tribological issues, SAE Engine Tribology (SP-919), Detroit Michigan (930793).
- Kerr, J.:** Cylinder Systems the Basics, Piston Products Group, AE Goetze, T&N Plc.
- Kim, K.,S., Godward, T., Takiguchi, M. and Aoki, S.** (2007): The effects of lubricating oil film thickness distribution on gasoline engine piston friction, SAE technical paper-offer number: 07PFL-667.
- Kim, K.,S., Shah, P., Takiguchi, M. and Aoki, S.** (2009): Part 3: A study of friction and lubrication behaviour for gasoline piston skirt profile concepts, SAE International (2009-01-0193).
- King, J.** (2007): 'The King Review of low carbon cars Part I: the potential for CO2 reduction' HMSO, October 2007.
- Kirk, A.T.** (1962): Hydrodynamic Lubrication of Perspex, Nature, Vol. 194, pp965-966.
- Kiuru, M. and Alakoski, E.** (2004): Low sliding angles in hydrophobic and oleophobic coatings prepared with plasma discharge method, Materials Letters, Vol. 58, Iss. 16, pp2213-2216.
- Kligermann, Y., Shinkarenko, A. and Etsion, I.** (2004): Improving tribological performance of piston rings by partial surface texturing, 2004 AIMETA International Tribology Conference, Rome, Italy.
- Knoll, G.D. and Peeken, H.J.** (1982): Hydrodynamic lubrication of piston skirts. Transaction of the ASME, Volume 104, pp. 504-509.
- Knopf, M., Eiglmeier, C. and Merker, G.** (1998): Calculation of Unsteady Hydrodynamic Lubrication and Surface Contact at the Piston-Ring / Cylinder-Liner Interface, Powertrain Tribology SP-1372, SAE, Dearborn, Michigan (981402).
- Kumar, P.R., Srinivas, P.N., Nelson, J.E.B. and Rao, S.S.** (2004): Experimental studies on energy appropriation in a single-cylinder diesel engine, The institution of engineers (India), Vol. 85 pp45-49.
- Kurbet, S.N. and Malagi, R.R** (2007): Review on effects of piston and piston ring dynamics emphasis consumption and frictional losses in internal combustion engines, SAE international, Naples, Italy (2007-24-0059).
- Kushwaha, M. and Rahnejat, H.** (2002): Transient Elastohydrodynamic Lubrication of

- Finite Line Conjunction of Cam to Follower Concentrated Contact, *J. Phys., Part D: Appl. Phys.*, 35, pp2872-2890.
- Kushwaha, M. and Rahnejat, H.** (2004): Transient concentrated finite line roller-to-race contact under combined entraining, tilting and squeeze film motions, *Journal of Physics D: Applied Physics*, Volume 37, Number 14, pp2018-2034.
- Kushwaha, M., Rahnejat, H. and Gohar, R.** (2002): Aligned and misaligned contacts of rollers to races in elastohydrodynamic finite line conjunctions. *Proc. Instn. Mech. Engrs.* Vol. 216 Part C.
- Lenhof, U. and Robota, A.** (1997): Assessment of Honed Cylinder Bore Surfaces for IC Engines, HONEN in Forschung und industrieller Anwendung: 3. Fachtagung am 27 und 28 Sptember 1995, Braunschweig / Institut für Werkzeugmaschinen und Fertigungstechnik, Technische Universität Braunschweig.
- Li, D.F., Rhode, S.M. and Ezzat, H.A.** (1983): An automotive piston lubrication model. *ASLE Transaction*, Volume 26, pp151-160.
- Ligier, J., and Ragot, P.** (2006): Small end con-rod lubrication, SAE 2006 World Congress & Exhibition, April 2006, Detroit, MI, USA SAE 2006-01-1101.
- Liu, K., Xie, Y.B. and Gui, C.L.** (1998): A comprehensive study of the friction and dynamic motion of the piston assembly, Vol 212 Part J (J02795).
- Liu, L. and Tian, T.** (2005): Modelling piston ring-pack lubrication with consideration of ring structural response, SAE international (SP-1964), Detroit, Michigan (2005-01-1641).
- Liu, Q., Baburamani, P. and Loader, C.** (2008): Effect of High Temperature Exposure on the Mechanical Properties of Cold Expanded Open Holes in 7050-T7451 Aluminium Alloy, Air Vehicles Division, Defence Science and Technology Organisation, Australia, DSTO-TN-0844
- Lloyd, P.** (2008): Electroless Nickel Composite Coatings, *Advanced Materials & Processes*, Volume 166, Issue 5, May 2008 (ASM International), pp36-38.
- Love, A.E.H.** (1906): *A Treatise on the Mathematical Theory of Elasticity*, 2nd ed. Cambridge, England: Cambridge University Press.
- Luo, W., Yan, M., Zhu, W.Z. and Cantor, B.** (2002): An experimental study on the melt spinning of AA2618 alloy, *Journal of Materials Science* 37, 2685-2691.
- Ma, M.T., Smith, E.H. and Sherrington, I.** (1995a): A three dimensional analysis of piston ring lubrication, Part 1: Modelling. *Proc. Institution of Mechanical Engineers Part J*, Volume 209, pp1-14
- Ma, M.T., Smith, E.H. and Sherrington, I.** (1995b): A three dimensional analysis of piston ring lubrication, Part 2: Sensitivity analysis. *Proc. Institution of Mechanical Engineers Part J*, Volume 209, pp15-27
- Maassen, F., Koch, F., Schwaderlapp, M., Ortjohann, T. and Dohmen, J.** (2001): Analytical and Empirical Methods for Optimisation of Cylinder Liner Bore Distortion, World Congress Detroit Michigan, SAE 2001.
- Mahle International GmbH** (2008.2): Performance customer magazine, Issue 2, 2008.
- Malaczynski, G.W., Qiu, X., Hamdi, A.H. and Elmoursi, A.A.** (1996): Bench test for scuff evaluation of surface modified piston and bore materials, SAE 960013.

- Mansouri, S.H. and Wong, V.W.** (2004): Effects of piston design parameters on piston secondary motion and skirt liner friction, SAE international (SP-1894), Tampa, Florida (2004-01-2911).
- McClure, F.** (2007): Numerical modelling of piston secondary motion and skirt lubrication in Internal Combustion Engines, PhD Thesis, Massachusetts Institute of Technology, USA.
- MDI** (1994): ADAMS/Solver – Users reference manual. MDI, Michigan.
- Mei, X and Xie, Y.** (1993): Numerical Solution of Impact Vibration in a Valve Train', Trans. CSICE, 11(3), pp249-254.
- Meyer, D.R. and Wilson, C.C.** (1971): Measurement of Elastohydrodynamic Oil Films and Wear in Ball Bearings by the Strain Gauge Method, Transactions ASME, Journal of Lubrication Technology, Vol. 93, pp224-230.
- Michail, S.K. and Barber, G.C.** (1995): The effects of roughness on piston ring lubrication – part 1: Model Development, Tribology Transactions, 38(1):19-26.
- Mishra, P.C., Balakrishnan, S. and Rahnejat, H.** (2008): Tribology of compression ring-to-cylinder contact at reversal, Engineering Tribology, Vol. 222 Part J, P815-826.
- Mishra, P.C., Rahnejat, H. and King, P.D.** (2009): Tribology of the ring-bore conjunction subject to a mixed regime of lubrication, Mechanical Engineering Science, Vol.223 Part C:J. P987-998.
- Mistry, K., Priest, M., Shrestha, S.** (2010): The potential of plasma electrolytic oxidised eutectic Al-Si alloy as a cylinder wall surface for lightweight engine blocks. Proceedings of the IMechE, Part J: Journal of Engineering Tribology, vol. 224, pp.221-229.
- Mistry, K.K.** (2008): 'Lubricated' Diamond-Like-Carbon: 'Truly' Diamond-like-performance, Mission of Tribology Research 17, IMechE, 3<sup>rd</sup> December 2008.
- Mitchell, G., Holt, J.W., Dubois, F. and Adams, D.R.** (1995): Lead time reduction for piston development, T&N Symposium 1995, Paper 17, Page 17.6.
- Mobley, A.V., Carroll, M.P. and Canann, S.A.** (1998): An Object Oriented Approach to Geometry Defeaturing for Finite Element Meshing, 7th International Meshing Roundtable, October 26-28 1998, Dearborn, Michigan, U.S.A.
- Mostofi, A.** (1981): Oil film thickness and pressure distribution in elastohydrodynamic elliptical contacts. PhD thesis, Imperial College of Science and Technology, University of London.
- Mostofi, A. and Gohar, R.** (1983): Elastohydrodynamic lubrication of finite line contacts. Trans. ASME, J. Lubric. Technol., 105, 598–604.
- Muskhelishvili, N.I.** (1963): Some basic problems of the mathematical theory of elasticity: Fundamental equations, plane theory of elasticity, torsion and bending, 2nd English ed., Noordhoff, Groningen, 1963. Reprinted 1975; translated from the 4th Russian edition. MR 31 #920.
- Nakayama, K., Tamaki, S., Miki, H. and Takiguchi, M.** (2000): The effect of crankshaft offset on piston friction in a gasoline engine, SAE technical paper (1-0992), pp.1-8.
- Nakayama, K., Yasutake, Y., Takiguti, M. and Furuhashi, S.** (1997): Effect of piston motion on piston skirt friction of a gasoline engine, SAE international (SP-1245), Detroit Michigan (970839).

- Navier, C.L.M.H.** (1821): “Sur les Lois des Mouvements des Fluides, en Ayant Egard a l’Adhesion des Molecules”
- Navier, C.L.M.H.** (1823): Memoire sur les du mouvement des fluides. Mem. Académie des Inst. Sciences Fr., Volume 6, pp. 389-416.
- Newmark, N.M.** (1962): A method of computation for structural dynamics. Transaction of ASCE, 127:1406-35, Paper No.3384.
- Newton, I.** (1687): Mathematical principles of natural philosophy. Lib. II, Sec. II, London.
- Ninomiya, K., Kawamura, M. and Fujita, K.** (1978): Electrical Observation of Lubricant Film Between a Cam and a Lifter of an OHV Engine, SAE Paper No. 780930
- Offner, G. and Priebisch, H.H.** (2000): Elastic body contact simulation for predicting piston slap induced noise in an IC engine. in Multi-body dynamics: monitoring and simulation techniques - II (Eds H. Rahnejat and R. Whalley), Mechanical Engineering Publications, London.
- Oh, K.P., Li, C.H. and Goenka, P.K.** (1987): Elastohydrodynamic lubrication of piston skirts. ASME Journal of Tribology, Volume 109, pp. 356-362, 1987.
- Ohlsson, R., Rosen, B.G. and Westberg, J.** (2003): The Interrelationship of 3D Surface Characterisation Techniques with Standardised 2D Techniques, Advanced Techniques for Assessment Surface Topography, Kogan Page Science, London.
- Pan, E., Bevis, M., Han, F., Zhou, H. and Zhu, R.** (2009): Method of Evaluating Surface Deformation, United States Patent US 7,627,428 B2.
- Parker, D.A., Adams, D.R. and Donnison, G.** (1989): The Measurement and Reduction of Piston Assembly Friction, 2<sup>nd</sup> International Conference on Combustion Engines – Reduction of Friction and Wear, London.
- Patir, N. and Cheng, H.S.** (1978): An average flow model of determining effects of three-dimensional roughness on partial hydrodynamic lubrication. Transactions ASME Journal of Lubrication Technology, 100:12-16.
- Paul, B. and Hashemi, J.** (1981): Contact Pressures on Closely Conforming Elastic Bodies, Journal of Applied Mechanics. Vol 48, issue 3, pp543-549
- Perera, M.S.M., Theodossiades, S. and Rahnejat, H.** (2007): A multi-physics multi-scale approach in engine design analysis, Proceedings of the Institution of Mechanical Engineers, Part K: Journal of Multi-body Dynamics, Vol. 221, pp335-348.
- Perera, M.S.M., Theodossiades, S. and Rahnejat, H.** (2010): Tribo-multi-body dynamics for Simultaneous Assessment of Engine Frictional Losses and NVH Refinement. Proc. IMechE, Part K, Journal of Multi-Body Dynamics, 224(3), 1-17.
- Petroff, N.P.** (1883): Friction in machines and the effect of the lubricant. Inzh. Zh. St. Petersburg, Volume 1, pp. 71-140; Volume 2, pp. 227-279; Volume 3, pp. 337-463; Volume 4, pp. 535-564.
- Podgornik, B., Hren, D., Vizintin, J., Jacobson, S., Stavlid, N. and Hogmark, S.** (2006): Combination of DLC coatings and EP additives for improved tribological behaviour of boundary lubricated surfaces, Wear, 261:32-40.
- Podgornik, B., Vizintin, J., Strnad, S. and Stana-Kleinschek, K.** (2008): Tribological interactions between DLC coatings and lubricants, Tribotest, Vol. 14, Iss. 2, pp81-95.
- Porsche** (1993): Porsche 911 Technical Specifications 1990-1993, Dr. Ing. h.c. F. Porsche

AG.

- Prasad, S.V. and Zabinski, J.S.** (1993): Tribology of tungsten disulphide ( $WS_2$ ): Characterization of wear-induced transfer films. *Journal of materials science letters* 12. P1413-1414.
- Prasse, H.F., McCormick, H.E. and Anderson, R.D.** (1967): Automotive piston rings 1967 state of the art. *SAE transaction*, 76, 670019, pp.115-132.
- Prasse, H.F., McCormick, H.E. and Anderson, R.D.** (1968): Heavy duty piston rings 1968 state of the art. *SAE transaction*, 77, 680238, pp.115-132.
- Prasse, H.F., McCormick, H.E. and Anderson, R.D.** (1981): New developments in piston rings for high BMEP engines. *SAE transaction*, 77, 690753, pp.4-19.
- Raghu, S.** (2009): Concepts of Computational Finite Elements and Methods of Static and Dynamic Analyses, 2nd Edition, Ove Arup & Partners International Ltd.
- Ragot, P. and Rebbert, M.** (2007): Investigations of crank offset and it's influences on piston and piston ring friction behaviour based on simulation and testing. *SAE international* (SP-2073) Detroit, Michigan (2007-01-1248).
- Rahmani, R., Mirzaee, I., Shirvani, A. and Shirvani, H.** (2010): An analytical approach for analysis and optimisation of slider bearings with infinite width parallel textures, *Tribology International* 43 (2010) 1551–1565.
- Rahmani, R., Shirvani, A. and Shirvani, H.** (2007): Optimization of Partially Textured Parallel Thrust Bearings with Square-Shaped Micro-Dimples, *Tribology Transactions*, 50: 401-406.
- Rahnejat, H.** (1984): Influence of Vibration on Oil Film in Concentrated Contacts. PhD. Thesis, Imperial College of Science and Technology, University of London.
- Rahnejat, H.** (1985): Computational modelling of problems in contact dynamics, *Engng. Ana.*, 2(4), 1985, pp. 192-197.
- Rahnejat, H.** (1998): *Multi-Body Dynamics; Vehicles, Machines and Mechanisms*, John Wiley & Sons.
- Rahnejat, H.** (2000): Multi-body Dynamics: historical evolution and application, *Proc. IMechE, J. Mech. Engng. Sci.*, 214(1), 2000, pp. 149-173.
- Rahnejat, H., Balakrishnan, S., King, P.D. and Howell-Smith, S.** (2006): 'In-cylinder friction reduction using a surface finish optimization technique', *Proceedings of the Institution of Mechanical Engineers, Part D: Journal of Automobile Engineering*, 220(D9), 2006, pp 1309-1318.
- Rahnejat, H., Johns-Rahnejat, P.M., Teodorescu, M., Votsios, V. and Kushwaha, M.** (2009): A review of some tribo-dynamics phenomena from micro to nano-scale conjunctions, *Tribology International*, Vol. 42, Iss. 11-12, Special Issue: 35<sup>th</sup> Leeds-Lyon Symposium pp1531-1541.
- Rao, V.D.N., Kabat, D.M., Rose, R. and Yaeger, D.** (1997): Engines studies of solid firm lubricant coated pistons. *SAE international* (SP-1225) Detroit, Michigan (970009).
- Reynolds, O.** (1886): On the theory of lubrication and its application to Mr. Beauchamp Tower's experiments, including and experimental determination of the viscosity of olive oil. *Phil. Transaction of Royal Society, London*, Volume 177, pp. 157-234.
- Rezeka, S. and Henein, N.** (1984): A new approach to evaluate instantaneous friction and

- its components in internal combustion engines, SAE 840179.
- Ricardo PLC** (2009), Personal correspondence between B Sherwood and S Howell-Smith.
- Richardson, D.E.** (2000): Review of power cylinder friction for diesel engines. Transactions of the ASME, Vol.122 no. 4, pp506-519
- Richiero, A., Bird, L.E., Cadamarteri, J. and Inwood, B.C.** (1995): Piston system design for improved engine refinement, T&N Symposium 1995, Paper 19, pp19.5-6.
- Ripperger, E.A. and Davids, N.** (1947): Critical Stresses in a Circular Ring. Transactions of ASCE 112 pp. 619-628.
- Roark and Young** (1988): Roark's Formulas for Stress & Strain 6th edition, McGraw-Hill Inc.,US; 6th Revised edition.
- Robinson, J.E.** (1959): Basic design and function of automotive engine piston rings. Hepolite Piston Technology , Hepworth and Grandage limited, England, pp51-60.
- Robinson, J.E.** (1960): Piston assembly for compression ignition engines, Part one: Pistons. Hepolite Piston Technology, Hepworth and Grandage limited, England, pp6-11.
- Robinson, J.E.** (1961): Pistons for spark ignition engines. Hepolite Piston Technology, Hepworth and Grandage limited, England, pp6-11.
- Robinson, J.E.** (1962): The Hepolite 'W' piston, Hepolite Piston Technology , Hepworth and Grandage limited, England, pp31-41.
- Robinson, J.E.** (1964): The design and development of piston for automotive engines. Hepolite Piston Technology, Hepworth and Grandage limited, England, pp17-30.
- Roelands, C.H.** (1966): Correlational Aspects of the Viscosity-Temperature-Pressure Relationship of Lubricating Oils, O.P. Books Program, University Microfilm, Ann Arbor, Michigan.
- Rohrle, M.D.** (1994): Piston for internal combustion engine-Fundamental of Piston Technology. MAHLE GMBH, pp.4-71.
- Ronen, A. and Etsion, I.** (2001): Friction reducing surface-texturing in reciprocating automotive components. Tribology Transactions, Vol.44 P359-366.
- Ruddy, B.L. and Hildyard, M.L.** (1991): A review of Tribological Aspects of Piston Assembly Design, Proceedings of the 17<sup>th</sup> Leeds-Lyon Symposium, Session 5, pp93-102.
- Ryk, G., Kligerman, Y. and Etsion, I.** (2002): Experimental investigation of laser surface texturing for reciprocating automotive components. Tribology Transactions, Vol.45 P444-449.
- Ryk, G., Kligerman, Y., Etsion, I. and Shinkarenko, A.** (2005): Experimental investigation of partial laser surface texturing for piston-ring friction reduction. Tribology Transactions, Vol. 48:4 P583-588.
- Saad, P., Kamo, L., Mekari, M., Bryzik, W., Wong, V., Dmitrichenko, N. and Mntsakanov, R.** (2007): Modelling and measurement of tribological parameters between piston rings and liner in turbocharged diesel engine. SAE international (SP-2073) Detroit, Michigan (2007-01-1440).
- Safa, M.M.A. and Gohar, R.** (1986): Pressure distribution under a ball impacting a thin lubricant layer. Trans. ASME Journal of Tribology, July, Vol. 108.

- Sagawa, J., Ono, S., Tsukurimichi, T. and Watanabe, T.** (1990) Hi-power steel ring for modern engine. Riken internal technical paper, Riken Corporation.
- Sagawa, J., Onuki, T. and Ikeda, Y.** (1991): MoS<sub>2</sub> coated piston ring to prevent piston aluminium sticking, SAE technical paper-911281, pp.1-6.
- Salama, M.E.** (1952): The effect of Macro-roughness on the Performance of Parallel Thrust Bearings, Proceedings of the IMechE, Vol. 163 pp149-161
- Salama, M.E.A. and Gohar, R.** (1986): Pressure distribution under a ball impacting a thin lubricant layer. Trans. ASME Journal of Tribology, July, Vol. 108
- Sasaki, T., Mori, H. and Okino, N.** (1962): Fluid Lubrication Theory of Roller Bearings, Trans. ASME, J. Basic Engineering.
- Sato, O., Takiguchi, M., Takayuki, A., Seki, Y., Fujimura, K. and Tateshi, Y.** (2004): Improvement of piston lubrication in a diesel engine by means of cylinder surface roughness. SAE Technical Paper 2004-01-0604.
- Seiciu, P. L. and Pavelescu, D.** (2006): A new EHD phenomenon The Rheological Hysteresis, Proceedings of the Romanian Academy, Series A, Volume 7, Number 2/2006.
- Shankara, A., Menezes, P.L., Simha, K.R.Y. and Kailas, S.** (2008): Study of solid lubrication with MoS<sub>2</sub> coating in the presence of additives using reciprocating ball-on-flat scratch tester. Sādhanā Vol.33 Part 3, P207-220.
- Shayler, P.J., Pegg, I., Leong, D. and Murphy, M.** (2008): Investigations of piston ring pack and skirt contributions to motored engine friction. SAE international, Vol. 1 Issue 1, (2008-01-1046).
- Shen, Q.** (1997): Development of material surface engineering to reduce the friction and wear of the piston ring. SAE international (SP-1245) Detroit Michigan (970821).
- Sherrington, I.** (2010): Measurement Techniques for Tribology of piston rings, 'Tribology and dynamics of engine and powertrain: Fundamentals, applications and future trends', Woodhead Publishing Group edited Rahnejat, R.
- Sibley, L.B. and Austin, A.E.** (1962): An X-ray Method for Measuring Thin Lubricant Films Between Roller, ISA Transactions, Vol. 3, pp237-243.
- Sibley, L.B., Bell, J.C., Orcutt, F.K. and Allan, C.M.** (1960): A study of the Influence of Lubricant Properties on the Performance of Aircraft Gas Engine Rolling Contact Bearings, WADD Technical Report, pp60-189.
- Spencer, A., Almqvist, A. and Larsson, R.** (2010): A numerical model to investigate the effect of honing angle on the hydrodynamic lubrication between a combustion engine ring and cylinder liner, Nordtrib 2010, 14<sup>th</sup> Nordic Symposium on Tribology, 8<sup>th</sup>-11<sup>th</sup> June.
- St Venant, A.** (1864): Historique abrégé des recherches sur la résistance et sur l'élasticité des corps solides, pp. xc-cccxj of C.-L.-M.-H. Navier, Résumé des Leçons...sur l'Application de la Mécanique..., Paris, Dunod, 1864.
- Stanley, R., Taraza, D., Henein, N. and Bryzik, W.** (1999): A simplified friction model of the piston ring assembly. SAE international. Detroit Michigan (1999-01-0974).
- Steiber, W.** (1933): "Das Schwimmlager," *Verein Deutscher Ingenieure*, Berlin.
- Stern, M.** (2006): The Stern Review, The Economics of Climate Change, Cabinet Office,



- HM Treasury.
- Stokes, G.G.** (1845): On the theories of the internal friction of fluids in motion, and of the equilibrium and motion of elastic solids. Transaction of Cambridge Philosophic Society, Volume 8, pp. 287-341.
- Strang, G. and Fix, G. J.** (1973): An Analysis of the Finite Element Method. New York: Prentice-Hall.
- Suhara, T., Ato, S., Takaguchi, M. and Furuhashi, S.** (1997): Friction and Lubrication Characteristics of piston pin boss bearings of an automotive engine, International congress & exposition, Detroit, Michigan, Feb 24-27, 1997, SAE 970840.
- Sui, P.C. and Ariga, S.** (1993): Piston ring pack friction and lubrication analysis of an automotive engine using a mixed lubrication model. SAE international. Phoenix, Arizona (931937).
- Sunnen** (1993): Sunnen CV616 Automotive Application Bulletin A-1001 1A, August 1993, Sunnen Products Company, USA.
- Swift, H.W.** (1932): "The Stability of Lubricating Films in Journal Bearings, "Proceedings of the Institute of Civil Engineers, Volume 233, pp267-288.
- Szabo, B.A. and Lee, G.C.** (1969): Derivation of Stiffness Matrices for Problems in Plane Elasticity by Galerkin's Method, Internat. J. Numerical Methods in Engng.. Vol. 1, pp. 301-310.
- Tagawa, M., Ikemura, M., Nakayama, Y. and Ohmae, N.** (2004): Effect of Water Adsorption on Microtribological Properties of Hydrogenated Diamond-Like Carbon Films, Tribology Letters, Vol. 17, No. 3, pp575-580.
- Takisawa Machine Tool Company** (1998): NC Lathe, TPS-4000 Operation Manual, KW04030-101A.
- Tao, L., Ramachandran, S., Nelson, C.T., Lin, M., Overzet, L.J., Goeckner, M., Lee, G., Willson, C.G., Wu, W. and Hu, W.** (2008): Durable diamond-like carbon templates for UV nanoimprint lithography, Nanotechnology 19, 105302.
- Tattersall, H.G.** (1973): The ultrasonic pulse-echo technique as applied to adhesion testing, Journal of Physics D: Applied Physics, Vol. 6, p819.
- Taylor, C.M.** (1992): Fluid-film lubrication in the internal combustion engine: an invited review, J. Phys. D: Applied Physics, 25, A91-A100.
- Taylor, C.M.** (1998): Automobile engine tribology – design considerations for efficiency and durability. Wear 221 1998 P1-8.
- Taylor, C.M.** (2003): Tribology – Motoring into the 21<sup>st</sup> Century, George Stephenson Lecture, IMechE..
- Taylor, R.I., Brown, M.A., Thompson, D. and Bell, J.** (1994): The influence of lubricant rheology on friction in the piston ring-pack. SAE international. Baltimore, Maryland (SP-1055 / 941981).
- Teraguchi, S., Suzuki, S., Takiguchi, M. and Sato, D.** (2001): Effects of lubricating oil supply on reductions of piston slap vibration and piston friction. SAE international, Detroit Michigan (2001-01-0566).
- Thring, R.H.** (1992): Engine friction modelling. SAE international (SP-919). Detroit,

- Michigan (920482).
- Tian, T., Wong, V.W. and Heywood, J.B.** (1996): A piston ring-pack film thickness and friction model for multigrade oils and rough surfaces. SAE international (SP-1209). San Antonio, Texas (962032).
- Timoshenko, S.P. and Goodier, J.N.** (1970): Theory of Elasticity. McGraw-Hill, Inc.
- Timoshenko, S.P. and Woinowsky-Krieger** (1964): Theory of Plates and Shells, McGraw-Hill Higher Education, 2nd Edition.
- Ting, L.L.** (1979): Development of laser fluorescence technique for measuring piston ring oil film thickness. Journal of Lubrication Technology, Transactions ASME, Volume 102, No. 2, pp 165-171.
- Ting, L.L.** (1993): Development of a reciprocating test rig for tribological studies of piston engines moving components – Part 2: Measurements of piston ring friction coefficients and rig test confirmation. SAE international (SP-959). Detroit, Michigan (930686).
- Ting, L.L.** (1995): Development of a reciprocating test rig for tribological studies of piston engine moving components – Part 1: Rig design and piston ring friction coefficients measuring method. SAE international (SP-959). Detroit, Michigan (930685).
- Tolansky, S.** (1951): The Measurement of Thin Film Thickness by Interferometry, J. Opt. Soc. Am. 41, 425-426.
- Tomanik, E. and Ferrarese, A.** (2006): Low friction ring pack for gasoline engines. ASME ICEF fall 2006. (ICEF2006-1566).
- Toshihide, O., Mamoru, T. and Yamamoto, M.** (1993): Influence of engine oil viscosity on piston ring and cam face wear. Tribological Insights and Performance Characteristics of Modern Engine Lubricants, SAE/SP-93/996/932782.
- Totten, G. and MacKenzie, D.** (2003): Handbook of Aluminum Volume 2 – Alloy Production and Materials Manufacture, Marcel Dekker, Inc.
- Tower, B.** (1883): First report on Friction Experiments (Friction of lubricated Bearings). Proc. Institution of Mechanical Engineers. P632-659. (Adjourned Discussion, January 1884, P29-35).
- Tower, B.** (1885): Second report on Friction Experiments (Experiment on the oil pressure in a Bearing). Proc. Institution of Mechanical Engineers. P58-70.
- Tung, S.C. and McMillan, M.L.** (2004): Automotive tribology overview of current advances and challenges for the future, Tribology International, Volume 37, Issue 7, pp517-536.
- Uras, H.M. and Patterson, D.J.** (1983): Measurement of piston and ring assembly friction instantaneous imep method. SAE International Congress and Exposition.
- Uras, H.M. and Patterson, D.J.** (1984): Effect of Some Lubricant and Engine Variables on Instantaneous Piston and Ring Assembly Friction, SAE Paper No. 840178.
- Usher, A.P.** (1970): A History of Mechanical Inventions, Harvard University Press, p135.
- Vadiraj, A. and Kamaraj M.** (2009): Comparative wear behaviour of MoS<sub>2</sub> and WS<sub>2</sub> on plasma-nitrided SG iron. Journal of materials engineering and performance, ASM International 1059-9495.
- Vogel, H.** (1921): Das Temperaturabhängigkeitsgesetz der Viskosität von Flüssigkeiten,

- Physik Z, 22, 1921, p645.
- Voit, K., Hildyard, M.L., Bird, L.E. and Winship, M.** (1995): Design analysis of the piston system, T&N Symposium 1995, Paper 14, Page 15.6.
- Wakabayashi, R., Mochiduki, K. and Yoshida, H.** (2009): Lubricating condition of piston ring and cylinder for significantly reducing piston friction loss. SAE international (2009-01-0188).
- Wang, E., Nelson, T. and Rauch, R.** (2004): Back to Elements - Tetrahedra vs. Hexahedra, 2004 International ANSYS Conference Proceedings, 24th-26th May, Pittsburgh, PA.
- Wang, Y and Tung S.** (1999): Scuffing and wear behaviour of aluminium piston skirt coatings against aluminium cylinder bore. Elsevier Science S.A, P1100-1108.
- Watt (a), J.** (1769): Steam Engines &c, GB Patent, Ref GB176900913 (A).
- Watt (b), J.** (20<sup>th</sup> September 1769): letter to Dr Small, The origin and progress of the mechanical inventions of James Watt, James Patrick Muirhead, Published by John Murray MDCCCLIV.
- Wedeven, L.D. and Cameron, A.** (1967): A Study of Elastohydrodynamic Lubrication in Rolling Bearings Using Optical Interference, Proc. Inst. Mech. Engrs., Vol. 182, Part 3G, 1967-68, pp.87-89.
- Wedeven, L.D. and Cameron, A.** (1968): The Observation of Elastohydrodynamic Lubrication in a Rolling Element Bearing Using Optical Interferometry, The Tenth Int'l. Symposium on Lubrication of Rolling Bearings, Halle, Germany, August 1968, pp. 27-31.
- Wedeven, L.D., Evans, D. and Cameron, A.** (1972): Optical Analysis of Ball Bearing Starvation, Trans. ASME, J. Lub. Tech., 93, no pp199-210.
- White Jr., L.** (1979): Medieval Technology and Social Change, Oxford University Press, Fig. 7.
- Williams, J.** (2005): Engineering Tribology, Cambridge University Press.
- Winer, W.O. and Sanborn, D.M.** (1978): Surface Temperatures and Glassy State Investigations in Tribology, NASA CR 3031, (June 1978).
- Wong, V., Tian, T., Moughon, L., Takata, R and Jocsak, J.** (2006): Low Engine Friction Technology for Advanced Natural Gas Reciprocating Engines, DoE Cooperative Agreement No. DE-FC26-02NT41339
- World Energy Council** (2007): 'Transport Technologies and Policy Scenarios to 2050'.
- Wriggers, P.** (2002): Computational Contact Mechanics, 2<sup>nd</sup> Edition, Springer Berlin Heidelberg New York.
- Xiaoming, Y., Guohua, C., Yankun, J. and Yunchuan, Z.** (2004): Numerical investigation of the EHL performance and friction heat transfer in piston and cylinder liner system. SAE international (SP-1856). Detroit, Michigan (2004-01-0778).
- Xie, Y.B., Xie, Y.B. and Gui, C.L.** (1998): A Comprehensive Study of the friction and Dynamic motion of the Piston assembly, Proc. Of Inst. Of Mech. Eng. Part J, Vol. 212, pp221-226
- Yakabe, F., Jinbo, Y., Kumagai, M., Horiuchi, T., Kuwahara, H. and Ochiai, S.**

- (2008): Excellent durability of DLC film on carburized steel (JISSCr420) under a stress of 3.0 GPa, *Journal of Physics: Conference Series* 100, 082049.
- Yan, X.B., Xu, T. and Yang, S.R.** (2004): Characterisation of hydrogenated diamond-like carbon films electrochemically deposited on a silicon substrate, *Journal of Physics part D: Applied Physics*, 37, 2416-2424.
- Yang, Q. and Keith Jr., T.** (1996): Two-dimensional piston ring lubrication (part 1): Rigid ring and liner solution, *Tribology transactions*, Vol. 39, 4, pp757-768.
- Yoshida, H., Kusama, H. and Sagawa, J.** (1990): Effects of surface treatments on piston ring friction force and wear. SAE international. Detroit, Michigan (900589)
- Yoshida, H., Kusama, K. and Mizuma, Y.** (1987): Measurement of piston friction on firing conditions, *Proceeding of 4<sup>th</sup> international conference on automotive engineering*, Melbourne, Australia, 219, pp1-7.
- Zhu, D., Cheng, H.S., Arai, T. and Hamai, K.** (1992): Numerical analysis for piston skirts in mixed lubrication. Part I: Basic modelling. *Journal of Tribology, Transactions of the ASME*, Vol. 114, No. 3, pp. 553-562.
- Zhu, D., Cheng, H.S., Arai, T. and Hamai, K.** (1993): Numerical analysis for piston skirts in mixed lubrication. Part I: Basic modelling. *Journal of Tribology, Transactions of the ASME*, Vol. 115, No. 1, pp. 125-133.
- Zienkiewicz, O.C. and Taylor, R.I.** (2000): *The Finite Element Method, Volume 1: The Basics*, 5<sup>th</sup> Edition, Butterworth-Heinemann.
- Zienkiewicz, O.C. and Taylor, R.I.** (2000): *The Finite Element Method, Volume 2: Solid Mechanics*, 5<sup>th</sup> Edition, Butterworth-Heinemann.
- Zisman, W.A.** (1962): Constitutional effects on adhesion and cohesion, in *Adhesion and Cohesion*, Weiss, P., ed., 176+, Elsevier.
- Zweiri, Y.H., Whidborne, J.F. and Seneviratne, L.D.** (2001): Detailed analytical model of a single-cylinder diesel engine in the crank angle domain. *Proceedings of the Inst. of Mechanical Engineers, Part D*, 215:1197.

## Appendix 1

### Side force validation

---

#### A1.1 Methodology

The equations of motion developed in chapter 3 were modified to include the inertial effects of the connecting-rod (A1.2) and simplified with regards to nil pin offset as per the piston cases analysed. Solid model geometry of the components was imported into the multi-body dynamics programme 'ADAMS' (A1.3) and the resulting forces were compared with those from the numerical calculations (Chapter 3 and A1.2). These verified forces were then used for the numerical calculations presented in chapter 7.

#### A1.2 Connecting rod dynamics

To calculate effective side force at any instant in time, yet including the inertial contribution of the connecting-rod, the following assumptions are made:

- The piston, cylinder, con-rod and crankshaft are completely rigid. i.e. no elastic deformations take place.
- The piston is a perfect fit in the cylinder bore. i.e. the piston cannot move sideways or rotate about the gudgeon pin axis. It can only move along the cylinder axis.
- There is no friction between the piston and the cylinder, at the gudgeon pin or at the big-end bearing.
- The resultant combustion gas force acts along the cylinder axis.
- The cylinder axis intersects the gudgeon pin axis and the crankshaft axis.
- The gravitational forces on the piston and con-rod (i.e. their weights) are negligible compared with the gas and inertia forces.
- The crankshaft rotates at a constant speed of  $\omega$  radians/second.

Figure A1.1 shows, in idealised form, the crank mechanism of a typical single-cylinder engine with zero pin offset. The crankshaft axis is at O, the gudgeon pin axis is at P, the big-end axis is at C and the con-rod centre of gravity is at G. OC ( $= r$ ) represents the crank throw and CP ( $= l$ ) the con-rod.

$$CG = l_g$$

$$GP = l_p$$

$\omega$  = angular rotation of G

$y_p$  = vertical deflection of P

$x_g$  = horizontal deflection of G

$y_g$  = vertical deflection of G

From the geometry of Figure A1.1 the following relationships can be derived:

$$\sin(\phi) = \frac{r}{l} \cdot \sin(\theta) \quad (\text{A1.1a})$$

$$\cos(\phi) = \sqrt{1 - \frac{r^2}{l^2} \cdot \sin^2(\theta)} \quad (\text{A1.1b})$$

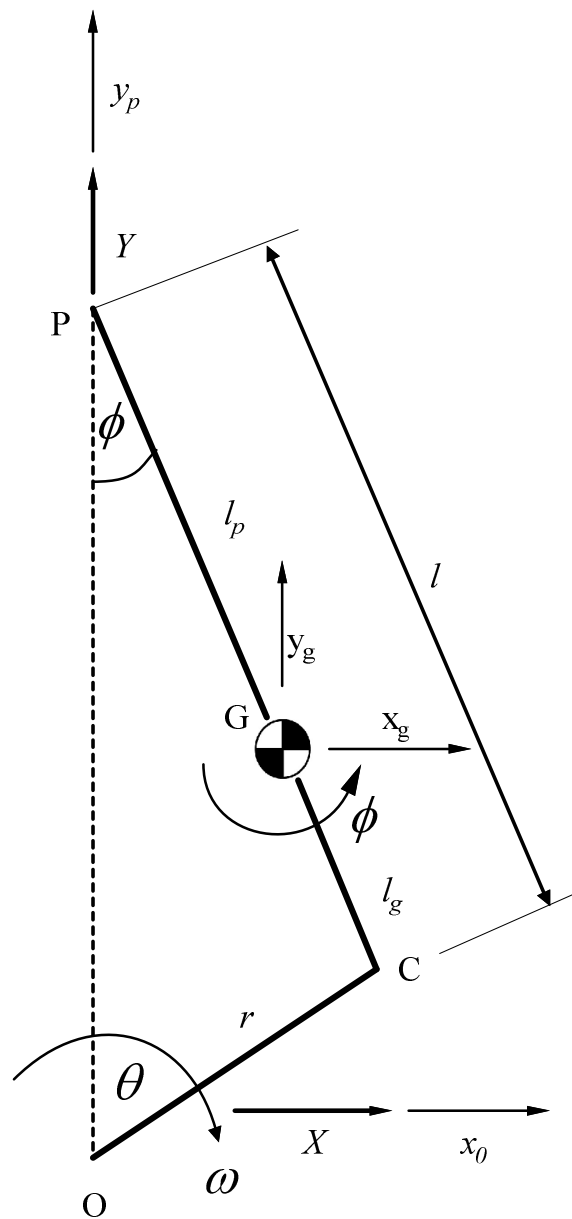


Figure A1.1 Kinematics of crank-slider mechanism

Differentiating equation (A1.1a) with respect to time gives:

$$\cos \phi \dot{\phi} = \frac{r}{l} \cdot \cos \theta \dot{\theta}$$

Now,  $\dot{\theta} = \omega = \text{a constant}$ . Therefore,

$$\dot{\phi} = \omega_r = \omega \cdot \frac{r}{l} \cdot \frac{\cos \theta}{\cos \phi} \quad (\text{A1.2a})$$

After differentiating again w.r.t. time and substituting equation (A1.2a) as appropriate,

$$\ddot{\phi} = \frac{\omega_r^2 \cdot \sin \phi - \omega^2 \cdot \frac{r}{l} \cdot \sin \theta}{\cos \phi} \quad (\text{A1.2b})$$

Now the upward (positive) vertical displacement of P is:

$$y_p = r \cdot (\cos \theta - 1) + l \cdot (\cos \phi - 1)$$

Differentiating this equation twice w.r.t. time and substituting equation (A1.2a) as appropriate gives:

$$\ddot{y}_p = \frac{\omega^2 \cdot r \cdot (\sin \theta \cdot \sin \phi - \cos \theta \cdot \cos \phi) - \omega_r^2 \cdot l}{\cos \phi} \quad (\text{A1.3})$$

The positive horizontal deflection of G is:

$$x_g = l_p \cdot \sin \phi$$

Differentiating this equation twice w.r.t. time and substituting equation (A1.2a) as appropriate gives:

$$\ddot{x}_g = -l_p \cdot \frac{r}{l} \cdot \omega^2 \cdot \sin \theta \quad (\text{A1.4})$$

Similarly, the positive vertical deflection of G is:

$$y_g = r \cdot (\cos \theta - 1) + l_g \cdot (\cos \phi - 1)$$

Differentiating this equation twice w.r.t. time and substituting equation (A1.2a) as appropriate gives:

$$\ddot{y}_g = \frac{\omega^2 \cdot \left( l_g \cdot \frac{r}{l} \cdot \sin \theta \cdot \sin \phi - r \cdot \cos \theta \cdot \cos \phi \right) - l_g \cdot \omega_r^2}{\cos \phi} \quad (\text{A1.5})$$

### A1.2.1 Component forces

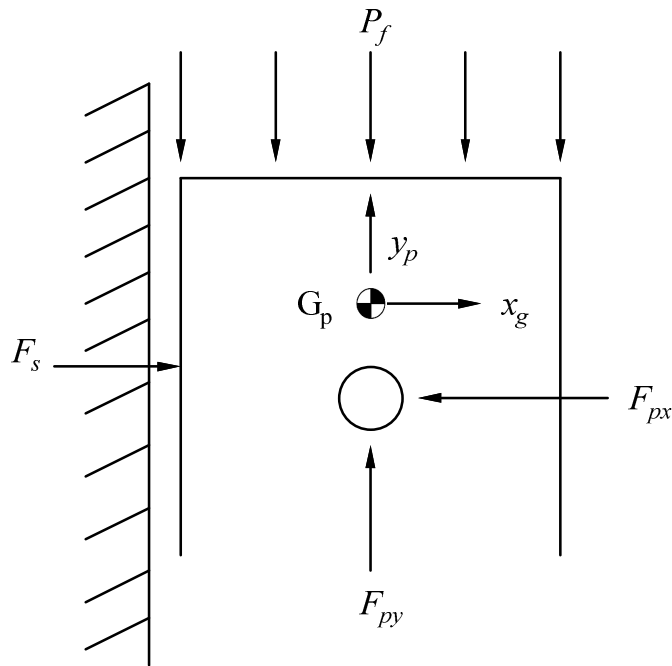


Figure A1.2 Resolved force diagram on piston



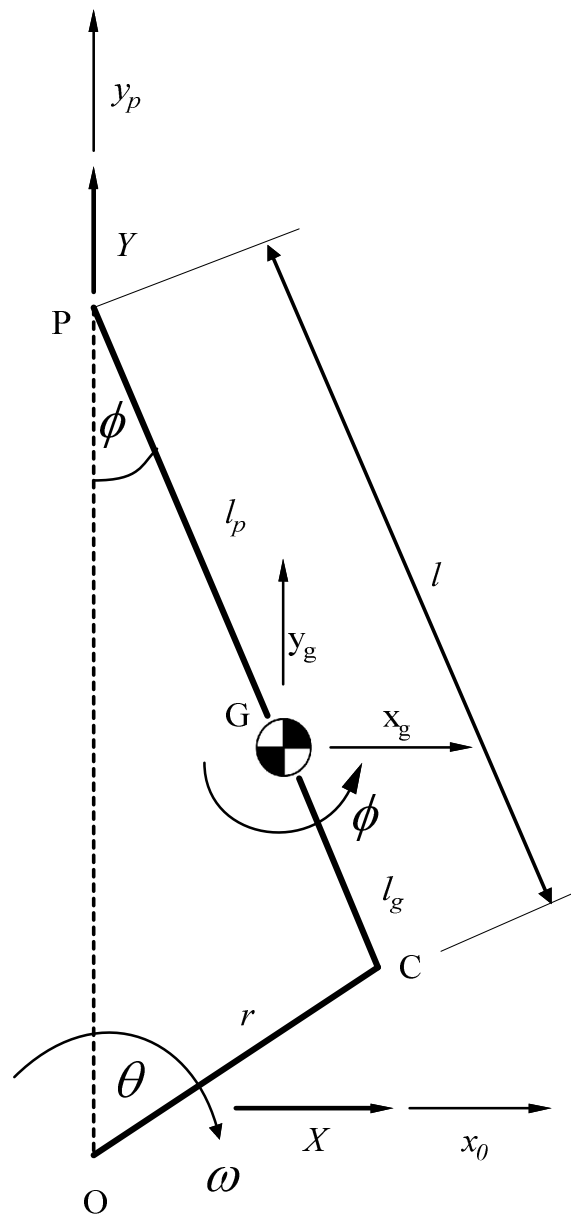


Figure A1.3 Resolved force diagram on the connecting rod

Each of the crank components must be in horizontal and vertical force equilibrium, and in moment equilibrium. For the piston (Figure A1.2) we do not need to consider moment equilibrium because the piston is not free to rotate about the gudgeon pin axis and the little end, being frictionless, cannot impose any torque on to the piston. Therefore, although in practice the effective point of action of the cylinder reaction force  $F_s$  will vary in order to satisfy the requirements of moment equilibrium, we are here only concerned with its magnitude. Thus, for horizontal force equilibrium of the piston:

$$M_p \cdot \ddot{x}_p = F_s - F_{px}$$

where,  $M_p$  = mass of the piston assembly including rings and gudgeon pin

Now  $\ddot{x}_p = 0$  (No horizontal motion of piston permitted), therefore:

$$F_s = F_{px} \quad (A1.6)$$

For vertical equilibrium of the piston:

$$M_p \cdot \ddot{y}_p = F_{py} - P_f$$

where,  $P_f$  = combustion gas force acting on piston crown.

Therefore,

$$F_{py} = P_f + M_p \cdot \ddot{y}_p \quad (A1.7)$$

Considering now the horizontal force equilibrium of the con-rod (see Figure A1.3):

$$M_r \cdot \ddot{x}_g = F_{px} + F_{cx} \quad (A1.8)$$

where,  $M_r$  = mass of the con-rod assembly

The vertical force equilibrium of the con-rod gives:

$$M_r \cdot \ddot{y}_g = F_{cy} - F_{py} \quad (A1.9)$$

The moment equilibrium of the con-rod gives:

$$I_r \cdot \ddot{\phi} = F_{cx} \cdot l_g \cdot \cos \phi + F_{cy} \cdot l_g \cdot \sin \phi - F_{px} \cdot l_p \cdot \cos \phi + F_{py} \cdot l_p \cdot \sin \phi \quad (A1.10)$$

where,  $I_r$  = moment of inertia of the con-rod about an axis through G.

These equations are most easily solved by arranging them in matrix form. Viz:

$$\begin{bmatrix} 1 & 0 & 0 & 0 \\ 0 & 1 & 0 & 1 \\ -1 & 0 & 1 & 0 \\ l_p \cdot \sin \phi & l_g \cdot \cos \phi & l_g \cdot \sin \phi & -l_p \cdot \cos \phi \end{bmatrix} \begin{bmatrix} F_{py} \\ F_{cx} \\ F_{cy} \\ F_{px} \end{bmatrix} = \begin{bmatrix} P_f + M_p \cdot \ddot{y}_p \\ M_r \cdot \ddot{x}_g \\ M_r \cdot \ddot{y}_g \\ I_r \cdot \ddot{\phi} \end{bmatrix}$$

Thus,

$$\begin{bmatrix} F_{py} \\ F_{cx} \\ F_{cy} \\ F_{px} \end{bmatrix} = \begin{bmatrix} 1 & 0 & 0 & 0 \\ -\sin \phi & \frac{l_p}{l} & -\frac{l_g \cdot \sin \phi}{l \cdot \cos \phi} & \frac{1}{l \cdot \cos \phi} \\ \cos \phi & \frac{l_g}{l} & \frac{l_g \cdot \sin \phi}{l \cdot \cos \phi} & -\frac{1}{l \cdot \cos \phi} \\ 1 & 0 & l & 0 \\ \sin \phi & \frac{l_g}{l} & \frac{l_g \cdot \sin \phi}{l \cdot \cos \phi} & -1 \\ \cos \phi & \frac{l_g}{l} & \frac{l_g \cdot \sin \phi}{l \cdot \cos \phi} & -1 \end{bmatrix} \begin{bmatrix} P_f + M_p \cdot \ddot{y}_p \\ M_r \cdot \ddot{x}_g \\ M_r \cdot \ddot{y}_g \\ I_r \cdot \ddot{\phi} \end{bmatrix} \quad (\text{A.11})$$

This gives:

$$F_{px} = F_s = \frac{\sin \phi}{\cos \phi} \cdot (P_f + M_p \cdot \ddot{y}_p) + \frac{l_g}{l} \cdot M_r \cdot \ddot{x}_g + \frac{l_g \cdot \sin \phi}{l \cdot \cos \phi} \cdot M_r \cdot \ddot{y}_g - \frac{1}{l \cdot \cos \phi} \cdot I_r \cdot \ddot{\phi} \quad (\text{A.12})$$

### A1.3 Validation of side force

ADAMS (MSC Software Corporation) is multi-body simulation software used to study the behaviour of systems consisting of rigid bodies undergoing large displacement. It can be used to predict characteristics of a new design, to evaluate the performances of an existing design, or to investigate extreme operating conditions. It has an open-ended architecture that allows users to create extensions using data set features and external subroutines (**MDI, (1994)**).

A model consists of part geometry and mass properties, reference frame definitions, body types, body compliance description, topological and analytical constraints, and externally applied forces. The spatial generalised co-ordinates consist of three Cartesian coordinates for each part's centre of mass with respect to the global reference frame and three Euler angles defining the orientation of the central principal axes of inertia of each part relative to mutually perpendicular, inertially fixed axes, **MDI (1994)**.

The first step in modelling is to define reference frames, co-ordinate systems, and system units. Then each part in the system model should be defined with its mass and inertial properties, the centre of mass location, and part position and orientation with respect to a fixed global frame of reference (GRF). The program allows these parts to be inertially fixed or moving. The parts (their mass or inertial properties) used to construct the single-cylinder piston model is described shown in table A1.1

After defining all parts with appropriate properties the required motions and constraints will be introduced between the parts to simulate required functional behaviour of real systems being modelled. The standard joints (constraints) in ADAMS include revolute, planar, cylindrical etc., which reduce the number of DOF of the system. Now the model is restricted to move in a way which complies with the introduced constraints and imposed motions, according to the kinematic relations needed. Physical components of the mechanical system are modelled using idealised ADAMS parts which can be either rigid bodies, flexible bodies, or particles. The holonomic constraints used to connect the individual parts (to each other and ground) are presented in table A1.2.

Markers are orthogonal triads of unit vectors which mark points of interest on a part. The markers are necessary in order to define joints, forces, centre of mass, inertia, etc. Markers can also be used when the displacement of a certain location of a part with respect to other points in the model is of interest. This is done by placing two markers on the appropriate locations and requesting the desired information.

Joints can be defined between two parts referred to as I part and J part by specifying their names, location, and orientation, or by specifying markers on the two parts. ADAMS permits description of the components of the system in terms of graphic primitives and icons which are used to track the motion of the system visually. The graphic representation of the models described are presented in figure A1.4.

### **A1.2 Single-cylinder model**

A single-cylinder internal combustion engine multi-body model, developed in this thesis, using ADAMS (see figure A1.4) comprises an assembly of inertial elements; piston, pin, connecting rod, crankshaft and flywheel. The assembly of parts has been achieved by the use of holonomic constraint functions (**MDI (1994)**).

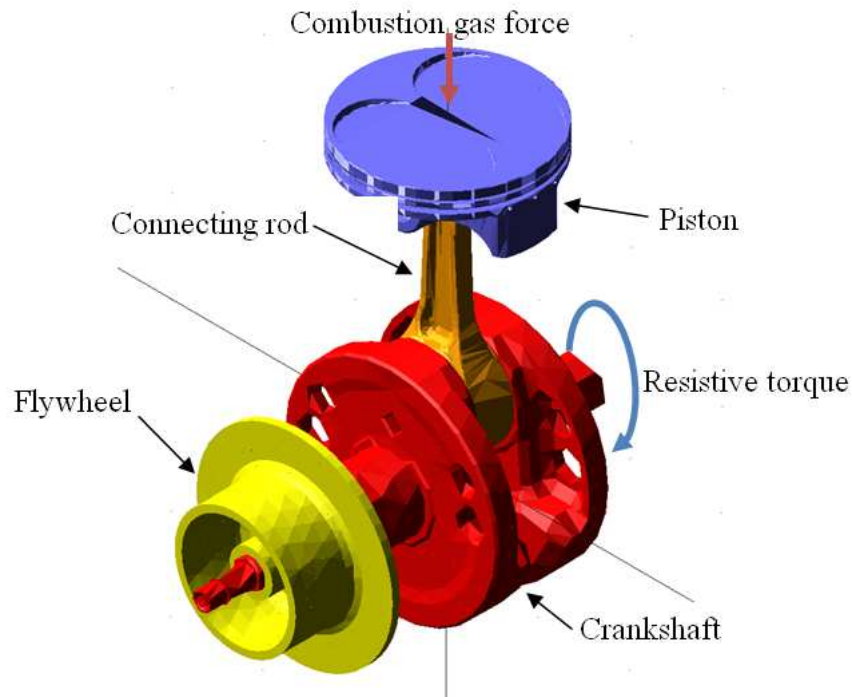


Figure A1.4 ADAMS single-cylinder engine assembly

All the rigid body inertial properties of the parts (mass and mass moments of inertia) are given in table A1.1. The joints and other constraining elements in the multi-body dynamic model are given in table A1.2. The table indicates the number of constraints imposed by each holonomic constraint in the assembly of the model. Due to the partial interference of the piston within the bore the piston is constrained to reciprocate without sideward motion.

Part name	Mass (Kg)	Ixx (Kgmm <sup>2</sup> )	Iyy (Kgmm <sup>2</sup> )	Izz (Kgmm <sup>2</sup> )
Piston	0.285	320.452	186.342	181.171
Pin	0.063	11.485	11.485	3.784
Con-rod	0.265	536.284	493.0	56.225
Crank	3.883	5884.292	5444.771	6847.001
Flywheel	0.531	415.259	605.593	415.267

Table A1.1 Parts in the multi-body single-cylinder engine model

I_Part	J_Part	Constraint type	DOF removed
Piston	Ground	Translational	5
Piston	Pin	Fixed	6
Piston	Connecting-rod	Spherical	3
Connecting-rod	Crank	Cylindrical	4
Crank	Ground	Revolute	5
Flywheel	Crank	Fixed	6

Table A1.2 Constraints imposed in the multi-body single-cylinder engine model

There is no significant motion between the piston pin and the piston. Therefore they are connected with a fixed joint. The gas pressures generated by the process of the combustion are applied to the piston crown as a single component force. The force is calculated by multiplying the instantaneous combustion pressure with the crown surface. The measured gas force is a discrete function and Akima fitting method is used to make it a continuous function. The load torque on the engine due to the tyres and road resistance is represented by an externally applied single component torque as given in Figure 1.1.

#### A1.4 Operating conditions and results

Gas loading from figure 5.37 (CRF) was used and applied to act on the piston crown. The crank rotational speed was 7,500rpm. A constant load torque of 77Nm was applied at the crank. Figures A1.5-A1-12 present results from this simulation compared to those calculated from equations developed in Chapter 3 and Appendix 1.

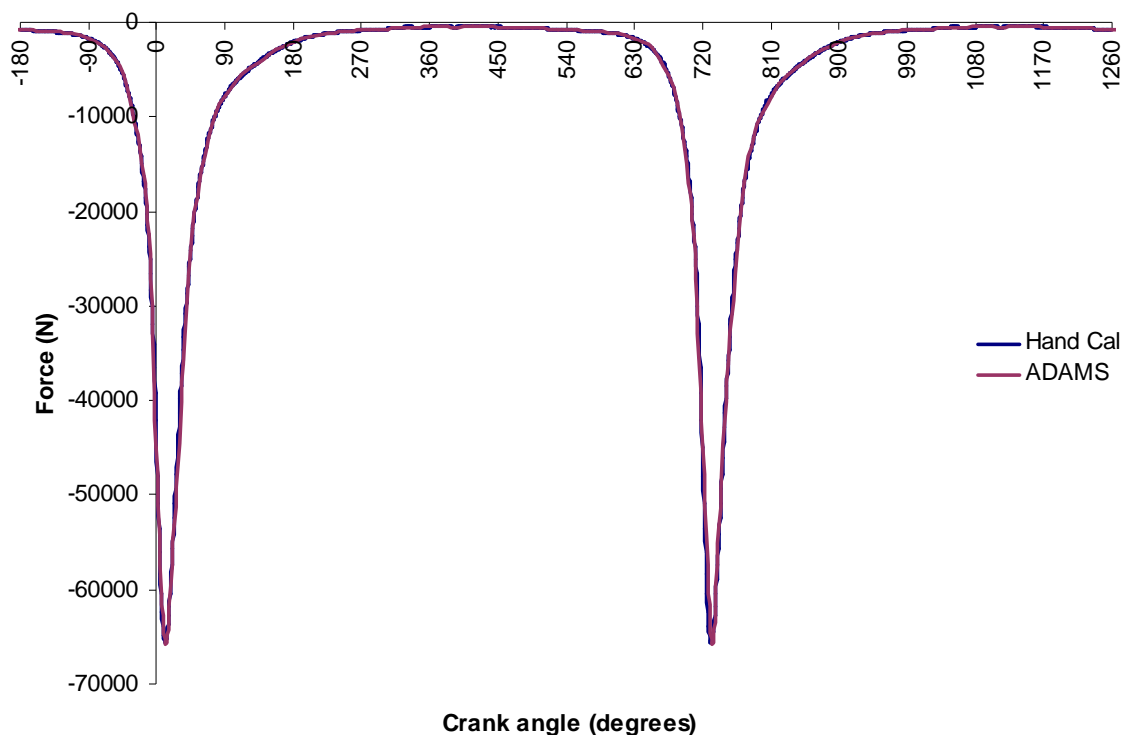


Figure A1.5 Combustion force on piston crown

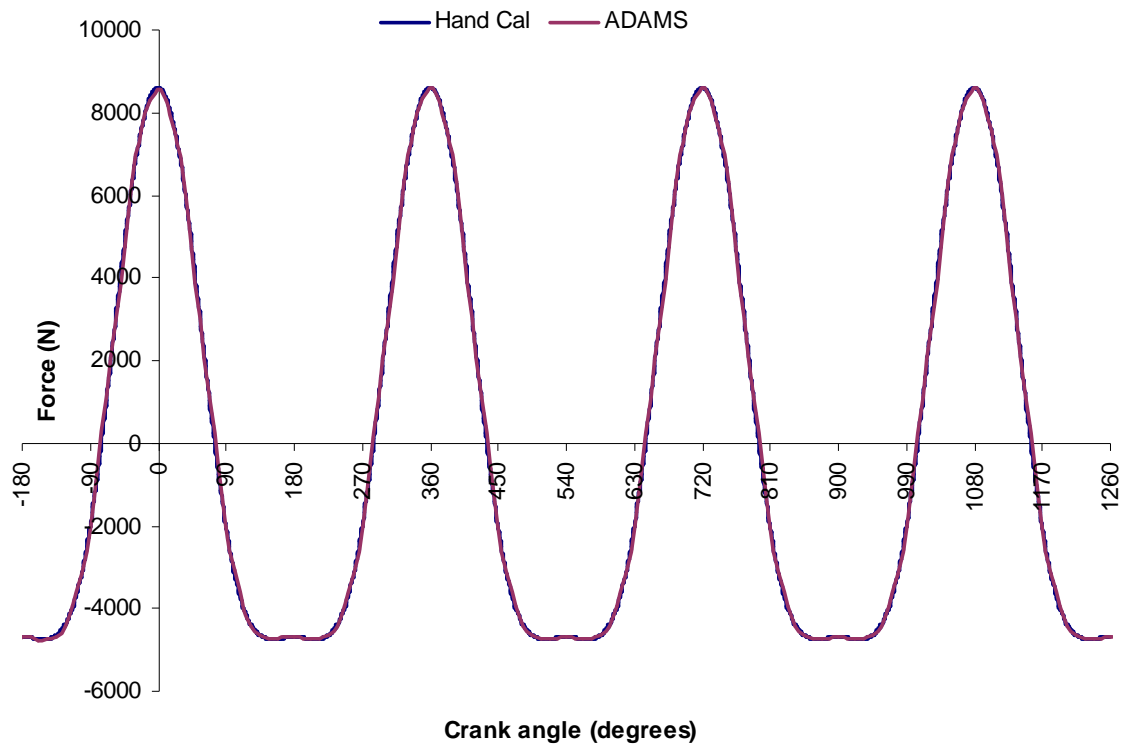


Figure A1.6 Vertical force due to inertia

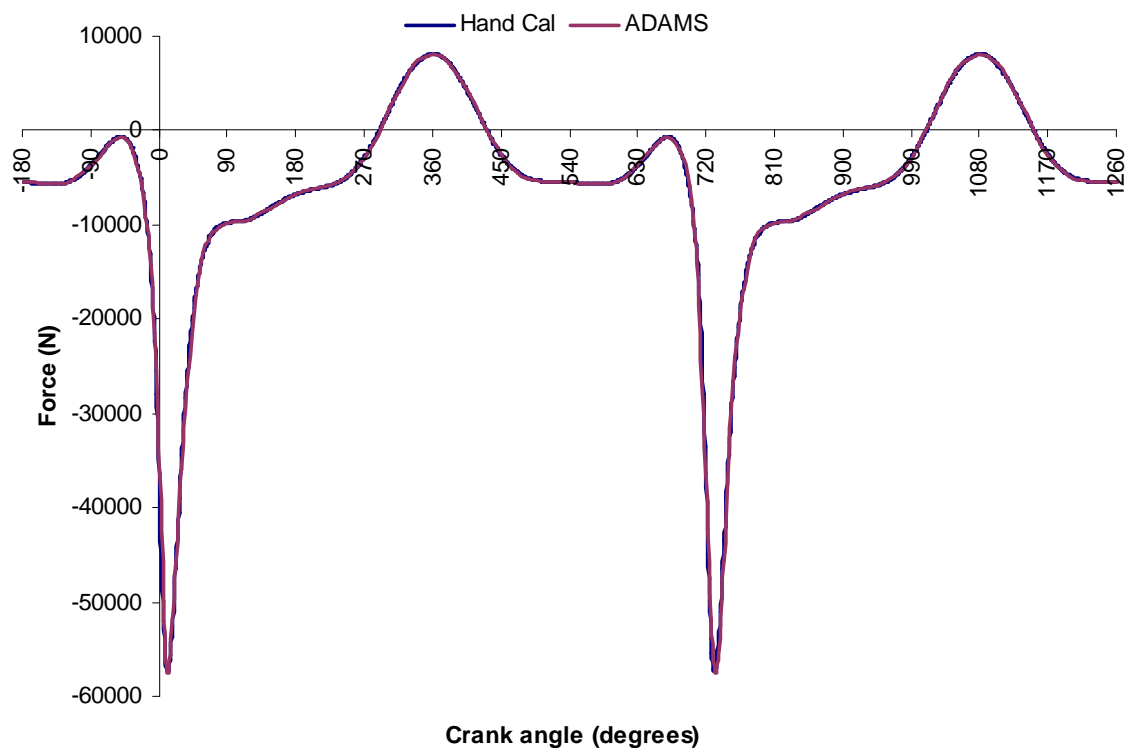


Figure A1.7 Resulting vertical force on piston

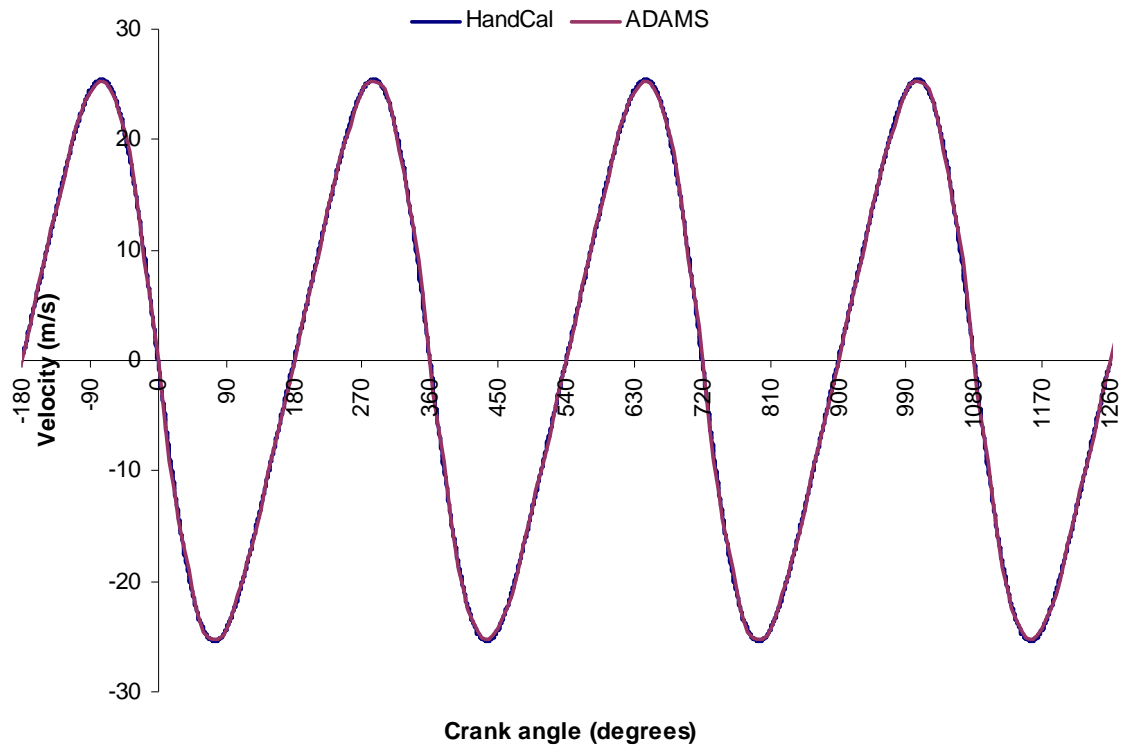


Figure A1.8 Piston velocity

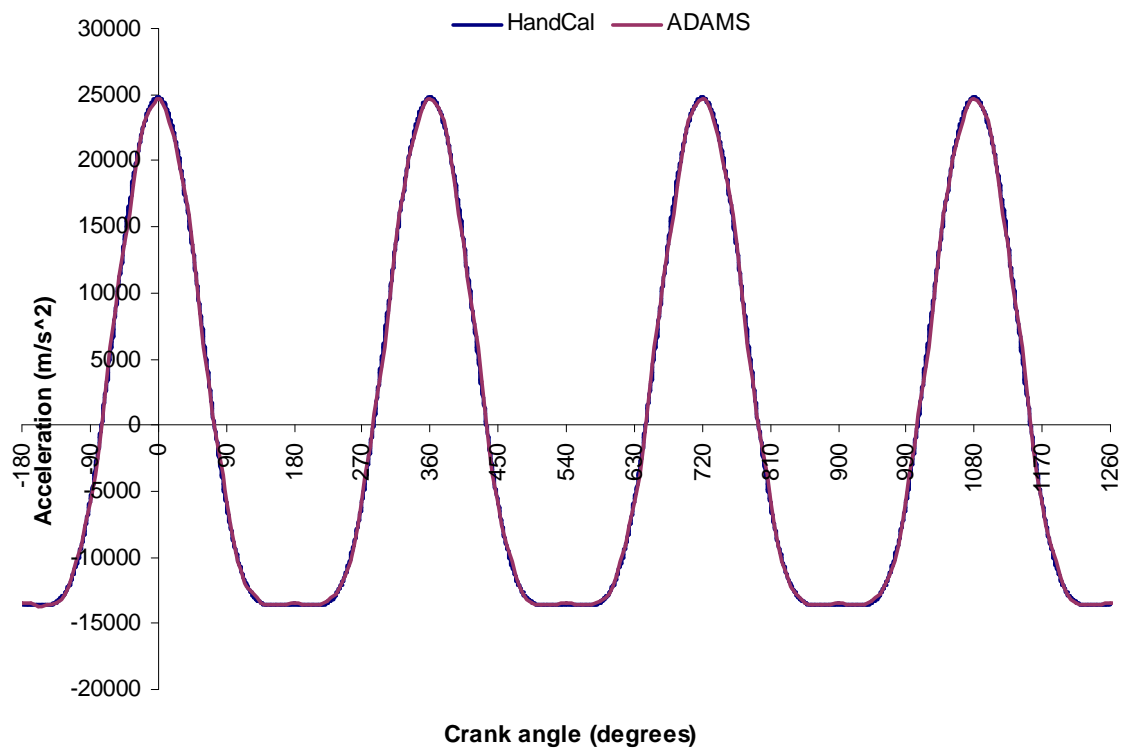


Figure A1.9 Resulting piston acceleration



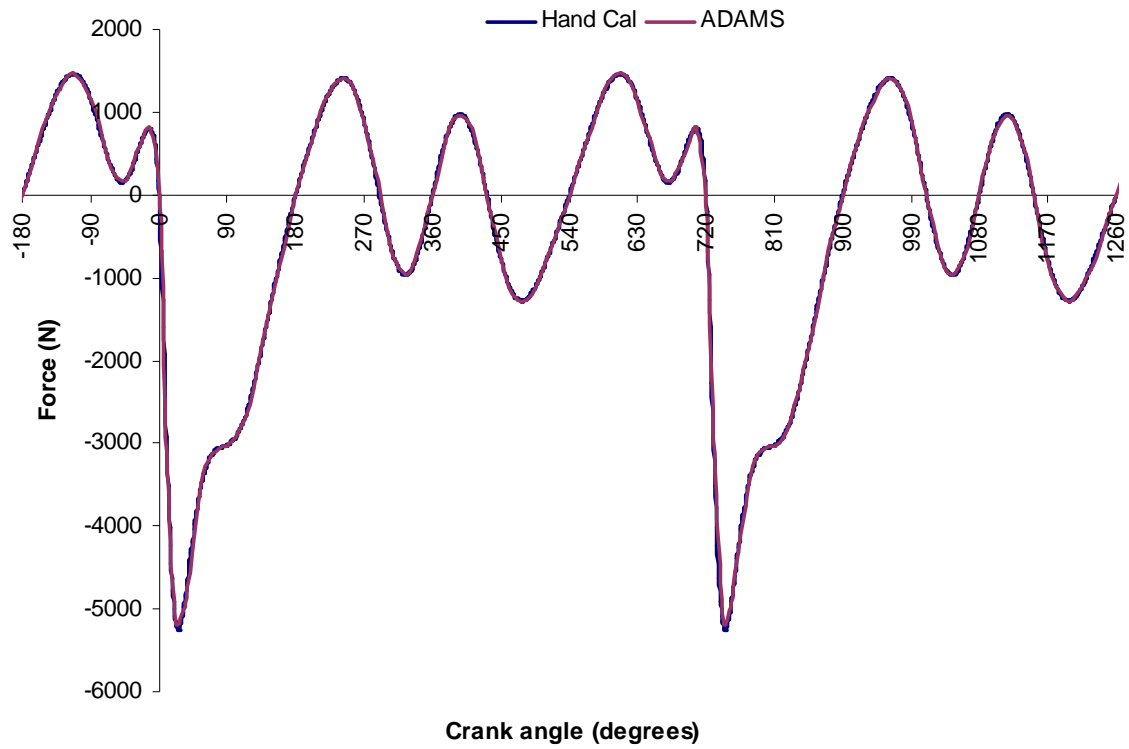


Figure A1.10 Horizontal piston-bore force not including rod inertia

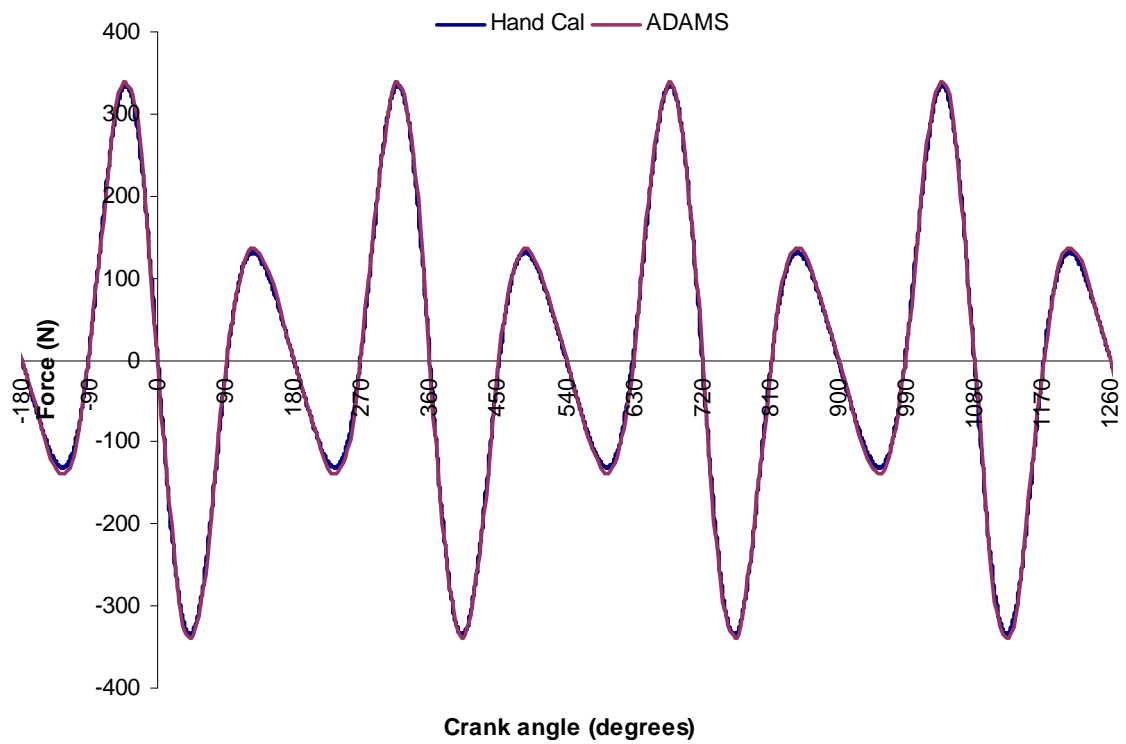


Figure A1.11 Horizontal force due to rod inertia

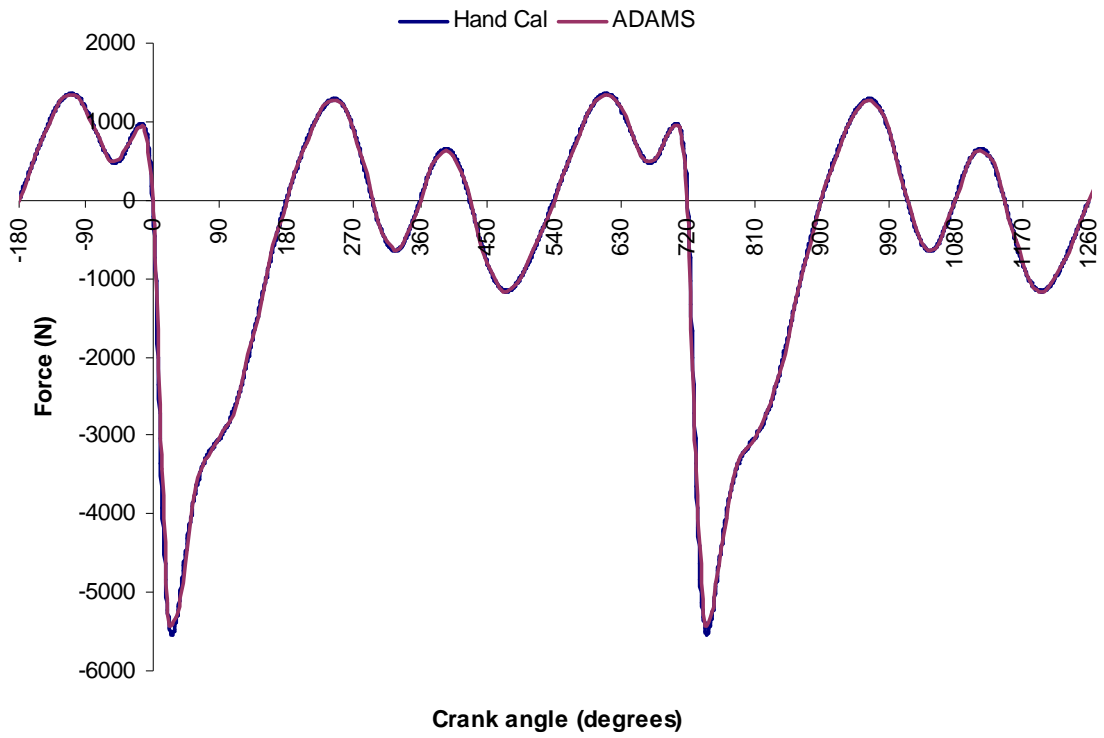


Figure A1.12 Total resulting piston horizontal force

## Appendix 2

### Gudgeon-pin contributory torque

---

#### A2.1 Introduction

The forces applied to the piston-connecting rod system are translated through the gudgeon pin and associated bearings. These connections are generally poorly understood (**Ligier and Ragot, (2006)**) resulting in a frictional torque (**Dursunkaya and Keribar, (1992)**, **Zweiri et al, (2001)**). **McClure (2007)** proposes the use of Petroff's equation to calculate this torque.

#### A2.2 Calculation of gudgeon pin torque

From figure A1.1, the velocity of the gudgeon pin joint is:

$$\dot{\phi} = \omega \Lambda \frac{\cos \theta}{\cos \phi}$$

The resulting revolutions / second ( $n$ ) is:

$$n = \omega \Lambda \frac{\cos \theta}{2\pi \cos \phi} \quad \text{A2.1}$$

If a half-pin is considered fixed within the half-section con-rod, and the pin to piston pin bore is considered a hydrodynamic bearing with no net flow of lubricant in the axial direction, the shearing stress due to rotation is given by:

$$\tau = \mu \frac{V}{s} = \frac{2\pi R \mu n}{c} \quad \text{A2.2}$$

Where the radius of the pin is  $R$ , the radial clearance of the pin in the pin bore is  $c$ , the length of the pin bearing on the bore is  $L$ , the pin / con-rod instantaneous angular speed is  $n$  rev/s, and the surface velocity is  $V$  ( $2\pi R n$ ). The lubricant is assumed to be Newtonian in behaviour and the velocity gradient is constant through the thickness of the film.

The force required to shear the film is given by:

$$F = \tau A$$

Where  $A$  is the pin-pin bore contact area:  $(2\pi RL)$ . The friction torque is as follows:

$$T_f = FR = (\tau A)R = \left( \frac{2\pi R \mu n}{c} 2\pi RL \right) R = \frac{4\pi^2 \mu n L R^3}{c} \quad A2.3$$

A small radial load ( $W$ ) is applied to the bearing resulting in the load per unit projected area ( $P$ ) such that  $P = \frac{W}{2RL}$ . The friction torque is given by:

$$T_f = fWR = f(2RLP)R = 2R^2 fLP \quad A2.4$$

Where  $f$  is the friction coefficient and  $fW$  is the friction force. Rearranging A2.3 and A2.4 results in Petroff's equation:

$$f = 2\pi^2 \left( \frac{\mu n}{P} \right) \left( \frac{R}{c} \right) \quad A2.5$$

To evaluate frictional torque for the CRF case, the SAE10W-40 lubricant is assumed to be at 120°C (average within the conjunction) with an absolute viscosity of 0.005Pa.s. From Chapter 4 the thermal expansion and elevated operating temperature of both the gudgeon pin and bore results in an operating radial clearance of 0.021mm ( $2.1 \times 10^{-5}$ m). Loads are provided as per Appendix 1 and projected area as per Chapter 5 section 5.3.2. The bearing area term ( $2RL$ ) is modified to be the actual bearing area (removal of axial and radial oil slots etc).

Results from this approach yield very low friction coefficients ( $\sim 0.0001$ ) indicating its unsuitability for this application.

**Fox (2005)** provides a detailed breakdown of baseline frictional contributions utilising simulation software produced by Ricardo PLC (table A2.1). **Suhara *et al* (1997)** instrument the connecting rod small end within a running engine reporting a large variation in friction coefficient ranging from a maximum before TDC of  $\sim 0.09$  reducing to  $\sim 0.007$  at peak combustion. Through the expansion phase there is an increase to 0.035 approximately increasing further towards the end of the exhaust stroke to 0.08 approximately. This data was provided for 2500rpm and full load.

Interface	Baseline friction coefficient	Simulation program used	Friction model
Cam-follower	0.005	VALDYN	Simple
Cam-cam bearing	0.02	VALDYN	Simple
Rocker arm-rocker support	0.02	VALDYN	Simple
Pushrod socket-pushrod	0.05	VALDYN	Simple
Rocker tip-valve bridge	0.05	VALDYN	Simple
Piston skirt-cylinder liner	0.08	PISDYN	Detailed hydrodynamic and boundary lubrication
Piston rings-cylinder liner	0.12	RINGPAK	Detailed hydrodynamic and boundary lubrication
Piston pin-piston	0.08	PISDYN	Detailed hydrodynamic and boundary lubrication
Connecting rod small end	0.12	ORBIT	Detailed hydrodynamic and boundary lubrication
Connecting rod large end	0.12	ORBIT	Detailed hydrodynamic and boundary lubrication
Crankshaft main bearing	0.12	ORBIT	Detailed hydrodynamic and boundary lubrication

Table A2.1 Friction coefficients as per Fox (2005)

A correlation between **Fox (2005)** and **Suhara *et al* (1997)** shows that the baseline value quoted by **Fox (2005)** is applicable for the majority of the piston 4-stroke cycle. However the friction coefficient drops markedly around the combustion event.

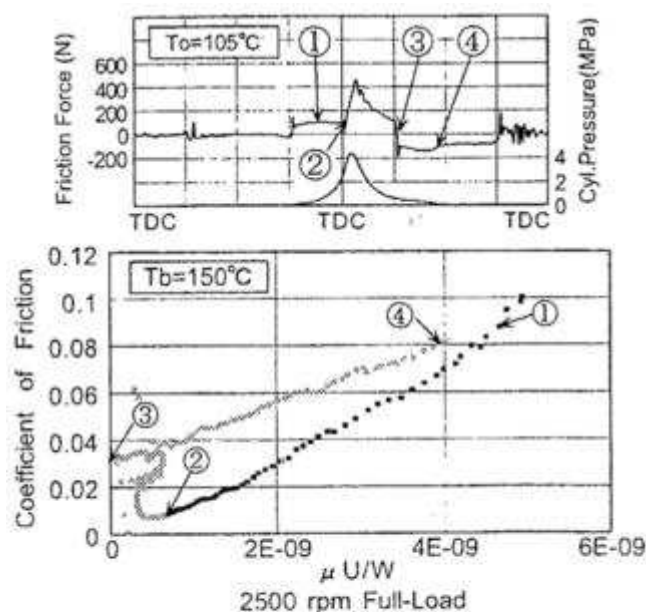


Figure A2.1 Pin bore friction measurements  
(**Suhara *et al*, (1997)**)

Figure A2.2 correlates data from figure A2.1 with crank angle with the inclusion of a truncated series (**Mistry, (2008)**) where a maximum coefficient of 0.05 (DLC). Figure A2.3 shows the resulting torque in the CRF application for both an uncoated and coated pin.

Of note, the very low frictional coefficient presented by **Suhara *et al* (1997)** results in a very reduced torque at the combustion event. Degradation in bearing performance during service

would lead to a rapid increase in bearing torque and likely result in failure. Generally the magnitude of the torque is considered low relative to the skirt thrust forces.

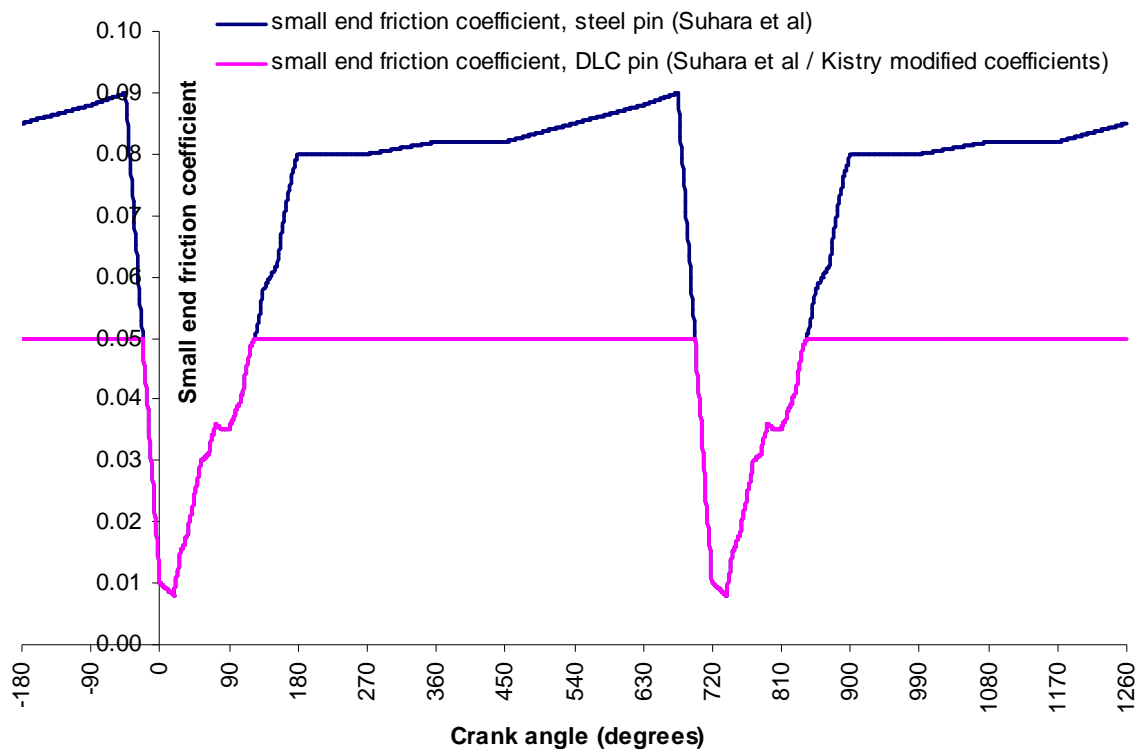


Figure A2.2 Connecting-rod small end friction coefficients

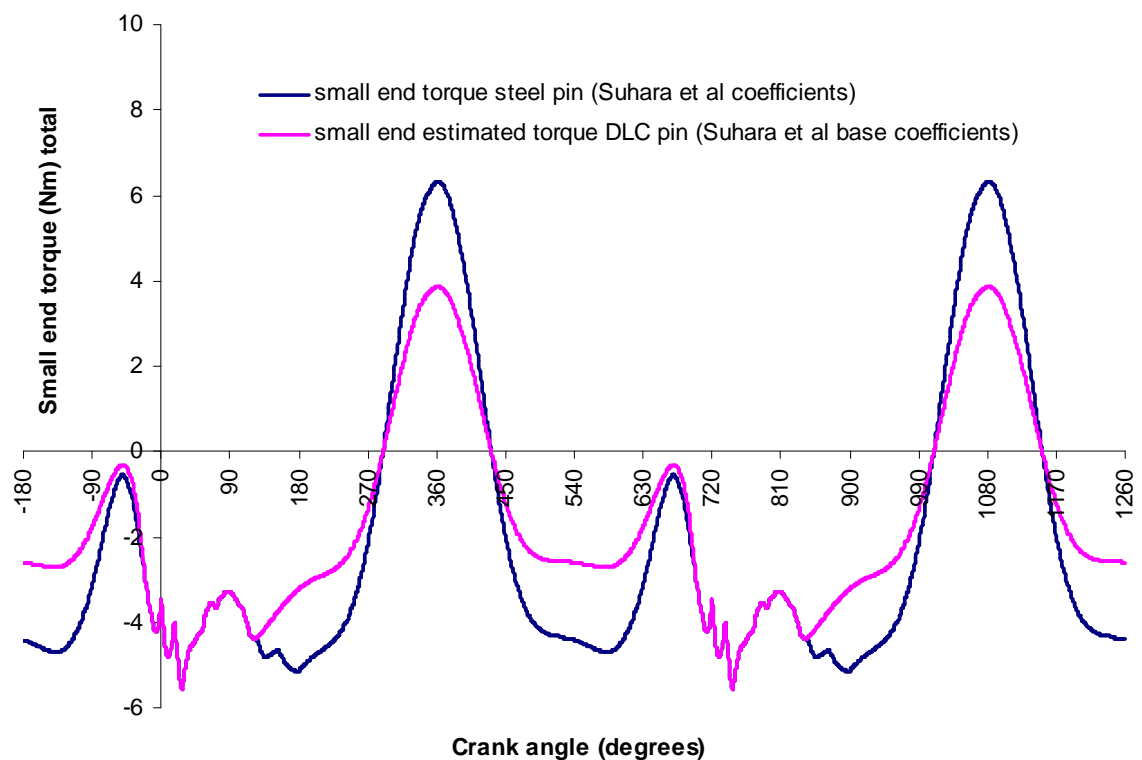


Figure A2.3 Connecting-rod small end resulting torque

## Appendix 3

### FE contact ‘footprints’

A range of CRF crank angles were investigated, corresponding to the domain after top dead centre when side force reaches 50% of maximum value ( $9^\circ$ ) and again decays to 50% ( $106^\circ$ ). Figure A3.2 details the resulting skirt contact pressure with all other bodies save the piston visually suppressed. Figure A3.1 provides a summary regarding the peak contact pressure (no lubricant) with other relevant parameters.

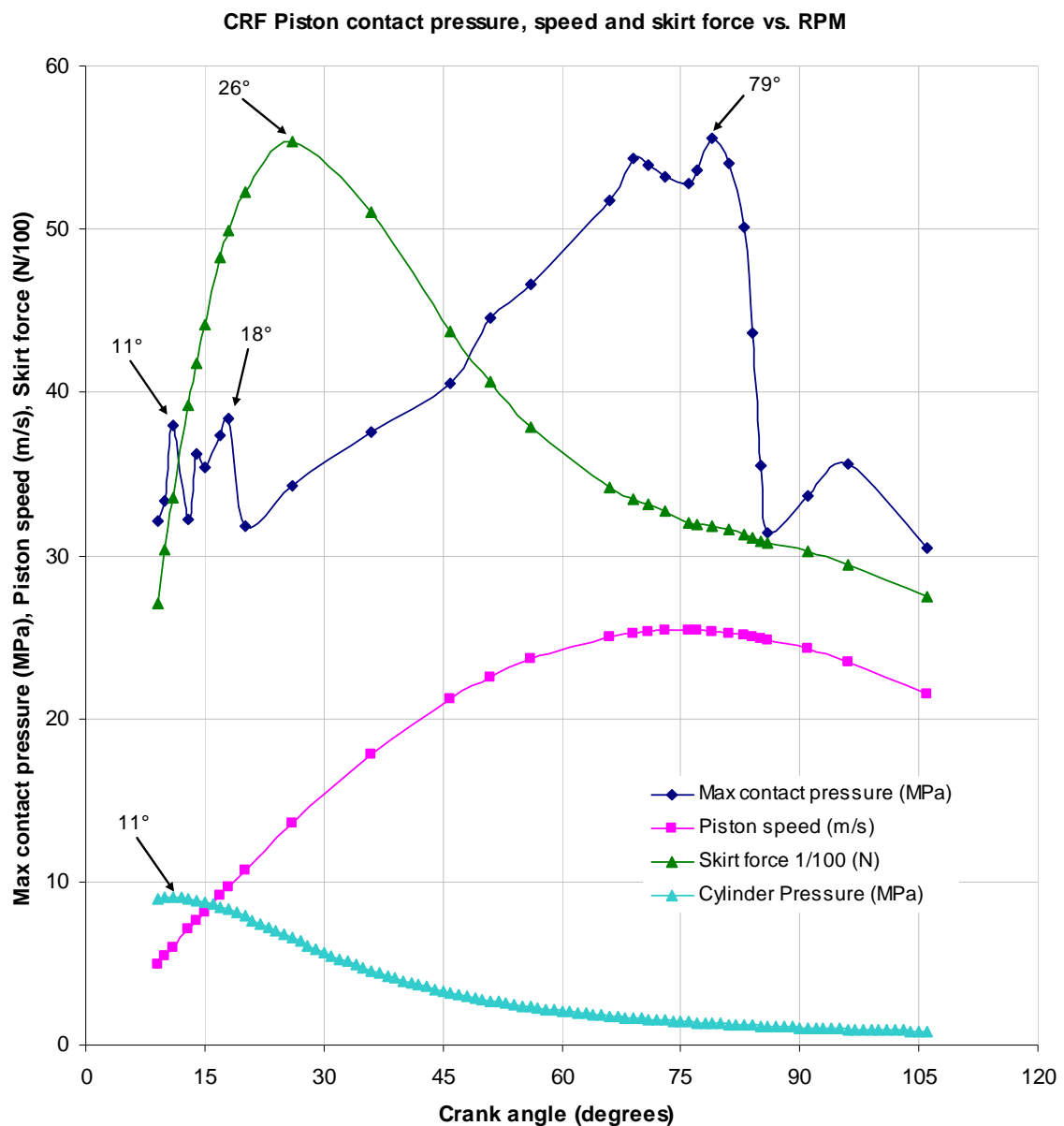
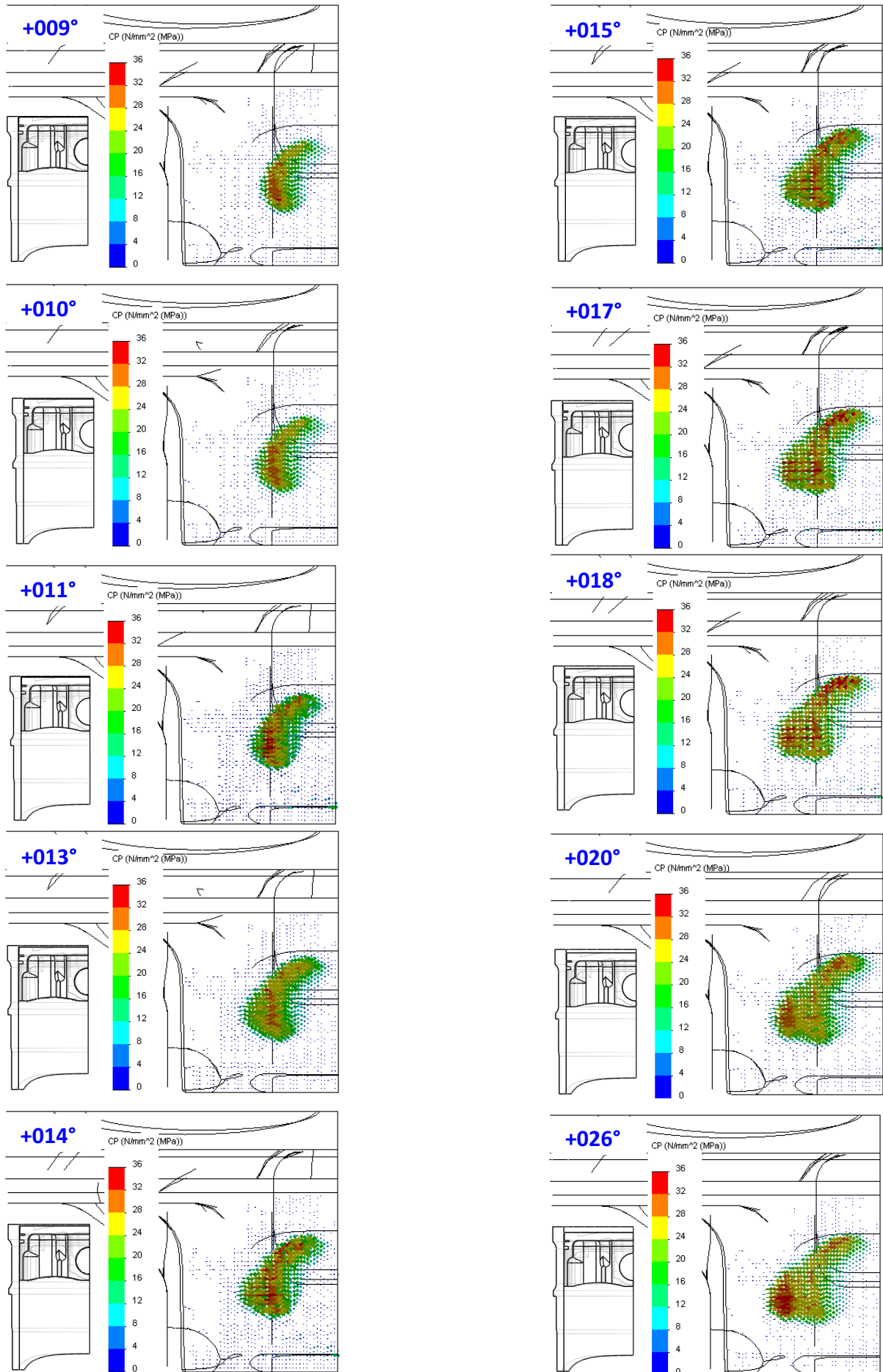
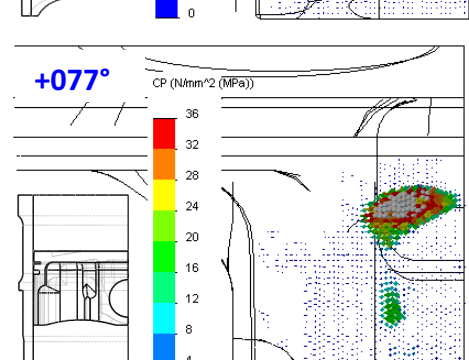
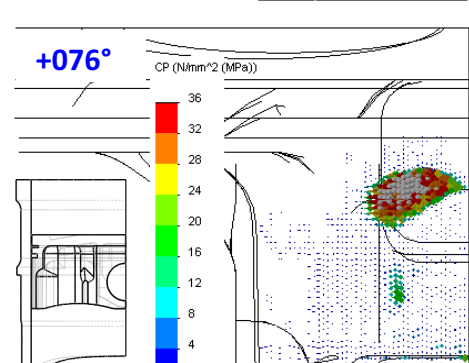
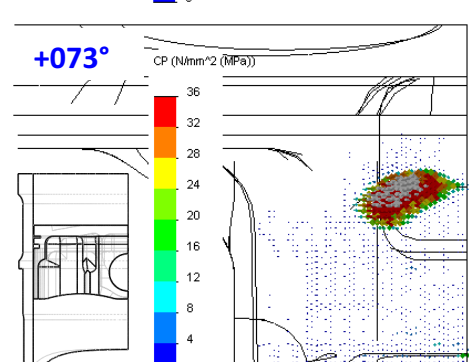
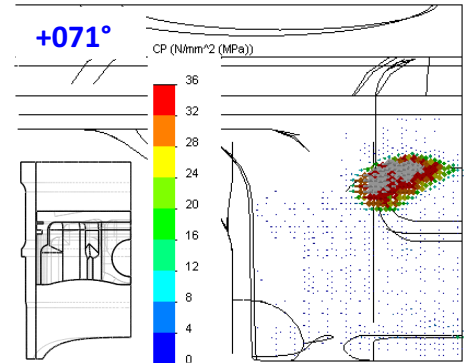
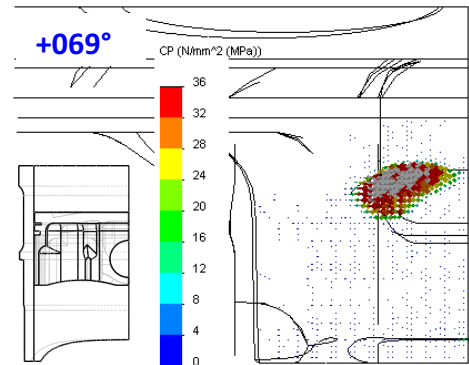
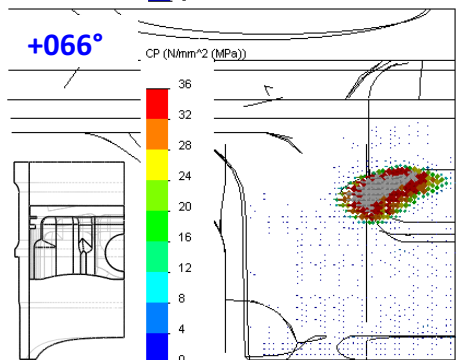
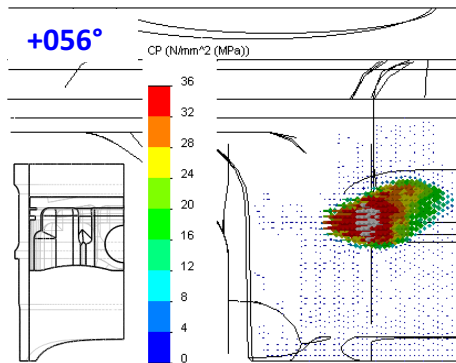
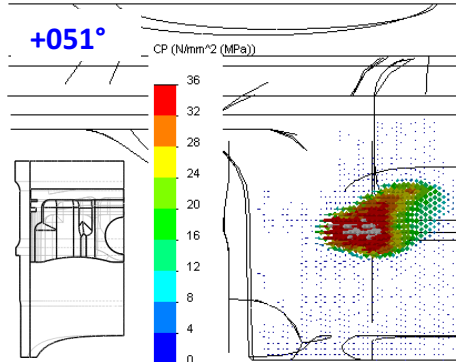
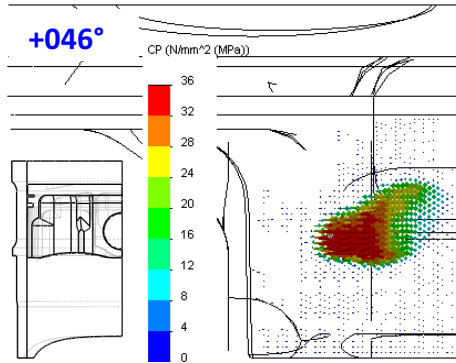
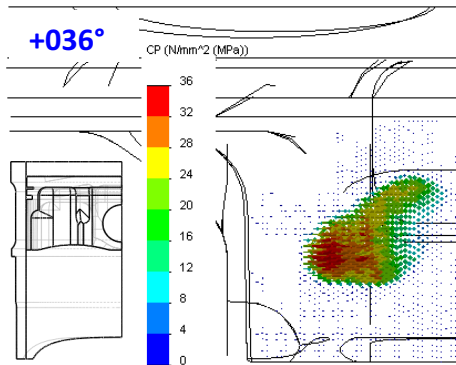


Figure A3.1 Piston to bore contact results







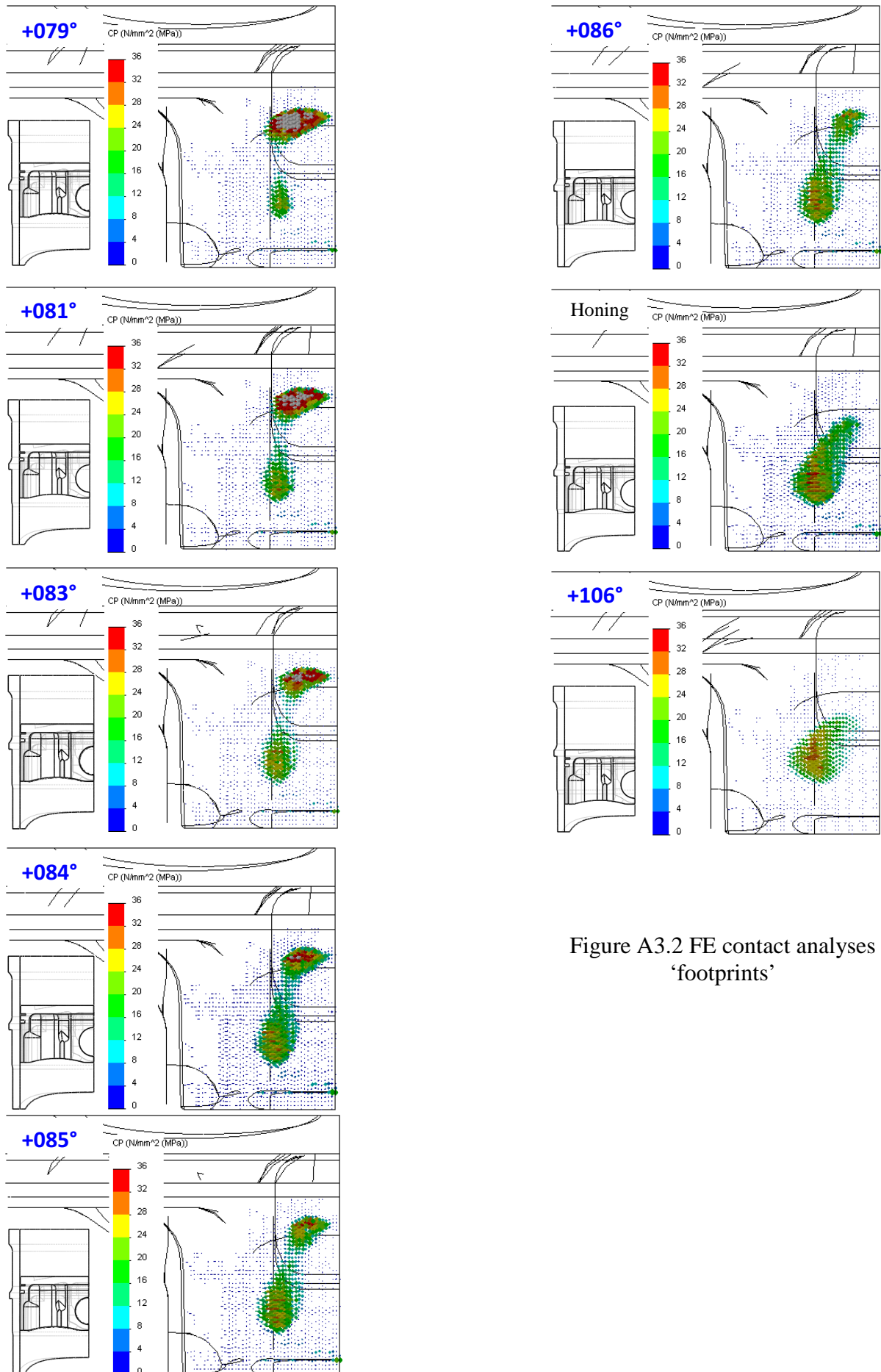


Figure A3.2 FE contact analyses  
'footprints'

## Appendix 3

Calculation time for the preceding results is significant. Details of hardware, software and time per angular solution are given in table A3.1 and figure A3.3.

Software vendor	Solidworks™ Corporation	
Software	Solidworks™ Professional 2009 SP4.0x64	
Operating system	Windows™ XP64	
Hardware vendor	Dell™ Corporation	
Hardware	Precision T7500	
Architecture	2 off Intel W5590 4 core 45nm scale processors 3.33GHz. 24Gb DDR3 ECC SDRAM 1333MHz nVidia Quadro FX 4800 graphics hardware	
Thermal Analysis	Analysis type	Thermal (steady-state)
	Element type (primary size)	10 noded tetrahedral (5mm)
	Element constraints (adaptive)	2mm mesh at contacts (no)
	Jacobian check points per element	29
	Number of elements (nodes, DOF)	23820 (37155, 109126)
Structural Analysis	Analysis type	Large displacement
	Element type (primary size)	10 noded tetrahedral (5mm)
	Element constraints (adaptive)	2mm mesh at contacts (yes)
	Jacobian check points per element	29
(pass 1)	Number of elements (nodes, DOF)	81513 (115944, 343247)
(pass 2)	Number of elements (nodes, DOF)	42024 (65628, 194141)
(pass 3)	Number of elements (nodes, DOF)	51888 (80553, 237763)
Solution time	Total per angle (hours)	3.6 hours (see figure 2)

Table A3.1 Computational requirements for one crank angle

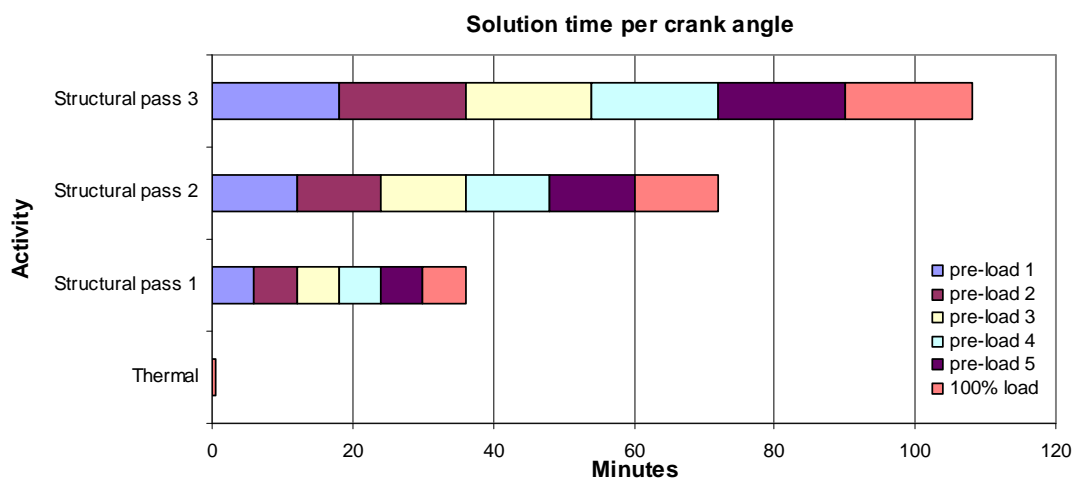


Figure A3.3 Typical solution time per crank angle investigated

## Appendix 4

### Development of CRF floating liner

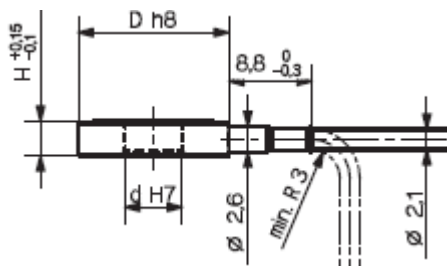
#### A4.1 Design and development

The development of a floating liner presented several engineering challenges – compounded by the restriction of operating within the given CRF minimal mass / minimal packaging architecture. Key challenges were:

- Adequate resolution of differential vertical force (piston-to-bore friction).
- Consideration towards manufacturing methods, conventional materials, and the retention of existing Ni-SiC bore coating.
- Decoupling of cylinder head clamp load transferral through cylinder bore structure.
- Removal of crevice area gas pressurisation on the upper surface of the cylinder bore.
- Lateral constraint of bore without inferring excess translational friction from assembly's temperature through to the operating temperature.
- Adequate access for assembly and disassembly.

Force transducers were chosen to measure the resolved cylinder bore frictional force. Due to limited space availability the smallest sensor commercially available was sought. Kistler Holding AG part number 9131B pancake sensor was selected with specifications given in figure A4.1.

Type	Measuring Range $F_z$ [kN]	Overload $F_z$ [kN]	Sensitivity [pC/N]	Rigidity [kN/ $\mu$ m]
9130B...	0 ... 3	3,5	$\sim$ 3,5	$\sim$ 1,0
9131B...	0 ... 2,5	3	$\sim$ 4,0	$\sim$ 0,7



Type	D [mm]	d [mm]	H [mm]	Weight (without cable) m [g]
9130B...	8,0	2,7	3,0	1
9131B...*	7,0	–	3,0	1

Linearity (preloaded)	%/FSO	$\leq \pm 1,0$
Hysteresis (preloaded)	%/FSO	$\leq 1,0$
Response threshold	N	$< 0,01$
Operating temperature range	$^{\circ}$ C	$-20 \dots 120$
Preloading force (recommended)	$F_v$	
Direct connection <sup>1)</sup>	%/FS	$\sim 50$
Shunt mode	%/FS	$\sim 20$
Protection rating <sup>2)</sup>	EN60529	IP65

Figure A4.1 Kistler 9131B Force transducer specification

To ensure planar stability the minimum number of sensors required was 3 units. However, 6 units were utilised so as to remove the stiffness influence of a necessary coupling of the cylinder liner to the water jacket. The transducers were arranged in pairs (figure A4.2) nominally at 120° separation.

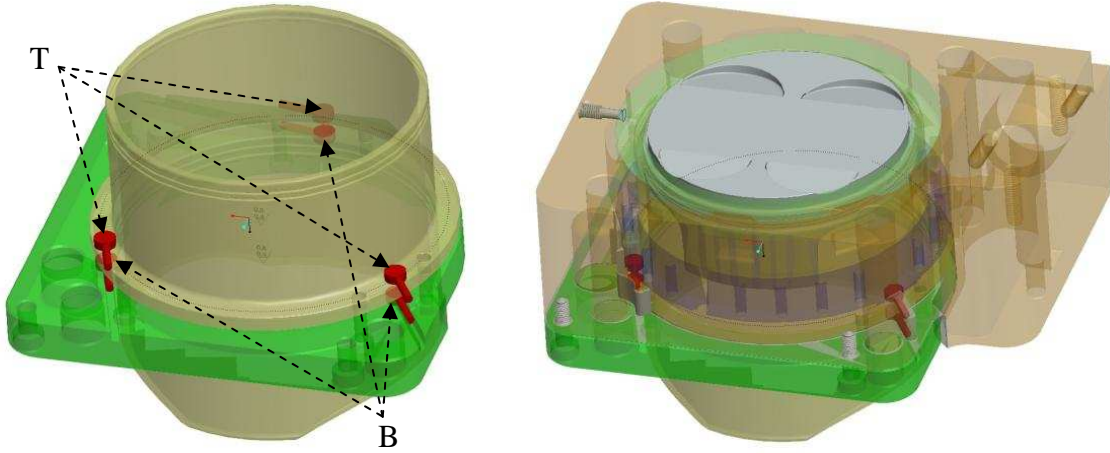


Figure A4.2 Kistler 9131B transducer ‘pairing’ within assembly

From figure A4.2 it can be seen that downward force registers an increased output in the lower pair (B) sensor, and a similar (post-calibration) reduction in the upper pair (T) sensor. In a single transducer set-up the stiffness ratio of the clamped structure to the transducer must be considered with the effect of reducing result resolution. In the paired configuration the force is more accurately computed using equation (A4.1).

$$\Delta F = \left( \frac{\Delta F_{1T} + \Delta F_{1B}}{2} + \frac{\Delta F_{2T} + \Delta F_{2B}}{2} + \frac{\Delta F_{3T} + \Delta F_{3B}}{2} \right) \quad (\text{A4.1})$$

The diameter of the available sensor, minimum recommended liner wall thickness, and engine architecture constraints excluded the use of a low elastic modulus light alloy cylinder liner. Furthermore, sensor bending limitations and stress concentrations due to the concentrated loads excluded the use of an aluminium alloy. 20MnV6 (table 5.4) low alloy steel was therefore chosen, due to its long successful use in cylinder liner applications when coated with Ni-SiC bore coating (Capricorn Automotive).

Due to differential temperature in operation, an absolute need to control clearance between cylinder liner and housing, and minimise induced stresses into the OEM aluminium structure, the choice of housing material was restricted to materials with a coefficient of thermal expansion between 16 and 18ppm/K, and yield strength significantly higher than the original CRF barrel. Austenitic stainless steel grade 304 satisfied these criteria (table A4.1), with the added benefit of minimal corrosion in an aqueous environment.

Property	OEM Barrel body	Floating liner barrel body
Material	Aluminium (casting) alloy A356	Austenitic Stainless Steel 304
Hardness Rockwell B	55	82
UTS	234min (260 typ.)	621MPa
YS	165min (195 typ.)	290MPa
Modulus of elasticity	72.4	193GPa
Poisson's ratio	0.33	0.24
CTE, linear 0-100C	21.4E-6 m/m°C	16.9E-6 m/m°C
Thermal conductivity, 100C	151W/mK <sup>-1</sup>	16.2W/mK <sup>-1</sup>

Table A4.1 Physical and mechanical properties of construction

Modal analysis of the steel liner was performed to check for forcing frequency issues due to engine operation. Maximum test engine speed was 9,500rpm (158Hz) and liner design work targeted to be significantly above this value. Two model configurations were used: unconstrained and constrained on 6 points equating to the force transducer pick-up points. Figure A4.3 details the meshed solid used (LHS), unconstrained configuration mode 7 response (centre) and constrained mode 1 response (RHS). Table A4.2 details output results from modal analysis.

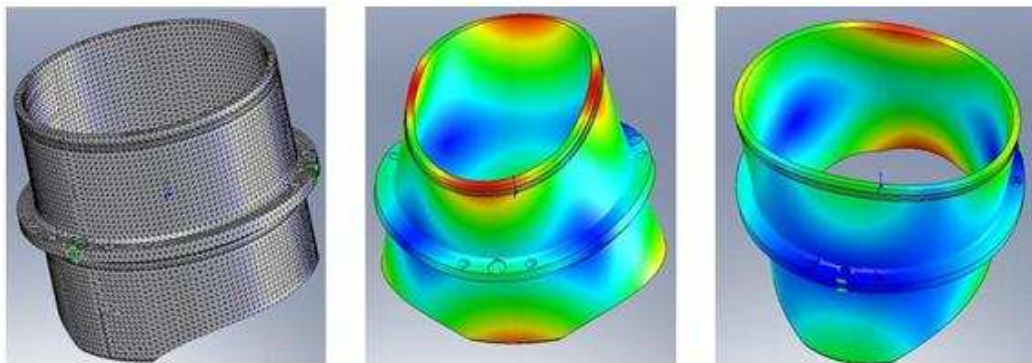


Figure A4.3 Modal analysis of 'floating liner'



Unconstrained configuration results		Constrained configuration results	
Mode No.	Frequency(Hertz)	Mode No.	Frequency(Hertz)
1	0	1	1599
2	0	2	1622.3
3	0	3	2856.2
4	0	4	3097.4
5	0	5	4117.6
6	0	6	4487.4
7	1166	7	4539.9
8	1181.8	8	4895.5
9	1383.2	9	5021.7
10	1388.3	10	5127

Table A4.2 Modal analysis tabulated results

To prevent spurious readings in service from the cylinder head clamping load and unload due to gas pressure a labyrinth seal is employed. This allows the de-coupling of the required seal clamping load from the actual liner, thereby allowing quasi-unconstrained vertical displacement. Figure A4.4 shows the top constrained 20MnV6 alloy steel seal ring (green component, vertically constrained), which is an overhanging precision fit over the same material floating liner. The ID intrusion of the alloy steel seal ring required a ‘stepped’ piston crown (figure A4.4).

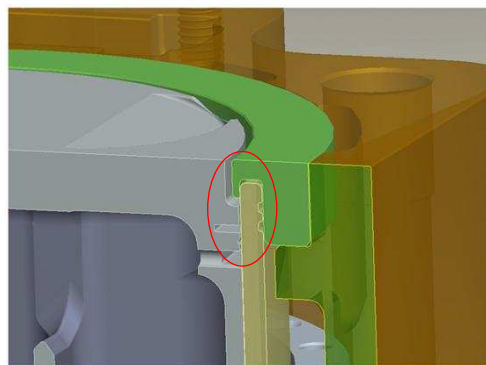


Figure A4.4 Upper detail of floating liner assembly

The seal ring lip was analysed for deformation under gas pressure and manufacturing limits, resulting in a designed radial gap of 20µm. Very small volumes of pressurised combustion gas progress through this channel. However, in this case there is an expansion volume directly above the upper surface of the liner, which is vented to the atmosphere. Sealing against any

coolant ingress into both the engine upper and lower compartments from the barrel water jacket is provided by means of 70+ shore Nitrile rubber (Buna N) 'O' rings. Typical modulus of elasticity for Nitrile rubber is 0.01-0.02GPa with a minimum elongation of 200% (IdeMat, Delft University of Technology). The low elastic modulus ensures minimum vertical traction yet, due to installed radial compression, provides good sealing performance.

'Stick slip' and corrosion protection between the liner, top seal ring, and water jacket is reduced by coating the 20MnV6 components with Apticote® 450F (Poeton Industries Ltd., UK), a composite electrode-less nickel coating containing PTFE. Applied at 6-8µm per surface with high consistency 450F provides low friction (<0.13), reduced surface galling, and wear resistance ten times that of unplated steel (Poeton Industries Ltd, **Lloyd, (2008)**).

The floating liner assembly consists of 6 transducers arranged in pairs to measure in-cylinder vertical friction. These are connected to 2-off Kistler ICAM Industrial charge amplifiers, part number 5073A311 (figure A4.5). Each charge amplifier has three inputs, with one unit amplifying the top three pressure transducers and the other amplifying the bottom three. The gain of each channel can be adjusted independently within software (LabView). The input to the charge amplifier is charge measured in coulombs with the amplified output in volts. The gain is adjusted with 2 settings; the sensitivity which adjusts the conversion of coulombs to 'units', and the range which converts these 'units' to volts. The full-scale deflection of the output is 10V. Current sensitivity was set to 4pC/MU (million 'units') and the range is 2500MU/10V. Combining these the total gain of the amplifier is 1000pC per volt, with a maximum input of 10,000pC providing an output of 10V.

Downstream of the charge amplifiers was a National Instruments BNC-2110 patch panel, further connected to a National Instruments (NI) PXI-6133 high-speed analogue-to-digital module, enclosed within a NI PXI-1031 chassis containing an acquisition-control computer. Calibration was conducted outside of the engine with the floating liner assembly complete with force transducers and 5073A charge amplifiers connected. Calibrated masses were used and the output signal was calibrated for zero point and gain by means of the RS-232 interface present on each amplifier for each of the transducers (figure A4.6).

National Instruments 'LabVIEW' (abbreviated 'LV') is commonly used for data acquisition, instrument control, and industrial automation on a variety of platforms including Microsoft



Windows, UNIX, Linux, and the Mac OS. LabVIEW version 8.5 (released 2007) was used for capturing, manipulating, and storing transducer output. The programming language used in LabVIEW, named 'G', is a data flow programming language. Execution is determined by the structure of a graphical block diagram (the LV-source code) on which the programmer connects different function-nodes by drawing connections. The block diagram produced for data capture and export is shown in figure A4.7, and the resulting operator window is shown in figure A4.8.

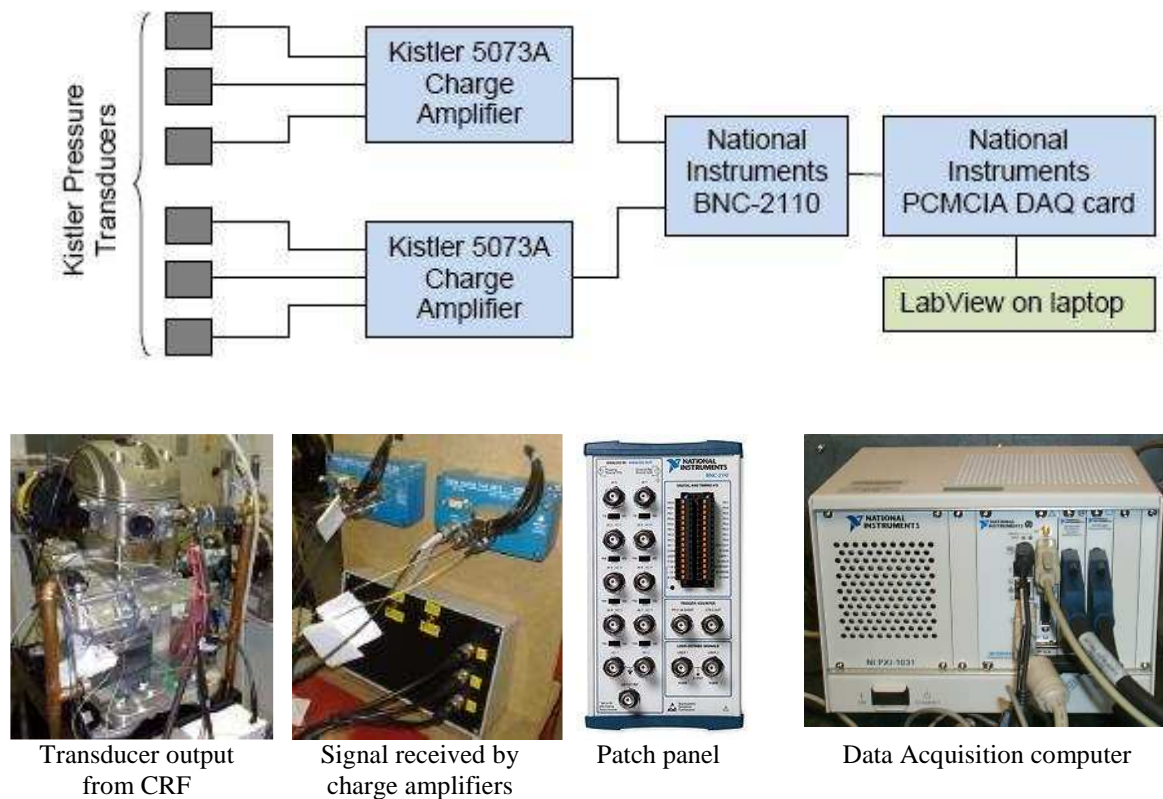


Figure A4.5 Flowchart and physical components used in data acquisition

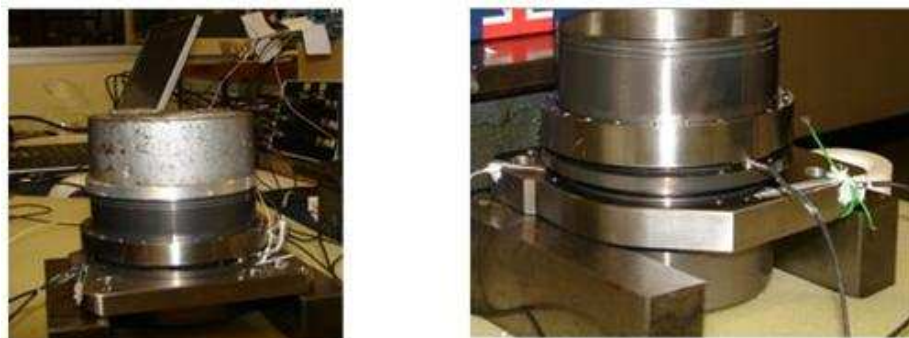


Figure A4.6 Calibration of floating liner and charge amplifier set-up

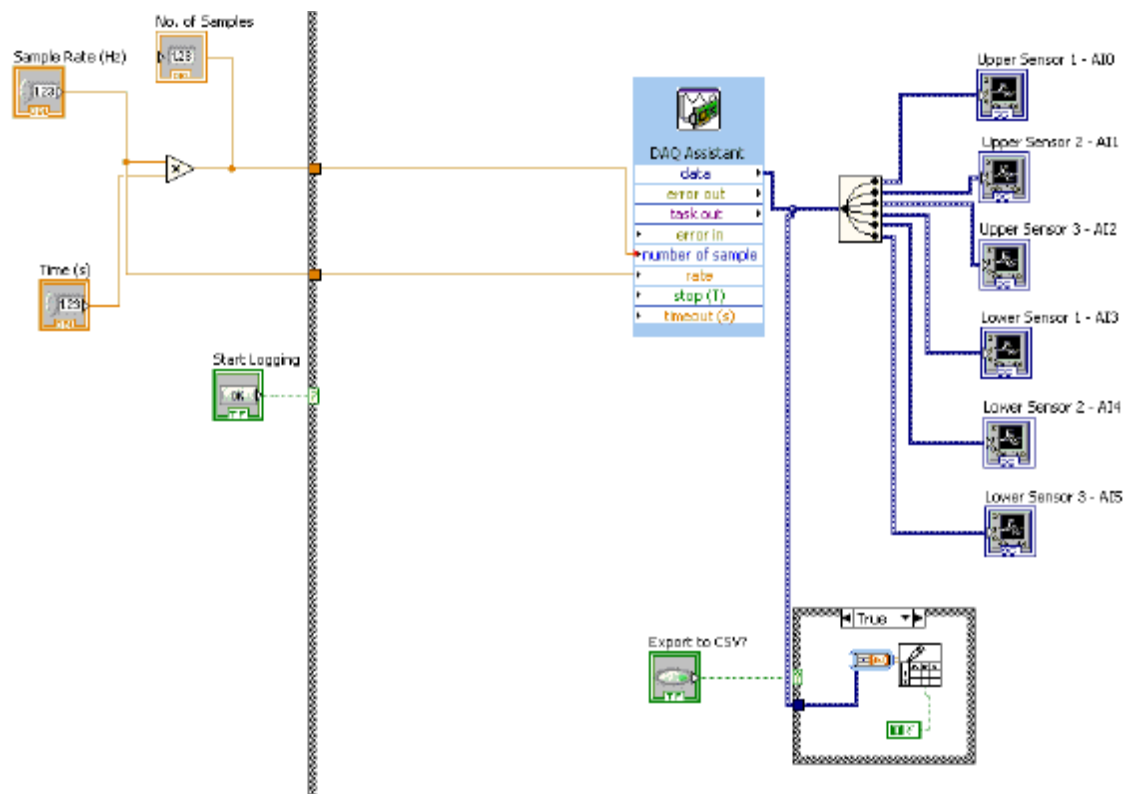


Figure A4.7 LabView block programming interface

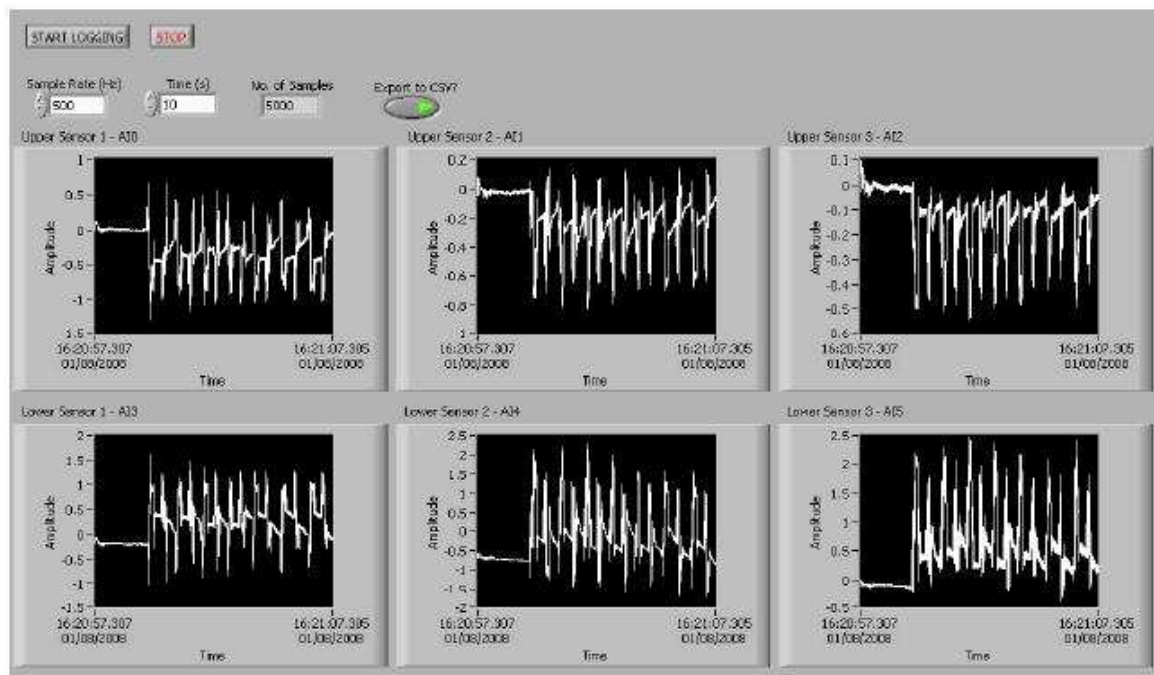


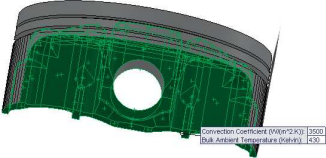
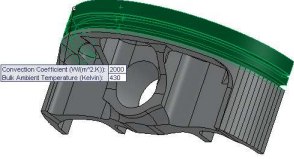
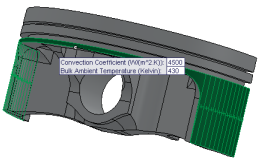
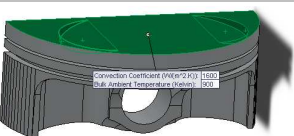
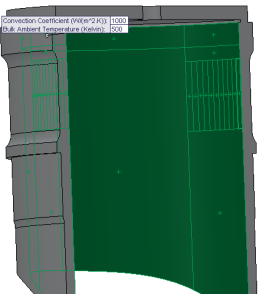
Figure A4.8 LabView operator interface / results screen

## Appendix 5

### Input parameters and boundary conditions

#### A5.1 QSTS Thermal boundary conditions

Table A5.1 details the convection coefficients prescribed surface temperatures and boundary conditions applied to the CRF QSTS model. All surfaces not detailed in table A5.1 may be considered perfectly insulating ( $0\text{Wm}^{-2}\text{K}^{-1}$ ).

	Description	Type/Values
	Underside of piston not including pin bore surface. Skirts and crown not included	Convection 430K (157°C) $2500\text{Wm}^{-2}\text{K}^{-1}$
	Ring pack of pistons including ring grooves. Does not include skirts, crown, pin bore, 3 <sup>rd</sup> land and underside	Convection 430K (157°C) $2000\text{Wm}^{-2}\text{K}^{-1}$
	Piston skirts and 3 <sup>rd</sup> land only	Convection 430K (157°C) $4500\text{Wm}^{-2}\text{K}^{-1}$
	Piston top surface (crown) only	Convection 900K (627°C) $1600\text{Wm}^{-2}\text{K}^{-1}$
	Liner internal surfaces at nominally bore diameter	Convection 500K (227°C) $1000\text{Wm}^{-2}\text{K}^{-1}$

	Liner OD lower engagement diameter	395K (122°C) Prescribed temperature
	Liner OD mid section (water jacket)	Prescribed temperature 389K (116°C)
	Liner OD upper section (above water jacket)	Prescribed temperature 403K (130°C)
	Liner internal section corresponding to liner top face not engaged by gasket	Prescribed temperature 418K (145°C)
	Thermal bonding of gudgeon pin outer surface to piston pin bore surface (perfect conductor)	N/A

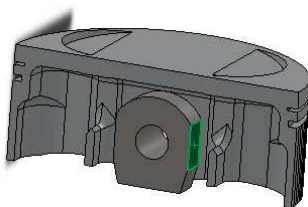
Table A5.1 Thermal boundary constraints for QSTS analysis

## A5.2 QSTS Structural analysis loads

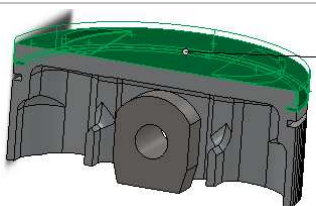
Applied forces are given in table A5.2. These loads are presented for the discrete cases presented in Appendix 3 and applied to positions further detailed in table A5.3.

Degrees after TDC	Cylinder pressure (Nm-2)	Half side force (N)	Vertical acceleration (ms-2)
9	8.923E+06	-1.354E+03	2.429E+04
10	9.007E+06	-1.519E+03	2.417E+04
11	9.035E+06	-1.677E+03	2.404E+04
13	8.957E+06	-1.962E+03	2.375E+04
14	8.866E+06	-2.088E+03	2.359E+04
15	8.755E+06	-2.206E+03	2.342E+04
17	8.486E+06	-2.414E+03	2.304E+04
18	8.310E+06	-2.497E+03	2.283E+04
20	7.884E+06	-2.616E+03	2.238E+04
26	6.567E+06	-2.770E+03	2.079E+04
36	4.576E+06	-2.551E+03	1.738E+04
46	3.205E+06	-2.189E+03	1.323E+04
51	2.721E+06	-2.033E+03	1.098E+04
56	2.324E+06	-1.894E+03	8.648E+03
66	1.761E+06	-1.707E+03	3.954E+03
69	1.640E+06	-1.675E+03	2.574E+03
71	1.569E+06	-1.658E+03	1.670E+03
73	1.496E+06	-1.636E+03	7.811E+02
76	1.392E+06	-1.602E+03	-5.193E+02
77	1.363E+06	-1.595E+03	-9.428E+02
79	1.316E+06	-1.590E+03	-1.774E+03
81	1.267E+06	-1.579E+03	-2.581E+03
83	1.216E+06	-1.563E+03	-3.363E+03
84	1.190E+06	-1.553E+03	-3.744E+03
85	1.165E+06	-1.544E+03	-4.119E+03
86	1.143E+06	-1.537E+03	-4.486E+03
91	1.056E+06	-1.515E+03	-6.214E+03
106	8.376E+05	-1.374E+03	-1.022E+04

Table A5.2 QSTS analysis applied loads



Side force (table A5.2) is applied to flat face shown. Force transfers through rod/pin into piston



Cylinder pressure (table A5.2) is applied to piston crown, headland and first ring groove surfaces. Pressure is also applied to the cylinder bore between top of the ID surface and the position where the top ring is located for a given crank angle

Table A5.3 QSTS analysis applied loads

### A5.3 Lubricant properties QSTS thermo-elastic analysis

Chapter 7.5 detailed analytical work based on thermo-structurally deformed input geometry. The chosen lubricant for analysis work was as per standard fill Honda CRF (ref chapter 5.7.3) manufactured by BP Castrol and used for CRF engine testing. The primary lubricant parameter of interest was viscosity and advice was sought from the lubricant manufacturer (**Brett, (2009)**) providing an absolute viscosity of 5cSt considering engine type and operating conditions (water and oil temperature etc.). Table A5.4 provides technical details of the BP Castrol lubricant.

Test	Method(s)	Unit	Typical
Density @ 15C, Relative	ASTM D4052		0.875
Appearance	Visual		Clear & bright amber liquid
Viscosity, Kinematic 100C	ASTM D445	mm <sup>2</sup> /s	14.5
Viscosity, Kinematic 40C	ASTM D445	mm <sup>2</sup> /s	100
Viscosity Index	ASTM D2270		149
Viscosity, CCS -25C (10W)	ASTM D5293	cP	7000 max
Flash Point, PMCC	ASTM D93	°C	194
Ash, Sulphated	ASTM D874	% wt	1
Total Base Number, TBN	ASTM D2896	mg KOH/g	8

Table A5.4 Lubricant properties

### A5.4 Calculation of part operating temperatures

To verify the numerical thermal model, FEA predicted temperatures were compared with those inferred by experimental retained hardness measurement. Structural aluminium alloys generally suffer reduction of mechanical properties, including hardness, with elevated temperature exposure (**Liu *et al*, 2008**). This reduction in hardness depends on several factors notably: exposure temperature, exposure time, alloy composition and condition. Figure A5.1 details typical time vs. temperature annealing for a 4000 series alloy AA4032-T6 with an initial hardness of 117Hb.

From the resulting softening curves (figure A5.1), indicative exposure temperature for a given hardness (constant exposure time) can be constructed (figure A5.3) by means of interpolation. For example, from figure A5.3, a component with a 50 hrs run time measuring 65Hb hardness would indicate a running temperature of 250°C. Figure A5.2 shows actual component hardness measurements to determine running temperature and thereby validate chosen heat transfer coefficients (chapter 7.4.2).

Figure A5.1 Retained hardness at temperature (softening curves), AA4032-T6



Figure A5.2 Hardness measurements on piston after running

Figure A5.3 Retained hardness vs. temperature, AA4032-T6



## Appendix 6

### Peer-reviewed publications

---

The following pages reprint publications made by the author and co-authors.

- A6.1      **Dwyer-Joyce, R.S., Green, D.A., Balakrishnan, S., Harper, P., Lewis, R., Howell-Smith, S., King, P.D. and Rahnejat, H.** (2006): The measurement of liner–Piston skirt oil film thickness by an ultrasonic means, SAE technical paper P5-06P-596 (2006-01-0648).
- A6.2      **Rahnejat, H., Balakrishnan, S., King, P.D. and Howell-Smith, S.** (2006): 'In-cylinder friction reduction using a surface finish optimization technique', Proceedings of the Institution of Mechanical Engineers, Part D: Journal of Automobile Engineering, 220(D9), 2006, pp 1309-1318.
- A6.3      **Balakrishnan, S., Howell-Smith, S., Rahnejat, H.** (2005): Investigation of reciprocating informal contact of piston skirt to surface modified cylinder liner in high performance engine. IMechE Vol.219 Part C.
- A6.4      **Balakrishnan, S., Howell-Smith, S., Rahnejat, H. and Dowson, D.** (2003): Investigation of reciprocating conformal contact of piston skirt and ring pack to cylinder liner under transient condition, 30<sup>th</sup> Leeds-Lyon Symposium.